Wind Plant Annual Energy Production Maximisation and Efficiency Improvement with considerations for Thrust and Turbulence Intensity

A Thesis Presented for the
Doctor of Philosophy
Degree

in

Electrical Engineering
University of Cape Town, South Africa

Mfon Okokon Charles
2025

Declaration

I hereby declare that:

1. This thesis is my own unaided work, both in conception and execution, and that apart from the usual guidance of my supervisor, I have received no assistance except where explicitly stated otherwise in the text.

2. Except where explicitly stated otherwise in the text, neither the substance nor any part of the thesis, has been submitted in the past, or is being submitted, or is to be submitted in whole or in part, for a degree or professional qualification in the University, or any other University.

   Parts of this work have been published in AFRICON 2023 and IEEE ACCESS (Volume 12).

I thereby grant the University a free license to reproduce the above thesis in whole or in part, for the purpose of research.

Name: MFON OKOKON CHARLES

Signature:

Date: May 11, 2025

I dedicate this dissertation to my late Dad, Professor Joseph Okokon Charles for being such a loving and examplery father and husband, and most especially for bringing me up in the ways of the Lord, Jesus Christ.

Acknowledgments

First, special thanks is reserved for the maker and giver of all good things, Jesus Christ for the several graces made available from the beginning to the end of this pulsating Ph.D journey. If God were not on my side, maybe I would have given up when the going was tough. Sincerest thanks goes to my family for the moral and spiritual support. God bless you immensely for all you do. Heartfelt thanks and love goes to my beautiful and dear wife, Elizabeth Charles. You have been a rock by my side in the last few months. I specially recognize the Petroleum Development Trust Fund (PTDF), Nigeria, and the Tertiary Education Trust Fund (TETFund), Nigeria, through the University of Calabar, for the funding made available for this research. Without you as the vessel and without your financial support, I would not have this beautiful story to tell. Thank you very much. I recognize in a special way, my supervisors Associate Professor David T. O. Oyedokun and Professor Mqhele E. Dlodlo for their moral, technical and all-round support and guidance throughout this journey. With both of you, the journey though tough, was definitely rewarding. To Prof. Dlodlo, thank you for accepting me as a Ph.D student despite the scantiness and unrealistic nature of my initial research proposal and moreso, taking me in notwithstanding the fact that you already had many Ph.D students to supervise. To Associate Professor David, thank you for not just being a supervisor, but a friend. Thank you too for accepting to be my main supervisor when Professor Dlodlo stepped into the co-supervisory role because of his appointment as the vice chancellor, National University of Science and Technology, Bulawayo, Zimbabwe. Thank you, and thank you again for your encouragement, patience, kindness, gentleness and rigorosity while advising, instructing, and working with me. I also recognise the Centre for Broadband Networks, Department

of Electrical Engineering, University of Cape Town for her financial, technical and moral support.

Abstract

Power maximisation in a wind plant (WP) is a necessary and continuous procedure to maintain a cost/benefit ratio required for profit making on the capital investment. Limited land availability with a good wind resource or high land leasing costs imposes close turbine deployments onshore, which increases the wind power plant power (WPP) density. However, the resulting shorter turbine-to-turbine (T-2-T) distances advance increased wake interactions between turbines that increase turbulence intensities and consequently loads within the WP hence hampering its power and energy efficiency. Although sparse turbine deployments are common offshore to reduce wake effects and maximise efficiency, these resulting large T-2-T distances could increase operational and maintenance costs due to long cabling and tedious movement between turbines. Current WPP optimisation studies employ layout optimization, turbine-level control, and plant-wide set-point optimisation to maximise WP power and/or minimise turbine loads, with a majority favouring layout optimisation over regular layouts. Layout optimisation, however, does not guarantee consistently large T-2-T distances throughout the wind plant in any wind direction and would not promote computational costs reduction imposed by turbine set-point optimisation in multi-directional wind plants. However, besides their more appealing outlook, regular layouts could afford directions of large T-2-T distances which promote low TI, low deficit, and where non-optimized operational benefits (e.g. reduced computational and communication overhead) can be enjoyed, along with directions of tight T-2-T distances to also enjoy optimized operational benefits (e.g. high turbine and power density). To exploit this feature, this study proposes and implements an axial induction-based cooperative power maximisation for annual energy production (AEP) maximisation in a hexagonally deployed multi-directional wind site with space restrictions, using particle swarm optimization (PSO) and genetic

algorithm (GA). Initial results confirm a significant increase in wind plant power and AEP, accompanied by increase in turbine-level turbulence intensity, thrust coefficient, and thrust as consequences imposed by the unconstrained optimisation-enhanced power increments. These observations have not been previously highlighted nor addressed in the literature of WP power optimisation. In addition to implementing a thrust coefficient-constrained WP power maximisation to manage turbine thrust coefficient and thrust, a novel upstream sectored implementation of a well-studied wake model is applied to improve the mean wind speeds at turbine positions, by eliminating upstream turbines' wake effects at a downstream turbine based on their axial and radial distances from the downstream turbine, and furthermore, based on their axial induction factors. Final results show a WP AEP gain of up to 25%, with significant improvements in WP energy efficiency that compares favourably with the conventional $7D$ non-optimised deployment typical of conventional WPs. A reduction in TI and turbine thrust magnitude is also achieved. These findings have implications on turbine loads, capital and operational expenditure, land use and space optimisation, visual aesthetics and environmental impact, and the economic viability of hexagonally deployed WPs in comparison to optimised layout WPs and conventionally deployed WPs.

Table of Contents

List of Tables

List of Figures

List of Abbreviations

C_P	Power Coefficient
C_T	Thrust Coefficient
AEP	Annual Energy Production
CAPEX	Capital Expenditure
CFD	Computational Fluid Dynamics
DOF	Degree of Freedom
GA	Genetic Algorithm
HAWT	Horizontal axis wind turbine
IEC	International Electrotechnical Commission
LES	Large-eddy simulations
LIDAR	Light Detection and Ranging
MWT	Megawatt turbine
OPEX	Operational Expenditure
PSO	Particle Swarm Optimisation
SCADA	Supervisory Control and Data Acquisition
T-2-T	Minimum Turbine-to-Turbine Separation Distance
TI	Turbulence Intensity
VAWT	Vertical axis wind turbine
WASA	Wind Atlas for South Africa
WFT	Wind Farm Turbulence
WP	Wind Plant
WPP	Wind Power Plant
WT	Wake Turbulence

Chapter 1

Introduction

1.1 Background and Motivation

In an effort to fully extract energy from a finite space and minimize capital and operational expenses, many wind turbines are deployed into a wind plant (WP) [5, 6]. This reduces costs of installation and maintenance, connection costs to the grid, thereby improving the cost/benefit ratio. However, positioning wind turbines in a WP introduces aerodynamic interaction between the turbines, which affect the power production and loads on each turbine in the plant [7, 8]. Behind each extracting turbine is a region of reduced wind velocity and a more turbulent flow compared to the freestream inflow wind. High inflow winds hitting a turbine tend to cause a reduced deficit at a downstream position in the wake zone, compared to lower inflow winds. This causes the temptation of wanting to place turbines closer together. However, at the same downstream position in the wake zone, a high inflow wind causes more turbulent mixing compared to a low inflow wind - hence, larger loads. This turbulent mixing results from large magnitude differences in wind speed between the high inflow and reduced wind available in the wake zone. However, this mixing phenomenon also helps to restore the wind in the wake zone to inflow conditions. These interactions between the wind speed, the extracting turbine's control parameter(s), the wake deficit, and the loads, make it very difficult for farm planners to position turbines effectively in a WP and to optimize a turbine's performance considering the effect this will have on turbines around it. In multi-directional WPs, the problem gets even more complex

because the different wind directions could present unique levels and nature of interactions. As a result, improving the power generation in WPs is crucial and often comprises two stages: (1) Pre-deployment (2) Post-deployment.

In the pre-deployment stage, focus is usually laid on optimisation of the turbine layout to allow more wind to be intercepted and hence, more power generated from a given area. Conventionally, this is achieved by intuitively placing turbines (using no recognized pattern) at sufficiently large distances of up to 6 - 10 rotor diameters (6 - 10 D) apart, to allow the wake from an upstream turbine recover to near freestream inflow conditions before it reaches a downstream turbine. This, however, does not maximise the use of a limited available space especially with large rotor diameter wind turbines, thereby rendering this solution unattractive for power density improvement. A widely-studied offshore wind farm - the Horns Rev 1, uses a staggered tetragonal layout, but its effectiveness in managing wake effects depends largely on the staggered nature of the tetragonal lattices, as well as on maintaining a sufficiently large turbine-to-turbine (T-2-T) distance. As a result, studies like [9, 10] have explored alternative layouts that better optimize space and wind resources. Regular hexagonal and regular octagonal lattice structures are also options in the literature with the hexagonal counterpart having an advantage in terms of accommodating the most number of turbines per given area when compared with the octagonal and tetragonal lattice structure [11], while also enhancing T-2-T distances in some directions that are as large as the traditional 6 - 10 D as demonstrated in [12]. Based on specifications in [13], T-2-T distances of that magnitude is enough to sufficiently degrade TI within the plant and allow sufficient wake recovery at a downstream turbine. Optimized/irregular turbine layouts is another pre-deployment improvement strategy which has been studied extensively in the literature as exhibited in [8, 7, 9], and they tend to yield better performance in terms of power production when compared to regular layouts. Even though to the best of the author's knowledge no study has yet demonstrated which is better between optimized layouts and regular layouts in terms of load alleviation, it is expected that this will be greatly dependent on the T-2-T distances within the WP, with loads increasing as T-2-T distance decreases. So, given that turbine positions are determined by an optimizer for optimized layouts, there is no guarantee of pre-determined T-2-T distances in any wind direction compared to the

regular layouts where T-2-T distances are pre-determined by the chosen lattice structure. In most optimisation studies, the optimizer is constrained to not create T-2-T distances below a set threshold distance. However, this threshold distance will only be maintained between some and not all the turbines in the WP for the wind direction considered since this is done by an optimizer and not intuitively. Whereas, in a regular layout such as the tetragonal and hexagonal layouts, these T-2-T distances in addition to being pre-determined are equal between all turbines in any considered direction, giving this deployment pattern an advantage in terms of load alleviation in those directions if the threshold or minimum T-2-T distance is carefully chosen.

The post-deployment stage involves the application of cooperative wind turbine control strategies to optimize the WP's performance in terms of power/energy production, loading, and efficiency. Broadly, WP control strategies employ two means of affecting the turbine's actuation degrees of freedom (DOF) to control the wake behind an extracting turbine, and hence optimize the wind available for turbines behind them. Predominantly, most control studies in the literature employ power curtailment of operating turbines whereby the blade pitch angles, generator torque or speed (which determines the turbine rotor speed), or even a parameter known as the axial induction factor, is adjusted (based on the region of operation of the turbine) to below its optimum value for the inflow wind speed, to optimize the wind in the turbine's wake. Alternatively, the wind in the wake of an extracting turbine can be optimized by applying yaw angle adjustments on upstream turbines to steer their wake away from downstream turbines as seen in [7, 8]. However, these studies admit that this method has the possibility to increase the loads on the yawing turbines. Moreso, these studies deploy turbines at such proximity that wake steering was required in all wind directions - suggesting the possibility of a continuous load build-up throughout these turbines' lifetime if this yaw angle adjustments actually increase loading on the yawing turbines. Recent studies in [14, 15] have proceeded to consider in their study, the trade-off in yaw-based WP power production, due to fatigue load damage considerations. However, both studies employed wake models that do not encapsulate the inherent wake skew observed in turbine wakes even when no intentional yawing is enforced. In addition, the effect on WP efficiency was not considered in these studies.

After the application of a pre-deployment stage layout optimisation, it is commonplace in the literature to arrive at new layouts that are more tightly-spaced compared to the initial layout, since the aim is to increase turbine density within a limited space and consequently power density, while in some cases also accounting for load reduction. Running costs to lease additional surrounding lands would incur extra costs, besides the fact that surrounding land owners are not obliged to sell. In addition, leaving turbines in the traditional sparse deployments would result in large T-2-T distances, making access to individual turbines much more cumbersome, and hence, leading to increased operation and maintenance (O & M) costs over time. Another common challenge that emerges from tightly-spaced or dense turbine deployments is the issue of decreasing WP efficiency. The authors in [4] have investigated and compared the power efficiency of a yaw-based controlled WP with that of the baseline layout of a real WP, while [3] in their study also compared the power efficiency of the same real WP baseline layout with an optimized WP layout. Both studies recorded remarkable improvements in WP efficiency, but these studies did not incorporate load considerations in their studies to ascertain how much trade-off this could impose on both WP power and efficiency.

Several attempts have been made to better manage space, through a combination of layout optimisation with either axial-induction-based optimisation or yaw-based optimisation or both, for a coordinated WP control. However, because the WP power optimisation problem is multi-dimensional and is almost impossible to completely consider all competing parameters, some studies have considered loads, some have employed models that do not completely represent the wake behaviour or shape (Gaussian) based on recent findings, when optimizing WP power. There has been no study however, that has investigated the effect on annual energy production (AEP) and WP efficiency of a densely deployed WP; with considerations for turbine-level turbulence intensities and thrusts; to give an idea what minimum spacing could be acceptable to maintain a competitive WP AEP and efficiency compared with a conventional sparse deployment, knowing that turbulence intensity (TI) is the major driving force for fatigue load build-up [16], while excessive turbine thrusts could cause overexertion .

Considering recent advancements in wake modeling, where static models such as presented in [3] are now capable of producing results that closely resemble in wake shape those of the more complex and time-consuming computational fluid dynamics (CFD) models, there is a particular motivation to take advantage of this to create a more encompassing system where WP power, AEP, and power or energy efficiency is significantly improved, while substantially managing turbulence intensity (TI) and thrust coefficient magnitudes.

Given onshore space constraints and the potential for greater space efficiency offshore, this study explores regular hexagonal layouts with optimally chosen turbine-to-turbine (T-2-T) distances to increase turbine density and enhance a multi-directional wind plant (WP) performance. By employing individual turbine set-point (axial-induction) optimisation, the study optimizes the resulting tightly spaced turbine system (enhanced by the application of the shortest acceptable axial direction T-2-T distance in literature as the minimum T-2-T distance in any direction), while considering total WP power, annual energy production (AEP), energy efficiency, turbulence intensity, and thrust coefficient magnitudes.

1.2 Research Aim

The research presented herein will aim to maximise the AEP in a restricted multi-directional WP through turbine axial-induction optimisation, while maintaining higher energy efficiency than a conventional sparsely deployed WP of similar layout and effectively limiting turbulence intensity and turbine thrust.

1.3 Research Objectives

Conforming with the aim of the study, and considering that the site under study has space restrictions, this research seeks to meet the following objectives:

1. Investigate and apply a turbine layout which can inherently afford increased turbine density and also ensure that T-2-T distances (in line with recommendations from literature) in any direction is at least $5D$, given the multi-directional wind scenario of the studied site.

2. Implement a plant-wide axial induction factor optimisation to maximise the annual energy production (AEP) of the multi-directional WP while ensuring that thrust coefficient and turbulence intensity magnitudes within the WP are constrained within desired limits, and further investigate the variations as minimum T-2-T distance increases from $5D$ to $7D$.

3. Ensure that the optimised energy efficiency of the shortest T-2-T distance deployed WP ($5D$) is competitive when compared to the efficiency of a non-optimised WP with the conventional sparse turbine deployment of $7D$ minimum T-2-T distance of similar layout.

4. Investigate the best directional positioning for the selected turbine layout, to ensure the best possible AEP and efficiency, considering the different wind directions and their frequencies of occurrence.

1.4 Research Hypothesis

Given a tightly deployed WP, it is hypothesized that wind turbine axial induction factor optimisation can be implemented to maximise AEP while concurrently limiting extreme loads caused by increasing turbine thrusts and fatigue damage caused by increasing turbulence intensities, such that the obtained WP efficiency compares favourably with that of a non-optimised and conventionally deployed WP ($7D$ minimum T-2-T distance) of similar layout.

1.5 Research Methodology

To solve the 4-way problem of AEP, turbulence intensity, turbine thrust and efficiency, this study proposes a regular hexagonal layout - which is known to guarantee determinate distances between turbines in all directions. A hexagonal layout by default affords a mixture of tight and sparse but determinate T-2-T distances, depending on the wind direction bin width considered in the WP. This allows the WP take advantage of the benefits of sparse deployments (e.g. reduced TI levels, reduced deficits) in certain directions while still enjoying

the benefits of increased turbine density (e.g increased power capture) in other directions. It also accommodates the possibility of shelving optimisation and hence power curtailment needs in those sparsely spaced directions whose T-2-T distances are sufficiently large enough (close to traditional sparse $7D$ deployments). Hence, reducing computational costs over time. It is envisioned that the efficiency from these directions of sparse deployments will compensate for the lost farm efficiency in other directions where the T-2-T distances are considered small and hence optimisation and power curtailment are necessary. To achieve this, the study opts for a regular hexagonal layout to not only guarantee determinate T-2-T distances in certain directions that will enhance the envisioned gains above, but also to further increase turbine density and hence WP power density. Using a modified implementation of a well-studied Gaussian wake model and turbulence intensity model, the study implements a coordinated plant-wide thrust coefficient-constrained axial-induction based optimisation to curtail the resulting efficiency reduction and increased turbine-level turbulence intensities caused by the turbine density increment, increase the mean wind speeds at turbines and consequently further increase WP power and efficiency, and simultaneously limit turbine thrusts. System model development, simulations, optimisations, plots and analysis are implemented using the Python programming software.

1.6 Scope of the Study

For all analysis, the variable-wind, variable-pitch, 3-bladed Gamesa-g128-5.0MW turbine model is employed. The wind data used for analysis represents a 10-year period between March 2011 to February 2012, October 2012 to December 2014, and January 2016 - May 2022 of the town Butterworth, in the Eastern Cape province of South Africa. A hypothetical WP comprising three different minimum T-2-T distances ($5D$, $6D$ and $7D$) of the studied turbine model is modeled on this onshore wind site, and analyses are made. Nonetheless, the study can easily be implemented with wind data from any other wind site/WP whether onshore or offshore, and using any other modern day megawatt wind turbine, and still obtain comparable gains.

1.7 Research Questions

This research will seek to answer the following research questions:

1. Can any layout be implemented both onshore and offshore on a multi-directional WP scenario to curb parameter optimisations and hence, power curtailments in some wind directions, yet maintain an efficiency which favourably compares with a traditional sparsely deployed non-optimised WP scenario of similar layout?

2. Can a densely-deployed WP be optimised to not only yield a superior AEP but also reduce turbulence intensity and thrusts, while still obtaining an efficiency that compares favourably to that of a traditional non-optimised sparsely deployed WP of similar layout?

3. In the event of seasonal and/or diurnal wind speed variations, can the proposed layout's efficiency still compare favourably with that of the traditional/conventional deployment?

1.8 Research Novelty

To the best of the author's knowledge,

1. Maximise the AEP and reduce turbulence intensities and thrusts within a hexagonally deployed WP, while simultaneously maintaining a comparable efficiency with a conventionally deployed ($6D$ and $7D$) non-optimised case of similar layout (hexagon).

2. Augment a well-studied Gaussian wake model to reduce its computational complexity while still achieving similar performances in terms of deficits at downstream turbines, hence, reducing post-deployment computational complexity and costs.

3. Propose a methodology for tightly spaced turbine deployments offshore that achieves efficiency comparable to onshore set-ups, addressing concerns about potential efficiency losses.

1.9 Publications and planned publications

As stated in the thesis declaration page, parts of this work have already been published in AFRICON 2023 and IEEE ACCESS (Volume 12).

1. The AFRICON 2023 publication carries a summary of the chapter 3 of this study, which sought to numerically and analytically demonstrate the WP problem that the rest of the thesis aimed to find solution(s) to.

2. The IEEE ACCESS (Volume 12) journal publication encapsulates the chapter 4 of this study, which implemented an axial induction-based optimisation with constrained thrust coefficient, to improve actual WP power and AEP within a hexagonal layout of turbines.

3. At the time of submission of this thesis, chapter 5 of this study, which explores a novel implementation of an existing wake model to further improve the AEP gains attained in chapter 4 while also reducing TI effects at turbines in the WP, is being formatted into an IEEE ACCESS template for publication in 2025.

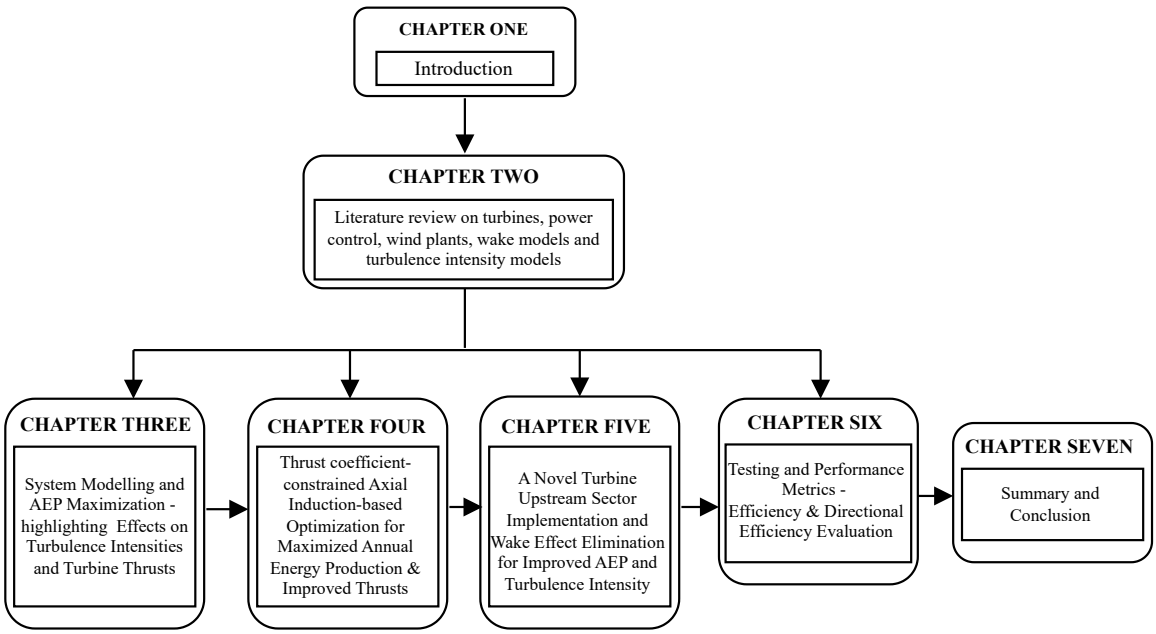

Figure 1.1: Complete Structure showing the study's contribution.

Chapter 2

Literature Review

2.0.1 Technologies in Wind Turbines

Wind turbines are classified as either large, medium or small. Generally, turbines with a diameter fewer than 15 m and a power output below 50 kW are classified as small [17]. However, a majority small wind turbines possess diameters 7 m or lower [17] and power outputs of 1 kW to 10 kW [18]. Medium turbines generally have a rotor diameter of 5-30m and an output of 50-250kW [17], whereas turbines with diameter and output power exceeding those of medium turbines are considered large wind turbines.

Wind turbines can rotate horizontally or vertically. Horizontal axis wind turbines (HAWTs) have rotor blades that spin about the horizontal axis, whereas vertical axis wind turbines (VAWTs) rotate about the vertical axis. They can also be configured as fixed-speed turbines, which rotate at a constant pace independent of wind speed, or variable-speed turbines, which can adjust their blade rotation speed based on wind inflow speed. Another benefit of a variable-speed turbine over a fixed-speed turbine is that the former can operate at optimal aerodynamic efficiency for the majority of the operating cycle, whereas the latter cannot. This is in addition to the fact that all variations in the inflow wind speed in a fixed-speed operation are transferred into torque in the mechanical system and into the electrical system unto the grid [19]. Hence, the current turbine designs in industry are variable-speed designs.

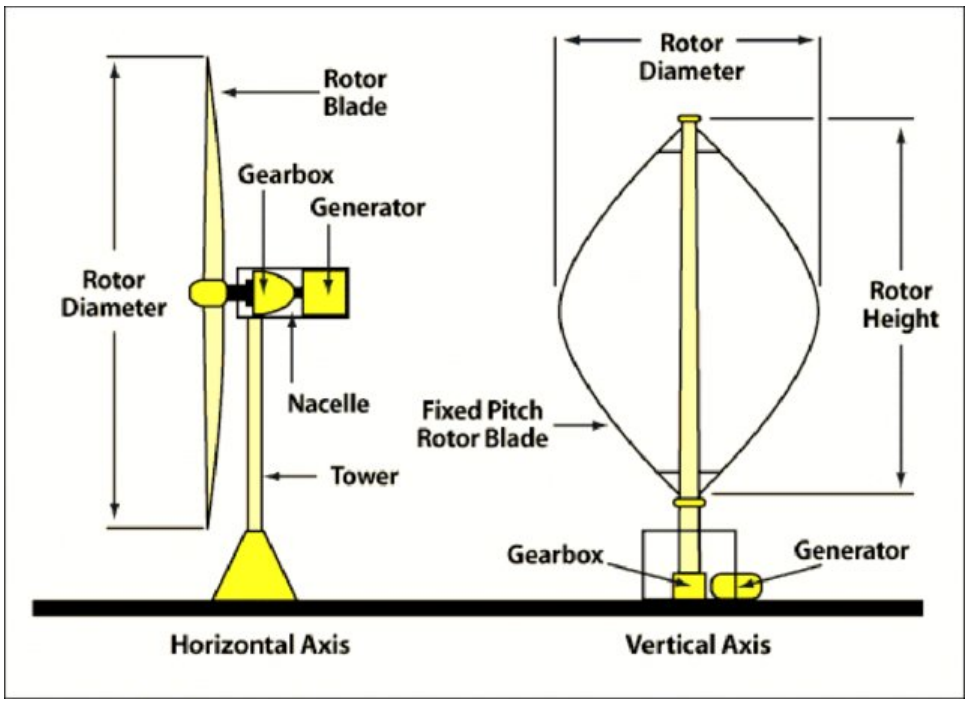

Figure 2.1: Horizontal-axis vs Vertical-axis turbine [20].

It is also possible to have turbines designed as either fixed pitch or variable pitch. The fixed-pitch operation maintains a fixed blade pitch angle δ $w.r.t$ the wind inflow direction) throughout the operating range of the turbine. This is is not very efficient however, as the turbine resorts to a passive stall control (a method that yields poor power regulation due to its dependence on the blade design to limit power generation) at wind speeds above rated. Whereas, the variable-pitch design allows a turbine to vary its pitch angle especially at speeds above its rated wind speed, to shed off excess wind and limit turbine generated power to within its rated capacity. Consequently, variable-speed, variable-pitch turbines are the designs that dominate the market currently.

2.0.2 The Power Curve

A wind turbine's power curve is generated using an anemometer fixed on a wind mast positioned in front of the considered turbine. This curve is developed by measuring the averaged wind speed from the anemometer and observing the resultant electrical energy generated by the considered turbine behind the wind mast. This provides an understanding

of the electrical power output of the turbine at different wind speeds. The cut-in, U_{in}, and cut-out, U_{out}, wind speeds signify the operational limits of the turbine to guaranty the structural health of the turbine while ensuring an extracted energy which is above a minimum threshold [21]. The rated speed is chosen by the turbine manufacturer because wind speeds above this value are rare [21]. From the rated wind speed till cut-out, some form of control must be effected by the turbine to reduce aerodynamic forces on blades and the resulting loading on the entire turbine structure, thus maintaining output power at the rated value [21]. Figure 2.2 depicts an ideal turbine power curve.

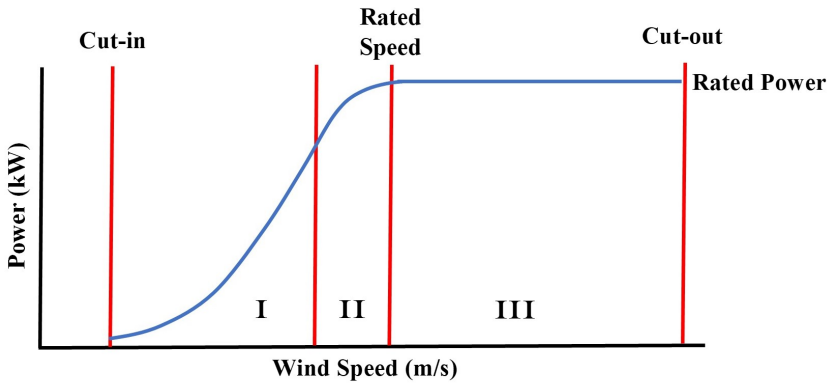

Figure 2.2: An ideal wind turbine's power curve.

Regions I and III of the curve are critical to the turbine's generation of power. Within region I, the inflow wind speed is below rated value, so the turbine is operated at maximum efficiency to extract all possible energy from the inflow. However, in region III, the turbine has already reached its rated wind speed and is generating it's maximum design power or rated power. As such, any further increase in the inflow wind speed above rated, should be curtailed through power control or optimisation methods. It can be said that the turbine operates with the aim of *optimization* within region I, and with the aim of *curtailment* in region III, while Region II is viewed as a region of transition, employed to reduce noise and keep the rotor torque low[21].

2.1 Power Control in Wind Turbines

Wind power quantifies the amount of kinetic energy in wind flowing through a unit area parallel to the wind direction, per unit time[22]. Mathematically, the power that can be generated from wind is given as the kinetic energy per mass flow rate [23].

$$P_{wind} = \frac{1}{2} * (\rho A \bar{U}) * \bar{U}^2 = \frac{1}{2} \rho A \bar{U}^3 \quad , \tag{2.1}$$

where $\bar{U}$ represents the mean wind speed at the turbine rotor surface, ρ represents air density, and A, defined mathematically as πR^2 is the rotor swept area, with R representing the rotor radius.

According to the aerodynamics actuator disc model, a wind turbine with rotor surface area A extracts the same amount of power from an incident wind inflow as an actuator disc with the same rotor surface area [24]. The power extracted by the actuator disc can be expressed in terms of its axial induction factor - a parameter which shows the extent to which the mean wind speed $\bar{U}$ before the disc is reduced just behind the disc due to a deceleration imposed by the rotor. This parameter is defined mathematically as:

$$\alpha = (\bar{U} - U_R)/\bar{U} \quad . \tag{2.2}$$

Here, U_R represents the mean wind speed just behind the disc/rotor [25]. As per the model, the axial induction factor α and the mean wind speed $\bar{U}$ can be used to express the wind turbine power P, which is represented by the disc [24].

$$P = \frac{1}{2} \rho A \bar{U}^3 4\alpha(1-\alpha)^2 \quad . \tag{2.3}$$

To relate the turbine's axial induction factor α to its efficiency of power extraction - also known as its power coefficient, C_P, which depicts the degree to which the power in the wind P_{wind} encountered by the rotor is extracted by the turbine, C_P is expressed by non-dimensionalising P with respect to P_{wind} as given [24, 26]:

$$C_P(\alpha) = \frac{P}{P_{wind}} = 4\alpha(1-\alpha)^2 \quad . \tag{2.4}$$

According to the Lancaster-Betz relationship in [25], C_P has a theoretical maximum value of 16/27, which approximates 59.26 percent at $\alpha = 1/3$. In aerodynamics, this value is known as the Betz limit and holds true to all wind turbine designs [27]. This implies only 59.26 percent of the energy in a wind inflow can be extracted by a turbine. Furthermore, the author in [27] suggests that this value is still subject to further reduction considering losses due to friction, blade surface roughness, and mechanical losses in the system. This perspective is supported by [24], where the author claims that blade imperfections prevent the Betz limit from being reached even in the absence of system losses, meaning that current wind turbines operate slightly below their ideal power coefficient, which is generally reported to be approximately $C_{P,prac} = 40$ percent [27]. Based on (2.1) and (2.4), (2.3) develops into:

$$P(\alpha, \bar{U}) = \frac{1}{2}\rho A \bar{U}^3 C_P(\alpha) \quad . \tag{2.5}$$

Here, an ideal wind turbine's extracted power is represented by the parameter P.

Similarly, the thrust coefficient C_T - which denotes the degree of opposing force exerted in the axial direction by the turbine in reaction to the momentum of the wind inflow [28], relates to the axial induction factor, α, as follows [24, 26]:

$$C_T(\alpha) = \frac{T}{\frac{1}{2}\rho A \bar{U}^2} = 4\alpha(1-\alpha) \quad , \tag{2.6}$$

where T represents the thrust force, and $C_T(\alpha)\frac{1}{2}\rho A\bar{U}^2$ is the opposing axial force exerted by the turbine against the wind inflow.

2.1.1 The Performance Curves

The performance of a wind turbine can be characterized by how its torque, power, and thrust force change with the wind speed. The power quantifies the energy in the wind intercepted by the turbine rotor and thus transferred into the electrical system [29], while the thrust determines the structural design of the tower. On the other hand, the resulting torque decides the gear box size and must align with the specifications of the generator driven by the rotor [24].

The thrust coefficient (C_T) and power coefficient (C_P) curves illustrate the variation of these dimensionless parameters (which directly influence a turbine's power output) across different wind speeds. It is also commonplace to have these curves feature these dimensionless parameters plotted against the blades tip-speed ratio λ, which is also contingent on the incoming wind speed Figure 2.3 shows the power, thrust and power coefficients plotted against the effective wind speed for the Mitsubishi MWT-1000A turbine.

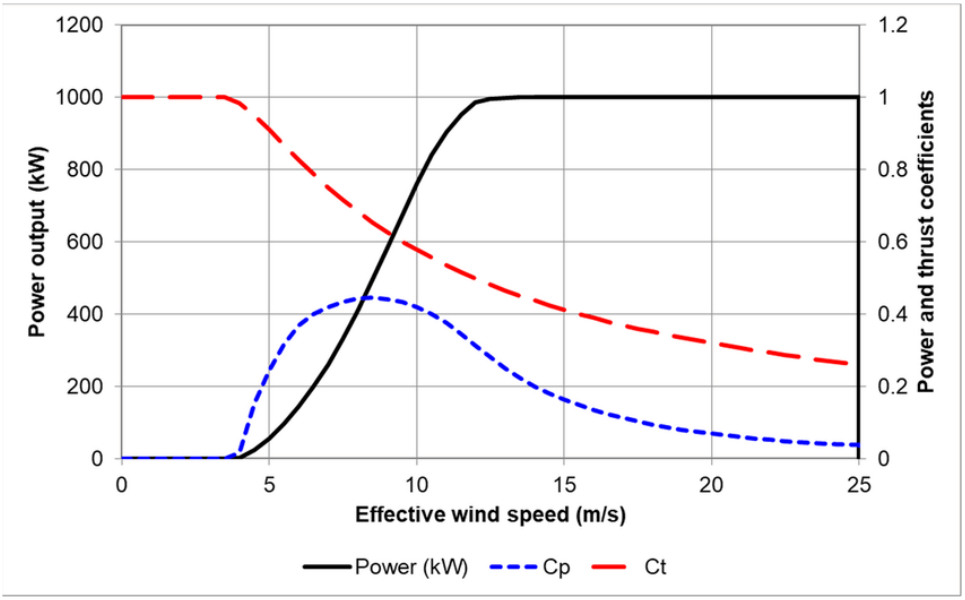

Figure 2.3: Power, C_P and C_T curves for the Mitsubishi MWT-1000A [30]

2.1.2 Power Control and Wind Turbine Actuation Methods

A wind turbine's highest efficiency is reached at above 10 m/s to 15m/s [19]. At this region of operation, the turbine must reduce the driving forces on its rotor and consequently on the entire turbine structure by controlling its output power [19], knowing that the thrust force on the rotor from the wind inflow is instantly transmitted into the tower which carries the rotor[24]. High wind speeds are usually momentary and consequently, have a marginal influence on the energy production, but must however, be controlled else they lead to problems in the drive train and turbine generator [31].

Three conventional methods exist in the literature through which the degrees of freedom (DOF) of a wind turbine is controlled to optimise or curtail power production. This is

achieved by - (1) controlling the generator speed or torque, (2) controlling the blades' pitch angle δ (pitching), and (3) rotation of the entire turbine rotor plane into or out of the wind inflow direction (yawing). Controlling the generator speed or torque allows for power management in regions I and II of the power curve (see Figure 2.2). To achieve optimal power in these zones, maintain the tip-speed ratio λ that corresponds to the ideal power coefficient C_P while keeping the pitch angle δ constant.

$$\lambda = \frac{\omega R}{\bar{U}}. \tag{2.7}$$

Here, ω represents the angular velocity of the rotor in $rads/s$, R is the radius of the rotor in m, and $\bar{U}$ is the inflow wind speed in m/s. The numerator is the rotor rotational speed U_{blade} with units in $rads/s$. By controlling the generator torque, U_{blade} is varied $w.r.t$ changes in U, thus maintaining a λ value that corresponds to the optimum C_P. In region III, power control is effected by adjusting the pitch angle δ, thereby maintaining the rated rotor rotational speed and ensuring a tip-speed ratio λ that aligns with the optimum C_P. In this case of region III, since the mean inflow wind speed $\bar{U}$ has already reached or exceeded rated speed, the optimum C_P maintained corresponds to the rated speed. The reason for this is that at rated speed, the turbine generator is already rotating at its rated or maximum number of revolutions per minute (revs/min), and cannot go any faster to avoid damaging the generator. Turbine yawing can be applied in all the regions of operation of the wind turbine. In regions I and II, it can be utilized to either align the plane of the rotor with the inflow wind direction to maximize the power output of a standalone turbine, or to misalign the rotor plane with direction of the wind, and hence curtail a turbine's power output. Yaw control can also be effected in region III or in turbulent conditions to misalign the plane of the rotor plane with the wind and shed excess aerodynamic power or totally reject the turbulent inflow.

The recognisable control input parameters in state-of-the-art wind turbines are the generator torque (a parameter which establishes the tip speed ratio λ), and the blade pitch angle δ. These parameters are thus adjusted to produce the intended axial induction factor that equates to the optimal C_P[32, 33]. Therefore, it is also commonplace to find the left-hand-side (LHS) of Equations 2.4 and (2.6) presented as functions of λ and δ (i.e., $C_P(\delta, \lambda)$

and $C_T(\delta, \lambda)$) as seen in [34]. In summary, only two common actuation methods exists, namely;(1) axial induction control, through the alteration of tip speed ratio of blade, *lambda*, in regions I and II or pitch angle, δ, in region III (2) Wake steering, by offsetting the yaw angle of the turbine. These apply both for standalone turbines and in WPs.

2.2 Wind Plants and Wakes

Wind plants are borne out of the desire to maximally exploit the energy resource from a confined land area, by deploying many wind turbines together in a wind plant [5]. Because the turbines are closer together than would have been in a larger land space, this practice has the advantage of reducing maintenance and installation costs, since proximity and accessibility to individual turbines is enhanced in the process [12]. The result of this arrangement, however, is that these close deployments introduce aerodynamic interactions between the operating turbines, which according to [7, 8] influences the power generation and loads on each individual turbine in the wind plant (WP).

Figure 2.4: A Wind Power Plant
[35]

The aerodynamic interplay occur because individual turbines are inevitably positioned within the wakes of neighboring turbines, irrespective of the turbine layout and wind direction. The only exception to this outcome is a single row of turbines deployed at right angle to a uni-directional wind. These interactions between turbines stem from the conversion of wind kinetic energy into electrical energy, resulting in a region of turbulent and slower moving air behind an extracting turbine's rotor, called the *wake zone* or *wake region* or *wake*.

2.2.1 Near Wake and Far Wake: Velocity deficit and Turbulence

Based on power losses and turbine loads, a wind turbine's wakes is categorised into; near and far wake. Stretching to approximately one rotor diameter ($1D$) from the turbine is the near wake zone. The extracting turbine's structural design determines the formation of the flow field behind it, affecting the performance of downstream turbines in this region. However, the structural design presents a minimal impact on the flow field formation in the the far wake, with attention shifting towards wake modeling, turbulence, and the effects of site topography. [36]. With the help of mixing with ambient wind, the extracting turbine's wake extends and recovers to freestream conditions as it travels towards the far wake from the near wake [7].

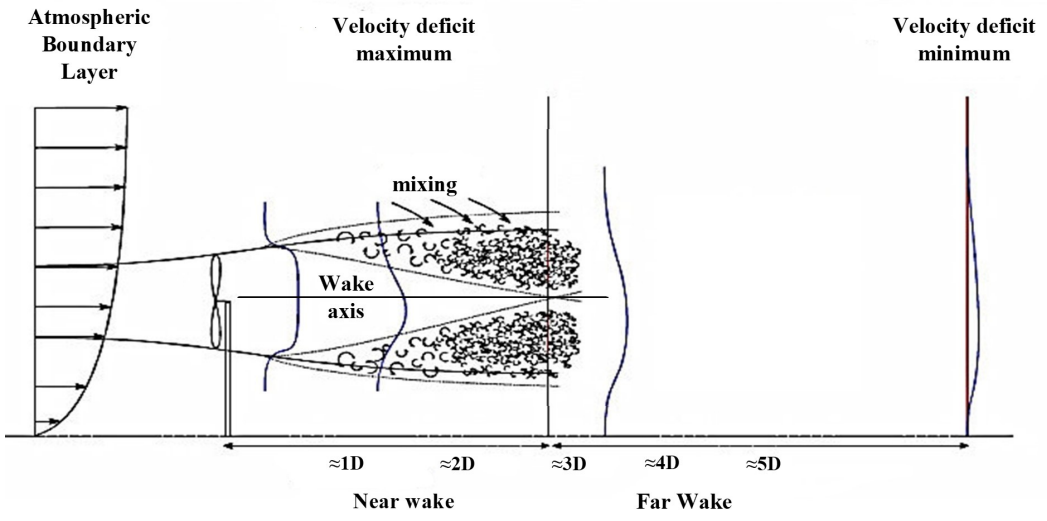

Figure 2.5: Wind turbine wake zone and velocity profile (on-shore)

If these turbines are deployed within considerable proximity, a downstream turbine that falls within a wake which has not fully recovered will experience a diminished wind speed compared to the freestream wind at the turbine upstream, resulting in a lower power generation. A deficit in downstream wind speed is estimated to peak post 1 - 2 rotor diameters (1 - 2D) [37], however, if low ambient turbulence levels are present, this peak may stretch a further distance [13]. The speed variation between air inside the wake and ambient air (the shear), introduces a shear layer that mixes the ambient air with the turbulent air in the wake. As the wake travels behind an extracting turbine rotor, the shear layer thickens, widens, and engulfs the wake axis somewhere between 2 - 5D downstream, as shown in Figure 2.5, thereby terminating the near wake zone [38, 39]. The work of [40], relying on experimental results and best comparisons of previous studies uses 2.25D as the downstream interval where the wake is fully developed. Extending from this point according to [41] at approximately an on-shore distance of 3 - 5D or an off-shore distance of 6 – 8D, is known as the far wake zone.

Due to turbulent mixing in an operating turbine's wake zone, there is elevated turbine-level turbulence intensities (TI) downstream[42]. Regions with elevated TI, particularly variations in wind speed along the wind inflow direction, impose higher turbine loads and blade fatigue. [43, 44]. The rate of decay of wind speed deficits in the wake is much quicker than the rate of decay of turbulence intensity according to [44], which also reckons that the mechanical turbulence in the wake is still 'evident' beyond 15D downstream. However, tip vortices from the blades (another source of turbulence, which is evident in the shear layer) will potentially be completely dissipated after roughly 4D [38, 37]. These turbines will suffer different levels of deficits and turbulence intensities (TI), contingent upon the wind farm layout and wind distribution, which ultimately dictates the power generation and loading on individual turbines [45].

2.2.2 Turbine Spacings and Layouts in Wind Farms

Consequent upon the deficits and increase in turbulence intensities in a WP, it is conventional to have turbines deployed 6 – 10D from one another *w.r.t* a dominant wind direction, but 1.5 – 3D in the perpendicular direction [13]. According to the Danish Wind

Industry Association [46], a turbine-to-turbine (T-2-T) distance of $5 - 9D$ in the dominant direction, with a $3 - 5D$ distance in the perpendicular direction is the general guideline. However, [47] warns that these large spacings in the dominant wind direction could amount to a cumulative annual revenue loss in the range 20 - 30 percent if wake effects are taken into consideration in addition to increased capital and operational expenses. A report presented in [45], recommends $5D$ to be the minimum distance in the dominant wind direction. The authors also note that economic reasons including expensive costs of cables, high maintenance costs due to long transit distances between turbines, and high land leasing costs could compel farm planners to resort to closer turbine deployments. Therefore, a T-2-T distance of $3 - 5D$ is permitted but a expert report must validate the turbine's structural integrity in the proximity of elevated loading [45]. It is vital to point out that the preceding recommendations apply only if the wind resource at the site is unidirectional. For multi-directional sites, however, there really is no dominant and perpendicular direction as such, since winds come from many different directions at different hourly/daily/weekly or seasonal intervals. The only characteristic that could categorise a direction as dominant in this case would be it's probability of occurrence. As a result, the aim in multi-directional sites is to create a layout that ensures minimum T-2-T distances in all directions that are equal to or greater than the "dominant direction" requirements.

Broadly, there are three classes of layouts employed in the literature, namely: single row, regular layouts, and irregular/optimised layouts. Regular layouts as studied in [9, 48] and with real world examples as would be given later in the paragraph, are created following a distinct lattice structure such as a hexagon, tetragon etc., while irregular layouts [49, 50, 8, 51] take no particular recognizable structure and are in most cases a product of layout optimisation using an optimisation algorithm. The Nørrekær Enge II wind plant sited in the North Jutland, on the south bank of the Limfjord, and which is approximately 36 km west of Ålborg and 8 km north-east of Løgstør has 42 turbines deployed in a tetragonal layout with radial distance of $6D$ in each row, and with a row-to-row (r-2-r) separation of 7-8D [44, 52]. The Horns Rev1 wind plant (offshore) sited off the west coastal region of Denmark's Jutland peninsula, has 80 turbines arranged in an obliqued tetragonal layout (rhombus-shaped) and with a radial and r-2-r distance of $7D$ each [53, 3]. Sited 23 km along the coastline of the

Netherlands is the Prinses Amalia wind plant with 60 turbines deployed in a hexagonal layout with a minimum T-2-T distance of $6.9D$ [54, 55]. Another hexagonally deployed wind plant is the Windpark Fryslân - a near-shore facility operating since 2021 and currently the largest freshwater wind farm in the world. It comprises 89 turbines of 130m rotor diameter and 103m hub height, each of 4.3 MW capacity, and is sited in the northern region of Lake Ijssel in the Netherlands.

Figure 2.6: Windpark Fryslân (near-shore)

Most power maximisation studies in the literature that are not entirely yaw-based (see [56], [8], [15], [57], [58]), prefer irregular/optimised layouts, and even when regular layouts are applied, lean towards regular tetragonal layouts (see [15]). However, regular hexagonal layouts as exhibited by its recent application in a modern wind plant (the Windpark Fryslân), show so much promise as regards visual impact - this being a cardinal reason according to its project director Mr de Groot [59] behind its choice as the employed layout. A research in the University of Strathclyde [11] was also able to show that hexagonal layouts can accommodate more turbines within a given irregular land area compared to a tetragonal or an octagonal layout.

2.3 Wake Modelling

The wake zone is a convoluted region, hampering an easy distinction between where the near wake ends and the far wake begins. Nevertheless, the far wake becomes the area of concentration for wind plant optimisation problems as the near wake's influence becomes the far wake's initial conditions [36]. A plethora of far wake models are seen in literature, which can be broadly categorised into two main types: (1) Analytical models as seen in [60, 61, 62, 1, 63, 64, 4] and (2) Field and Wake edded turbulence models as seen in [37, 65, 66]. According to [63], analytical models can further be divided into: (i) Kinematic models, where each turbine's wake is computed in isolation, and then combined with wakes of other upstream turbines using superposition principles to obtain a multiple wake effect at a given downstream position/turbine as in [1, 62, 63, 64], and (ii) Distributed roughness models, where turbines represent distributed roughness elements which modify the ambient atmospheric flow as the flow encounters them, as seen in [60]

The momentum equation is the only tool used by analytical wake models to simulate the turbine's wake velocity deficit. However, many of these models do not consider variations in turbulence intensity within the wake, so they often need to be combined with a turbulence model if turbine-level turbulence intensity are required within the wind plant, and also if load estimations are necessary[67]. Whereas, field models are employed in the computation of the entire flow field through a wind plant, or wind plant section if it has an irregular geometry. This is achieved using Computational Fluid Dynamics (CFD) technology to solve the Reynolds-averaged Navier-Stokes equations (RANS) or perform Large-eddy simulations (LES). These models provide high fidelity solutions but are computationally expensive and slow. Even though some of these models solve a linearised form of the Navier-Stokes equations for simplicity, such as in [37, 65], it is still quite slow for power predictions and real-time control parameter optimisation applicability in WPs [68], as those are recursively computed. Hence, field models are impracticable for engineering applications such as stated above, but can be applied in tuning model parameter as seen in [4, 3], or for control validation as seen in the works of [69, 70]. Table 2.1 presents some analytical wake models, highlighting some notable features and possible limitations. A proper review of some of the wind turbine

wake models mentioned here including requisite equations can be seen in [71, 36], while a comprehensive summary of wake superposition methods can be found in the work of [72].

The simplicity and computational efficiency of kinematic models make them preferable in engineering applications [75], as well as in off-line WP applications such as layout optimisation [76]. Jensen model as in [1] which is modified into the Park model in [2] is the most renown and well-studied of the kinematic wake models in the literature, upon which many other models and commercial software have been developed.

2.3.1 Park Model

Imagine a sequence of turbines, i through n, designated according to the direction of the wind, where i and n are at the extremes upstream and downstream, respectively. Based on the conservation of momentum, Katic *et. al.* in [2] define the deficit in wind speed at a downstream turbine j caused by a single upstream turbine's wake, i, as:

$$U_{def}(d, r, \alpha) = 1 - \frac{\bar{U}}{U_\infty} = 2\alpha \left(\frac{R}{R(d)} \right)^2 \quad . \tag{2.8}$$

From the equation, U_∞ signifies the freestream wind speed hitting i, the mean wind speed available at downstream turbine j is denoted by $\bar{U}$, R represents the rotor radius of i. This model also implies a wake radius $R(d)$ behind an extracting turbine of radius R that expands linearly, relative to an axial downstream distance, d, as follows:

$$R(d) = R + \kappa d \quad . \tag{2.9}$$

The term d specifies the axial distance from i to j, κ specifies how quick the wake expands behind an extracting turbine [1], which depends on the roughness length z_{r_l} of the WP site containing both turbines and the upstream turbine's hub height, z_0, causing the deficit (i.e i)[77]. The European Wind Atlas, as outlined in [78], provides varying roughness lengths for different types of landscapes. Nonetheless, it recommends setting the default value of z_{r_l} to 0.04 for offshore cases and 0.075 for the majority of terrestrial cases. [67, 41, 36].

$$\kappa = \frac{0.5}{\ln \frac{z_0}{z_{r\_l}}} \quad . \tag{2.10}$$

The Park model further assumes that at any downstream distance, the wind speed is consistent within the entire wake but equal to the freestream wind, outside the wake, thus creating a top-hat wind profile with a wind speed deficit as expressed:

$$U_{def}(d, r, \alpha) = \begin{cases} 2\alpha \left(\frac{R}{R + \kappa d} \right)^2, & \text{if } r \leq R + \kappa d \\ 0, & \text{if } r > R + \kappa d \end{cases} \quad . \tag{2.11}$$

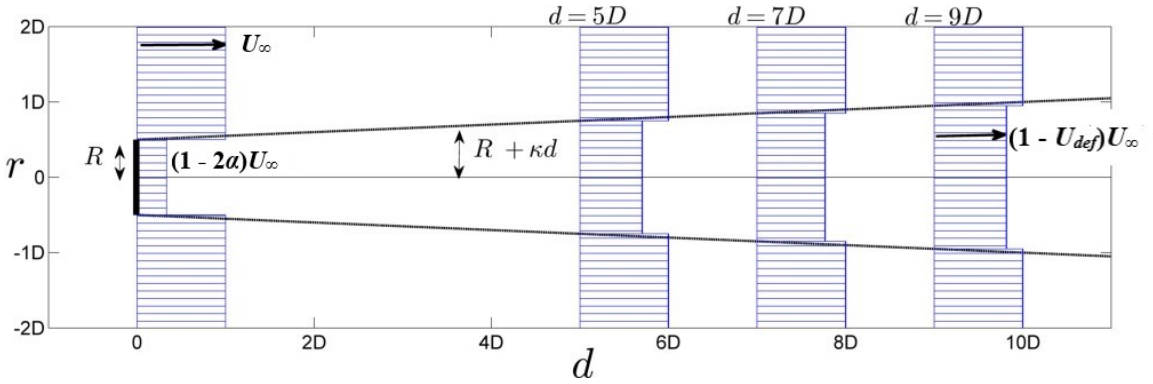

Figure 2.7: Top hat wake profile [1, 2]

From Equation 2.8, if we consider that the upstream turbine is the first in the row of turbines, the Park model describes the wind speed at a downstream turbine in terms of the freestream wind speed U_∞ and its deficit U_{def}. This deficit parameter, U_{def}, relies on d - the axial distance from the upstream to the downstream turbine, r - the radial wake distance between both turbines, and α - the upstream turbine's axial induction factor as follows:

$$\bar{U}(d, r, \alpha) = (1 - U_{def}(d, r, \alpha))U_\infty \quad . \tag{2.12}$$

2.3.2 Park and Law Model

Observations from [37, 79] confirm a wake's wind speed configuration to resemble an inverted Gaussian configuration. Given that the Park model described in subsection 2.3.1 is top-hat shaped, an improved model is presented in [3, 4], describing the wind speed

variations in perpendicular/radial wake orientation of an extracting turbine as Gaussian. Consistent with the Park model, the model presented in [3, 4] which can be called the *Park and Law* model, describes longitudinal/axial wake wind speed variations using momentum conservation. From these, a continuous wake model is obtained that describes the wind speed within an extracting turbine's wake, as a smooth and continuous function both axially and radially. Consequently, the wind turbine and plant power functions is expressed as continuous, with dependence on the yaw offset angle(s) ϕ and axial induction factor(s) α of the turbine(s) in the wind plant.

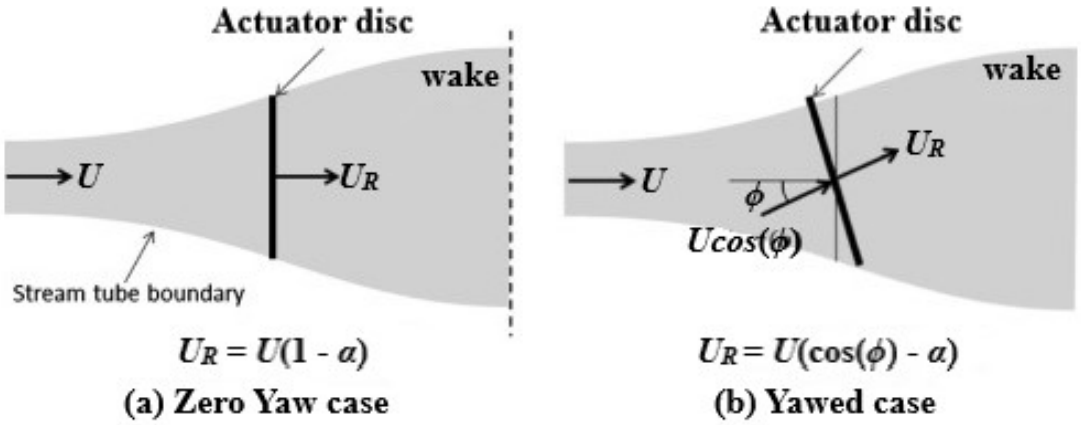

Figure 2.8: Actuator disc theory

By altering the yaw offset by an angle ϕ ($where\ \phi \neq 0$), the normal component of the freestream wind is decreased, altering the thrust on the rotor, and consequently the turbine extracted power. Considering Figure 2.8b, a yaw offset angle of ϕ changes the normal component to $\bar{U}\cos(\phi)$ while U_R becomes:

$$U_R = \bar{U}(\cos(\phi) - \alpha) \quad , \tag{2.13}$$

as opposed to that shown in Figure 2.8a, and can be derived from Equation (2.2) as $U_R = \bar{U}(1-\alpha)$ when the rotor is not yawed ($\phi = 0°$). Consequently, the power function in Equation (2.3) is re-defined below in terms of α and ϕ as in [24]:

$$P = \frac{1}{2}\rho A \bar{U}^3 C_p(\alpha, \phi) \quad , \tag{2.14}$$

where the power coefficient in Equation 2.4 is modified as given in [24]:

$$C_P(\alpha, \phi) = \frac{P}{\rho A \bar{U}^3/2} = 4\alpha(\cos(\beta\phi) - \alpha)^2 \quad . \tag{2.15}$$

With the introduction of β to influence ϕ, Equation (2.15) can be fitted to different wind turbine power curves.

Park's model assumes that inside the wake, regardless the r distance, the deficit at any d distance is uniform along r (i.e no variation $w.r.t$ r or in the radial direction), but reduces to zero outside the wake. To create a continuously varying deficit along r (i.e in the radial direction), Park and Law [3, 4] modify Equation (2.11) with an exponential term, enabling the wind speed deficit to vary not only $w.r.t$ d but also $w.r.t$ r, resulting in an axially and radially continuous function. Hence, the deficit in wind speed at a relative downstream position (d, r) due to an extracting upstream turbine having an axial induction factor, α, is given as:

$$U_{def}(d, r, \alpha) = 2\alpha \left(\frac{R}{R + \kappa d}\right)^2 \exp\left(-\left(\frac{r}{R + \kappa d}\right)^2\right) \quad . \tag{2.16}$$

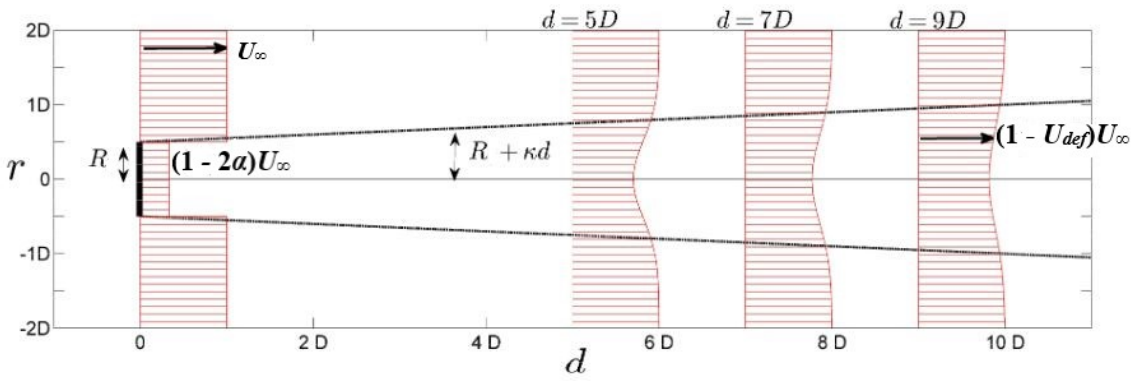

Figure 2.9: Continuous wake model [3, 4]

Modifying an upstream turbine's ϕ value consequently influences the wake configuration and severity of the deficit at a downstream position. Maximum power extraction is achievable at a zero-yaw turbine orientation, as this orientation maximises the power coefficient, C_P, of the wind turbine. Yawing a turbine's rotor reduces its efficiency, hence less energy extraction, but the possibility of a reduced deficit in its downstream because the wake is being steered

away from turbine(s) downstream. Hence, for multi-turbine cases as is obtainable in WPs, yawing an upstream turbine could result in a collective advantage with respect to total wind plant power.

Figure 2.8b, depicts that the rotor surface area perpendicular to the wind inflow is decreased by $\cos(\phi)$ when yawed. Consequently, Park and Law modifies Equation (2.16) to incorporate yawing effect into the wind speed deficit at a downstream position as:

$$U_{def}(d, r, \alpha, \phi) = 2\alpha \cos(\gamma\phi) \left(\frac{R}{R + \kappa d}\right)^2 \exp\left(-\left(\frac{r}{R + \kappa d}\right)^2\right) \quad , \tag{2.17}$$

where γ controls the responsiveness of wind speed deficit U_{def} to changes in yaw offset angle ϕ.

Effects of yaw misalignment on wake orientation and configuration

In an extracting turbine's downstream, the intensity of a wake on any turbine depends on the relative radial and axial distance separating them (extracting downstream turbine). The larger these relative distances, the less the deficit imposed on the downstream turbine, and the more power it generates.

Again, imagine a sequence of turbines labelled i, j through n, designated according to the direction of the wind, θ^W, and positioned at $p_i = (x_i, y_i)$, $p_j = (x_j, y_j)$ through $p_n = (x_n, y_n)$, where turbine n is at the extreme downstream and i is at the extreme upstream, and encountering the freestream wind speed U_∞, with j following behind it. Park and Law defines the distance separating i and j in terms of; the axial T-2-T distance $d_{j,i}$ of turbine j relative to turbine i and the radial T-2-T distance $r_{j,i}$ of turbine j relative to turbine i, as shown in Figures 2.10a and c, respectively. From the figure, $d_{j,i}$ is defined as follows:

$$d_{j,i} = \|p_j - p_i\|_2 \cos(|\theta_{j,i} - \theta^W|) \tag{2.18}$$

where $\|p_j - p_i\|_2 = ((x_j - x_i)^2 + (y_j - y_i)^2)^{1/2}$ is the the euclidean norm and $\theta_{j,i} = \tan^{-1}((x_j - x_i)/(y_j - y_i))$ is the angle between turbines i and j. Equation (2.17) shows that wind speed deficit decreases accompanied with wake recovery, with increase in axial T-2-T distance d (i.e. $d_{j,i}$).

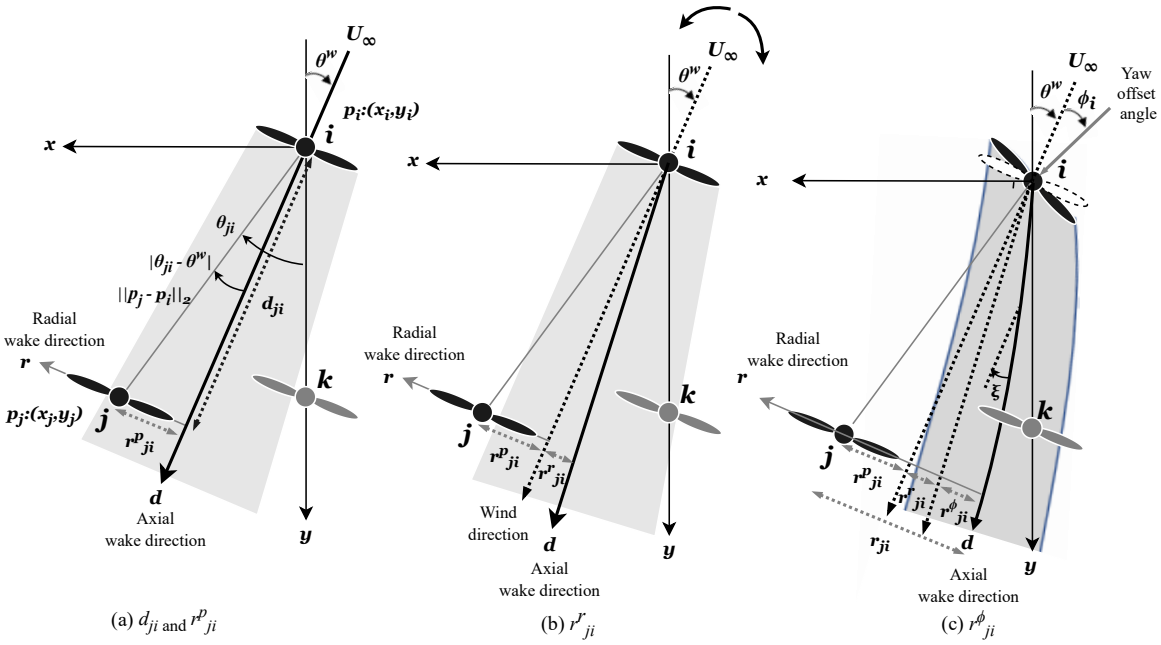

Figure 2.10: Yaw offset effects on T-2-T distances $d_{j,i}$ and $r_{j,i}$ [4]

The radial T-2-T distance r_{ji} signifies the distance between the wake axis of an upstream turbine i and the rotor centre of a downstream turbine j. In contrast to $d_{j,i}$, Equation (2.17) indicates that the wind speed deficit at a downstream position decreases and the wake recovers, as r (*i.e.* $r_{j,i}$) decreases. However, if a downstream turbine is positioned at $r = 0$, the wake axis of both turbines (upstream and downstream in non-yawed situation) are aligned, thus, a maximum wake effect and wind speed deficit is experienced at downstream turbine. Considering Figure 2.10c, the more $r_{j,i}$ increases, the more likely that turbine j will be in a partial wake position, rather than in a full wake position where the upstream turbine's wake engulfs its entire rotor. According to Park and Law, r_{ji} is influenced by three factors; (1) the positions of the turbines relative to one another, just as $d_{j,i}$, (2) turbine blade rotation, which slightly skews its wake orientation, and (3) the upstream turbine's yaw offset.

1. Depicted in Figure 2.10a for a considered wind direction θ^W, is the position-influenced radial T-2-T distance, dependent on the positions of i and j relative to each other, and

expressed as follows:

$$r^{p}_{j,i} = \|p_j - p_i\|_2 \sin(|\theta_{j,i} - \theta^W|) \tag{2.19}$$

2. Figure 2.10b depicts the blade rotation-influenced radial T-2-T distance. The study in [80, 70] observes that behind a turbine the wake configuration is marginally skewed despite not yawing (i.e., when the turbine is perpendicular to the wind inflow and hence $\phi = 0$). These investigations suggest that this phenomena results from the interaction between the revolving blades and the vertically variable wind speed profile. This interaction causes the wake to rotate and skew counter-clockwise owing to the rotor/blades' clockwise rotation. Noteworthy is the fact that this "clockwise" rotation is viewed looking from behind the upstream turbine i, which means that the blade rotation becomes counter-clockwise if viewed from behind the downstream turbines j and k as illustrated in 2.10. So, considering 2.10b, and viewing from behind the downstream turbines j and k, the blades rotate counter-clockwise from the wind direction axis towards the left of the rotor axis, hence the wake itself will be skewed towards the right of the rotor axis. From their CFD simulation studies, the radial offset term $r^{r}_{j,i}$ as depicted in Figure 2.10b and which is caused by turbine blade rotation, varies linearly with the axial T-2-T distance between turbines i and j ($d_{j,i} = \|p_j - p_i\|_2 \cos(|\theta_{j,i} - \theta^W|)$). Consequently, the authors model the blade rotation-influenced radial T-2-T distance as:

$$r^{r}_{j,i} = \chi d_{j,i} = \chi \|p_j - p_i\|_2 \cos(|\theta_{j,i} - \theta^W|) \quad , \tag{2.20}$$

where the parameter χ is the skewed wake configuration's slope.

3. Figure 2.10c depicts the yaw-influenced radial T-2-T distance. Investigations in [81, 82] as well as CFD simulations in [83, 84, 85] have established that a yaw angle offset can temporarily deflect the wake from the ambient/freestream inflow trail. According to [83], turbine yawing causes a wake deflection in the counter direction to the yaw rotation. After travelling some distance in the downstream and after interaction and influence from the freestream inflow, the wake path is realigned with that of

the freestream inflow. This initial deflection and then influence from the freestream inflow causes the wake flow to meander. This meandering as studied in [37, 66] is very important in WPs as it can increase downstream turbines' fatigue loads due to the back and forth movement of the flow in and out of the turbine rotor(s), while also having the capacity to reduce the wind speed deficit on downstream rotor(s), if properly controlled [13]. As illustrated in Figure 2.10a, in a zero-yaw condition, the wake axis is parallel to the normal of the freestream inflow hitting the rotor. However, yawing redirects the wake, skewing its axis from the normal by an angle $\xi(d)$ in relation to the zero-yaw rotor position. Therefore, Gebraad *et al.* in [70] define this skew angle at a downstream distance d, $\xi(d)$, in terms of the yaw offset angle ϕ of the yawing upstream turbine, and its thrust coefficient C_T in zero-yaw conditions as given:

$$\xi(d) \approx \frac{\tilde{C_T}(\alpha_i, \phi_i)}{(1 + \frac{2\tau d}{D})^2} \quad , \tag{2.21}$$

where

$$\tilde{C_T}(\alpha_i, \phi_i) \approx \cos^2(\phi_i) \sin(\phi_i) \frac{C_T}{2} \quad . \tag{2.22}$$

and where Equation (2.22) defines the initial skew angle of the wake axis just behind the rotor at $d = 0$ and wake width $\approx D$. The parameter τ controls the responsiveness of wake deflection to yawing, C_T as given in Equation (2.6) is the turbine's thrust coefficient in zero-yaw condition. The authors in [70] obtain the yaw-influenced radial T-2-T distance $r^{\phi}_{j,i}$ of turbine j due to i, by integrating a second-order Taylor series approximation of the tangent of the skew angle ξ over the distance $d_{j,i}$ where the downstream turbine j experiencing the yaw-influenced wake from i is positioned, as given:

$$r^{\phi}_{j,i} = \int_0^{d_{j,i}} \tan(\xi(d))\, dx = \left. \frac{\tilde{C_T}(\alpha_i, \phi_i) \left(15(1 + \frac{2\tau x}{D})^4 + \tilde{C_T}(\alpha_i, \phi_i) \right)}{\frac{2\tau x}{D}(1 + \frac{2\tau x}{D})^5} \right|_{x=0}^{x=d_{j,i}} \quad . \tag{2.23}$$

The effective radial T-2-T distance $r_{j,i}$ is thus described by [70] as a total of all the radial components as follows:

$$r_{j,i} = r^{p}_{j,i} + r^{r}_{j,i} + r^{\phi}_{j,i} sign(\theta_{j,i} - \theta^{W}) \quad . \tag{2.24}$$

Here $sign(\theta_{j,i} - \theta^{W})$ tells the direction of $r^{\phi}_{j,i}$, whether it is increasing the effective radial T-2-T distance $(r^{p}_{j,i} + r^{r}_{j,i} + r^{\phi}_{j,i})$ of turbine j due to i, or it is decreasing it. As illustrated in Figure 2.10c, yawing turbine i in the clockwise (+ve) direction increases $r^{\phi}_{j,i}$ but decreases $r^{\phi}_{k,i}$. However, a -ve yaw of i will have a reverse effect on both $r^{\phi}_{j,i}$ and $r^{\phi}_{k,i}$. Hence, the yaw offset angle of an upstream turbine can either increase or decrease the radial T-2-T distance of a downstream turbine depending on its (downstream turbine's) relative position with the upstream turbine, and this is independent of the quadrants these downstream turbines are located, assuming that the upstream turbine is at the origin as illustrated in Figure 2.10. So, as long as a downstream turbine is located to the left of an upstream turbine (*w.r.t.* the wind direction, and looking from behind the upstream turbine), a +ve yaw angle offset from the upstream turbine will always decrease the radial T-2-T distance of that downstream turbine, while increasing the radial T-2-T distance of a downstream turbine located to its (upstream turbine's) right.

Wind turbine power due to a single wake

The wind speed at any location on the rotor surface of the downstream turbine (i.e., $U_{j,i}$ at any (r', θ')) may be found by using local polar coordinates (r', θ'). Park and Law in [4] achieve this first by replacing the parameters d and r in Equation (2.17) with $d_{j,i}$ (i.e., Equation (2.18)) and $\sqrt{(r_{j,i} - r'\cos\theta')^2 + (r'\sin\theta')^2}$, respectively, to obtain the wind speed deficit $U_{def_{j,i}}$ at any downstream location (d, r) as:

$$U_{def_{j,i}}(d_{j,i}, r, \alpha_i, \phi_i) = 2\alpha\cos(\gamma\phi)\left(\frac{R}{R + kd_{j,i}}\right)^2 \exp\left(-\left(\frac{(r_{j,i} - r'\cos\theta')^2 + (r'\sin\theta')^2)^{1/2}}{R + kd_{j,i}}\right)^2\right) \quad . \tag{2.25}$$

At the downstream location (d, r), the wind speed $U_{j,i}$ at any point (r', θ') on a downstream turbine j rotor surface can be obtained by substituting Equation (2.25) into Equation (2.12) as thus:

$$U_{j,i}(r', \theta', \alpha_i, \phi_i; U_\infty, \theta^W) = \begin{cases} (1 - U_{def_{j,i}}(d_{j,i}, r, \alpha_i, \phi_i))U_\infty, & \text{if } d_{j,i} \geq 0 \\ U_\infty, & otherwise \end{cases} . \tag{2.26}$$

Equation (2.26) shows that the turbine j only experiences the wake-influenced wind speed from i, $(1 - U_{def_{j,i}}(r', \theta', \alpha_i, \phi_i))U_\infty$, if it is located in $i's$ downstream $(i.e., d_{j,i} \geq 0)$; else it experiences the freestream wind speed U_∞. It should also be noted that turbine i is assummed to not have any turbine in its upstream, hence, experiencing the freestream wind speed as depicted on the first line of Equation (2.26). Applying conservation of momentum, the momentum acting on the entire rotor disc due to the averaged wind speed $\bar{U}_{j,i}$ is set equal to the momentum acting on the same rotor due to the different wind speeds $U_{j,i}$ at each location (r', θ') (i.e., integrating the different wind speeds $U_{j,i}$ across the entire rotor radius, and then over the entire rotor circumference), as given:

$$\bar{U}_{j,i}(\alpha_i, \phi_i; U_\infty, \theta^W) = \frac{1}{\pi R^2} \int_{\theta'=0}^{\theta'=2\pi} \int_{r'=0}^{r'=R} U_{j,i}(r', \theta', \alpha_i, \phi_i; U_\infty, \theta^W) r' \, dr' d\theta' \quad . \tag{2.27}$$

Having estimated the averaged wind speed hitting the downstream wind turbine rotor j due to wake from an upstream turbine i, the power $P_{j,i}$ generated by j can be estimated as:

$$P_{j,i}(\alpha_i, \phi_i, \alpha_j, \phi_j; U_\infty, \theta^W) = \frac{1}{2} \rho A \bar{U}^3_{j,i}(\alpha_i, \phi_i; U_\infty, \theta^W) C_p(\alpha_j, \phi_j) \quad . \tag{2.28}$$

Equation 2.28 establishes that the power generated by a jth turbine is not only decided by its own control parameters via the term $C_p(\alpha_j, \phi_j)$ but also by the control parameters of the upstream turbine via $\bar{U}_{j,i}(\alpha_i, \phi_i; U_\infty, \theta^W)$.

Wake interference from multiple upstream turbines

In a wind power plant (WPP), multiple wakes are simultaneously generated from multiple extracting turbines, and these affect the power generation of one another, depending on the wind direction. As illustrated in Figure 2.11, depending on the direction considered, different levels of effects will be experienced by each turbine due to turbines in its upstream. At least four (4) methods have been employed in literature to combine multiple wake effects

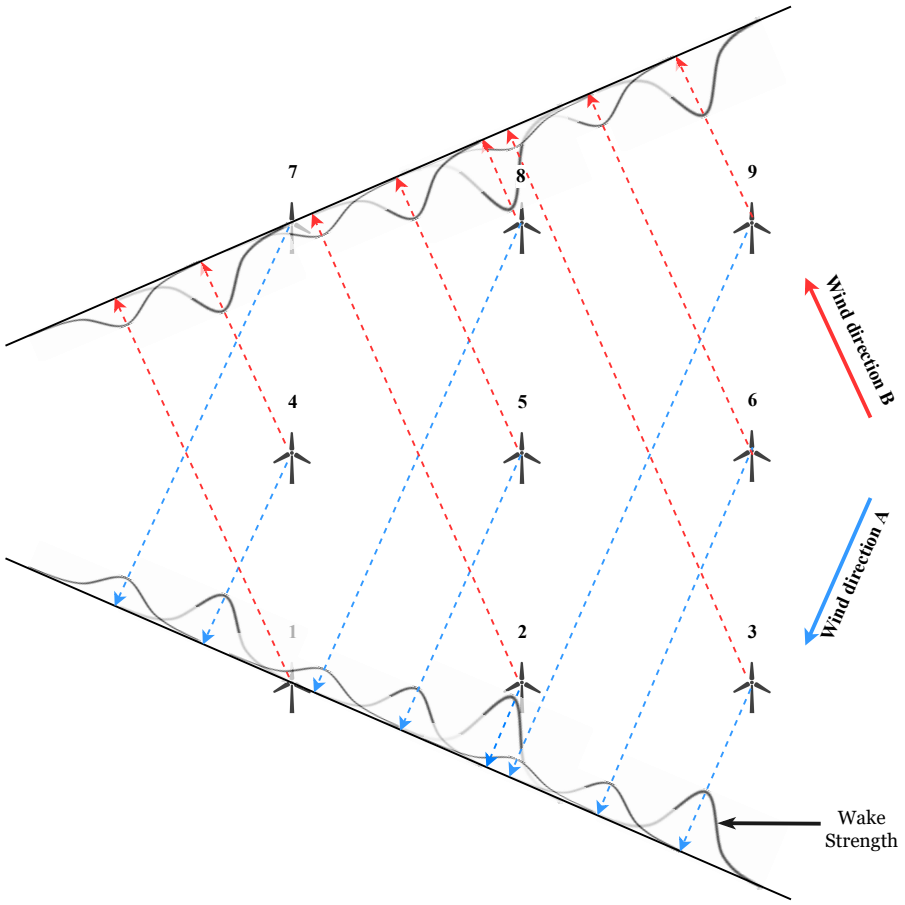

Figure 2.11: Multiple wake effect on downstream turbines.

at a downstream location/turbine as summarised in the work of [72]. The Park and Law multiple wake model in [4] adopts the root sum square method to aggregate multiple turbine wakes as proposed in [2] and also employed in the work of [62, 86]. Park and Law, however, applies rotor-based wind speeds (i.e., the averaged wind speed on the downstream turbine rotor surface) in computing this aggregated wake effect as seen in [62, 86], instead of the ambient-based/freestream wind speed applied by Katic *et.al.* in [2]. Hence, [4] applies the

rotor-based root sum square method of aggregating deficits from multiple upstream turbines. The deficit at a downstream turbine j is thus computed by taking the square root of the sum of the squares of the individual deficits from all upstream turbines i for which $d_{j,i} \geq 0$.

Considering that Equation (2.26) is the wind speed $U_{j,i}$ at any point (r', θ') on a downstream turbine $(j's)$ rotor surface, due to a single upstream turbine i, an averaged wind speed on the entire downstream turbine rotor $\bar{U}_{j,i}(\alpha_i, \phi_i; \theta^W)$ was derived subsequently in Equation (2.27). Hence, the relationship in Equation (2.12) can be presented in terms of averaged quantities and with U_∞ substituted with U_i to denote a rotor-based averaged parameter:

$$\bar{U}_{def_{j,i}} = 1 - \frac{\bar{U}_{j,i}}{\bar{U}_i} \quad , \tag{2.29}$$

and an averaged deficit factor can be obtained by expressing Equation (2.27) in terms of deficits $\bar{U}_{def_{j,i}}$ and expressed in the format of Equation (2.26) as

$$\bar{U}_{def_{j,i}}(\alpha_i, \phi_i; \theta^W) = \begin{cases} \dfrac{1}{\pi R^2} \displaystyle\int_{\theta'=0}^{\theta'=2\pi} \int_{r'=0}^{r'=R} U_{def_{j,i}}(d_{j,i}, r, \alpha_i, \phi_i) r' \, dr' d\theta', & \text{if } d_{j,i} \geq 0 \\ 0, & otherwise \end{cases} . \tag{2.30}$$

In addition, given that the continuous multiple wake model as illustrated in Figure 2.11 has an indefinitely expanding wake width, the downstream turbine is affected by all turbines in its upstream (i.e., all turbines x for which $d_{j,i} \geq 0$). Hence, the aggregated deficit factor $\bar{U}_{def_j}(\boldsymbol{\alpha}, \boldsymbol{\phi}; \theta^W)$ for wind turbine j can be generalized as thus:

$$\bar{U}_{def_j}(\boldsymbol{\alpha}, \boldsymbol{\phi}; \theta^W) = \sqrt{\sum_{i=1}^{\mathcal{T}} (\bar{U}_{def_{j,i}}(\alpha_i, \phi_i; \theta^W))^2} \tag{2.31}$$

where $\mathcal{T}$ is a set of all turbines in the upstream of j, $\boldsymbol{\alpha}$ is the axial induction factor vector of all upstream turbines' axial induction factors (i.e., $\boldsymbol{\alpha} = (\alpha_1, ..., \alpha_\mathcal{T})$), $\boldsymbol{\phi}$ is the yaw offset angle vector of all upstream turbines' yaw angles (i.e., $\boldsymbol{\phi} = (\phi_1, ..., \phi_\mathcal{T})$), θ^W is the considered wind direction.

Finally, considering a wind condition (U_∞, θ^W), the averaged wind speed hitting turbine $j's$ rotor can be expressed from Equation (2.29) as:

$$\bar{U}_j(\boldsymbol{\alpha}, \boldsymbol{\phi}; U_\infty, \theta^W) = (1 - \bar{U}_{def_j}(\boldsymbol{\alpha}, \boldsymbol{\phi}; \theta^W))U_\infty \quad . \tag{2.32}$$

Accordingly, the power of the jth turbine is expressed as per the control actions α and ϕ of all turbines in the upstream of j, as given:

$$P_j(\boldsymbol{\alpha}, \boldsymbol{\phi}; U_\infty, \theta^W) = \frac{1}{2}\rho A \bar{U}_j^3(\boldsymbol{\alpha_{-j}}, \boldsymbol{\phi_{-j}}; U_\infty, \theta^W) C_p(\alpha_j, \phi_j) \quad . \tag{2.33}$$

It is immediately observed that the jth turbine's power is determined not only by its own control action (α_j, ϕ_j) but by the control actions of all other turbines in its upstream, which are captured in the vectors $\boldsymbol{\alpha_{-j}} = \boldsymbol{\alpha} \setminus \{\alpha_j\}$ and $\boldsymbol{\phi_{-j}} = \boldsymbol{\phi} \setminus \{\phi_j\}$. The WP power can then be computed by the summation of the generated power of all $\mathcal{N}$ turbines in the WP as:

$$P_{\mathcal{N}} = \sum_{j=1}^{\mathcal{N}} P_j(\boldsymbol{\alpha}, \boldsymbol{\phi}; U_\infty, \theta^W) \quad . \tag{2.34}$$

2.4 Turbulence Intensity Modelling

Several studies such as in [87, 88, 89, 63] have delved into modelling the TI in WPs. Generally these models employ the freestream turbulence intensity alongside the turbines' thrust coefficient, in estimating the added wake turbulence I_+ at the hub height of a turbine as:

$$I_+ = \sqrt{I_{wake}^2 - I_\infty^2} \quad , \tag{2.35}$$

where I_{wake}^2 is the wake-influenced turbulence from turbines in the upstream and I_∞^2 is the freestream turbulence squared.

Other models

The authors in [87] employ an empirical solution to describe the added turbulence that a turbine i induces at a downstream turbine j, as given:

$$I_+ = 4.8C_T^{0.7} - I_\infty^{0.68}(d_{j,i}/d_n)^{-0.57} \quad . \tag{2.36}$$

Here, $d_{j,i}$ is as earlier defined in Equation (2.18) of this study, C_T represents turbine i's thrust coefficient, while d_n represents the near wake length, defined by [90] using the semi-empirical expression below. However, with no unified definition of where the near wake actually ends, which could vary depending on the turbine rotor radius, number of blades, and maybe even with inflow wind speed, as well as site terrain, d_n has to be computed as given, thus increasing the complexity of the model:

$$d_n = \frac{\sqrt{0.214 + 0.144m}(1 - \sqrt{0.134 + 0.124m})}{(1 - \sqrt{0.214 + 0.144m})\sqrt{0.134 + 0.124m}} \frac{r_0}{dl/dx} \quad , \tag{2.37}$$

where $m = \frac{1}{\sqrt{1-C_T}}$, $r_0 = (D/2)\sqrt{\frac{m+1}{2}}$, and dl/dx is defined by the expression that follows:

$$dl/dx = \sqrt{\left(\frac{dl}{dx}\right)_a^2 + \left(\frac{dl}{dx}\right)_m^2 + \left(\frac{dl}{dx}\right)_\lambda^2} \quad , \tag{2.38}$$

where $\left(\frac{dl}{dx}\right)_a^2 = 2.51I_\infty + 0.005$, $\left(\frac{dl}{dx}\right)_m^2 = \frac{(1-m)\sqrt{1.49+m}}{9.76(1+m)}$, and $\left(\frac{dl}{dx}\right)_\lambda^2 = 0.012B\lambda$, with B being the number of turbine blades and λ the blade tip speed ratio.

With the need to compute d_n separately as defined by [87], the authors in [89] also maintain a comparable level of complexity but however, define the added turbulence as:

$$I_+ = 5.7C_T^{0.7} - I_\infty^{0.68}(d_{j,i}/d_n)^{-0.96} \quad . \tag{2.39}$$

A relatively simpler model is seen in [88] to estimate the added turbulence by an extracting turbine i at j:

$$I_+ = 0.73\alpha^{0.8325} - I_\infty^{0.0325}(d_{j,i}/D)^{-0.32} \quad , \tag{2.40}$$

subject to the following parameter ranges; $5 < d_{j,i}/D < 15$, $0.07 < I_\infty < 0.14$, and $0.1 < \alpha < 0.4$, with all already defined parameters $I_\infty, \alpha, d_{j,i} and D$ retaining their definitions.

The work of [63] proposes the use of a top-hat distribution with the assumption of a wake diameter of 4σ, where σ has been obtained experimentally using LES data [91], and represents the standard deviation of the Gaussian-shaped wind speed deficit:

$$\sigma/D = \kappa d/D + \epsilon \quad , \tag{2.41}$$

where κ specifies how quick the wake expands behind each turbine and is given as $\kappa = 0.38371I + 0.003678$, and I is the localised turbulence whose considered range must be limited to $0.065 < I < 0.15$.

Previous studies in [91, 92] have shown that increase in turbulence inside a WP quickly saturates after about 2 - 3 rows. Furthermore, based on a recommendation from the study in [93] that when predicting turbulence in WPs for a particular turbine, it is only necessary to consider the turbulence from its direct neighbouring turbines (discarding freestream turbulence impact), the authors in [63] propose an added turbulence intensity which depends solely on the nearest turbine upstream in the considered wind direction.

$$I_{+_j} = max\left(\frac{A_w 4}{\pi D^2} I_{+_{ji}}\right) \quad , \tag{2.42}$$

where I_{+_j} depicts the added turbulence at turbine j, A_w is the wake overlap from nearest upstream turbine on turbine j's rotor surface area (and which can be obtained from Equation (2.41)), and $I_{+_{ji}}$ is the turbulence at j due to nearest upstream turbine i.

Frandsen model

Frandsen's model [43] is employed by the IEC standard 61400-1 edition 3 to assess turbulence intensity (TI) levels in WPs. Based on this specification, the effective TI at a location in a WP for any wind direction considered, shall be estimated by utilising 90th percentile of wind speed standard deviations for that direction, denoted as the representative standard deviation σ_{repr}. This "representative" value of standard deviation according to [43] is the standard deviation of wind speed measurements for a specific wind direction,

made within 10-minute intervals, typically sampled every 1-2 seconds. According to [43], this "representative" figure of standard deviation is the standard deviation of wind speed measurements made for a specific wind direction within a 10-minute interval, usually recorded at a frequency of 1-2 seconds. For different cluster considerations, Frandsen [43] specifies three different methods to compute the representative standard deviation σ_{repr}.

The first method is employed in a WP location assumed to be experiencing only "freestream turbulence" (i.e turbulence due to the freestream wind). Hence, this method is used to compute TI for turbines at the borders of a WP cluster, given that it is these turbines that by default experiences the freestream wind blowing from the direction considered. Other inner turbines in the cluster may also experience the freestream wind, but this depends strictly on the T-2-T distance of separation in the direction considered. This method assumes that with a minimum T-2-T separation distance greater than $10D$, inner turbines in a considered row for direction considered can also experience the freestream wind and hence, be subjected to freestream turbulence. However, beyond five turbines in the row and direction considered, the model is not considered as valid because changes in boundary layer condition begins to take effect. Consequently, this method whose expression is given below as in [42], cannot be used for very large turbine arrays.

$$\sigma_{repr,\infty} = \langle \sigma_\infty \rangle + 1.28 stdev(\sigma_\infty) \quad . \tag{2.43}$$

Here, $\langle \sigma_\infty \rangle$ specifies an average of the 10-minute standard deviations obtained from measurements of freestream wind speed in the site or WP, while $stdev(\sigma_\infty)$ represents the standard deviation of these 10-minute standard deviation values

An alternative method applies in computing σ_{repr} for very large farm arrays (with more than five turbines in a row) that also have a T-2-T distance greater than $10D$ similar to the first method. It is considered that any turbines or rows of turbines positioned beyond the fifth turbine or turbine row are subject to freestream wind farm turbulence (WFT) (described earlier in section 2.4 as *freestream turbulence*. The resulting TI on these turbines can be computed using the given expression for representative standard deviation.

$$\sigma_{repr,\infty,wf} = \langle \sigma_{\infty,wf} \rangle + 1.28 stdev(\sigma_\infty) \quad . \tag{2.44}$$

The term $\langle \sigma_{\infty,wf} \rangle$ specifies an average of the 10-minute standard deviation, and $stdev(\sigma_\infty)$ represents the standard deviation of the 10-min freestream wind speed standard deviations.

Frandsen [43] also specifies a third method to handle scenarios where turbines are deployed at T-2-T distances less than $10D$ apart. At such proximity, it is expected that the wake-influenced turbulence resulting from mixing in the shear layer continues to exist at a sufficiently high intensity to engulf all other sources of turbulence. Hence, the name "wake turbulence" (WT). In this scenario, only the border turbines experience freestream turbulence while all other turbines inside the WP because of their T-2-T distance of separation, experience the WT. The representative standard deviation σ_{repr} for the WT model is thus defined mathematically as:

$$\sigma_{\infty,wake} = \sqrt{\frac{U_\infty}{\left(1.5 + 0.8\left(\frac{d_{norm}}{\sqrt{C_T}}\right)\right)^2} + \sigma^2_{repr,\infty}} \quad , \tag{2.45}$$

where d_{norm} (defined mathematically as $d_{j,i}/D$) represents the axial T-2-T distance from the turbulence causing turbine to the considered downstream position or turbine, normalised by the rotor diameter, D, of the turbulence causing turbine and $\sigma^2_{repr,\infty}$ is the square of the value obtained from (2.43).

As explained, Equations (2.43), (2.44), and (2.45) represent the 90th percentile of the normally distributed fluctuations in wind speed (turbulence) and are used to compute the representative TI values for making fatigue load predictions. Frandsen also modifies these equations to compute mean TI values for all three methods, by making the following substitutions, respectively, as given.

$$\sigma_{mean,\infty} = \langle \sigma_\infty \rangle \tag{2.46}$$

$$\sigma_{mean,\infty,wf} = \langle \sigma_{\infty,wf} \rangle \tag{2.47}$$

$$\sigma_{\infty,wake} = \sqrt{\frac{{U_\infty}^2}{\left(1.5 + 0.8\left(\frac{d_{norm}}{\sqrt{C_T}}\right)\right)^2} + \sigma^2_{mean,\infty}} \quad , \tag{2.48}$$

The obtained representative and mean standard deviation values, respectively, are applied as given to obtain the turbulence intensity TI.

$$TI = \frac{\sigma(\theta, U_\infty)}{U_\infty} \quad , \tag{2.49}$$

However, the "simplified" version of the TI model proposed by Frandsen which is investigated by [42], does not assume any freestream wind farm turbulence at an arbitrary distance as proposed by Frandsen at a $10D$ distance. Consequently, the "simplified" version only utilises Equations (2.48) and (2.46) for mean TI computations of inner and border turbine computations, respectively, and Equations (2.45) and (2.43) for representative TI computations of inner and border turbine computations, respectively. Hence, $\sigma(\theta, U_\infty) \equiv \sigma_{\infty,wake}$ in Equation (2.48), and $\equiv \sigma_{mean,\infty}$ in Equation (2.46) for the "simplified" version's mean TI computation and $\sigma(\theta, U_\infty) \equiv \sigma_{\infty,wake}$ in Equation (2.45), $\equiv \sigma_{repr,\infty,wf}$ in Equation (2.44), and $\equiv \sigma_{repr,\infty}$ in Equation (2.43) for Frandsen's model's mean TI computation.

As noted by [42], very little work has been done in validating standalone TI models that are applicable to large WPs. The authors in this study proceeded to analyse TI levels within a large array offshore WP. In their study they established that it was unnecessary to assume an freestream wind farm turbulence at certain distances inside the WP for large arrays as proposed by Frandsen in [43]. Through a comparison of measurements from a large offshore array having T-2-T distances $\leq 10D$ against the predictions made by Frandsen's model and also against those made by their "simplified" version of the TI model proposed by Frandsen - where consideration of any freestream wind farm turbulence is ignored, they demonstrated that even without considering any freestream turbulence, the simplified model which rather considered individual wake-influenced turbulence, was more reliable compared to Frandsen's model irrespective of distance.

2.5 Wind Plant Optimisation and Control

The work of [94] presents an in-depth survey on (i) WP control as it concerns WP energy maximisation, (ii) WP power control based on an enforced total WP power reference to be followed, and (iii) WP energy maximisation with minimisation of turbine fatigue loads in mind. The authors in [95] go further to review control strategies aimed at maximising power generation within WPs, focusing on the three main actuation methods as highlighted in subsection 2.1.2 of this study; power-curtailment through pitching or generator speed or torque control, and power-curtailment through wake re-direction, while also considering layout optimisations.

Wind plant optimisation motivated by any of the three control methodology mentioned in the preceding paragraph can be achieved via a centralised, distributed or cascaded control architecture. As highlighted in [94], the most common and straightforward approach is the *centralised* approach. The authors, however, bemoan the massive amount of set-point updates that must be communicated between turbines and the centralised controller to ensure reliable operations. This has inspired *distributed* control methodologies as studied in [94] and [96], reducing communications to only between nearest neighbour turbines. In [97] turbines exchange local non-sensitive information for sake of privacy, with the aim to attain a reference total WP power that produces minimum total fatigue loading. These "*distributed*" control design studies admittedly, are revolutionary but have their challenges in terms as complexity and initial implementation costs which affects the capital expenditure (CAPEX) of a WF project. The WP optimisation problem is complex in itself, and a reduction in system complexity with comparable power generation will be a default desire of a WF planner.

Regardless the control architecture, inputs to the WF controller(s) could be the freestream wind speed (U_∞) as achieved using Light Detection and Ranging (LIDAR) sensors in [98, 99, 100, 101, 102], wind direction, the localised turbines mean wind speeds ($\bar{U}_j$), the mechanical loads, and the total WP power - in the case where there is an enforced total WP power reference to be followed [94, 103]. Whereas, outputs from the controller could either be the axial induction factor α, the blade tip speed ratio (λ), the blade pitch angle (δ), the rotor rotational speed reference (U_{blade})[94].

As already stated in subsection 2.2.2, economic reasons could compel farm planners to resort to closer turbine deployments within a restricted land. Although this approach increases turbine density and power density, this generally degrades the wind farm efficiency compared to deploying less number of turbines within the same area using the conventional 6 - 10D spacing. As far as the author is aware, there hasn't been extensive investigation of this complex scenario in the WP optimization literature. Rather, studies apply layout optimisation to improve total WP power or annual AEP of the base case/greedy control of a real or hypothesized WP of known dimensions as seen in [104], [105], and [72], and in some cases end up with a compressed WP area compared to the real or hypothesized WP studied [8]. Other studies apply power-curtailment or wake-steering using one or more algorithms to improve the total WP power and in few cases, the total WP power efficiency against the base case/greedy control of the same WP with similar WP dimensions[4, 51]. In addition to power maximisations, the authors in [16] also consider turbine loads, which has the tendency to further degrade the WP efficiency but they do not consider this metric in their study.

The variance of thrust forces on a turbine is employed by [16] to capture the fatigue damage that the turbine could incur. This thrust variance depends on the turbulence intensity at the turbine rotor position. Hence, reducing the turbulence intensity could have a positive effect on the fatigue damage. However, increasing turbine density and by extension power density is likely to increase turbulence intensity within the WP because of the positive relationship between the T-2-T distance parameters and TI as given in the different TI models Equations 2.36, 2.39, 2.40, and 2.36. The authors in [16] also minimise the turbine extreme loads by minimising the mean turbine thrust. This move, however, could still leave the turbines overexerting themselves especially when power maximisation is carried out simultaneously such as in [16]. The reason is that reducing the mean turbine thrust over time does not guarantee that the individual static thrust values will not exceed the thrust value necessary for optimal power extraction at the static wind speed as specified by the turbine thrust curve or C_T table. Additionally, a joint optimisation of WP power and mechanical loads as studied in [16] can reduce the WP power efficiency, given that WP power cannot be at its maximum when considering loads. The authors did not consider the resulting WP power efficiency trade-off given the load considerations.

In a field experiment, [106] applies the analytical model proposed in [64] to forecast turbine powers considering atmospheric conditions in the turbine vicinity and their yaw offsets. Findings demonstrate turbine power generation enhancements of up to 47% contingent upon the freestream wind speed U_∞. Their model, however, gave no consideration for possible yaw-influenced turbine loads. Furthermore, the model fails to account for the inherent wake skew noted in [80, 70]. The revised model introduced in [72], an advancement of the model outlined in [64] and extended to predict turbulence intensity (TI) at turbines, is employed in a parallel investigation outlined in [58]. The objective being to optimise turbine yaw offset angles, consequently enhancing wind plant power output and concurrently mitigating load on turbines. The wake model fails however, to consider wake skew and furthermore, applies freestream TI entirely across the wind plant to forecast loads. This deviates from the norm in a real wind plant unless in the presence of exceptionally massive T-2-T distances. Additionally, there is no examination of the trade-off between WP power, efficiency and load considerations.

The model seen in [107] considers TI estimations to optimise wind plant energy energy, while also integrating axial induction and wake deflection control. However, regardless of the number of turbines upstream, it uses an extremely simplistic method to combine wakes from many turbines, choosing to use only the biggest velocity deficit from all upstream turbines as the overall deficit on a downstream turbine. Additionally, the utilised wake deflection model features a rectangular rather than Gaussian profile, resulting in lower accuracy side-by-side newly proposed models in [63, 64, 3]. These models also employ more sophisticated wake combination methods, as seen in [72, 108].

In a comparative examination conducted by [109], several prior studies focused on enhancing grid-based WPs are analyzed. For every turbine, the writers in the works that are compared retain a constant C_T value of 0.88. On the other hand, this problem is resolved in the comparison analysis by optimising various plant layouts and adopting rotor wind speed-equivalent C_T values, $C_T(\bar{U})$. This refined approach even though failing to account for turbine loads, improved wind plant efficiency in every layout that was examined.

An extensive investigation is conducted in [110] to assess various Genetic Algorithm (GA) implementations' efficacy in enhancing Wind Plant (WP) power while simultaneously

reducing the cost of energy (COE). In order to attain an optimal turbine layout, the authors modify the traditional GA with a "bi-criteria identification and relocation (BCIR) mechanism" to relocate the most obstructive and least efficient turbines. The outcomes show notable improvements in wind plant power, wind plant power efficiency, and cost of energy. However, the incorporated wake model in the study does not account for wake skew. Furthermore, as pointed out in [111], the study overlooks potential extreme load impacts that could arise from power increments regardless of the U_∞ values investigated.

In maximising WP energy via power-curtailment, many studies in the literature are based on optimisation using static models, rather than dynamic control [94]. A very recent example is seen in [112]. In this case, static C_T tables of the employed turbine model is used to model the power as in (2.5). In order to obtain the projected energy increase in these studies, it is important to assume a constant wind speed and possibly wind direction at a given time. According to [94], it is necessary that the power curtailment set points on all turbines be applied correctly when the considered wind direction assures tight T-2-T distances. However, a change in wind direction that results in sparse T-2-T distances, should enforce a quick reduction or removal of the applied curtailment, else energy is lost compared to base case operation. WP power maximisation is also achieved via wake-steering in the works of [113] and [51], with [72] employing a wake model that can inherently predict turbulence intensity locally at turbine positions. Table 2.2 summarizes related investigations, including their features as well as their limitations in relation to this study's considerations.

Since the current research aim is to maximise WP power and consequently AEP by increasing turbine density, it is necessary to consider the TI at turbine positions within the WP. Furthermore, substituting Equation 2.6 into 2.4, and then the resulting expression into 2.5 will reveal a positive relationship between turbine power $P(\alpha, \bar{U})$ and C_T. Knowing that C_T also has a positive relationship with the turbine thrust based on Equation 2.6, then it is probable that maximising power will increase thrusts and thrust coefficients beyond rotor mean wind speed-equivalent C_T value for each individual turbine at each considered instance of time.

Considering the features and limitations of closely related studies in the literature of WP optimisation and control, the present study proposes to model a wind plant as a collection of

wind turbines deployed in a hexagonal lattice structure while increasing turbine density within a fixed WP area, and then further apply a centralised control via turbine axial induction factor optimisation to increase total WP power. The choice of a hexagonal layout or lattice deployment is its ability to afford directions of tight and sparse T-2-T distances that are equal and determinate. This way, the sparse T-2-T distances are the same plant-wide, so that a complete plant-wide removal of curtailment as advised by [94] is easily implemented centrally if and when needed. Whereas, in optimised layouts where the sparse T-2-T distances will not occur plant-wide but will be distributed around the wind plant, the curtailment will have to be on selected turbines that maintain a large distance with their nearest downstream turbine in considered direction. This could introduce another level of computation for the controller to identify those turbines, and this process will be necessary in all wind directions because T-2-T distances in each direction are not equal, neither are they determinate. Also, the optimisation will be implemented with considerations for the expected turbine density increase-enforced high turbulence intensities within the WP, and the expected maximisation-imposed high turbine thrust magnitudes.

In the next chapter, the study will model the wind plant and validate the expectations on turbine C_T values and turbulence intensities within a confined wind plant area, when the turbine density is increased and power maximised, and compare it to a conventional WP deployment of $6D$ and $7D$.

Table 2.1: Analytical wake models: Features and Limitations

Analytic Model	Features	Limitations
1. Jensen [1], Katic [2]	1. Linear wake expansion as function of axial distance d and decay rate k. 2. Axially-symmetric flow and self-similar Gaussian wind speed profile. 3. Cone-shaped wake profile. 4. Ambient-based root sum square method for superposition of multiple wakes.	1. Top-hat wind profile. 2. No wake-meandering. 3. No yaw offset capabilities. 4. No TI accountability.
1. Frandsen [60]	1. Linear wake expansion. 2. Axially-symmetric flow and self-similar wind speed profile. 3. Logarithmic wind profile above and below hub height. 4. WP split into three (3) wake regimes. 5. TI accounted for in a separate turbulence model.	1. Top-hat wind profile. 2. No wake-meandering. 3. No yaw offset capabilities. 4. Predicts a larger initial wake expansion and highest wind speed deficit for both single and multiple wake scenarios, compared to other analytical models [73].
1. Larsen [61]	1. Axially-symmetric flow and self-similar logarithmic velocity profile 2. Ambient-based linear sum method and ambient-based root sum square method for superposition of multiple wakes. 3. Wake expansion rate and wind speed deficit are functions of ambient TI.	1. For narrow wind direction bins, model underestimates energy production [74] 2. No wake-meandering. 3. No yaw offset capabilities. 4. Wake-generated TI unaccounted for.
1. Niayifar & Porté-Agel [63]	1. Axially-symmetric flow. 2. Wake expansion rate is a function of axial-wise TI. 3. Wake-generated TI accounted for. 4. Rotor-based linear sum method for superposition of multiple wakes.	1. No wake-meandering. 2. No yaw offset capabilities.
1. Qian & Ishihara [72]	1. Non-uniform flow assumed on rotor plane $w.r.t$ wind speed and TI 2. Wake-generated TI accounted for. 3. Rotor-based linear sum method for superposition of multiple wakes. 4. Rotor-based linear sum square method for superposition of TIs.	1. No wake-meandering.

Table 2.2: Related studies: Features and Limitations

Study	Features	Limitations
1. Bo *et. al.* [112]	1. 2-D Jensen-Gaussian wake model with turbine axial induction factor as optimisation variable. 2. Total WP power maximisation	1. No wake-meandering feature. 2. No fatigue damage or extreme load consideration 3. No WP power or energy efficiency consideration
1. Park *et. al.* [113]	1. 2-D Gaussian wake model with turbine axial induction factor and yaw offset angles as optimisation variable. 2. Total WP power maximisation 3. Wake meandering capability	1. No fatigue damage or extreme load consideration 2. No WP power or energy efficiency consideration.
1. Qian & Ishihara [72]	1. 2-D Gaussian wake model with turbine axial induction factor and yaw offset angles as optimisation variable. 2. Total WP power maximisation 3. Wake-generated TI unaccounted for.	1. No extreme load considerations 2. No wake-meandering. 3. No WP power or energy efficiency consideration.
1. Gebraad *et. al.* [51]	1. CFD model with with turbine axial induction factor and yaw offset angles as optimisation variable. 2. Model captures wake meandering and skew	1. No fatigue damage or extreme load consideration 2. No WP power or energy efficiency consideration.
1. Park & Law [4]	1. 2-D Gaussian wake model with turbine axial induction factor and yaw offset angles as optimisation variable. 2. Model captures wake meandering and skew 3. WP power efficiency considered 4. Total WP power maximisation	1. No fatigue damage or extreme load consideration
1. Barradas-Berglind & Wisniewski [16]	1. Top-hat 2-D actuator disc model with axial induction factor as optimisation variable 2. Total WP power maximisation with extreme loads and fatigue damage consideration	1. No WP power or energy efficiency consideration 2. No wake meandering and skew in wake model
1. This study	1. 2-D Gaussian wake model with turbine axial induction factor and yaw offset angles as optimisation variable 2. Model captures wake meandering and skew 3. Total WP power maximisation with extreme loads and fatigue damage consideration via thrust coefficient and TI control. 4. Wake model captures wake meandering and skew 5. WP energy efficiency considered and analysed 6. Total WP power and AEP maximisation	1. No explicit computation of extreme loads and fatigue damage because the optimisation model is static, and based on static C_T relationships with the wind speed and turbine power.

Chapter 3

System Modelling and Power Maximisation

3.1 Introduction

Wind turbines and wind plants (WPs) are continuing to grow in size and number of installations as the world move towards achieving the envisioned net zero carbon emissions by the year 2050. Because energy from wind is a readily available source of clean energy, the magnitude and efficiency of its generation, safety and reliability of its transmission, and the efficiency of distribution are fields of significant research interest. With respect to generation, state-of-the-art wind plants employ a fusion of supervisory control and data acquisition (SCADA) systems, safety systems and closed-loop control systems (e.g., yaw, pitch) to enable an efficient safe, and reliable operation [114] needed to achieve optimum performance. Moreover, the International Electrotechnical Commission (IEC) 61400-25 series [115] offers guidelines to enhance a consistent communications platform for WPP component supervision and control with regard to data flows between measuring equipment. Wind plant performance objectives are often conflicting, such as simultaneously maximising power production and reducing turbine loads. Consequently, system optimisation is an ongoing process that is required to reliably address the trade-offs that inevitably arise. Furthermore, there are numerous interacting components in the wind plant optimisation problem that make it multidimensional and impossible to fully account for as optimisation

variables. It is therefore typical for some WP parameters to be disregarded based on the purpose of the WP deployment.

Performance optimisation and cost reduction are the main objectives of WP optimisation. These are encapsulated in (1) The capital expenditure (CAPEX), which includes the cost of leasing land, the cost of installing turbines, and cost of monitoring vehicles. (2) The operational expenditure (OPEX) which comprise accessibility and operations costs, maintenance costs, fatigue load reduction, and potentially the management of extreme events, and (3) Revenue, which is influenced by wake losses, prevailing market prices, site's wind resource, and potential electrical losses. As aforementioned, capturing all contending factors is almost infeasible because they are enormous. Therefore, in a site with a favorable wind resource, opting for the optimal turbine deployment during the pre-operation phase, and maximising the WP power production concurrently with turbine load reduction in the operational phase can typically address other factors affecting operational expenditure (OPEX) and revenue. These factors include the reduction of wake losses and enhancement of accessibility, which in turn lowers maintenance and operational costs, consequently reducing the market price per kilowatt-hour of electricity. As a result, the focus of current research in WP optimisation and control has been on power maximisation and/or mitigating turbine loads.

All WPPs depend on a combination of SCADA and control systems, which govern most operations from individual turbines to the collection substation [114], offers real-time visibility into plant operations, facilitating a centralized, yet local and remote control of the WPP. The WP controller sits in a local SCADA station, and based on various output measurements from the SCADA system, issues power references or turbine control parameter set-points to each turbine that is actuated by the turbine-level controller to yield the power references and which will ultimately result in a maximised plant power or grid enforced wind power reference. However, because AEP maximisation is the goal in this study, a year-round plant power maximisation is the goal rather than following a grid enforced wind power reference.

More often in the literature and probably more easily, the axial induction factor α of turbines in a WP is regulated by adjusting the turbine's generator speed or torque below

rated wind speeds, or its pitch angle above rated wind speeds. Since the axial induction factor specifies the degree of reduction between the wind speed immediately behind a rotor compared to the that in front of it, it is then critical to know the wind speeds in front and behind the rotor before any control set-point is issued by the controller and the control is effected by the turbine. In a feedback control mode, some optimality may be initially lost while awaiting wind speed measurements behind the rotor to compute and issue optimised set-points. However, estimated measurements upstream of these turbine rotors can be obtained in feed-forward control modes using Light Detection and Ranging (LIDAR) sensors mounted on the turbine nacelle of selected turbines. Such optimality issues may be circumvented by computing local wind speeds at various positions downstream of these select turbines, based on their applied axial induction factors, and taking into account the presence of all other turbines affecting one another. Therefore, for the remainder of this study, it is assumed that

Assumption 3.1. *The WP is controlled centrally by a local SCADA station using live wind speed and direction measurements from nacelle-mounted LIDAR sensors on some turbines.*

3.2 Power maximisation

According to the global wind report of 2021 [116], 2021 will be remembered as the year when a real breakthrough was reached in achieving the projected global net zero carbon emission by 2025, as accepted paths for accelerated growth was established and countries had begun implementing their plans to meet this goal. This accelerated growth can be attributed partly to the huge research directed towards optimising the reliability and efficiency of wind plant operations, in recent years.

To improve the efficiency of WPs, maximising their power production as a unit is inevitable, as studies have already shown that greedy turbine power maximisation is not as beneficial as achieving such with all turbines acting cooperatively and collectively.

Park and Law presented a yaw-suited, intrinsically-skewed Gaussian wake model in [3]. They used CFD simulation data to calibrate the wind plant power function of this model in order to identify the required constants and set a range of yaw angle offsets. Next, by

optimising the turbine layouts in [3] and the turbine yaw angles in [69], the wake model that has been suggested is employed to maximise WP power production. The authors however do not consider the effects of turbulence intensities which could induce fatigue damage and negatively affect turbine health.

The authors in [51] apply CFD simulation to maximise the annual energy production (AEP) of a wind plant by maximising the WP power for each bin. By applying yaw angle offsets to individual turbines to redirect the wake behind them, the WP power and consequently the AEP is maximised. Their study however, does not consider the possible effects of these intentional yaw offsets on turbine loads which on the long term can result in fatigue damage and shorten turbine lifetime.

In [76], a distributed approach is employed to optimise wind plant power either for a maximum WP power or a maximum allowed power injection from a grid. Their distributed approach effectively solves the rapid convergence problem of the optimisation algorithm, rendering it appealing for real-time WP control solutions. However, the study ignores turbulence intensity effects which may arise due to the power maximisation.

Another power maximisation study by [108] employs only the gaussian wake deficit model proposed in [3] without incorporating the turbine and plant power definitions proposed by [3], making their study non yaw-suitable and non skew-innate. The WP is treated as a collection of rows of turbines, consequently each turbine x affects only turbines that are positioned along the wake axis behind them, as opposed to affecting every turbine j whose position-influenced T-2-T distance $d_{x,j} \geq 0$. Their study also considers the turbulence intensity at each turbine by constraining it's power production by a maximum allowable threshold turbulence intensity value. In this study, turbines are deployed in a hexagonal lattice structure, with the assertion that this regular layout although considered traditional and limiting, could offer other significant gains such as reducing or eliminating the need for parameter optimisations in wind directions where the minimum T-2-T spacing is large enough to render such effort unnecessary. However, the study does not show this advantage since the study only considered one wind direction.

[117] examines how to maximise wind plant power production by combining layout optimisation, yaw angle offsets, hub height, and turbulence intensity adjustments inside

the wind plant. For their study, a Gaussian yaw-suitable wake model is employed but the model fails to consider the innate wake skew noticed in [80, 70], while also failing to account for possible excessive turbine thrust as a consequence of the power maximisation.

In this chapter and throughout the investigation, the intrinsically-skewed, yaw-suitable Gaussian model proposed in [3] is employed to optimise the axial induction factors of a hexagonally deployed wind plant with fixed area dimensions, to maximise the wind plant power and consequently, the AEP. A "simplified" execution of Frandsen's turbulence intensity model [43] studied in [42] and which was found to be more reliable in the prediction of turbulence intensities compared to Frandsen's ambient wind TI model, is augmented to enable constrainment of TI at border turbines, and then coupled with the power function in [3], for both TI and power estimations. The desire is an all-encompassing system model with constituent yaw and skew-innate wake model and a localised-wind rather than an ambient-wind TI model, to enhance consideration and monitoring of turbine thrust and TI while maximising WP power and AEP. Since these parameters influence turbine fatigue damage and extreme loads, it is important to consider and determine their behaviour when maximising power and AEP, moreso using a regular hexagonal turbine layout, rather than an optimised layout or the conventional sparse deployment.

Hence, guided by the research aim and the pros and cons of different WP layout as observed from the literature, this chapter will optimise without constraints using PSO and GA, the WP power and AEP of a hexagonally deployed WP with restricted dimensions, while monitoring the resultant effects on turbine thrust and TI. The decision to optimize without constraints is inspired by the aim to obtain maximal WP power and AEP values, as constraints tend to restrict the search space and hence, the optimal values.

3.3 System Modelling

The WP system comprises the wind turbines within a wind plant of fixed area, centrally controlled using information from four border turbines to compute and issue axial induction factor (α) set points that influence the wake behaviour within the WP, and consequently, turbulence intensity at the turbine positions. The WP system also encompasses the

wake and turbulence intensity models that aid in the observation and analysis of these interactions within the WP. The WP controller then applies the evolutionary and meta-heuristic algorithms (GA and PSO, respectively) to the entire WP system to obtain optimal α values for all turbines, at all speeds and directions, maximizing the AEP over numerous iterations and trials.

Meta-heuristic and evolutionary algorithms, especially PSO and GA have been widely applied in the literature of wind farm optimisation including layout optimisation and have shown great ability in producing significant improvements in all studied cases. For example, the authors in [49] and [118] applied a genetic algorithm (GA) to optimally place turbines, aiming to maximise total power output and efficiency while minimising a simplified cost function. Similarly, [119] developed two GA-based optimisation models for a real offshore wind farm, targeting cost minimisation and power maximisation with a fixed turbine count. Their models outperformed the layouts proposed by [49]. Pillai *et al* in [120] applied both binary GA and binary PSO to offshore wind plant layout optimisation. The results demonstrated that both algorithms effectively optimised layouts considering the levelized cost of energy (LCOE). Notably, they achieved lower LCOE values compared to some previously published studies, indicating their competitiveness even against newer methods. In [76] a distributed PSO-based control strategy is implemented to maximise wind plant power generation under constraints. Although the optimisation is cooperative, the PSO still demonstrates fast convergence and effective power gains. The authors in [110] introduce a bi-criteria approach to both the conventional genetic algorithm (GA) and its modified variants to identify and reposition underperforming turbines, thereby reducing the cost of energy (CoE). The modified GAs demonstrated marginal improvements over the conventional GA, with the best variant achieving approximately a 2 percent increase in efficiency and a 0.29 reduction in CoE. Although focused on optimal power flow rather than wind farm layout optimization, this comprehensive review found that both GA and PSO deliver high accuracy, with GA slightly edging, but with PSO requiring less computational effort. These results indicate that these traditional algorithms remain highly effective, depending on the specific application and performance priorities. Notwithstanding, [121] evaluated twelve metaheuristic algorithms, including GA and PSO, for wind farm layout optimisation. While

newer methods like Moth-Flame Optimisation (MFO) performed strongly, GA and PSO remained competitive due to their simplicity and ease of implementation. The study highlighted that algorithm performance is problem-dependent, reinforcing the continued relevance of traditional approaches in optimisation. While newer metaheuristic algorithms often bring innovative strategies to optimization problems, traditional algorithms like GA and PSO continue to demonstrate strong performance in wind farm layout optimization. Their effectiveness, combined with their simplicity and well-understood behavior, makes them reliable choices.

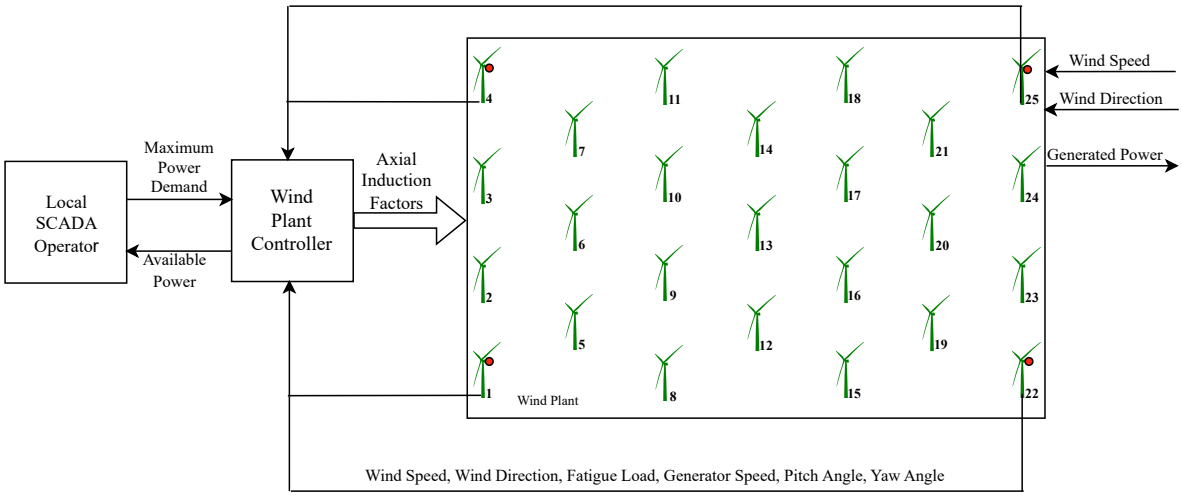

Figure 3.1: Wind Plant System.

3.3.1 Wind Plant Model

Because this study leans towards simplicity, it has chosen the hexagonal layout of turbines against its regular counterparts based on its reported advantage as discussed in paragraphs 2 and 3 of chapter 2, section 2.2.2. To buttress this choice, this study using Figure 3.2, demonstrates this advantage based on the unique considerations of the study. Consider Figure 3.2 with subfigures a, b and c representing an octagon with a square/tetragon fitted into it, a hexagon with a tetragon fitted into it, and a tetragon, respectively. Because a tetragon has four equal sides and is fitted to lap with one side of the octagon and hexagon, it can be inferred that all sides of the octagon and all sides of the hexagon are equal in length

to each/all sides of the tetragon. Also, because a hexagon comprises six equilateral triangles, it can be inferred too that $A = ab = af$ in terms of length.

It is intended that the smallest T-2-T distance considering all directions, is $5D$. Assume that A is $5D$ long and turbines are positioned at the vertices and at the centre of the octagon and hexagon, but only at the vertices of the tetragon. Then, regardless the direction from which each of the polygon is viewed, the minimum T-2-T distance will be $5D$ in length.

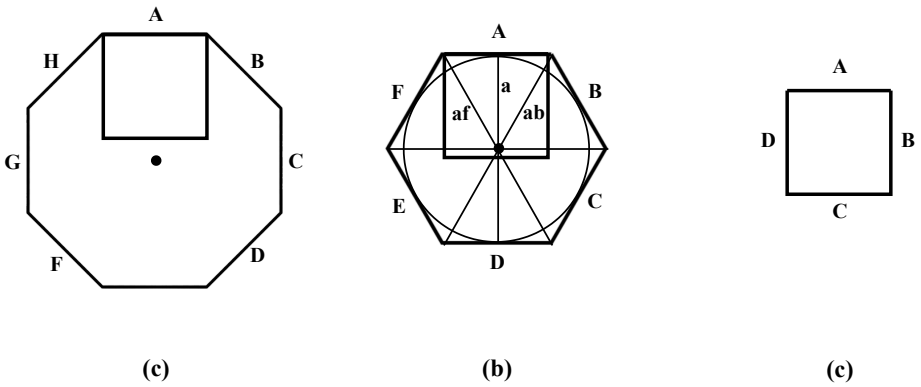

Figure 3.2: Layout comparisons

With the understanding established in the previous two paragraphs, Figures 3.4, 3.3, and 3.5 are created by superimposing a 2-D hexagonal lattice structure, a 2D-tetragonal lattice structure, and a 2-D octagonal lattice structure, respectively, on a 15x15 grid of tetragons. This 15x15 grid of tetragons represent a fixed regular plant area on which a hexagonal, octagonal, and tetragonal layout of turbines are to be deployed. Comparing all three figures (Figures 3.4 - 3.5), and recalling the assumptions of the preceding paragraph, it can be deduced that although the hexagonal layout of turbines and the tetragonal layout of turbines enhance space maximisation as they leave no gaps in-between inner cells. However, the hexagonal layout will pack more turbines (313) within the fixed regular plant area compared to the tetragonal (256) and the octagonal (203) layouts. The octagonal layout is shown to be the most inefficient given that it cannot be created without gaps, which are identified by the red-coloured diamonds. Considering that space maximisation is always a priority in wind plant projects as it affects not only the CAPEX, but also the OPEX and revenue components, the octagonal layout will not be a good choice.

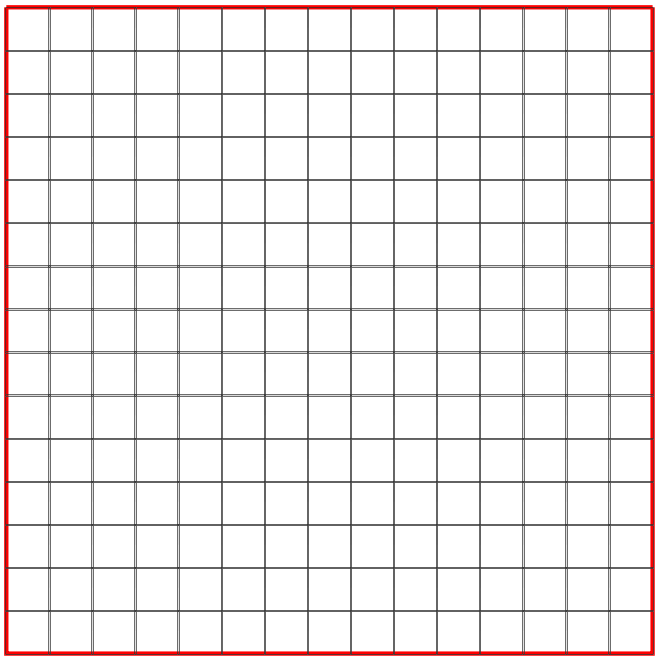

Figure 3.3: 2-D Tetragonal lattice with turbines positioned on vertices of tetragons

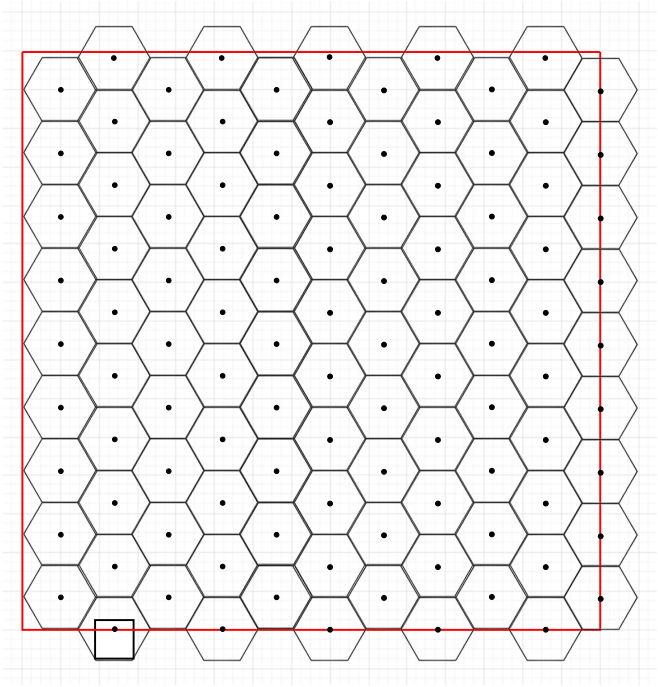

Figure 3.4: 2-D Hexagonal lattice with turbines positioned on vertices and centre of hexagons

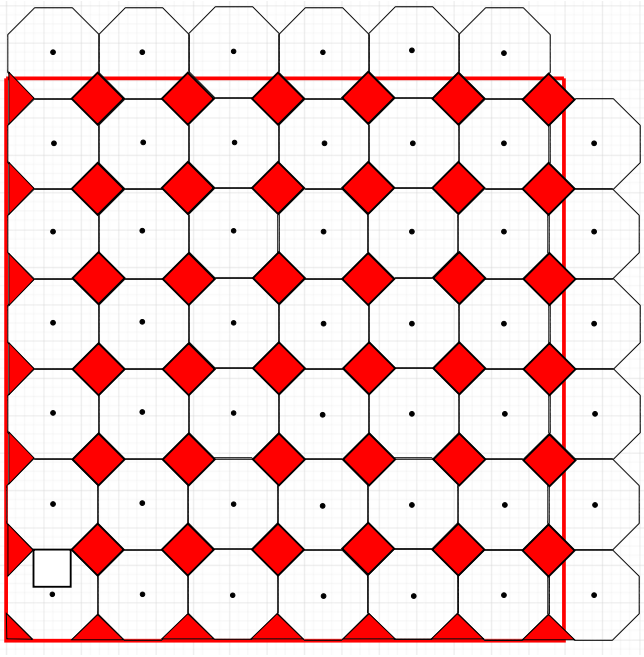

Figure 3.5: 2-D Octagonal lattice with turbines positioned on vertices and centre of hexagons

Hence, to maximize the utilization of a confined area of land, turbines are deployed hexagonally in this study, as depicted in Figure 3.6, to achieve the highest turbine density within the designated area. Three T-2-T distances or scenarios (5, 6, and 7 D) are studied to determine how maximised AEP, as well as TI-levels and thrust values vary with increasing T-2-T distance. An additional benefit of the chosen layout is its capacity to provide T-2-T distances in some directions that meet the conventional deployment distances of at least $7D$. The hypothetical multi-directional WP studied is partitioned into 12 wind bins ($\theta^W \pm 15°$) for simplicity, matching the studied site's wind rose. Table 3.1 is then generated with reference to Figure 3.6 to provide clarity regarding the wind plant area, wind bins, T-2-T distance/scenario, number of turbines in the wind plant per T-2-T distance, and border control turbines for each wind bin.

Assumption 3.2. *Over the WP length and in all considered directions, the pair* (U_∞, θ^W) *is uniform and does not fluctuate much. The* θ^W *variation frequency occurs at most once every hour. It is also possible to assume slower oscillations, such as daily, weekly, or even seasonal.*

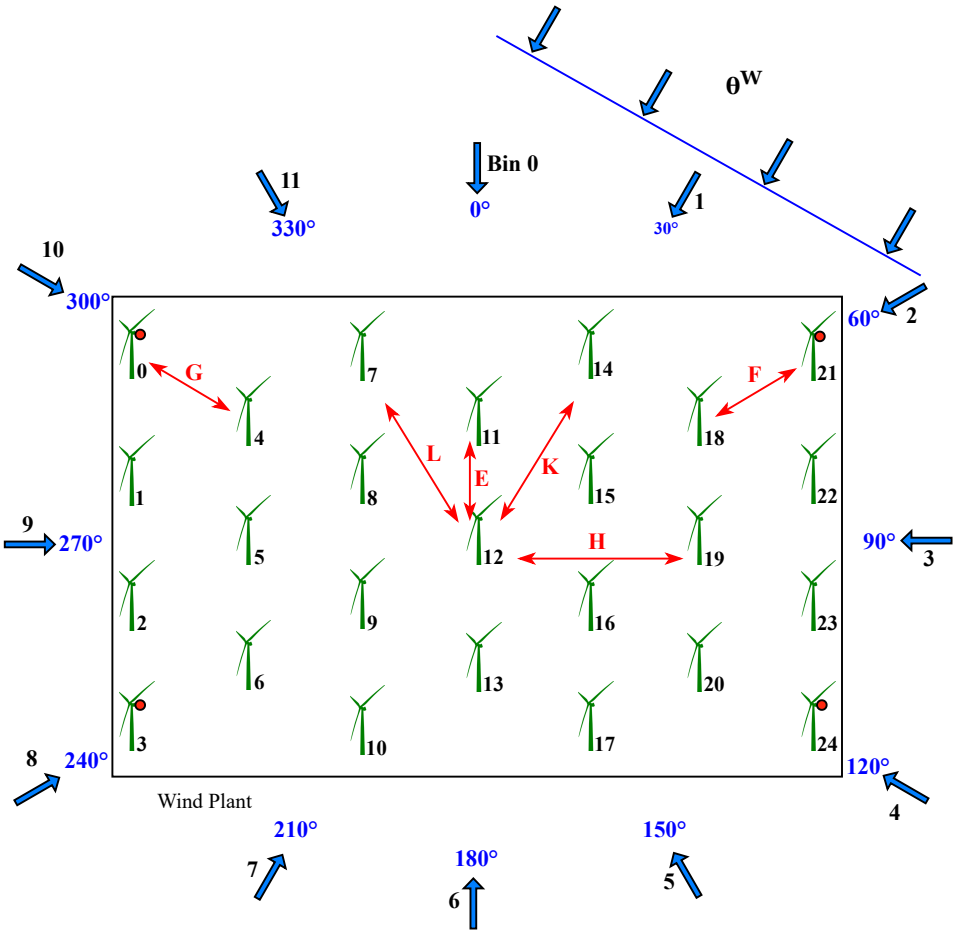

Figure 3.6: Wind plant layout model.

Table 3.1: Wind plant features

Parameter	Meaning	Value	Unit
$\mathcal{A}$	Farm Area	4655 x 2880	m^2
T-2-T distance/scenario	Minimum distance between turbines	5, 6, 7	D
$\mathcal{N}$	Number of turbines in wind plant	$7D = 25$ $6D = 32$ $5D = 45$	Turbines ” ”
bins	Wind directions $\pm 15°$	12 (0 - 11)	°
$\mathcal{C}$	Border control turbine(s) per bin bins 0 1 and 2 3 4 and 5 6 7 and 8 9 10 and 11	Turbine 0 and 21 21 21 and 24 24 24 and 3 3 3 and 0 0	

3.3.2 Wind Turbine Model

The Gamesa-g128-5.0MW turbine model, which is variable wind and pitch, and has three blades, is used in all analyses. The turbine data is provided in Table 3.2 and can be accessed publicly online at en.wind-turbine-models.com [122].

Table 3.2: Wind turbine model parameters

Parameter	Meaning	Value	Unit
P_r	Rated power	5.0	MW
U_{in}	Cut-in wind speed	3	m/s
U_r	Rated wind speed	14.5	m/s
U_{out}	Cut-out wind speed	27	m/s
D	Rotor diameter	128	m
z_0	Hub height	140	m

3.3.3 Wake Model

Wake interference from a single upstream turbine

Taking into account the infeasibility of applying CFD models to provide solutions in real-time, [3] proposed a continuous analytical model that is differentiable, and has a Gaussian feature both axially and radially(in the perpendicular direction). This model-based alternative provides a comparable level of fidelity to CFD tools, as demonstrated in [3, 4] where it has been calibrated with CFD simulation results using a real wind plant data. Hence, a single turbine wake is modelled according to the gaussian-shaped continuous analytical model proposed by [3].

In this chapter, the emphasis lies in examining how maximizing AEP impacts turbulence intensity and thrust values. As a result, all turbine yaw angles, ϕ, within the wind plant are preallocated 0° values, for the sake of simplicity. Based on this decision to maintain a 0° yaw angle for all turbines in the WP, the wind speed deficit at any location in a single turbine wake originally defined in Equation (2.8), reduces to

$$U_{def}(d, r, \alpha) = 2\alpha \left(\frac{R}{R + \kappa d} \right)^2 \exp\left(- \left(\frac{r}{R + \kappa d} \right)^2 \right) \quad . \tag{3.1}$$

The axial T-2-T distance d relative to i and j and the effective radial T-2-T distance r relative to i and j, are both defined respectively as in Equations (2.18) and (2.24) based on [3] and [70], respectively. Regardless of the choice to maintain a 0° yaw angle, the axial T-2-T distance $d_{j,i}$, along with two of the constituent terms that make-up the effective radial T-2-T distance, $r_{j,i}$, (i.e. $r^p_{j,i}$ and $r^r_{j,i}$) remain active. However, the third term ($r^\phi_{j,i}$) equates to 0 because of the *sine* term in Equation (2.22). Hence, the effective radial T-2-T distance originally expressed in Equation (2.24), reduces to

$$r_{j,i} = r^p_{j,i} + r^r_{j,i} \quad . \tag{3.2}$$

The wind speed deficit $U_{def_{j,i}}$ at any downstream location (d, r) is then expressed below, devoid of dependence on ϕ:

$$U_{def_{j,i}}(d_{j,i}, r, \alpha_i) = 2\alpha \left(\frac{R}{R + \kappa d_{j,i}}\right)^2 \exp\left(-\left(\frac{(r_{j,i} - r'\cos\theta')^2 + (r'\sin\theta')^2)^{1/2}}{R + \kappa d_{j,i}}\right)^2\right) \quad , \tag{3.3}$$

and the wind speed $U_{j,i}$ at any point (r', θ') on a downstream turbine's rotor ($j's$ rotor) originally expressed in Equation (2.26) is also expressed devoid of dependence on ϕ as

$$U_{j,i}(r', \theta', \alpha_i; U_\infty, \theta^W) = \begin{cases} (1 - U_{def_{j,i}}(d_{j,i}, r, \alpha_i))U_\infty, & \text{if } d_{j,i} \geq 0 \\ U_\infty, & otherwise \quad . \end{cases} \tag{3.4}$$

The generalized power $P_{j,i}$ generated by a controlled wind turbine j due to the presence of i, is thus defined based on [6] as:

$$P_{j,i}(\alpha_i, \alpha_j; U_\infty, \theta^W) = \begin{cases} 0, & \text{if } U_\infty < U_{in} \\ \frac{1}{2}\rho A \bar{U}^3_{j,i}(\alpha_i; U_\infty, \theta^W) C_P(\alpha_j), & \text{if } U_{in} \leq U_\infty < U_r \\ P_r, & \text{if } U_r \leq U_\infty < U_{out} \\ 0, & \text{if } U_{out} \leq U_\infty \quad . \end{cases} \tag{3.5}$$

Wake interference from multiple upstream turbines

Concurrent wakes from multiple upstream turbines as depicted in Figure 2.11, are commonplace in modern WPPs, and in combining these wakes, Park and Law in [4] adopts the rotor-based root sum square method contrary to the ambient-based root sum square method employed by the well-known Park model [2]. Consequently, Park and Law express the averaged deficit at a downstream turbine $\bar{U}_{def_{j,i}}$, as a function of the rotor-averaged wind speed in front of its closest upstream turbine, $\bar{U}_i$, and the averaged wind speed $\bar{U}_i$ at the downstream turbine position as given in Equation (2.29).

The aggregated deficit factor for a downstream wind turbine j is then generalized as:

$$\bar{U}_{def_j}(\boldsymbol{\alpha};\theta^W) = \sqrt{\sum_{i=1}^{\mathcal{T}} (\bar{U}_{def_{j,i}}(\alpha_i;\theta^W))^2} \tag{3.6}$$

where $\mathcal{T}$ is the total number of turbines in the upstream of j, $\boldsymbol{\alpha}$ is the axial induction factor vector of all upstream turbines' axial induction factors (i.e, $\boldsymbol{\alpha} = (\alpha_1, ..., \alpha_{\mathcal{T}})$), and θ^W is the considered wind direction. With respect to Figure 2.11, Table 3.3 is obtained, showing each turbine and its set of upstream turbines $\mathcal{T}$, sorted in order of decreasing wake strength, for the two wind directions depicted in the figure.

This study also maintains the optimum parameter values $\gamma = 1.5410, \chi = 0.0211, \tau = 0.5617$, $\beta = 0.7850$, and $\kappa = 0.0313$ as presented in [3].

Table 3.3: Turbines and their direction-dependent upstream turbines.

Direction A		**Direction B**	
$j \in \mathcal{G}$	$\mathcal{T}$	$j \in \mathcal{G}$	$\mathcal{T}$
1	{2,3,4,5,6,7,8,9}	7	{8,9,4,5,6,1,2,3}
2	{3,4,5,6,7,8,9}	8	{9,4,5,6,1,2,3}
3	{4,5,6,7,8,9}	9	{4,5,6,1,2,3}
4	{5,6,7,8,9}	4	{5,6,1,2,3}
5	{6,7,8,9}	5	{6,1,2,3}
6	{7,8,9}	6	{1,2,3}
7	{8,9}	1	{2,3}
8	{9}	2	{3}

where the set $\mathcal{G} = \{1, 2, 3, 4, 5, 6, 7, 8\}$ for Direction A and $\mathcal{G} = \{1, 2, 4, 5, 6, 7, 8, 9\}$ for Direction B, is a set containing all turbines that have at least one turbine in their upstream, and the set $\mathcal{T}$ for each j is the set of all turbines in its upstream.

Finally, for a given wind condition (U_∞, θ^W), the average wind speed encountered at the rotor of a downstream turbine can be determined using Equation (2.32) as follows:

$$\bar{U}_j(\boldsymbol{\alpha}; U_\infty, \theta^W) = (1 - \bar{U}_{def_j}(\boldsymbol{\alpha}; \theta^W))U_\infty \quad , \tag{3.7}$$

and the power output of any downstream turbine j can be formulated as a function of the control actions α of all upstream turbines i preceding j in the considered direction:

$$P_j(\boldsymbol{\alpha}; U_\infty, \theta^W) = \frac{1}{2}\rho A \bar{U}_j^3(\boldsymbol{\alpha_{-j}}; U_\infty, \theta^W) C_P(\alpha_j) \quad . \tag{3.8}$$

Hence, from Equation (3.8), the jth turbine's power generation depends both on its own control action (α_j) and the control actions of all other turbines in its upstream, which are captured in the vector $\boldsymbol{\alpha_{-j}} = \boldsymbol{\alpha} \setminus \{\alpha_j\}$, or $\boldsymbol{\alpha_{\mathcal{T}}}$ based on our set description. The total power output of the WP is calculated by summing the power generated by all $\mathcal{N}$ turbines within the WP as follows:

$$P_{\mathcal{N}} = \sum_{j=1}^{\mathcal{N}} P_j(\boldsymbol{\alpha}; U_\infty, \theta^W) \quad . \tag{3.9}$$

3.3.4 Turbulence Intensity Model

For analysis of turbulence intensity (TI) variations within the WP, Frandsen's model [43] which is utilised in the IEC standard 61400-1 edition 3 [77] to assess TI levels and the suitability of turbines for a site, is adopted, for mean TI analysis. Nevertheless, the research employs a "simplified" version of this model, as investigated in the work of [42], where it assumes no ambient wind farm turbulence regardless of a turbine's position within the wind plant. This "simplified" implementation was demonstrated to be more reliable in predicting TI values regardless of downstream distance compared to Frandsen's ambient wind farm turbulence model. It uses Equations (2.43) and (2.46) to compute representative

and mean TI, respectively, for all border turbines (turbines without any upstream turbine in the direction considered), while using Equations (2.45) and (2.48), respectively, for all other inner turbines. This study however, proposes to further augment this "simplified" implementation to capture the studied scenario and also reflect a more standard definition of TI. This augmentation involves utilizing local wind speeds to normalize the representative standard deviation.

Using the freestream wind speed data collated via meteorological masts before erection of a WP, the effective TI at any given location (d, r) within a site by utilising the 90th percentile value of freestream wind speed standard deviations also known as turbulence, obtained every 10 minutes during the duration of measurement [77]. This value, termed the representative standard deviation σ_{repr}, is derived from wind speed measurements collected for a specified wind direction θ^W, typically sampled at frequencies of 1-2 seconds [43]. Relying on freestream wind data, both the mean and the representative values of the distribution for Frandsen's model are developed. In this study however, we substitute the freestream wind with the locally measured mean wind speed at the turbine location, while maintaining the parameters $\sigma^2_{repr,\infty}$ and $\sigma^2_{mean,\infty}$ as presented in Frandsen's model and its simplified form, to represent respectively, the representative values squared and the mean values squared of the 10-min freestream turbulence values in the direction considered.

It is known that altering the axial induction factor α of a turbine affects its thrust coefficient C_T and the thrust force acting on its rotor. Consequently, this affects how much wind it captures, the TI it suffers as well as the conditions of the wake behind it (which affects wind speed and TI of turbines in its wake). Equations (2.43) and (2.46) however, do not offer such liberty to alter α for all border turbines and so cannot be used for optimisation cases where it is expected that every turbine in the WP including border turbines will alter their α to ensure a plant-wide optimised power and TI levels. Considering this limitation in Frandsen's border turbine equations ((2.43) and (2.46)), this study employs Equations (2.45) and (2.48) albeit with augmentations, to compute TI for both border and inner turbines. Additional refinements are applied to the inner turbines to incorporate locally estimated wind speeds within the wind plant. Consequently, equations for the representative and mean values of the distribution for border turbines are provided as follows:

$$\sigma_{\infty,wake} = \sqrt{\frac{{U_\infty}^2}{\left(1.5 + 0.8\left(\frac{d_{norm}}{\sqrt{C_T}}\right)\right)^2} + \sigma^2_{repr,\infty}} \quad , \tag{3.10}$$

$$\sigma_{\infty,wake} = \sqrt{\frac{{U_\infty}^2}{\left(1.5 + 0.8\left(\frac{d_{norm}}{\sqrt{C_T}}\right)\right)^2} + \sigma^2_{mean,\infty}} \quad , \tag{3.11}$$

$$TI = \frac{\sigma(\theta, U_\infty)}{U_\infty} \quad , \tag{3.12}$$

where $\sigma(\theta, U_\infty) \equiv \sigma_{\infty,wake}$, and d_{norm} is the distance of a hypothetical nearest upstream turbine ahead of the border turbine, normalised by D. This hypothetical upstream turbine is considered to be positioned at a considerable distance ($1000D$ meters away), symbolizing an effectively non-existent upstream turbine, which really is the case for border turbines. Hence $d_{norm} = 1000D/D$, making its effect on the border turbine negligible.

Furthermore, the representative value and the mean value of the distribution can be obtained respectively, for inner turbine(s) as:

$$\sigma_{j,wake} = \sqrt{\frac{{U_j}^2}{\left(1.5 + 0.8\left(\frac{d_{norm}}{\sqrt{C_T}}\right)\right)^2} + \sigma^2_{repr,\infty}} \quad , \tag{3.13}$$

$$\sigma_{j,wake} = \sqrt{\frac{{U_j}^2}{\left(1.5 + 0.8\left(\frac{d_{norm}}{\sqrt{C_T}}\right)\right)^2} + \sigma^2_{mean,\infty}} \quad , \tag{3.14}$$

$$TI = \frac{\sigma(\theta, U_j)}{U_j} \quad , \tag{3.15}$$

where $\sigma(\theta, U_j) \equiv \sigma_{j,wake}$, and d_{norm} signifies the closest upstream turbine's distance from the considered inner turbine, normalised by the rotor diameter D.

Because the turbines are required not to yaw ($\phi = 0°$) but only affect their axial induction factors α, a downstream turbine j is most influenced by an upstream turbine i when it is directly on the wake axis of i (i.e. $r_{j,i} = 0$). Based on Figure 3.6, if we consider $\theta^W = 0°$ (bin 0), then turbine 5 will be most affected by turbine 6, hence turbine 6 is the nearest upstream turbine whose d_{norm} is considered when computing turbine $5's$ TI.

For this study, the analysis is focused on mean TI assessment, but Table 3.4 (rounded off to 3 decimal places) is presented as a validation to the Gaussian nature of the 10-min freestream turbulence/standard deviation data utilised in the study. This verifies that the 90th percentile of the 10-min freestream turbulence values (i.e. the representative value), approximately equals the mean value of all the 10-min freestream standard deviation (turbulence) values plus 1.28 multiplied by the standard deviation of all the individual standard deviation (turbulence) values as suggested in [43].

Table 3.4: Wind data validation

bins	Mean $\langle\sigma_\infty\rangle$	STD $stdev(\sigma_\infty)$	90th Percentile $\sigma_{repr,\infty}$	$\langle\sigma_\infty\rangle + 1.28 stdev(\sigma_\infty)$
bin 0	0.554	0.310	0.937	0.951
bin 1	0.654	0.321	1.041	1.064
bin 2	0.706	0.280	1.049	1.065
bin 3	0.613	0.272	0.955	0.961
bin 4	0.584	0.288	0.934	0.952
bin 5	0.659	0.332	1.061	1.085
bin 6	0.728	0.365	1.175	1.195
bin 7	0.703	0.368	1.166	1.174
bin 8	0.697	0.423	1.242	1.221
bin 9	0.813	0.484	1.469	1.433
bin 10	0.830	0.484	1.476	1.450
bin 11	0.602	0.368	1.065	1.073

The wind data utilized in this analysis covers a duration of 10 years, spanning March 2011 - February 2012, October 2012 - December 2014, and January 2016 - May 2022. Access to this data is available through a complimentary registration at the WASA-1 Project. Detailed representations of the wind characteristics are depicted in Figures 3.7 and 3.8, showcasing the wind rose and wind speed distribution, respectively. Butterworth, located in the Eastern Cape province of South Africa, is the focus area for the provided wind data.

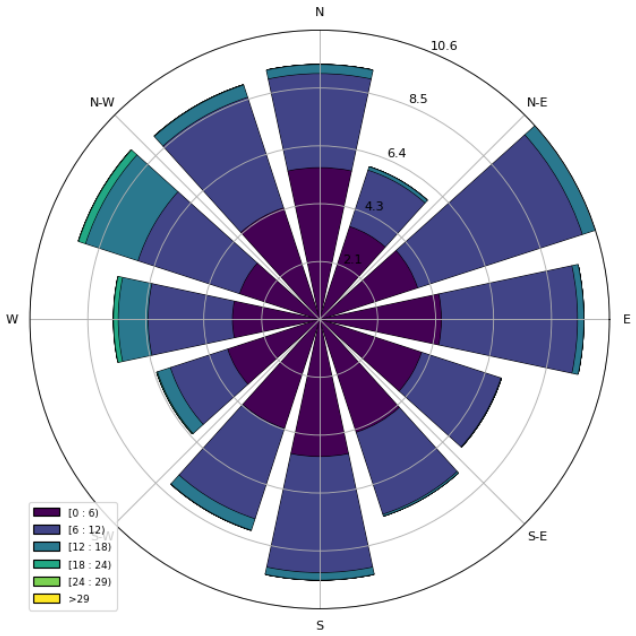

Figure 3.7: Wind rose for studied site (WM10 Butterworth) obtained at 60 m above ground level.

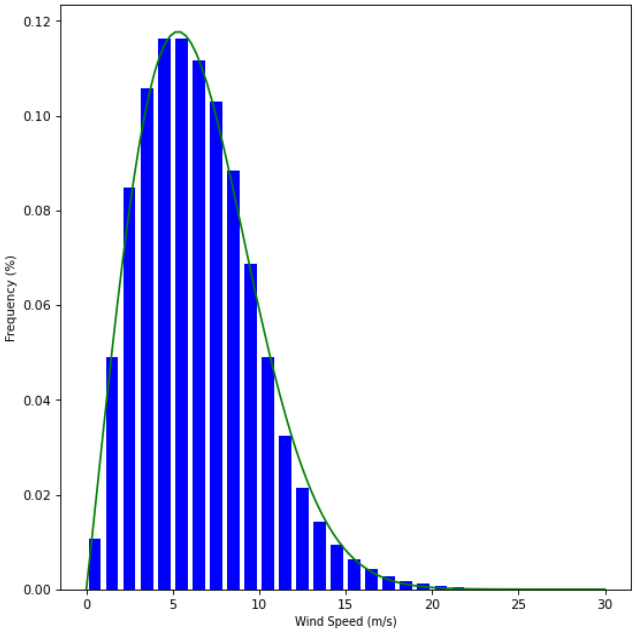

Figure 3.8: Wind speed distribution for studied site (WM10 Butterworth) obtained at 60 m above ground level.

The investigation continues by verifying the proposed enhancements to the equations utilized for calculating the representative and mean values of the distribution, specifically

for border turbines. At different wind speeds and their corresponding thrust coefficients (assuming no optimisation, hence no alterations in α regardless of inflow/freestream wind speed), a plot is given in Figure 3.9 to compare the resultant border turbines TI values obtained from the mean values of the distribution, both for Frandsen's model and the proposed augmented model. That is, comparing Equation (2.49) (which stems from (2.46)) with Equation (3.12) (which stems from (3.11)). A similar plot for the representative values of the distribution is presented in the Appendix C section. The plots demonstrate no visible difference between the TIs due to Frandsen's model and the proposed augmented model.

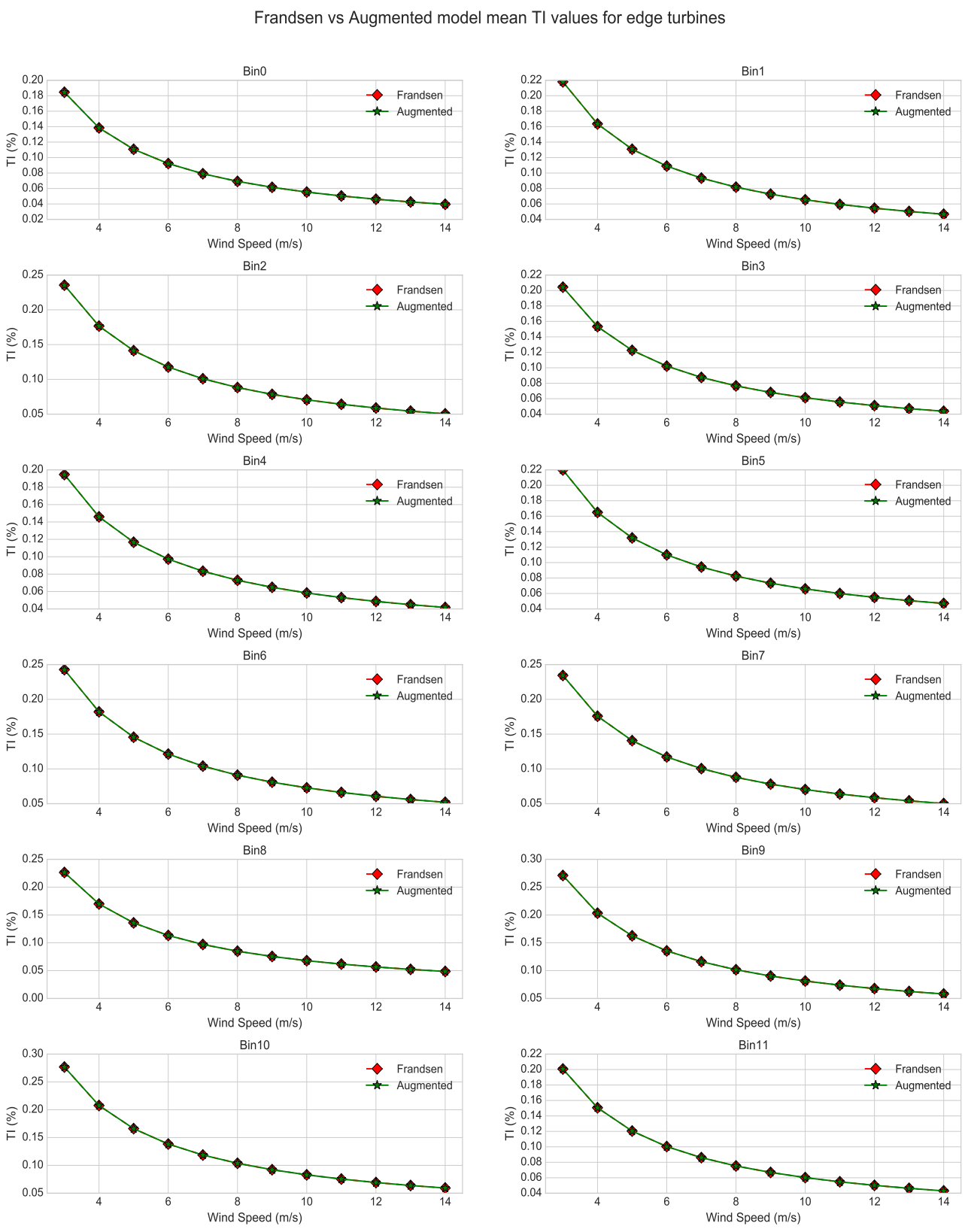

Figure 3.9: Border turbine TI comparison for all wind speeds and bins

3.3.5 Formulation of Optimisation Problem

A coordinated wind plant optimisation for AEP maximisation is presented herein.

Assuming wind flows uniformly into a confined hypothetical WP from one direction at any given time, as depicted in Figure 3.6, with variability in speed as well as direction. Let $\mathcal{N}$ denote the set of all turbines in the wind plant, $\mathcal{B}$ represent all wind directions or bins, $\mathcal{U}$ indicate a set of operating wind speeds ranging from U_{in} to U_r for all turbines (utilizing the same turbine model throughout the WP), and $\mathcal{T}$ be the set of turbines upstream of each turbine, with this set varying based on wind direction. Adjusting the α value of any turbine $i \in \mathcal{T}$ impacts the power production and turbulence intensity at downstream turbine j, and other turbines in its downstream, for all wind speeds $u \in \mathcal{U}$ and wind directions $b \in \mathcal{B}$. Consequently, optimizing α for all turbines $j \in \mathcal{N}$, over all wind speeds $U \in \mathcal{U}$, and through all wind direction bins $b \in \mathcal{B}$, aims to maximize WP power output per time instance and thus the AEP.

To obtain the AEP, the sum of all $P_{b,u,j}$ from all the turbines, $\mathcal{N}$, across the operating wind speed range, $\mathcal{U}$, is evaluated for each wind bin to obtain the *bin power*. This *bin power* value by each wind bin is then weighted by each bin's frequency of occurrence, f_b, summed for all bins, $\mathcal{B}$, and multiplied by the number of hours in a year, N_h (8760).

$$AEP = N_h \sum_{b=1}^{\mathcal{B}} \sum_{u=1}^{\mathcal{U}} \sum_{j=1}^{\mathcal{N}} P_{b,u,j} * f_b \tag{3.16}$$

Consequently, the optimisation problem is formulated as thus:

$$\max_{(U_{b,u,j}, P_{b,u,j})} \quad AEP \tag{3.17}$$

Considering that the ϕ of all turbines i in $\mathcal{N}$ is preallocated a 0° value, the expression for $P_{b,u,j}$ can be written in closed form as:

$$P_{b,u,j}(\boldsymbol{\alpha}; U_\infty) = \frac{1}{2}\rho A \bar{U}^3_{b,u,j}(\boldsymbol{\alpha_{b,u,-j}}; U_\infty) C_p(\alpha_{b,u,j}) \quad . \tag{3.18}$$

No constraints are applied in Equation (3.17) to the TI and thrust values at turbines because the objective is to determine the behaviour of these parameters.

Equation (3.16) reflects the standard and widely accepted method for calculating AEP, as supported by literature [51, 105]. While this approach is robust, it can be extended to include the frequency of occurrence of specific wind speeds—or center wind speeds—within the turbine's operating range. However, considering the formula, it can be noted that f_b is a constant value for each wind bin/direction, so too is the frequency of occurrence of each centre wind speed, f_u. These f_u values can be estimated for each centre wind speed using Figure 3.8 or derived directly from the underlying data. By definition, f_u should be placed within the second summation ($\sum_{u=1}^{\mathcal{U}}$), as it serves to weight the contribution of each center wind speed. Alternatively—and more commonly—it can be placed after the innermost summation ($\sum_{j=1}^{\mathcal{N}}$) as a multiplier to f_b. Mathematically, both placements yield the same effect on the calculated AEP that accounts for f_u. To compute this f_u-adjusted AEP, the power output $P_{b,u,j}$ from all turbines $\mathcal{N}$ is first evaluated for each center wind speed u, weighted by its frequency f_u, and summed over the wind speed range $\mathcal{U}$. This result is then evaluated for each wind direction bin b, weighted by f_b, summed over all bins $\mathcal{B}$, and finally multiplied by the total number of hours in a year, $N_h = 8760$ as given;

$$AEP = N_h \sum_{b=1}^{\mathcal{B}} \sum_{u=1}^{\mathcal{U}} \sum_{j=1}^{\mathcal{N}} P_{b,u,j} * f_u * f_b \tag{3.19}$$

While incorporating f_u into AEP computation provides a more thorough evaluation in a single scenario, it becomes computationally expensive and redundant when comparing multiple scenarios, case studies, or optimizers. This is because f_u, like f_b, acts as a constant weighting factor applied after the summation of the *total WP power* obtained through optimisation. Each scenario already yields a *total WP power*, which is then uniformly scaled by f_u, f_b, and the annual hours N_h (8760) to compute the total AEP. Since f_u affects all scenarios equally, its inclusion does not influence the relative comparison between them. Since f_u is constant across all scenarios, it introduces an equal degree of change (increase or decrease) in the *total actual WP power* and AEP values, without altering the underlying *total WP power*. Consequently, f_u inclusion has no effect on the relative comparison between scenarios. Therefore, this study adopts the AEP formulation used in [51, 105], where only f_b is considered as a directional weighting factor.

In open terrain, wind measurements conducted by [123] aligns with the logarithmic fit up to about 100 meters above the earth's surface, which corresponds to the surface layer of the atmospheric boundary layer. However, beyond this height, the average wind speed remained nearly constant up to 1000 meters. Based on this, the study ignores terrain effects on wind speed considering the employed turbine hub height of 140 m. Furthermore, it is assumed in the literature that an infinite turbine array effectively increases the surface roughness of the earth surface, hence, having an effect on the velocity profile deep within the farm. This modified roughness regime requires that the turbines are within the atmospheric boundary layer - which as demonstrated, these turbines might not be, especially if atmospheric conditions are stable. Moreso, this modified roughness phenomenon is only truly valid above the top of the rotor tips rather than at hub height [42]. So given the hub height, z_0, of the employed turbine, the top of the rotor tip which will be at approximately $((D/2)+z_0)$ meters (i.e 204 meters) will be far above the region of the atmospheric boundary layer known to align with the logarithmic fit (for open terrain). Hence, the effect of an infinite turbine array on the velocity profile is also ignored in this study.

3.4 Modelling and Simulation Environment

The optimisation model presented therein is static, using the C_T curve of the employed turbine which ia available at en.wind-turbine-models.com[122] and shown in Figure 1 in the Appendix A section. All simulations are carried out considering the repeatability feature of the Monte-Carlo simulation technique. The Monte-Carlo simulation relies on the laws of large numbers for accuracy, and this has been taken into consideration in this study. By repeating each simulated case several times and investigating the results, the simulations can be assumed to have converged to the true expected global optimum value of the simulated case, hence, greater confidence can be given to the simulated results.

For each bin/wind direction, each centre wind speed between U_{in} and U_r (i.e 3, 4, ..., 14 m/s) is optimised for maximum WP power, and then all the WP power from all bins are summed up to obtain the total WP power, from where the AEP is computed. Above the rated capacity, modern wind turbines employ blade pitching to reduce the aerodynamic

impact of high wind speeds and maintain a constant rated number of rotations per minute (rpm), thereby protecting the turbine generator from mechanical damage. Since this study does not delve into turbine dynamics, it assumes that pitching control operates efficiently, ensuring that the rpm remains constant for wind speeds exceeding the rated threshold of 14 m/s. As discussed in subsubsection 2.1.2, this pitching mechanism effectively reduces the aerodynamic influence of wind speeds above the rated level to that experienced at rated conditions, thereby maintaining the turbine's maximum rpm.

As a result, key operational parameters such as turbine thrust and thrust coefficient remain consistent with those at the rated wind speed, leading to constant power output. This behavior is evident in the turbine's power curve (Figure 2.2) and is mathematically represented in Equation (3.5). Accordingly, the same control parameters and resulting outputs apply to all wind speeds beyond 14 m/s. To avoid unnecessary computational effort and redundancy, wind speeds above the rated value were excluded from simulation in this study, as their outcomes would merely replicate those observed at 14 m/s.

The system model is also discrete given the application of only the centre wind speeds, and bins for the simulation. Finally, the application of optimisation algorithms *GA* and *PSO* designed to inherently generate randomly distributed random variables, make the optimisation stochastic in nature. The entire system modelling is built on the Python 3.9 programming software and all plots are generated using the same software. Key python libraries utilised include *numpy*, *scipy*, *glob*, *pandas*, *operator*, *windrose*, *matplotlib*.

The coupling of the wake, TI and optimisation algorithms models, and the inter-flow between all necessary equations in these models is captured in Algorithm 1 that follows. This algorithm is executed statically to obtain the numerical results presented. In addition to the algorithms provided in subsequent chapters, this algorithm shows how the optimisation algorithm(s) is/are applied to the system model for AEP maximization. An explanation on the operations of both optimisation algorithms (GA and PSO) have been incorporated in the Appendix E section since these conventional metaheuristics are regarded as general knowledge algorithms.

Algorithm 1: Axial optimisation algorithm for AEP maximisation.

Input: scalar $fixed\_area$, D, ρ, κ, γ, ψ, τ, β, TI_{max}, N_h, pop_size, max_it
vector $\vec{\mathcal{U}}$, $\vec{\mathcal{B}}$, $\vec{\mathcal{N}}$, $\vec{f_b}$

Select minimum T-2-T separation distance
From origin (0,0), evaluate turbine locations $l_i(x_i, y_i)$ based on D, store in $\vec{i_{pos}}$ and deploy over $fixed\_area$
Compute A using D
$\theta^W \leftarrow 0^\circ$ considering Figure 3.6, $BIN_P \leftarrow 0$;
for $b \in \mathcal{B}$ **do**
  Apply coordinate axes rotation by θ^W
  $sorted \leftarrow$ Sort $\vec{i_{pos}}$ in descending order based on y-coordinate value and then x-coordinate value, considering bin direction b
  $first\_turbs \leftarrow$ a set containing the topmost turbines in each column, considering the bin direction b
  Compute σ_{mean} for b
  $\phi \leftarrow 0^\circ$;
  $P_b \leftarrow 0$;
  for $u \in \mathcal{U}$ **do**
    $P_u \leftarrow 0$;
    for $it \leftarrow 1$ **to** max_it **do**
      Randomly initialize a population of pop_size particles each with position vectors (α) of length $\mathcal{N}$ using PSO/GA
      Set constants c1 = 1.8, c2 = 1.5, wMax = 0.9, wMin = 0.2 to allow continually decreasing particle velocity as swarm tends towards local/global maximum
      $P_{it} \leftarrow 0$;
      for $particle \in pop\_size$ **do**
        $\mathcal{T} \leftarrow [\,]$
        for $i \in sorted$ **do**
          if $i = sorted[0] \quad \vee \quad i \in first\_turbs$ **then**
            Compute $\sigma_{j,wake}$ from Equation (3.11) and TI_i from Equation (3.12)
            Compute P_i from Equations (3.8) with $\bar{U}_j = U_\infty$
            $P_{it} \leftarrow P_{it} + P_i$;
            Add i to $\mathcal{T}$
            else
              $sum\_sqr\_def \leftarrow 0$
              for $i \in \mathcal{T}$ **do**
                Compute $d_{j,i}$ and $r_{j,i}$ from Equations (2.18) and (3.2), respectively
                Compute $\bar{U}_{def_j}$ from Equation (3.6)
                $sum\_sqr\_def \leftarrow sum\_sqr\_def + \bar{U}^2_{def_j}$
              end
              Compute $\bar{U}_j$ from Equation (3.7)
              Compute $\sigma_{j,wake}$ from Equation (3.14) and TI_j from Equation (3.15)
              Estimate P_j from Equations (3.8)
              $P_{it} \leftarrow P_{it} + P_j$;
            end
          end
        end
        Compute fitness function values for population of particles/genes
        Update personal bests for each particle/gene in population
        Update local/global best for entire population of particles/genes
        Update P_{it}
      end
      $P_u \leftarrow P_{it}$;
    end
    $P_b \leftarrow P_b + P_u$;
  end
  $P_b \leftarrow P_b * f_b$;
  $BIN_P \leftarrow BIN_P + P_b$;
end
$AEP = BIN_P * N_h$
Output: AEP

3.5 Numerical Simulation Results with Classical Examples for Demonstration

In this section, results from simulation of different scenarios are presented. The wake (Equation (3.8)) and TI (Equations (3.12) and (3.15)) models are utilised to estimate turbine TI and power for the non-optimised (*Base* case) and the optimised cases. For the non-optimised case, each turbine is allowed to greedily extract power based on the mean wind speed, $\bar{U}_j$, at its rotor position, without consideration of turbines in its downstream. In contrast, downstream turbines are taken into account for the optimised case, enabling the adjustment of turbines' α values, thereby enhancing an improved wind plant power.

Given that time is required for the duo (U_∞, θ^W) to be measured by border control turbines, communicated to control station and optimal control parameters computed and communicated back to turbines, the study makes a final assumption that -

Assumption 3.3. *The border control turbines as apportioned in Table 3.1 for each bin, can accurately estimate inflow wind speeds from a distance using feedforwarded LIDAR techniques, send this estimation to a local control station which can then compute and optimise the control variable (α) for each turbine based on their relative positions, then distribute these optimised α values to the respective turbines before the wind reaches the control turbine(s).*

Given a SCADA system's ability to remotely and centrally control the WP, the algorithm that a controller domiciled in a local SCADA station has to perform to continually maximise the bin power for each mean inflow wind speed per instance of time, to maximise the AEP of the WP, is presented in Algorithm 1 in the Appendix E section. With the hexagonal deployment of turbines as shown in Figure 3.6, turbines 11, 8, 9, 13, 16, 15, and 12 constitute the vertices and centre of a typical hexagon. Let distances in rotor diameter, D, from turbine 11 to 12, 18 to 21, and 0 to 4, be denoted by the letters E, F, and G, respectively. Also, let distances from turbine 12 to 19, 12 to 14, and 12 to 7 be denoted by H, K, and L respectively. Based on these considerations, Table 3.5 outlines the examined scenarios, each

representing the shortest possible T-2-T distances of separation, which are equivalent to the lengths of the hexagonal sides.

Table 3.5: Scenarios under analyses .

Scenario	$\boldsymbol{E = F = G}$	$\boldsymbol{H = K = L}$
$5D$	$5D$	$\approx 8.66D$
$6D$	$6D$	$\approx 10.4D$
$7D$	$7D$	$\approx 12.12D$

Based on Table 3.5 and Figure 3.6, two main separation distances can be deduced for each scenario. For $5D$ scenario, bins 0, 2, 4, 6, 8, and 10 (even-numbered bins) have a $5D$ separation distance between turbines while 1, 3, 5, 7, 9, 11 have an $8.66D$ separation distance. For $6D$, the even-numbered bins have a $6D$ separation whereas the odd-numbered bins have a $10.4D$ separation. $7D$ has a $7D$ separation for all even-numbered bins but a $12.12D$ separation for the odd-numbered bins. For each scenario, and for all U_∞ values between U_{in} and U_r, a comparison is made between the $Base$/non-optimised case and the optimised cases using two optimisation algorithms; PSO and GA. Each algorithm's ability to maximise power is explored without the application of any constraints to C_T values and TI levels at individual turbines. A summary of operation of the GA and PSO algorithms can be found in the Appendix E section. Table 3.6 presents a summary of all simulation parameters including those that appear in the GA and PSO operation summaries, as well as those in the system model optimisation algorithm (Algorithm 1).

Table 3.6: Parameters for simulation.

Symbol	Meaning	Unit	Value
$fixed\_area$	Fixed wind plant area dimension	m^2	4665 × 2880
$\vec{\mathcal{N}}$	Set containing all turbines in the wind plant	-	variable
$\vec{\mathcal{U}}$	Set containing all studied wind speeds (U_{in} - U_r)	-	3 - 14
$\vec{\mathcal{B}}$	Set containing all wind direction bins	-	0 - 12
$\vec{f_b}$	Set containing the frequencies of occurrence of all bins	-	variable
i	Wind turbine	-	-
α	Axial induction factor of turbine	-	variable
ρ	Air density	kg/m^2	1.2253
κ	wake growth constant	-	0.0313
χ	Slope of naturally skewed wake trajectory	-	0.0211
ϕ	Yaw offset angle	-	0
τ	Controller of wake deflection by Yaw offset angle	-	0.5617
β	Controller of Yaw offset angle sensitivity to fit to turbine model power curve	-	0.7850
γ	Controller of Yaw offset angle sensitivity on deficit factor $\bar{U}_{def_j}$	-	1.5410
D	Turbine rotor diameter	m	128
TI^{max}	Recommended turbulence Intensity	%	20
N_h	Number of hours in a year	-	8760
max_it	Maximum iteration	-	300
pop_size	Population size	-	25
$c1$	Swarm's cognitive coefficient	-	1.8
$c2$	Swarm's social coefficient	-	1.5
W_{max}	Maximum inertial weight	-	0.9
W_{min}	Minimum inertial weight	-	0.2
CR	crossover rate/percentage	-	0.1
pc	Offspring-to-parent population proportion	-	1
μ	Mutation rate/percentage	-	0.01
σ	Mutation step-size	-	0.1

For both optimised cases, 300 iteration runs each are executed and results compared and analysed. Multi-core parallel processing was implemented in Python 3.9 using the *multiprocessing* package to execute 300 runs each for all twelve (12) inflow wind speeds from U_{in} up to U_r (i.e 3 to 14 m/s) in each bin. This cycle is then repeated for the remaining bins, and for all optimisation scenarios considered. Hence a total of 300 * 12 (wind speeds) * 12 (bins) * 2 (optimised cases) = 86,400 total iterations for each scenario. Therefore, a total of 259,200 iteration runs were implemented to cover all three (3) studied scenarios.

3.5.1 Power analysis

This subsection presents in Figures 3.11 to 3.13, the actual WP power profile by bins, and the WP power profile with varying freestream inflow wind speeds (U_∞).

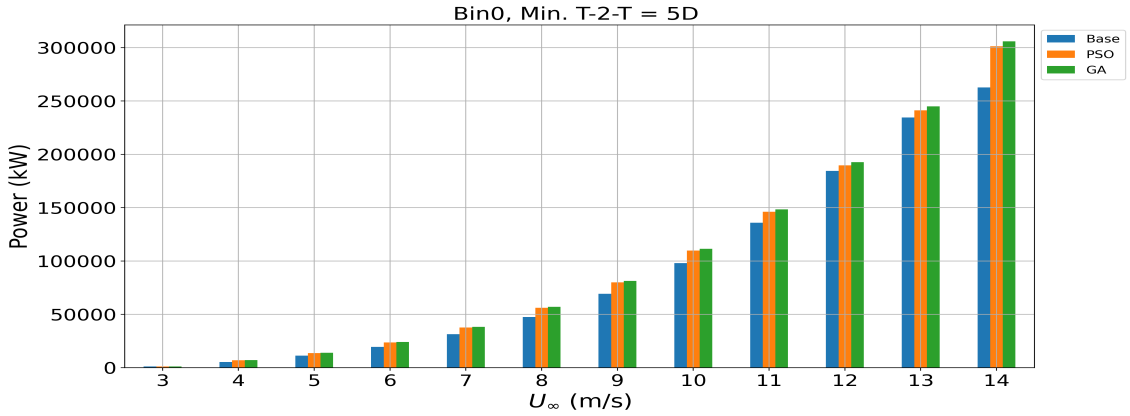

Figure 3.10: Generated power for different wind speeds: Scenario = $5D$.

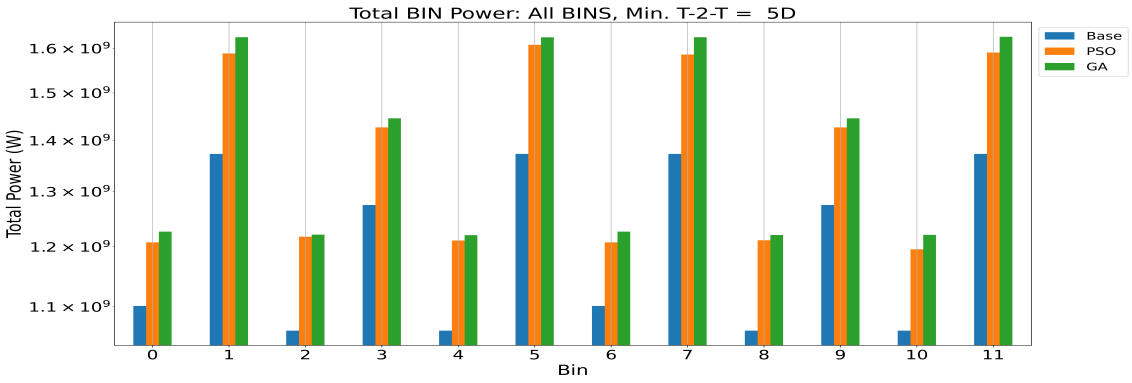

Figure 3.11: Actual WP power per bin: Scenario = $5D$.

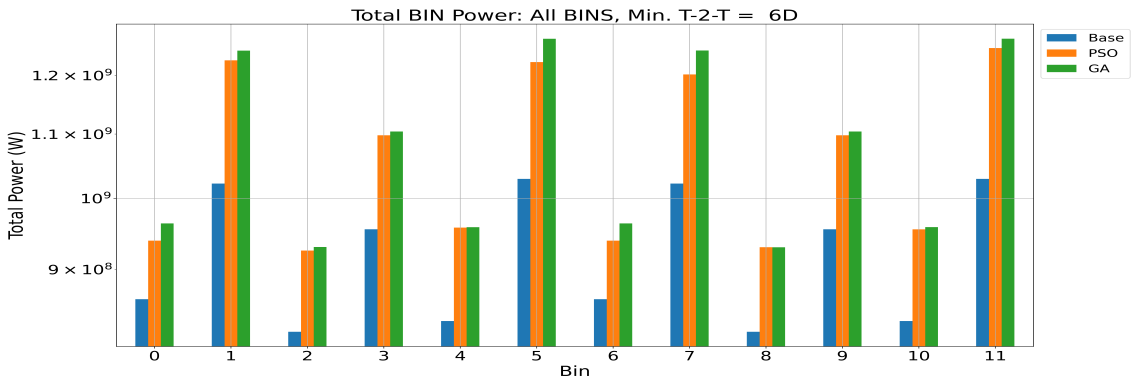

Figure 3.12: Actual WP power per bin: Scenario = $6D$.

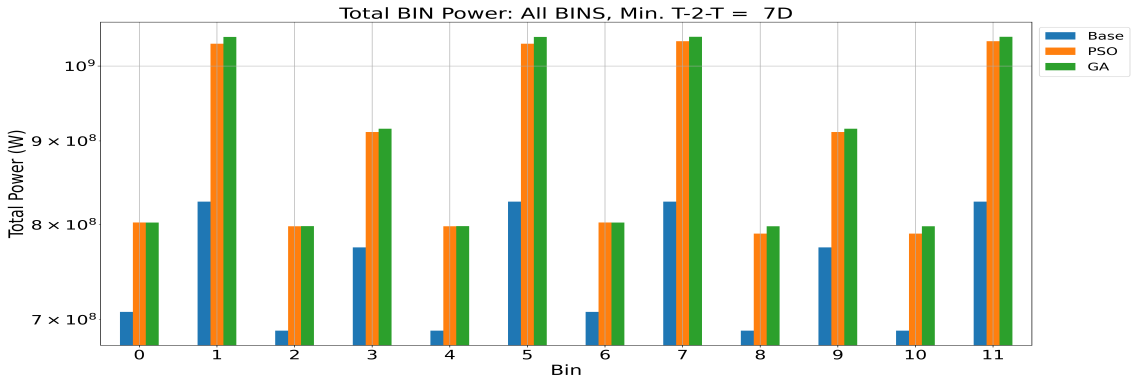

Figure 3.13: Actual WP power per bin: Scenario = $7D$.

There is a general trend of increase in generated power of all studied cases (optimised and non-optimised) as inflow wind speed ,U_∞, increases as shown in Figure 3.10. This is caused by the direct relationship between a wind turbine's generated power and the cube of the inflow wind speed. This trend is consistent for all studied scenarios ($5D$, $6D$, and $7D$) as demonstrated in Figures 17 and 18 in the Appendix D section. It is worth noting that summing the powers from all wind speeds for each studied case on Figure 3.10, yields Bin 0 results on Figure 3.11. Another interesting relationship is observed in Figures 3.11 to 3.13 with respect to bins. It is seen that the odd-numbered bins - which possess large T-2-T distances, yields larger bin powers. This is a straightforward benefit of the chosen turbine deployment, enabling higher turbine density in a restricted space, while also ensuring large T-2-T distances in certain directions. This facilitates better recovery of wind in the wake and therefore a reduction in deficits.

Additionally, a striking disparity is observed among these odd-numbered bins, with bins 3 and 9 exhibiting lower total wind plant power compared to bins 1, 5, 7, and 11. For a clearer understanding, one must refer to Figure 2, and Figures 5 to 15 in the Appendix B section. In comparison with bins 3 and 9 (both comprising a total of nine columns of turbines) with each column comprising five turbines, bins 1, 5, 7, and 11 all comprise 17 columns each, with some columns comprising just a single turbine while some have two and others three, but with a maximum of four turbines in a column. Taking into cognisance that turbines in each column are aligned under the wake axis of one another from the north-most upstream turbine to the south-most, this imposes larger deficits on one another. Hence the more turbines contained in each column, the larger the wind speed deficit and the larger the reduction in turbine generated power, and vice versa. So, although the sparse T-2-T separation distances give all odd-numbered bins an advantage, this "shallow array" effect, caused by a reduced number of turbines in a column, for bins 1, 5, 7, and 11 give them an added advantage in actual WP generated power compared to bins 3 and 9. Another advantage will be that since bins 1, 5, 7, and 11 comprise seventeen (17) columns of turbines, then they by default have 17 border turbines - which are privy to insignificant deficit since they are not positioned in the wake axis of any turbine. Hence, the more turbines that can be positioned away from the wake axis of any upstream turbine, the larger the bin power will be, for any considered bin or θ^W. Note that the caption *bin power* specifies the WP power for that bin, since it sums all the powers from all the turbines in the WP for all operating wind speeds.

3.5.2 AEP numerical results and analysis

The annual energy production based on each studied scenario is presented in Table 3.7 for all cases and analysed. Note that all AEP values for each bin is quoted in gigawatt-hours (GWh). Following the argument presented in subsection 3.3.5 regarding the exclusion of f_u from the AEP calculation, it is importnat to consider the implications of this decision in the context of Table 3.7. Recalling that every value in the table is computed using Equation (3.16) - where each row represents each outermost summation step (i.e. each bin), each value is effectively multiplied by the bin/directional frequency f_b and the net sum of wind speed frequencies f_u. Assuming that the cummulative sum of f_u values for each bin (i.e., each

row) is 0.5, incorporating f_u into the AEP calculation as described in Equation (3.19) would reduce every value in each row by half. Consequently, all entries in the "Total AEP" row would be halved. However, the "Percentage Increase" values, which are relative comparisons between different cases and scenarios, would remain unchanged. This further supports the rational for excluding f_u in comparative AEP analyses, as its inclusion would uniformly scale all values without influencing their relative differences.

Table 3.7: AEP table for all considered scenarios

Bins	**5D**			**6D**			**7D**		
	Base	PSO	GA	Base	PSO	GA	Base	PSO	GA
0	0.903	0.989	1.005	0.706	0.769	0.789	0.579	0.658	0.658
1	0.708	0.819	0.839	0.527	0.633	0.642	0.426	0.532	0.537
2	0.989	1.133	1.137	0.764	0.861	0.866	0.641	0.743	0.743
3	1.081	1.209	1.225	0.809	0.931	0.936	0.657	0.772	0.776
4	0.651	0.742	0.748	0.511	0.586	0.587	0.422	0.489	0.489
5	0.912	1.069	1.080	0.684	0.813	0.842	0.549	0.686	0.692
6	0.923	1.012	1.028	0.722	0.787	0.807	0.593	0.673	0.672
7	0.979	1.130	1.159	0.729	0.857	0.887	0.589	0.738	0.743
8	0.584	0.666	0.671	0.451	0.511	0.511	0.379	0.434	0.439
9	0.844	0.944	0.957	0.632	0.727	0.731	0.513	0.603	0.606
10	0.865	0.974	0.994	0.679	0.778	0.780	0.561	0.643	0.650
11	1.089	1.262	1.291	0.816	0.991	1.005	0.655	0.821	0.826
Total AEP (TWh)	**10.53**	**11.95**	**12.13**	**8.029**	**9.244**	**9.383**	**6.566**	**7.792**	**7.831**
Percentage Increase (%)	0	11.91	13.25	0	13.15	14.44	0	15.74	16.16

It was demonstrated in Figures 3.11 to 3.13 that certain bins show an advantage in terms of actual generated bin power. However, with respect to AEP, this advantage does not seem to be obvious as demonstrated on Table 3.7 for both optimised cases and across all studied scenarios. This is because AEP computations further take into cognisance the frequency/probability of occurrence of winds from each bin/wind direction. It is therefore possible that an odd-numbered bin which demonstrated a larger actual bin power has a low bin probability, hence, negating the gains of sparse T-2-T deployment. Observing the wind rose presented in Figure 3.7 in section 3.3.4, it can be validated that bins 4 and 8 (even-numbered bins) maintain a low AEP, given that they are not only tightly-spaced but have low bin probabilities. Comparing similar cases across all scenarios, the table shows a decrease in actual bin power as T-2-T distance increases, reaffirming the advantage imposed by the increased turbine density on total actual generated WP power and consequently AEP.

3.5.3 Thrust coefficient numerical results and analysis

Given the study's priority of maximising total WP power, the turbine-level thrust coefficient variations based on bins and inflow wind speeds ,U_∞, are presented for the optimised cases (PSO or GA) in Figures 3.14 to 3.21. Although, bins with larger actual bin power do not extend this advantage to the AEP, the study examines them for any correlation between high power generation - synonymous with sparse T-2-T spacings, and high thrust values at individual turbines.

Comparing plots of corresponding bins for the two optimised cases, similarities are noticed with respect to wind speed and position of turbines in the WP. Each subplot comprises two line graphs namely: (1) *Control* - which signifies the thrust coefficient, C_T, synonymous with the mean wind speed, $\bar{U}$, at every turbine under consideration. It relies on the axial induction factor, α, of the specific turbine, as well as all turbines situated upstream. It is estimated from the wake model, and (2) *Optimised* - which is the C_T synonymous with the algorithm-generated α value for the specific turbine. The two graphs are products of algorithm-generated α values. Nevertheless, the *Control* graph relies on all α_i values of turbines upstream of the turbine under consideration, whereas the *Optimised* only takes into account the axial induction of the specific turbine under consideration, denoted as α_j. In this investigation, the theoretical maximum value of α (1/3) which is consistent with the Betz limit ($C_P = 16/27$) is not employed for turbines even when they are greedily extracting power in the *Base* case. Instead, the turbine-specific α values synonymous with the locally estimated $\bar{U}$ values are used for *Base* case analysis. It is important to highlight that this particular α value, which corresponds to the mean wind speed $\bar{U}$ at each turbine, referred to as *Control* for the purposes of this analysis, represents the optimal α value. This optimal α value corresponds to the optimum power coefficient C_P, which, consequently, results in the highest power extraction for that specific wind speed, considering the manufacturer's design specifications. Taking this into account, the optimal scenario would entail ensuring that the α value chosen by the algorithm (*Optimized*) for each turbine does not surpass the α value synonymous with the wind speed at its rotor (*Control*) - this $\bar{U}$ influenced by the *Optimised* values of all turbines upstream of the turbine in question.

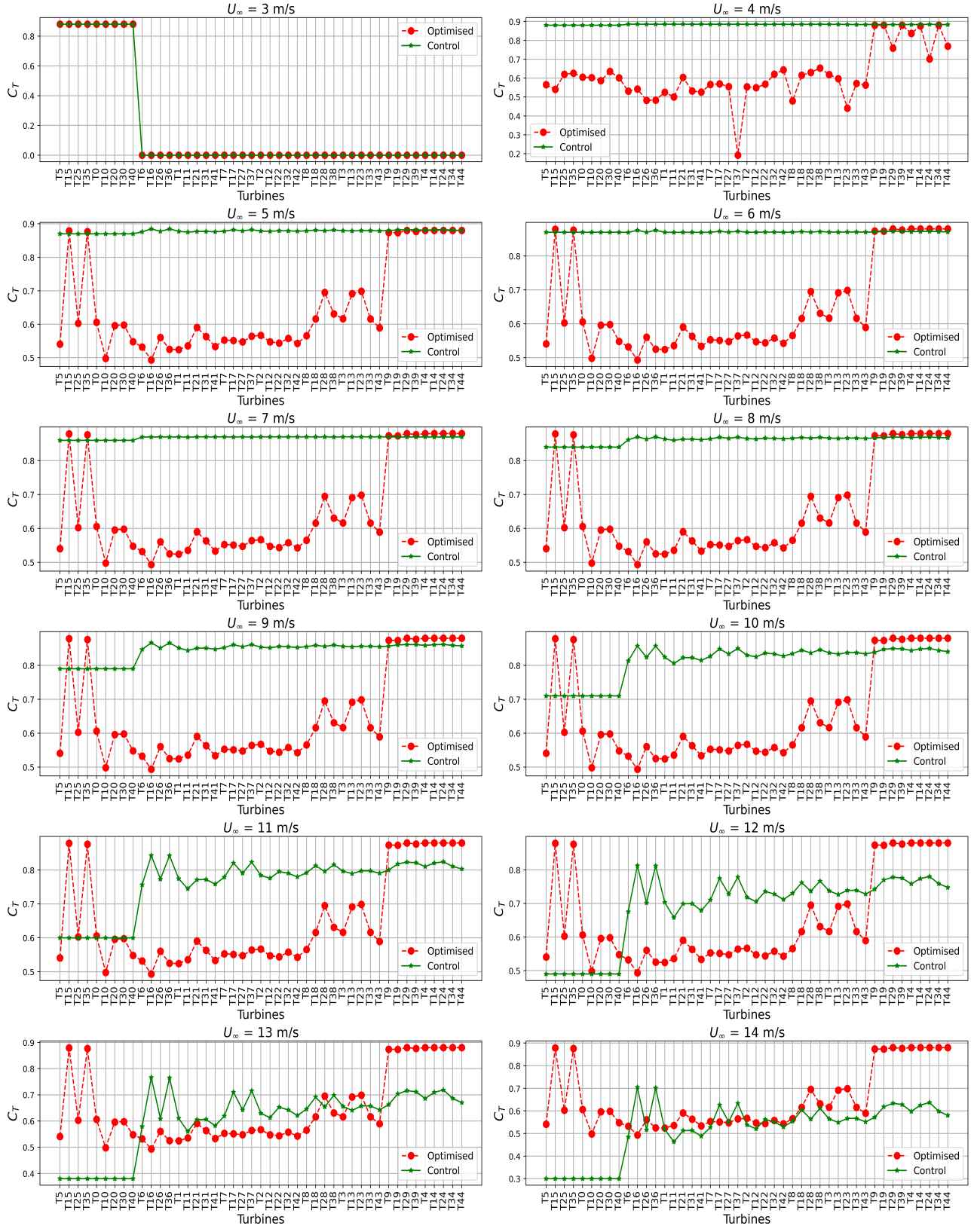

Figure 3.14: Turbines thrust coefficient values with PSO: $5D$, bin0.

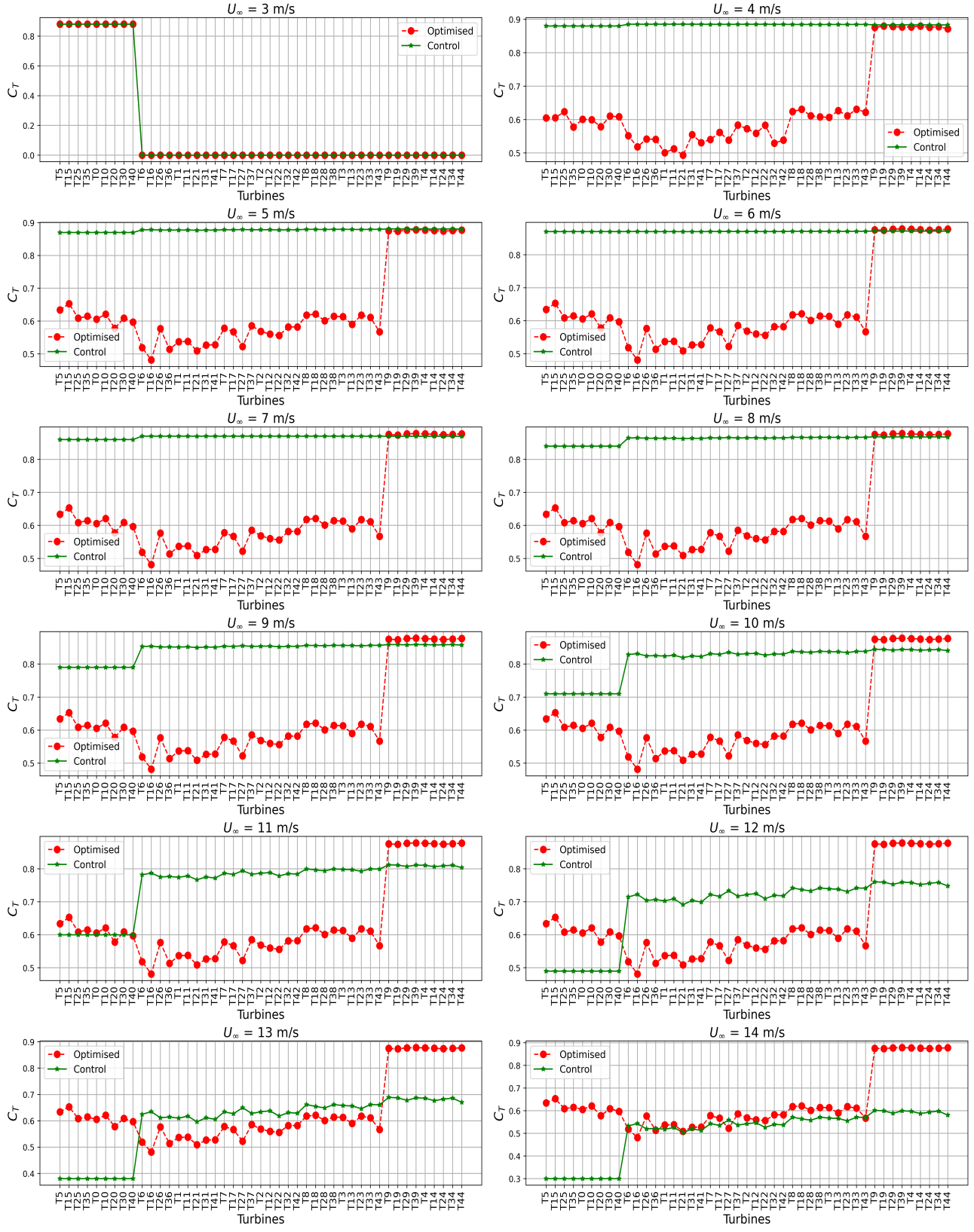

Figure 3.15: Turbines thrust coefficient values with GA: $5D$, bin0.

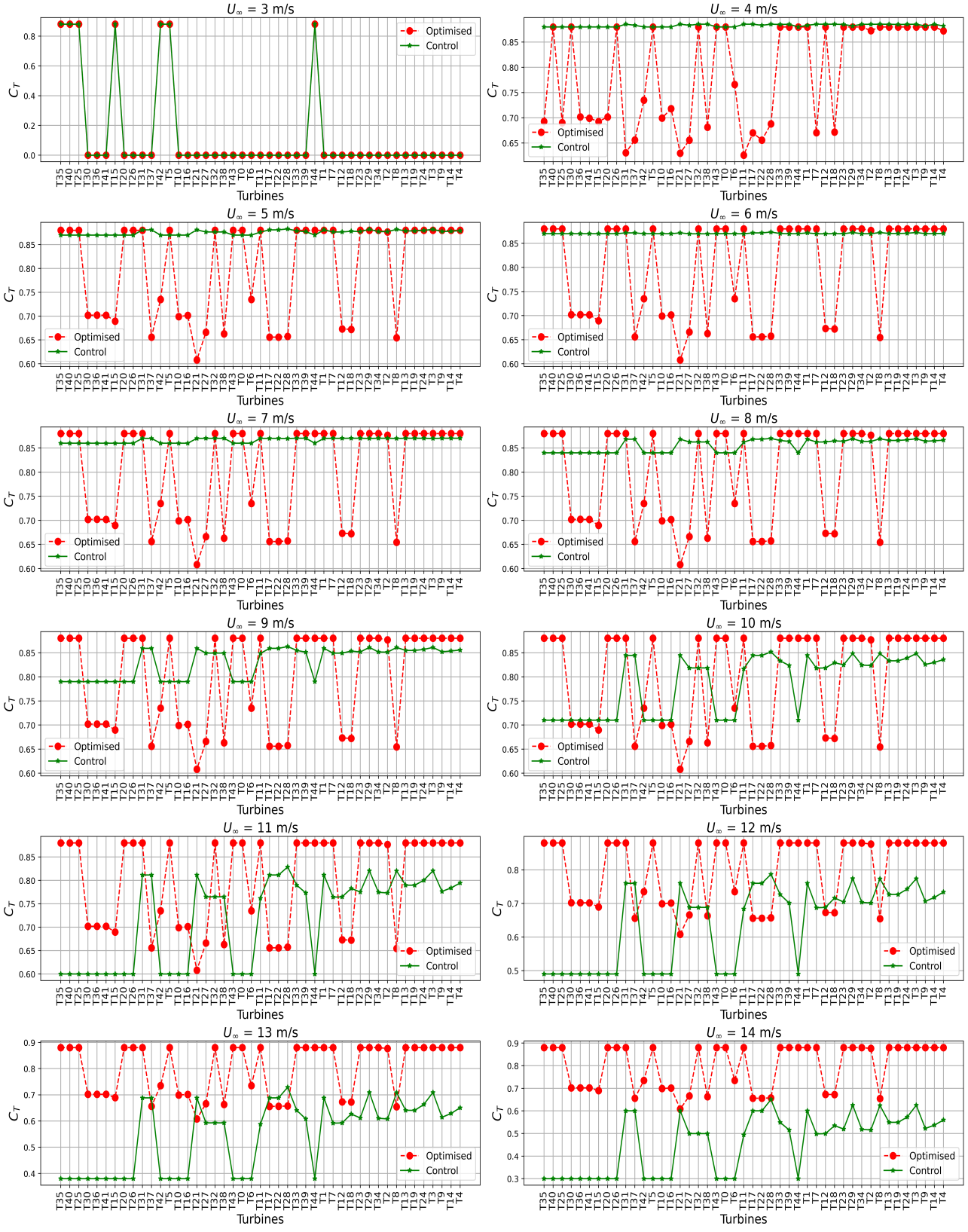

Figure 3.16: Turbines thrust coefficient values with PSO: $5D$, bin1.

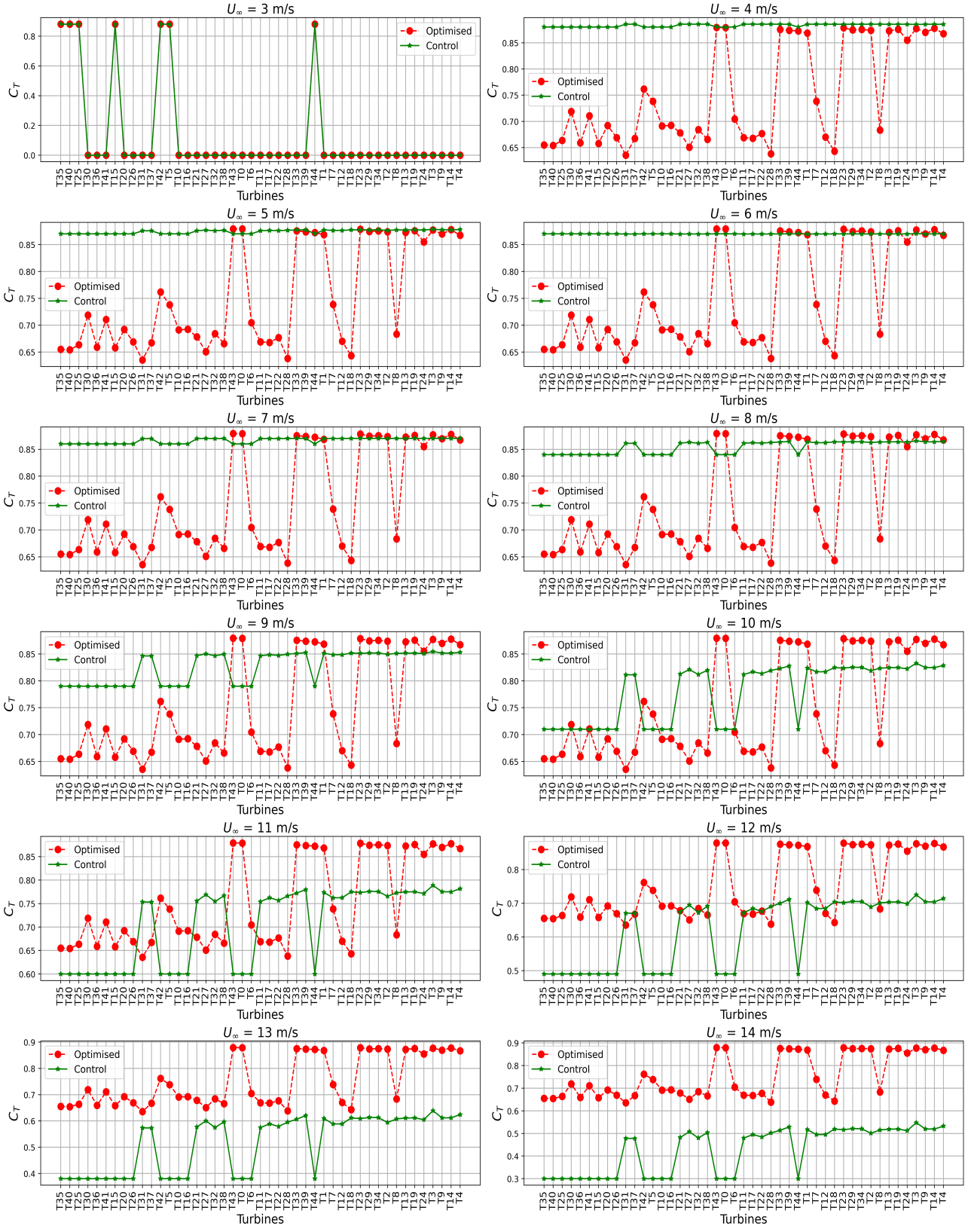

Figure 3.17: Turbines thrust coefficient values with GA: $5D$, bin1.

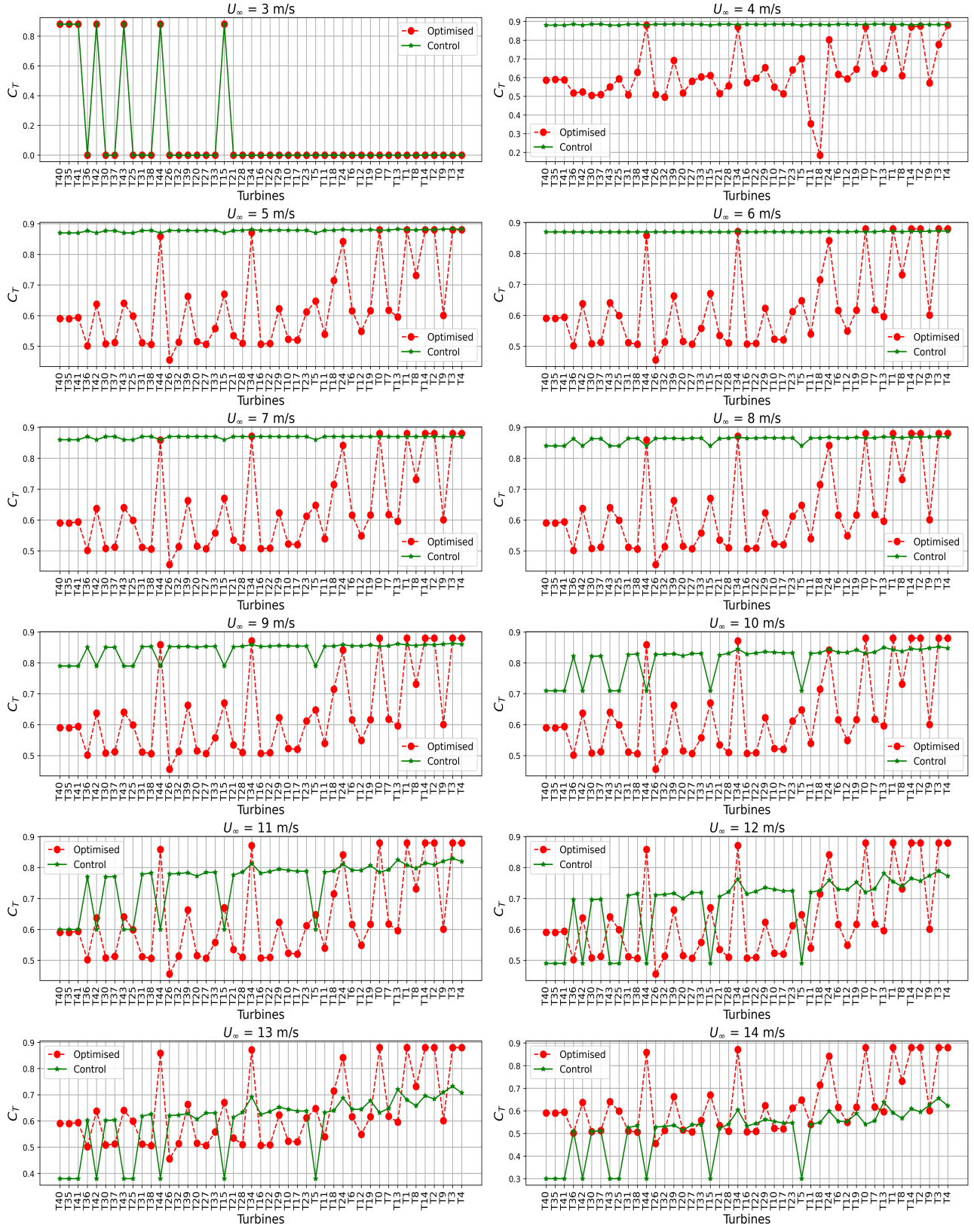

Figure 3.18: Turbines thrust coefficient values with PSO: $5D$, bin2.

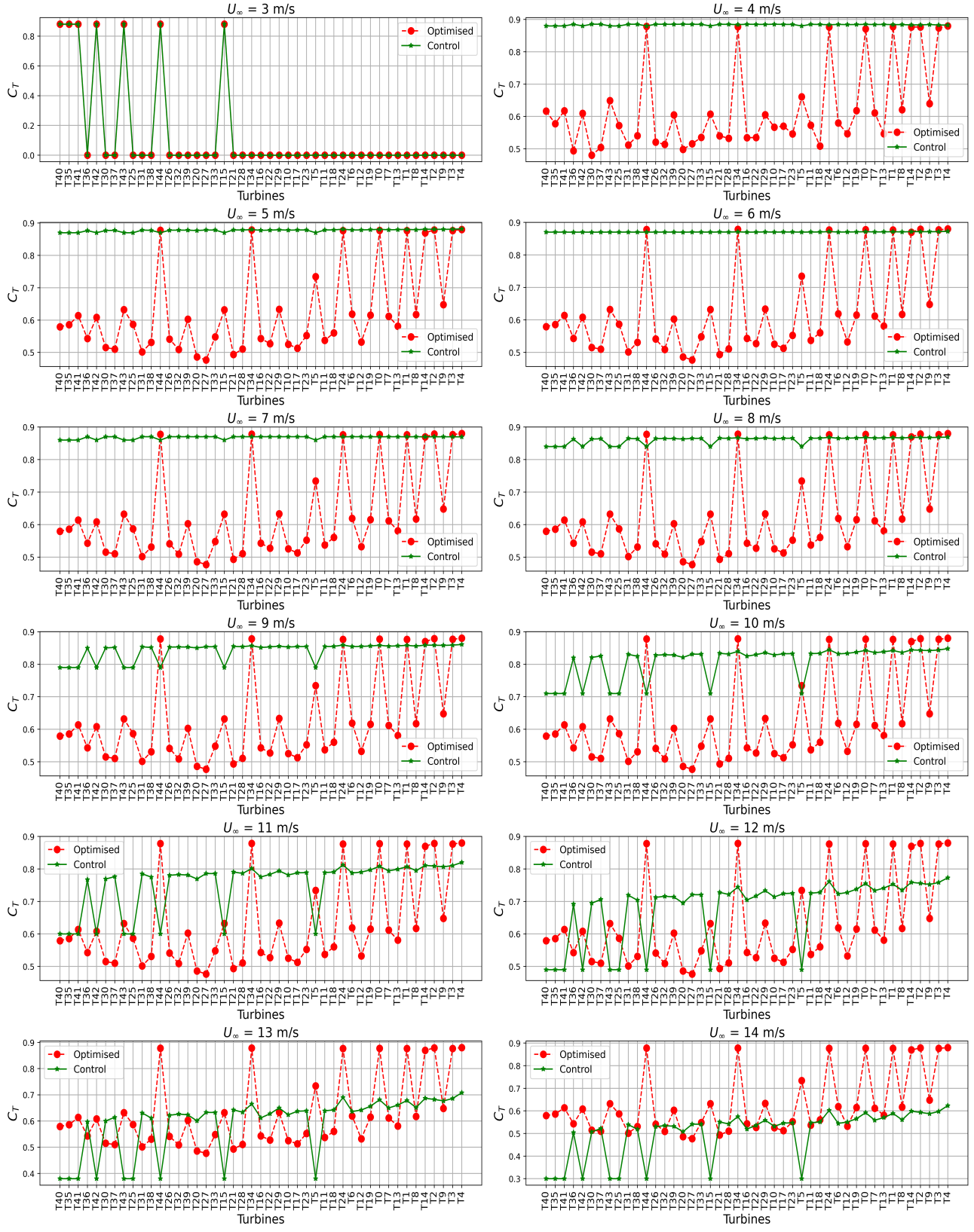

Figure 3.19: Turbines thrust coefficient values with GA: $5D$, bin2.

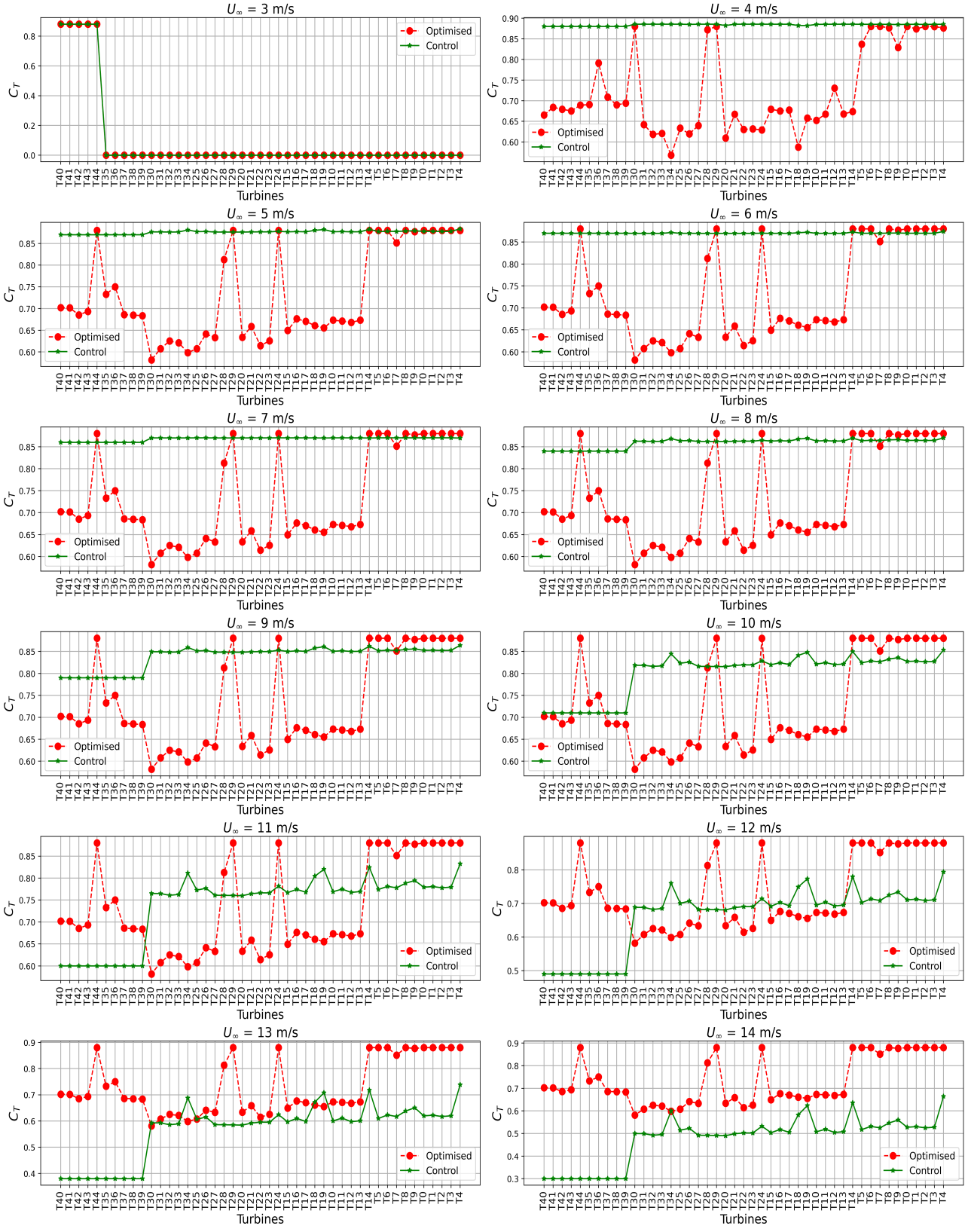

Figure 3.20: Turbines thrust coefficient values with PSO: $5D$, bin3.

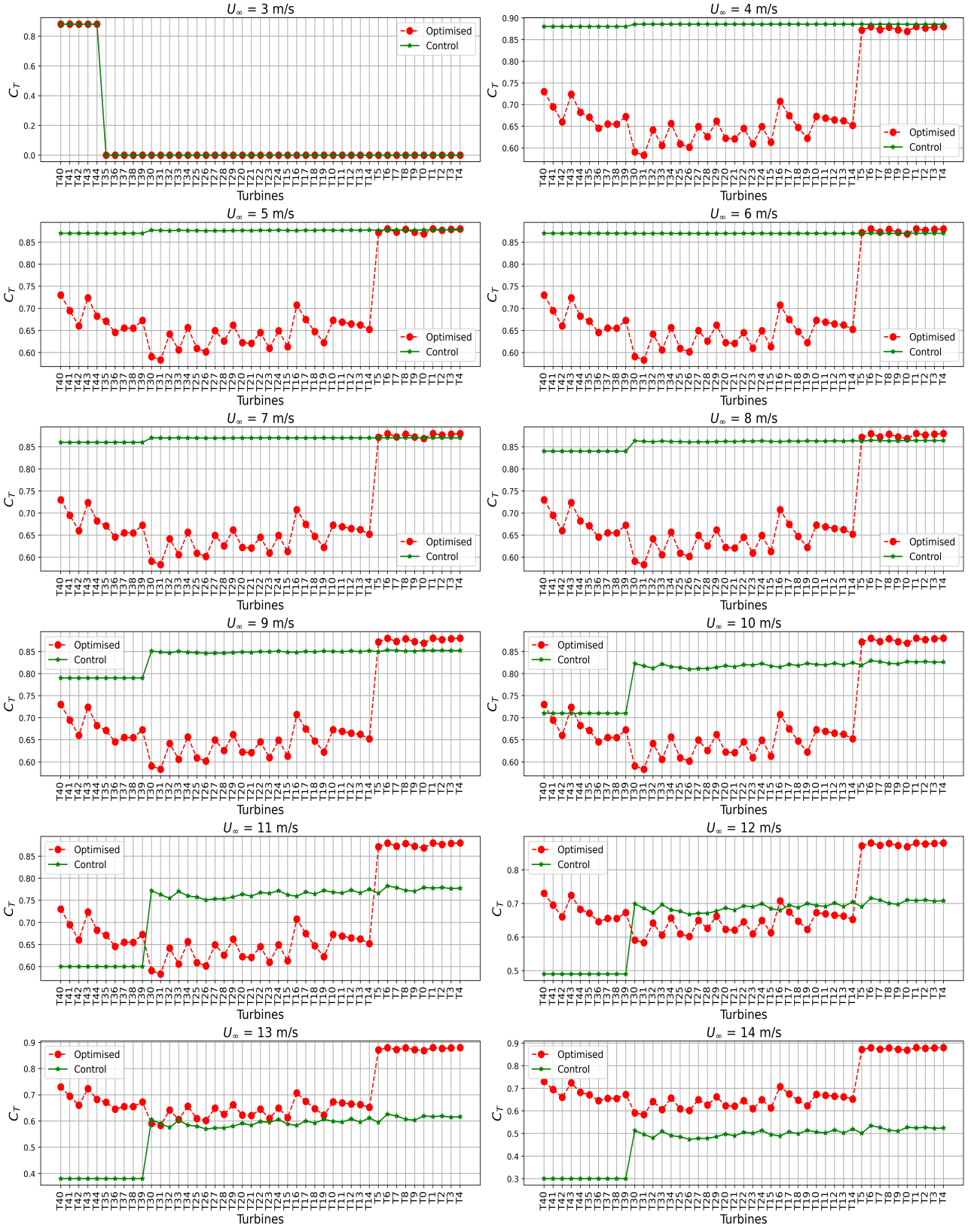

Figure 3.21: Turbines thrust coefficient values with GA: $5D$, bin3.

If this happens, then the turbines will be overexerting itself, given that it would then be exerting a thrust that exceeds that imposed by the wind at its rotor. The thrust generated by a turbine is contingent upon its own α value and those of all turbines located upstream of it, which, in essence, are influenced by the average wind speeds ($\bar{U}$) experienced by these upstream turbines. Furthermore, because the mean of thrust forces over time captures the extreme loads at any considered turbine [16], it's evident that these mean thrust values will be high if the instantaneous thrusts are high, indicating increased loading on these turbines. Figures 3.22 and 3.23 show the thrust force exerted by each turbine (*Optimised*) against that exerted by the $\bar{U}$s at it rotor(*Control*). Using two representative bins (one with sparse minimum T-2-T distances and the other with tight T-2-T distances), the figures confirm the positive relationship between C_T and thrust (T) for all U_∞ values and verifies the excessive thrusting of most turbines due to the unconstrained power maximisation.

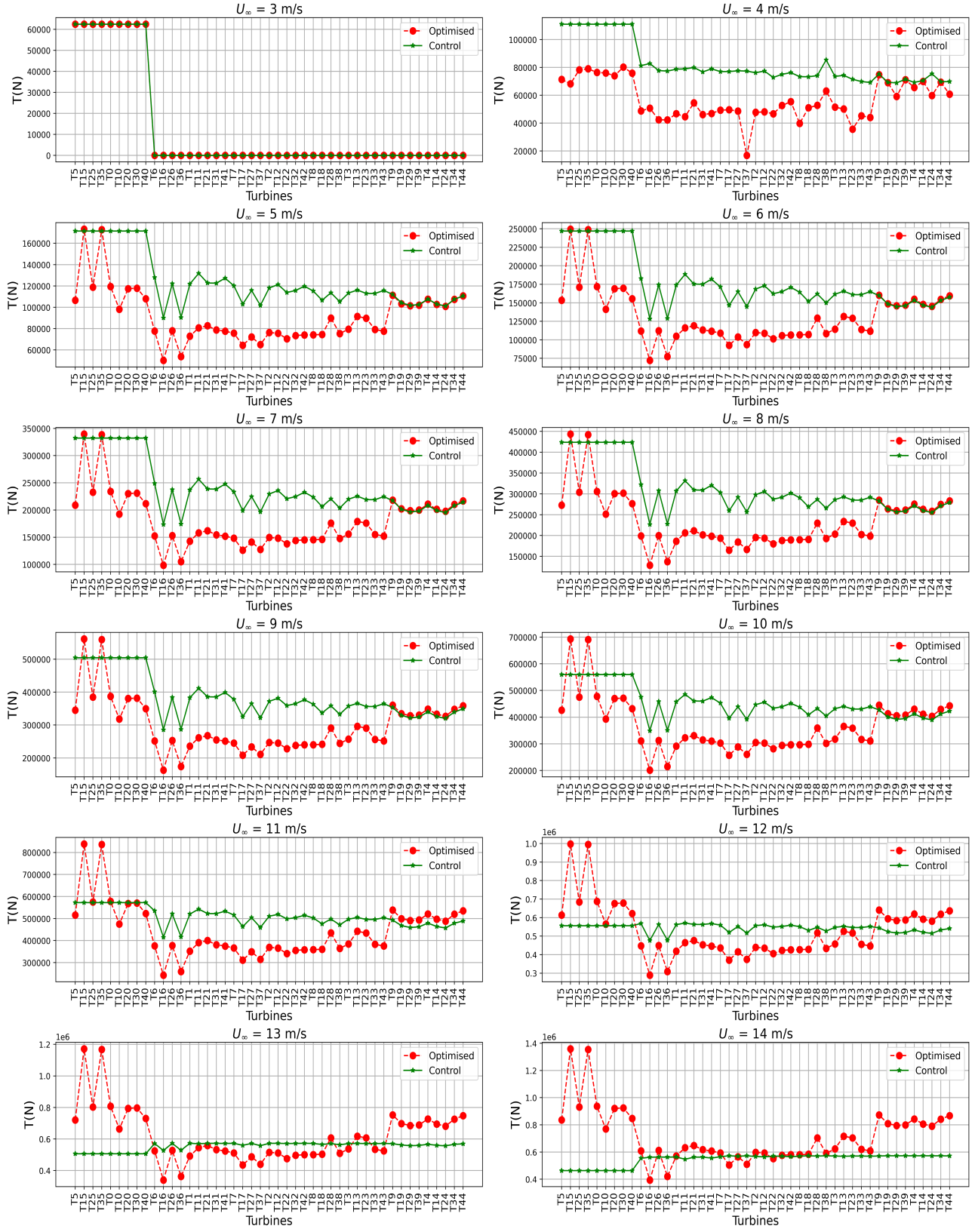

Figure 3.22: Thrust by individual turbines with PSO: $5D$, bin0.

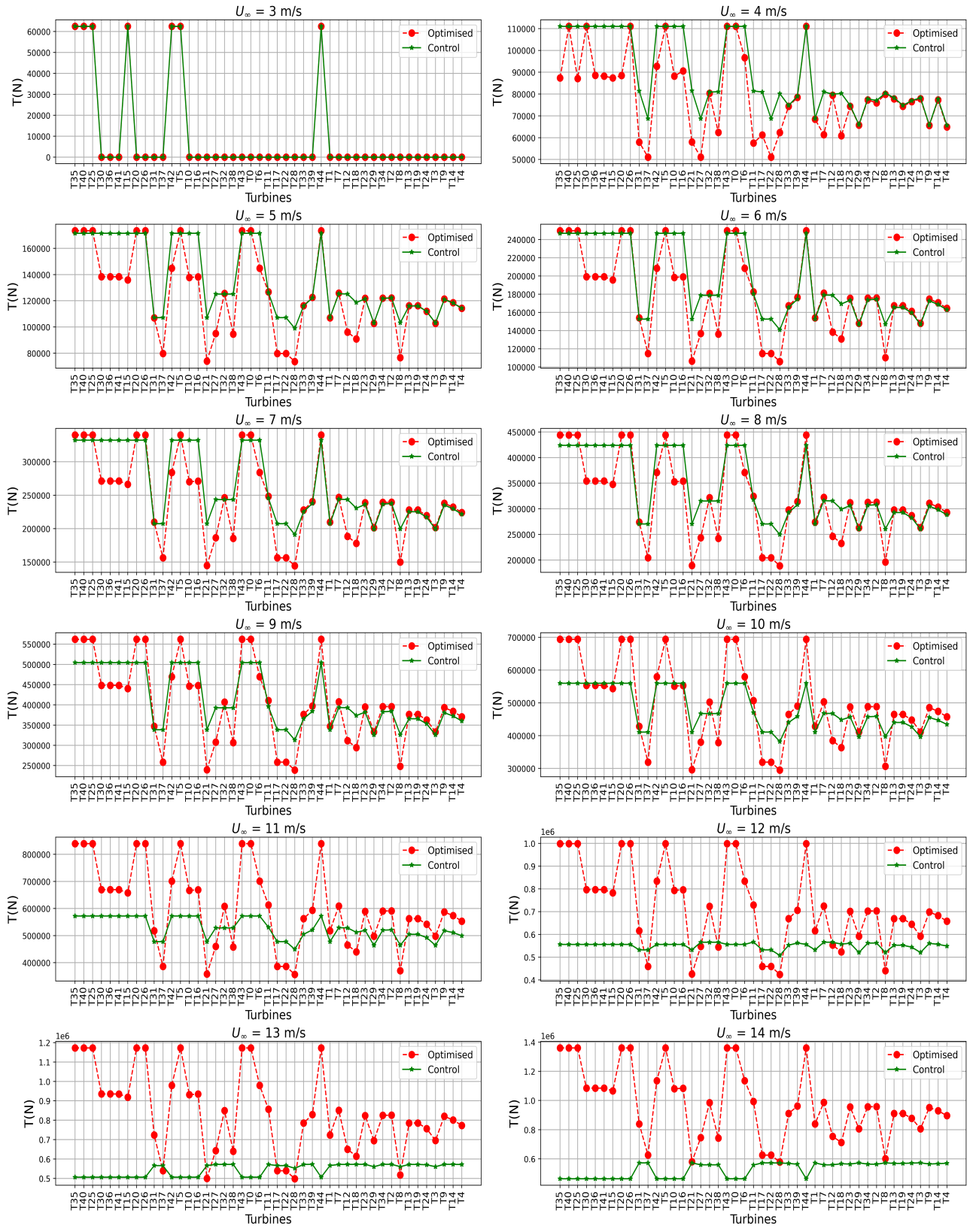

Figure 3.23: Thrust by individual turbines using PSO: $5D$, bin1.

For normal operations, low U values are synonymous with high thrust coefficient, C_T, values and consequently high thrust from the turbine. Because U is low, the turbine rotor speed is naturally capable of intercepting almost the entire inflow without exceeding its rated number of rotations per minute, hence, encountering a large thrust as a result. However, as U increases, it becomes too fast for turbine rotors to efficiently intercept much of it, hence a low thrust force on rotors and a resulting low thrust coefficient values as evident on the *Control* graphs for low wind speeds. This variation can be observed for each inflow wind speed graph by also considering Figures 2, 5, 6, and 7 in the Appendix B section to examine the positions of the turbines from upstream to downstream as they appear in the graphs. It is seen that as one goes further into the WP (considering the wind direction/bin), the wind speeds at turbines continue to decrease due to wake deficits, hence increasing C_T values and thrusts as one travels further into the WP.

For both optimised cases and across all bins, the *Optimised* C_T values of a number turbines surpass their counterpart *Control* values beginning from U_∞ values around 5 m/s. This number of defaulting turbines increases as U_∞ increases. This implies that some turbines could be suffering extreme loads from as low as a 5 m/s inflow due to parameter optimisation.

For each optimised case, a comparison of corresponding wind speeds between odd-numbered and even-numbered bins (for e.g comparing 9 m/s subplot in Figure 3.15 to 9 m/s subplot in Figure 3.17) shows that sparse deployments is positively correlated with high turbine C_T values, as the number of defaulting turbines (turbines whose *Optimised* C_T values surpass their *Control* values) is more significant in sparsely-spaced (odd-numbered) bins in comparison to tightly-spaced even-numbered bins. Recall from the WP power results per bin in Figures 3.11 - 3.13 of subsection 3.5.1, that sparsely-spaced bins yield high WP power. Considering this, a positive correlation can be implied between high power generation and high turbine thrust and thrust coefficient values. This assertion can be further verified by plotting the total defaulting turbines for each U_∞ value, across all bins as given in the Figures 3.24 and 3.25. It is further observed in these figures that among the sparsely-spaced bins, bins 1, 5, 7, and 11 are more susceptible to this high C_T values. This can be attributed to the "shallow effect" explained in section 3.5.1 which cause this set of sparsely-spaced bins to generate more power compared to their counterparts - bins 3 and 9. Hence, the

greater the maximisation-enhanced turbine generated power, the higher the C_T values and thrusts exhibited by these turbines. Furthermore, the fewer the turbines in a column of turbines (a shallow array), the greater the maximisation-enhanced turbine generated power, and consequently the higher the C_T values of turbines in the considered column or WP.

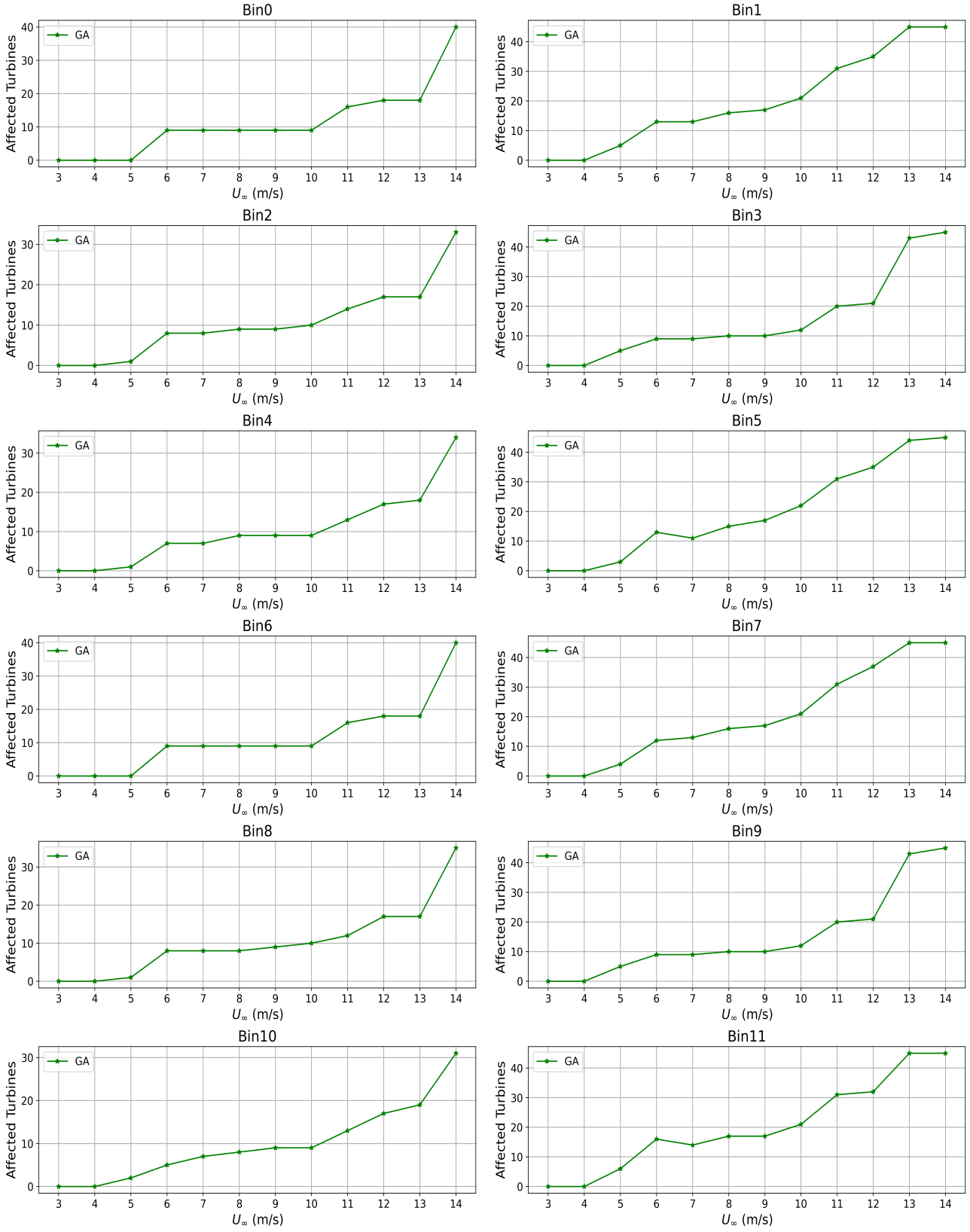

Figure 3.24: Total C_T-defaulting turbines for GA-optimised $5D$ scenario: Unconstrained case, All bins.

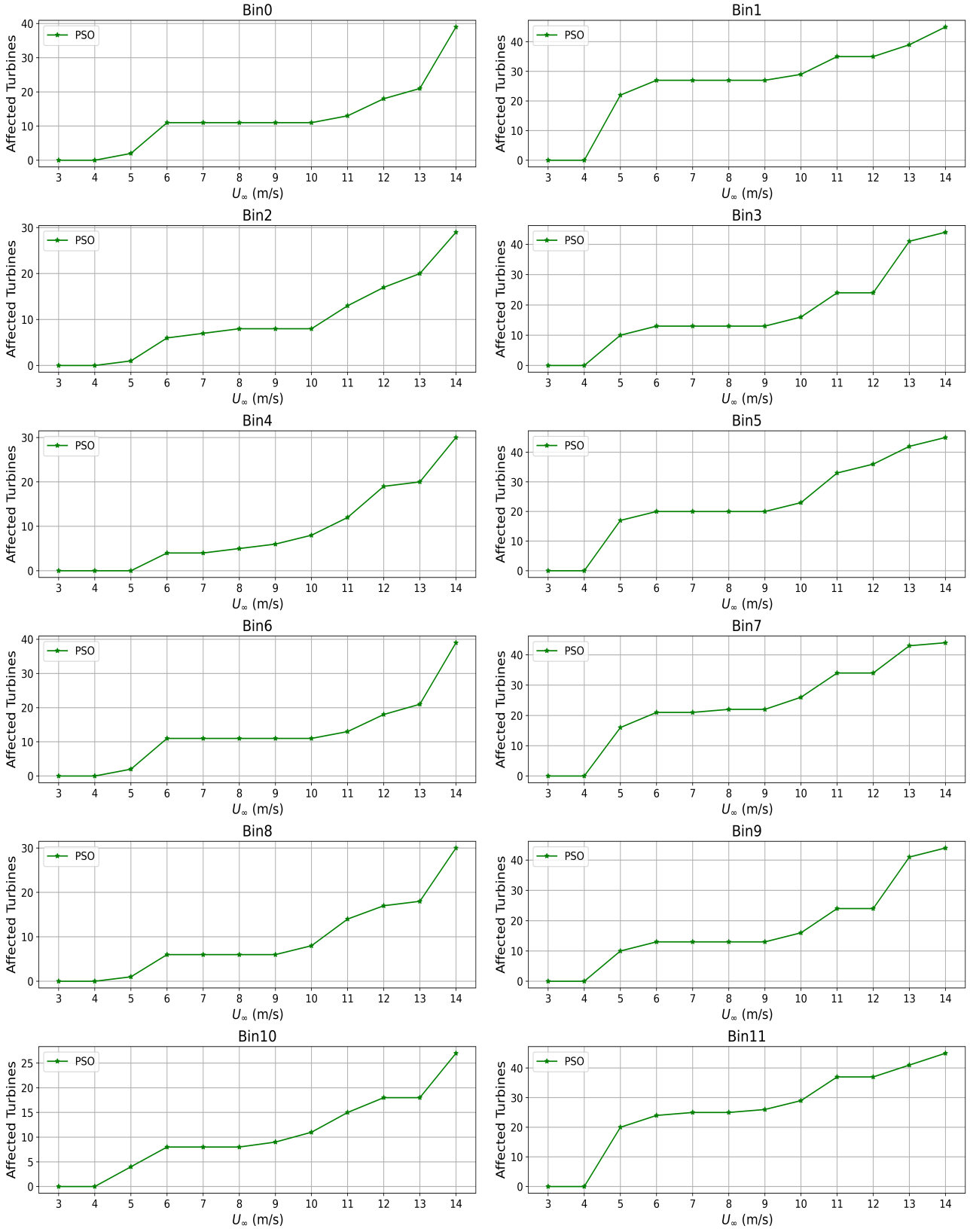

Figure 3.25: Total C_T-defaulting turbines for PSO-optimised $5D$ scenario: Unconstrained case, All bins.

3.5.4 Turbulence intensity numerical results and analysis

The German Institute for Building Techniques (DIBt) suggests that turbines should be designed to last for 20 years, considering an ambient turbulence intensity (TI) of 20 per cent [45]. Given that this research utilises Frandsen's "wake turbulence" (WT) model albeit with slight modifications, and moreover, this model assumes that the wake-generated turbulence encompasses other turbulence sources because of the T-2-T distance consideration for applicability of this model ($< 10D$), this study consequently establishes the maximum permissible TI (*Threshold*) at each turbine as 20 percent.

Figures 3.26 to 3.28 illustrate the TIs at turbines imposed by different freestream wind speeds U_∞ for both non-optimised (*Base*) case and optimised cases, for bin 0, and for all studied scenarios (5, 6, and $7D$). Each box plot represents the TIs at all turbines in the WP, where the upper whisker shows the turbine experiencing the largest TI and vice versa. Indeed, all three plots validate the decrease in TI values with increasing U_∞ values, as observed in previous studies [42]. Notably, the plots demonstrate that this relationship remains consistent regardless of the separation distance between turbines, as represented by the different scenarios $5D$, $6D$, and $7D$ according to column 1 of Table 3.5. The plots also reveal an increase in TI values for both optimised cases - reiterating the negative effect of unconstrained power maximisation as already demonstrated by increased turbine C_T values in section 3.5.3. It is important to note that TI results at $U_\infty = 3$ m/s and at a $5D$ are not visible because at such a low U_∞ value, only the border turbines are exposed to sufficient winds to enable start-up. With all inner turbines seeing insufficient $\bar{U}$ values (hence, zero $\bar{U}$ and C_T assigned), the result are large negative TI values, causing invisible box plots.

Figures 3.29 and 3.30 depicts TIs by bin for $U_\infty = 4$ m/s and 7 m/s, respectively. Bin 0 in Figures 3.29 and 3.30 corresponds to the TI box plots under 4 m/s and 7 m/s in Figure 3.26. These figures highlight that the adverse impacts of power maximization on WP TI are more evident in tightly-spaced (even-numbered) bins. Figure 3.31 summarizes the total number of TI-defaulting turbines by bin, for the studied U_∞ range (U_{in} to U_r).

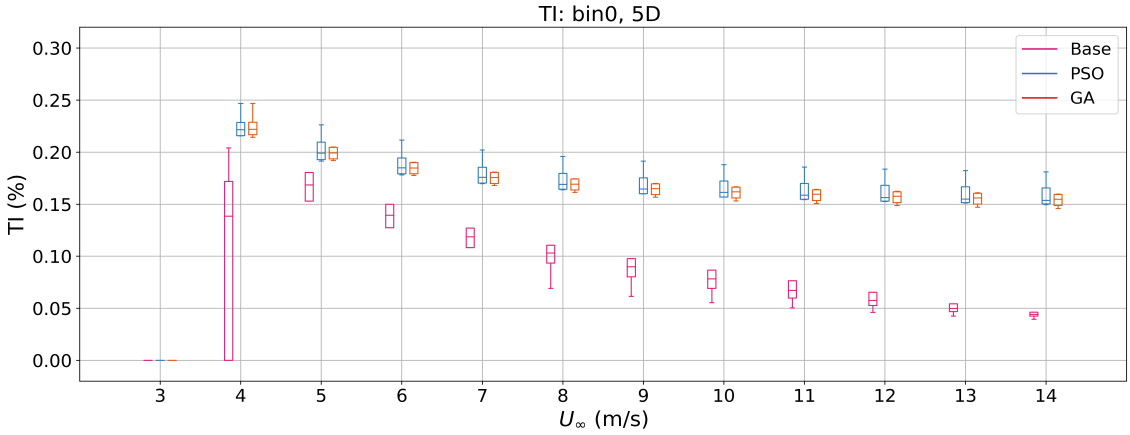

Figure 3.26: Box plots of WP turbulence intensities at all U_∞ values: Bin 0, $5D$.

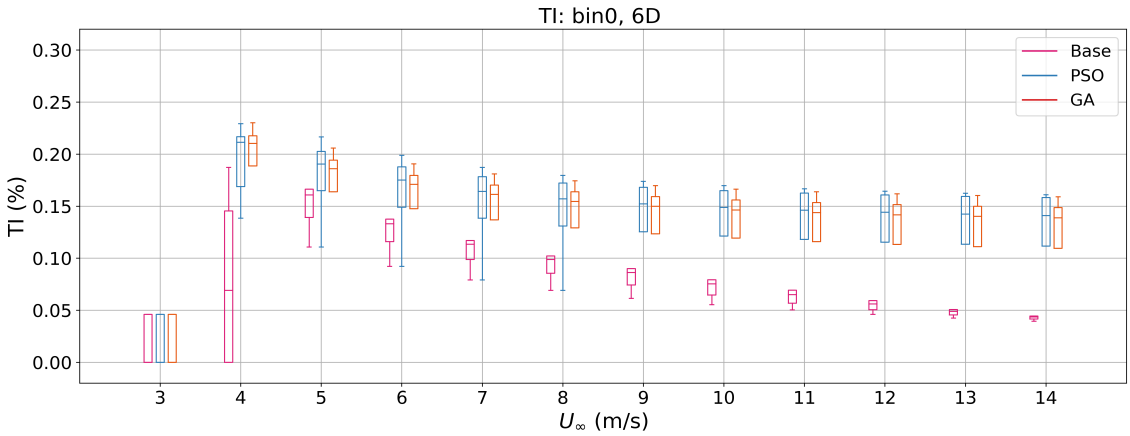

Figure 3.27: Box plots of WP turbulence intensities at all U_∞ values: Bin 0, $6D$

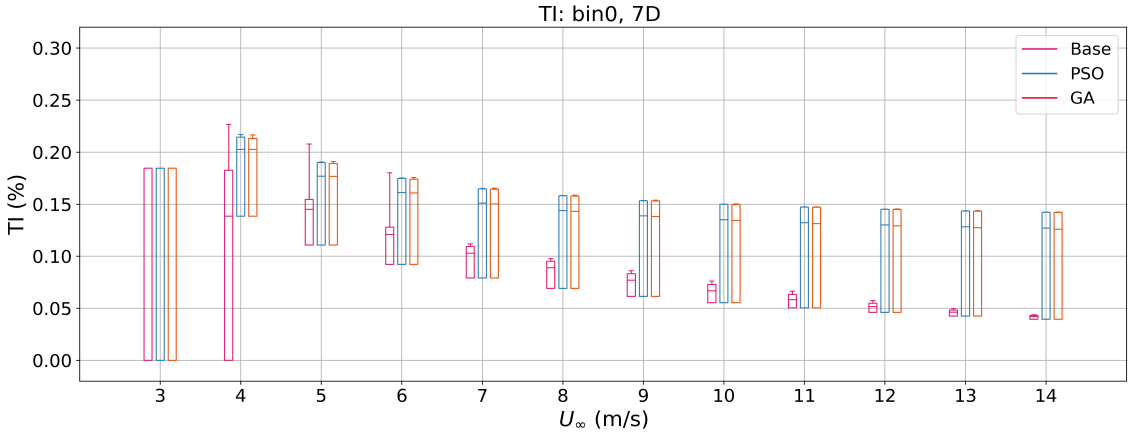

Figure 3.28: Box plots of WP turbulence intensities at all U_∞ values: Bin 0, $7D$

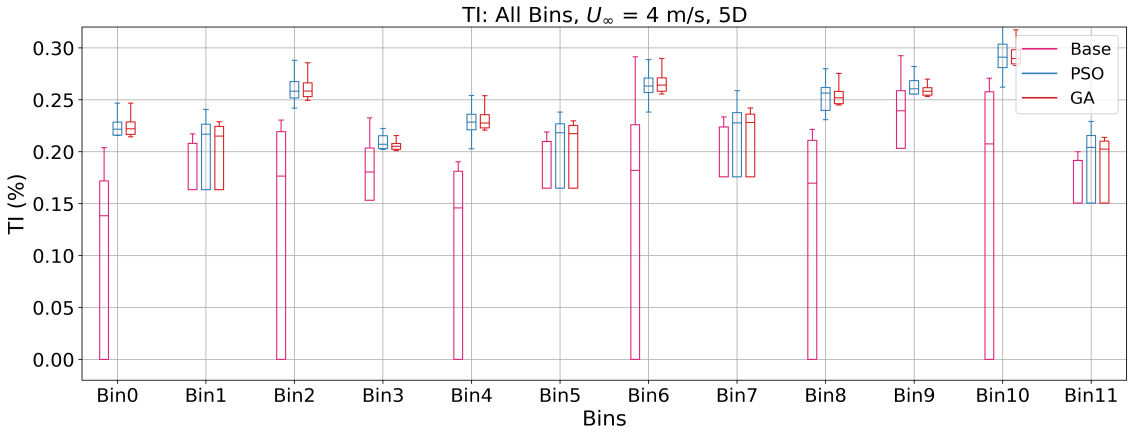

Figure 3.29: Turbulence Intensity by bins: $U_\infty = 4$ m/s.

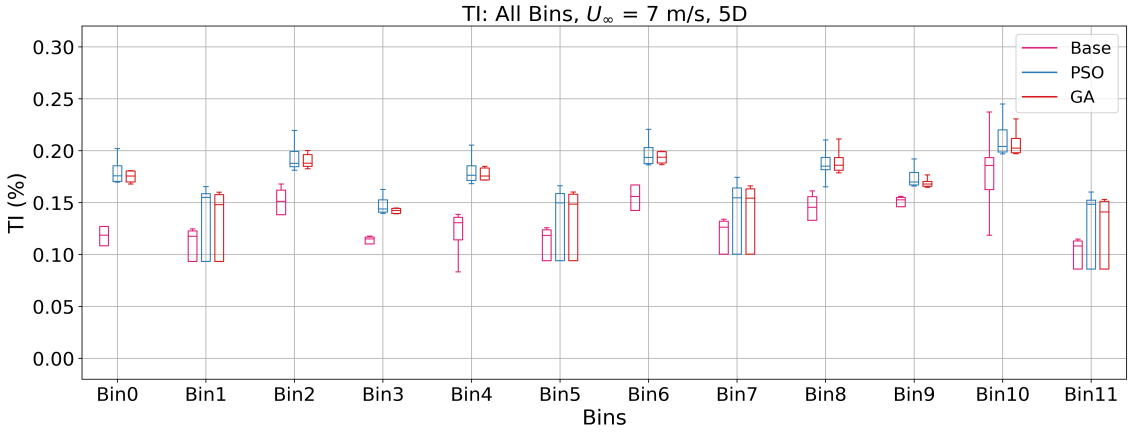

Figure 3.30: Turbulence Intensity by bins: $U_\infty = 7$ m/s.

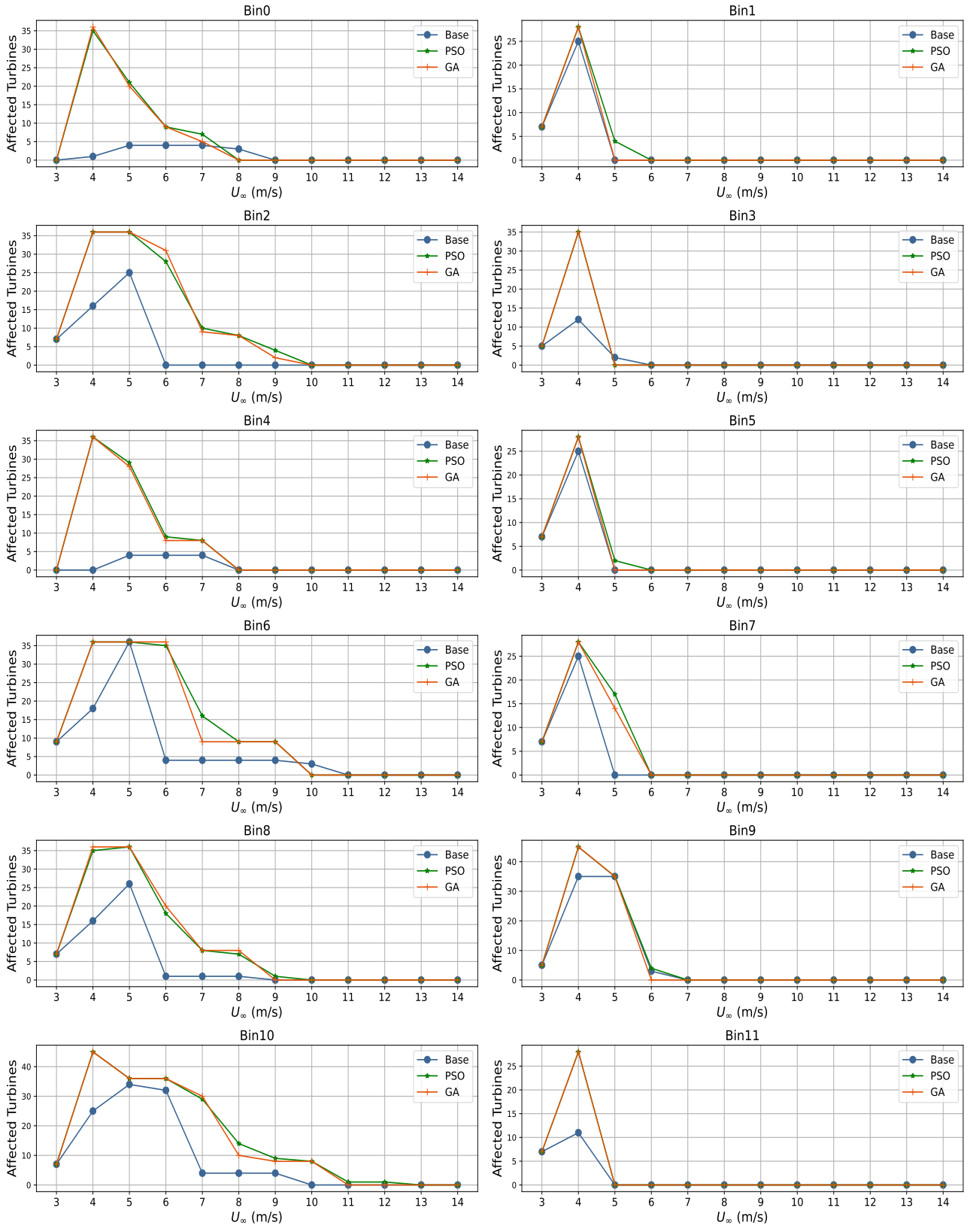

Figure 3.31: Total C_T-defaulting turbines for $5D$ scenario: All cases

3.6 Summary and Recommendations

In this chapter, a 2-D Gaussian wake model, known for its high accuracy and capable of yielding results similar to those obtained from CFD tools, was integrated with an enhanced implementation of the "simplified" version of Frandsen's turbulence intensity model. This enhancement was necessary to enable variable optimisation for border turbines and hence, ensure a plant-wide maximised power and optimised TI levels. Employing PSO and GA, axial induction optimisation of all turbines within the plant was implemented for maximisation of WP AEP. The analysis compared three scenarios ($5D$, $6D$, and $7D$) to determine how AEP varies with minimum T-2-T spacing, and to determine how this maximisation impacts turbine thrust coefficients and turbine-level TI within the plant.

From the results presented on Table 3.7, it is obvious that increasing turbine density through a decrease in minimum T-2-T distances can significantly increase the total AEP achieved in a WP. When compared to the $6D$ and $7D$ minimum T-2-T distances, a $5D$ minimum spacing using a hexagonal array was able to yield an improvement of 23.75% and 34.64%, respectively, for the Base case. With PSO and GA optimisation, an improvement of 22.64% and 34.79% against the $6D$ and $7D$, respectively, was recorded. The table also shows that gains of up to 45.05% is possible through turbine density increment by comparing the GA-optimised $5D$ case against the non-optimised $7D$ Base case - a minimum T-2-T spacing which is widely regarded as common practice in the literature according to [13].

Results for both optimised cases show that many turbines at U_∞ values as low as 5 m/s, are prone to overexertion or excessive thrusts. This is a direct effect of implementing unconstrained power maximisation, and the implication is turbine exposure to extreme loads. The number of turbines suffering this anomaly is shown to increase as U_∞ increases. Also, a positive correlation is observed between sparse deployments, high power generation and high C_T values at turbines. Hence, it is paramount that for all optimisation cases, more than just improving power production, the C_T values should be investigated and constrained or optimised to prevent extreme loads which could negatively impact the turbines' lifespan.

The analysis indicates that turbulence intensity (TI) decreases as freestream wind speed (U_∞) increases, and this trend remains consistent regardless of the separation distances

between turbines in the wind plant. The findings reveal too that unconstrained power maximisation leads to increased turbulence intensity within the wind plant, particularly evident in tightly spaced turbine layouts. However, this effect diminishes as the inflow wind speeds (U_∞) rise.

These results affirm the expectations cited in chapter 2 section 2.5 in terms of thrusts and TI values, and also underscore the importance of considering both turbulence intensity (TI) and thrust coefficient (C_T) constraints in wind plant power maximization studies, as neglecting them could lead to increased extreme loads and fatigue damage on turbines.

In the next chapter, the study goes ahead to implement a single objective thrust coefficient-constrained axial induction optimisation to not only maximise WP power and AEP but also prevent turbine overexertion and avert extreme loads.

Chapter 4

Thrust Coefficient constrained Axial Induction-based Optimisation

4.1 Introduction

The optimisation problem for wind plants is multi-faceted, encompassing a wide array of interrelated factors that cannot all be encapsulated as optimisation variables. Hence, it is advantageous to examine how optimising specific turbine or wind plant variables impacts others, leveraging these relationships to account for additional factors not directly addressed in the optimisation problem but correlated with those that are. The study conducted in the previous chapter demonstrated that optimising turbines' axial induction factors (α) at the plant level for the purpose of maximising annual energy production (AEP) has a direct impact on turbine-level turbulence intensities (TIs) and thrust coefficient (C_T) values. This is crucial because cumulative turbine thrusts, which are primarily influenced by C_T, are identified as the primary enhancer of extreme loads, as highlighted in [16]. It was also demonstrated that maximising WP AEP and/or increasing T-2-T distances result in high turbine C_T values and thrust, possibly imposing extreme loads.

A model proposed in [**?**] indicates the possibility of employing the thrust coefficient value of a turbine to estimate its tower bending moments as well as its blade bending moments. Moreso, according to the study by [16], the cumulative thrusts experienced by turbines serve as the primary factor enhancing extreme loads on these turbines. Although turbine loads are

considered in [16] while optimising WP power, they employed the very simplistic actuator disc model to describe the wake interactions between turbines.

Exceeding the manufacturer's design C_T specification as represented by its thrust curve may indeed enhance wind energy capture, as demonstrated in the preceding chapter. Nonetheless, this could lead to turbine overexertion from heightened thrusts, potentially transferring mechanical stresses to the electrical system. It is therefore imperative to ensure these C_T values and thrusts do not exceed optimum values even in the face of power maximisation, to ensure turbine safety and longevity. Because each turbine experiences a different mean wind speed, $\bar{U}$, locally regardless of the freestream, U_∞, makes this task non-trivial compared to enforcing all turbines to operate below a set threshold C_T value or thrust. Given that turbine C_T is directly proportional to turbine thrust, and the mean of cumulative thrusts has a bearing on the extreme loads, constraining individual turbines' C_T values below optimum would reduce the mean thrust value of individual turbines and could favourably affect turbine extreme loads.

Hence, this chapter aims to incorporate turbine thrust coefficient (C_T) values into the optimization process for maximizing Wind Plant Annual Energy Production (AEP), while also examining the impact of this constraint on AEP and turbine-level TI.

Building on insights from existing research, this study maximises the AEP of a WP using real site wind data, while ensuring that each turbine's C_T stays within optimum limits. The thrust generated by turbines is directly influenced by their C_T values. Therefore, limiting each turbine's C_T value within the optimal limits according to the thrust curve, for the corresponding wind speed experienced by the turbine, is crucial for maintaining the turbine's healthy operation and prolonging the wind plant's longevity. A high-fidelity 2-D Gaussian wake model that is inherently skewed and has yaw capabilities was employed to simulate wake interactions within the wind plant. This model was integrated with an enhanced implementation of Frandsen's TI model [43], studied in [42], to examine variations in turbulence intensity resulting from C_T-constrained AEP maximization.

4.2 Wind Plant Modelling and Power Optimization

4.2.1 Wind Plant and Turbine Model

The wind plant (WP) and wind turbine model which has been extensively discussed in the previous chapter are maintained. Table 3.1 can be consulted for more clarity on WP features, Figure 3.6 is maintained as the WP model, while the turbine model parameters remain as given on Table 3.1.

The wake and turbulence models are as presented in sections 3.3.3 and 3.3.4 respectively and all assumptions made in chapter 3 are maintained. Consistent with chapter 3 and to reserve focus on AEP maximisation with constrained turbine C_T, all turbines in the set $\mathcal{N}$ have been pre-allocated a 0° yaw angles, ϕ.

4.2.2 Optimization Problem Formulation

A coordinated control strategy is described in this section for a WP with the aim to maximise AEP while ensuring that turbine thrust coefficients are maintained within the optimal levels specified by the thrust curve. The mean wind speeds observed at the rotor of each downstream turbine (j) are determined by the axial induction (α) of all the turbines (i) located upstream of it. The resultant mean wind speed $\bar{U}_j$ subsequently dictates the thrust coefficient of turbine j and the corresponding thrust force it applies to the inflow. Since each mean wind speed corresponds to an optimal C_T value for achieving optimum output power at that wind speed, it is crucial to ensure that during the optimisation process of α for all turbines to maximise AEP, the optimiser is restricted from selecting α values that exceed the corresponding α value of the wind speed available at each turbine. This wind speed ultimately depends on the α values of all turbines upstream.

Assuming a uniform inflow of wind from one direction per instance of time, into a confined hypothetical WP, as depicted in Figure 3.6, with this inflow varying in speed as well as direction per instance of time. The sets $\mathcal{N}$, $\mathcal{B}$, $\mathcal{U}$, and $\mathcal{T}$ retain their definitions from chapter 3 subsection 3.3.5, paragraph 2, and the entire paragraph is maintained for this chapter.

The wind plant AEP can be estimated from Equation (3.16) and the optimization problem as given:

$$\begin{aligned} \max_{(U_{b,u,j}, P_{b,u,j})} \quad & AEP \\ \text{s.t.} \quad & C_{Tj} \leq {C_T}^{\bar{U}_j} \quad . \end{aligned} \tag{4.1}$$

Considering that the ϕ of all turbines i in $\mathcal{N}$ is preallocated a 0° value, the expression for $P_{b,u,j}$ can be written as:

$$P_{b,u,j}(\boldsymbol{\alpha}; U_\infty) = \frac{1}{2}\rho A \bar{U}^3_{b,u,j}(\boldsymbol{\alpha_{b,u,-j}}; U_\infty) C_P(\alpha_{b,u,j}) \quad . \tag{4.2}$$

The constraint in Equation (4.1) prevents each turbine's thrust coefficient, C_{Tj}, from surpassing its local mean wind speed equivalent thrust coefficient value, ${C_T}^{\bar{U}_j}$. The power and thrust coefficient curves establish the turbine's operational limits up to its cut-out wind speed, accounting for its mechanical and electrical systems. Therefore, constraint 2 ensures that the turbine operates within these limits to avoid placing excessive strain on its mechanical systems, which could result in excessive loading.

The modeling, simulation environment, programming software, and key libraries used in the preceding chapter remain unchanged for this chapter.

The coupling of the wake, TI and optimisation algorithms models, and the inter-flow between all necessary equations within these models is captured in Algorithm 2 which is given below. This algorithm is executed statically to obtain a maximised AEP with constrained C_T values and the numerical results are presented in the section that follows. In the algorithm, the variable BIN_P initialized with value 0 is the *bin power* (i.e. the total power from all the turbines in the WP for all operating wind speeds (3 - 14 m/s)), $C_T(U_\infty)$ is the U_∞ synonymous C_T value, and $C_T(\alpha_{opt})$ is the algorithm-selected C_T value for each considered turbine.

Algorithm 2: Axial optimisation algorithm for AEP maximisation with C_T control.

Input: scalar $fixed\_area$, D, ρ, κ, γ, ψ, τ, β, N_h, pop_size, max_it
vector $\vec{\mathcal{U}}$, $\vec{\mathcal{B}}$, $\vec{\mathcal{N}}$, $\vec{f_b}$
table U_{lookup}
Select minimum T-2-T separation distance
From origin (0,0), evaluate turbine locations $l_i(x_i, y_i)$ based on D, store in $i_{\vec{pos}}$ and deploy over $fixed\_area$
Compute A using D
$\theta^W \leftarrow 0^\circ$ considering Figure 3.6, $BIN_P \leftarrow 0$;
for $b \in \mathcal{B}$ **do**
  Apply coordinate axes rotation by θ^W
  Compute σ_{mean} for b
  $\phi \leftarrow 0^\circ$, $P_b \leftarrow 0$;
  for $u \in \mathcal{U}$ **do**
    $P_u \leftarrow 0$;
    for $it \leftarrow 1$ **to** max_it **do**
      Randomly initialize a population of pop_size each with position vectors (α) of length $\mathcal{N}$ using PSO/GA
      Set constants c1 = 1.8, c2 = 1.5, wMax = 0.9, wMin = 0.2
      Sort $i_{\vec{pos}}$ in descending order based on y-coordinate value and then x-coordinate value, considering bin direction b
      $sorted \leftarrow sorted(i_{\vec{pos}})$
      $P_{it} \leftarrow 0$;
      for $particle \in pop\_size$ **do**
        $\mathcal{T} \leftarrow [\,]$
        for $i \in sorted$ **do**
          if $i = sorted[0] \quad \vee \quad i \in first\_turbs$ **then**
            Extract $C_T(U_\infty)_i$ and $C_T(\alpha_{opt})_i$
            $C_{T_{new}} = max(0, C_T(\alpha_{opt})_i)$
            $C_{T_{new}} = min(C_{T_{new}}, C_T(U_\infty)_i)$
            if $C_{T_{new}} = C_T(U_\infty)_i$ **then**
              $C_P = C_P(U_\infty)_i)$
              else
                $C_P = C_P(\alpha_{opt})_i$
              end
            end
            Compute $\sigma_{j,wake}$ from Equation (3.11) and TI_i from Equation (3.12)
            Compute P_i from Equations (3.8)
            $P_{it} \leftarrow P_{it} + P_i$;
            Add i to $\mathcal{T}$
            else
              $sum\_sqr\_def \leftarrow 0$
              for $i \in \mathcal{T}$ **do**
                Compute $d_{j,i}$ and $r_{j,i}$ from Equations (2.18) and (3.2), respectively
                Compute $\bar{U}_{def_j}$ from Equation (3.14)
                $sum\_sqr\_def \leftarrow sum\_sqr\_def + \bar{U}^2_{def_j}$
              end
              Compute $\bar{U}_j$ from Equation (3.7)
              Extract $C_T(\bar{U}_j)$ and $C_T(\alpha_{opt})_j$
              $C_{T_{new}} = max(0, C_T(\alpha_{opt})_j)$
              $C_{T_{new}} = min(C_{T_{new}}, C_T(\bar{U}_j))$
              if $C_{T_{new}} = C_T(\bar{U}_j)$ **then**
                $C_P = C_P(\bar{U}_j)$
                else
                  $C_P = C_P(\alpha_{opt})_j$
                end
              end
              Compute $\sigma_{j,wake}$ from Equation (3.14) and TI_j from Equation (3.15)
              Compute P_j from Equations (3.8)
              $P_{it} \leftarrow P_{it} + P_j$;
            end
          end
        end
        Compute fitness function values for population of particles/genes
        Update personal bests for each particle/gene in population
        Update local/global best for entire population of particles/genes
        Update P_{it}
      end
      $P_u \leftarrow P_{it}$;
    end
    $P_b \leftarrow P_b + P_u$;
  end
  $P_b \leftarrow P_b * f_b$;
  $BIN_P \leftarrow BIN_P + P_b$;
end
$AEP = BIN_P * N_h$
Output: AEP

4.3 Numerical Simulation Results with Classical Examples for Demonstration

Results from simulation of the three studied scenarios ($5D$, $6D$, and $7D$) are presented for AEP, thrust coefficient, and TI within the hexagonally deployed WP of fixed area $4665 \times 2880\ m^2$. For all the analysed parameters, comparisons are also made across the studied scenarios to determine the variation between a WP with increased turbine density (represented by the $5D$ scenario, and a traditional T-2-T spacing of $6D$ and $7D$. The wake (Equation (3.8)) and TI (Equations (3.12) and (3.15)) models are employed for all studied cases in computing wind turbine power, turbine thrust coefficient, and in estimating turbulence intensity at turbine positions within the WP. The base-case represents the greedy operation of individual turbines while the optimised cases represent a cooperative operation for plant-level power maximisation while constraining turbine C_T values. Variable optimization is accomplished through genetic algorithm and particle swarm optimisation, while retaining the simulation parameters detailed in Table 3.6, except for *pop_size* and *max_it*, which have been revised to 25 and 500, respectively.

With reference to Table 3.5 and Figure 3.6, the study introduces two new cases; PSO_CT, GA_CT which are the PSO and GA-optimised cases with C_T constraints, for a performance comparison with the cases studied in the preceding chapter; *Base*, PSO and GA-optimised cases without C_T constraints (PSO, GA). This performance comparison is done for each studied scenario, and across the operating range of U_∞ values (U_{in} - U_r).

For all optimised cases, 500 iterations are executed and results analysed. Multi-core parallel processing was implemented in Python 3.9 using the *multiprocessing* package to execute 500 runs each for all twelve (12) U_∞ value range (i.e 3 to 14 m/s) in each bin. This is repeated for the remaining bins, and for all four (4) optimization cases. Hence a total of 500 * 12 (wind speeds) * 12 (bins) * 4 (optimization cases) = 288,000 iterations for each scenario and 864,600 iteration runs for the three studied scenarios.

4.3.1 Power analysis

This subsection presents the actual WP power by bins and freestream inflow wind speeds (U_∞). It is evident that constraints on turbine thrust coefficients hinder the generation of wind power in the WP. Moreso, Figures 4.1 and 4.2 confirm the observations from chapter 3, section 3.5.1, that odd-numbered bins, characterized by wider T-2-T separation distances, result in a greater overall WP power output. An advantage attributed to the chosen turbine layout.

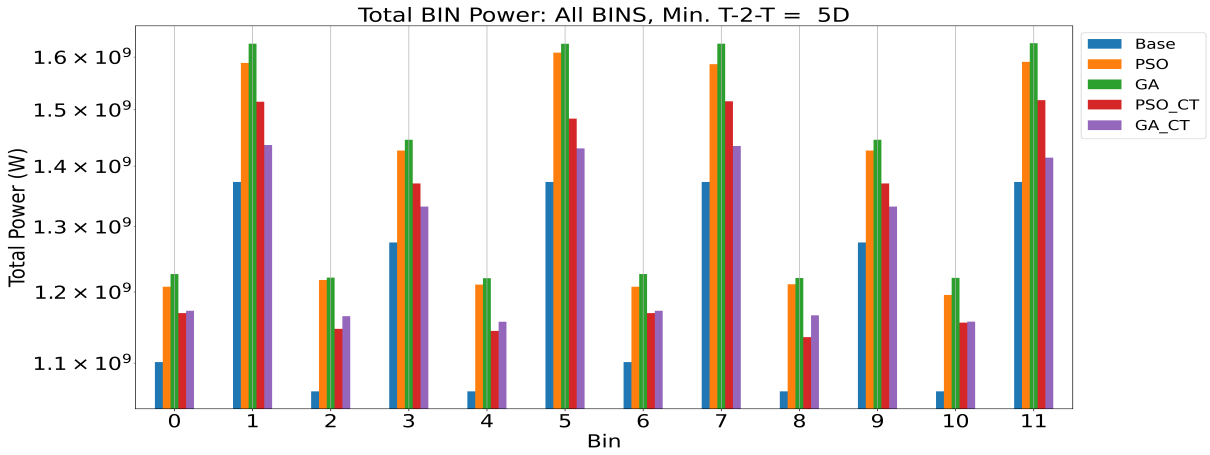

Figure 4.1: Actual WP power per bin: Scenario = $5D$.

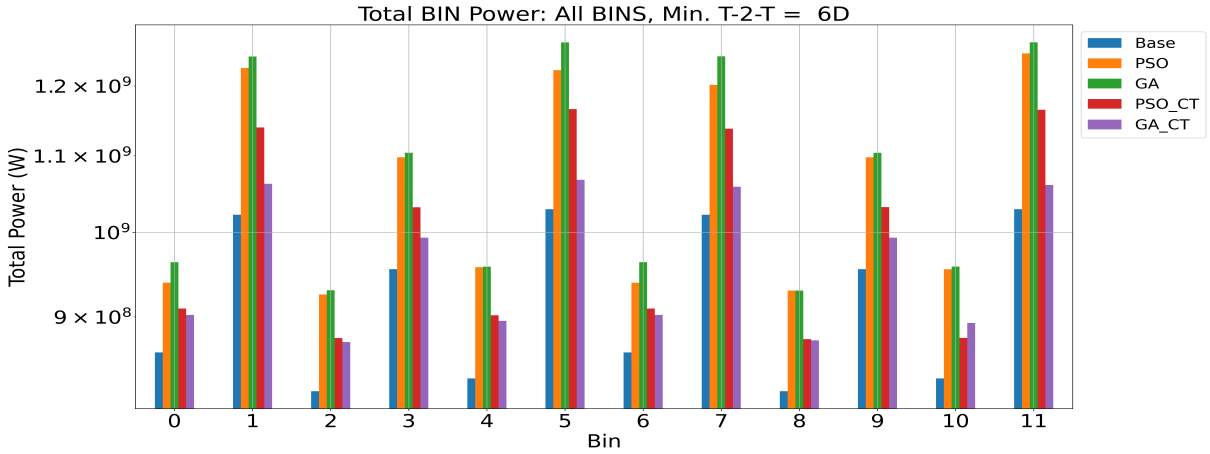

Figure 4.2: Actual WP power per bin: Scenario = $6D$.

The difference in bin power between odd-numbered bins persists, as observed in bins 3 and 9, which show a lower total WP power compared to bins 1, 5, 7, and 11. Referencing

Figure 2, and Figures 5 to 15 in the Appendix B section, this difference can be attributed to the "shallow array" characteristic of bins 1, 5, 7, and 11, where turbine columns contain a maximum of four turbines. In contrast, bins 3 and 9 have turbine columns with up to five turbines, leading to a more significant wind speed deficit for downstream turbines and a consequent decrease in turbine-generated power. As a result, there is a decrease in the overall WP generated power. Furthermore, bins 3 and 9, each having nine (9) turbine columns, contrast with bins 1, 5, 7, and 11, which possess seventeen (17) turbine columns, totaling 17 border turbines. Therefore, these bins encompass a higher number of turbines encountering the freestream wind inflow, as there are no turbines upstream causing deficits. Therefore, a greater number of border turbines contributes significantly to the total power generated by the WP.

4.3.2 AEP numerical results and analysis

Table 4.1 provides a summarised comparison of the total WP AEP and gain in percentage for all studied scenarios. It indicates that power maximisation increases WP AEP, but some of the power and AEP gains must be traded-off to simultaneously keep turbines' C_T values within optimum.

Table 4.1: Summary AEP table for all studied scenarios

	Base	**PSO**	**GA**	**PSO_CT**	**GA_CT**
Total AEP(TWh) - 5D	**10.53**	**11.95**	**12.13**	**11.39**	**11.17**
Percentage increase (%)	0	11.91	13.25	7.59	5.74
Total AEP(TWh) - 6D	**8.029**	**9.244**	**9.383**	**8.725**	**8.415**
Percentage increase (%)	0	13.15	14.44	7.98	4.60
Total AEP(TWh) - 7D	**6.566**	**7.792**	**7.831**	**7.272**	**6.805**
Percentage increase (%)	0	15.74	16.16	9.72	3.52

4.3.3 Thrust coefficient numerical results and analysis

Plots depicting the C_T variations at turbines are presented for all U_∞ values within the turbines operating range, using selected bins which are a reflection of other bins in terms of T-2-T distance.

The freestream inflow U_∞ for each time instance of wind plant operation, leading to equivalent variations in each turbine's experienced deficit. These deficits result in varying $\bar{U}$ values at each turbine depending on their relative positions. Consequently, varying $C_T(\bar{U})$ values (which are the *Control* values) are necessary for maintaining optimal operations at any given time instance. Implementing C_T constraints effectively decreases the number of turbines that surpass their designated *Control* values for optimal operations at each U_∞ value. The approach also diminishes the range of U_∞ values where turbines are prone to unhealthy operations (*Optimised* C_T values $>$ *Control* values) as illustrated in Figures 4.3 - 4.6, when compared with their unconstrained counterparts in Figures 3.15, 3.17, 3.19, and 3.21, respectively, of chapter 3, section 3.5.3. This implies that regardless the thrust from the $\bar{U}$ at turbine rotor (represented by the *Optimised* C_T value) the optimiser is able to ensure a reduced or at most equal counter thrust (not excessive) from a majority of the turbines in the WP and for a greater percentage of the U_∞ values between U_{in} and U_r. This can be achieved by varying the generator torque or speed to reduce the tip speed ratio, λ, and as a result reduce the generating efficiency of the turbines.

Figures 4.7 - 4.9 highlight the number of defaulting turbines over the operating U_∞ value range, for all bins and for the $5D$ scenario, utilizing the genetic algorithm to highlight this observation. It is evident upon comparison across these figures, for corresponding U_∞ value plots where defaulting turbines are present, that defaulting turbines are more pronounced in odd-numbered (sparsely-spaced) bins (bins 1, 3, ...). This observation is consistent for both the GA and GA_CT cases.

Figures 4.10 - 4.12 compare the performance of both algorithms, with the PSO results further confirming the trends observed with the GA algorithm. These findings suggest that sparse deployments are positively correlated with elevated C_T at turbines. This could be credited to the the direct proportionality existing between C_T and d_{norm}. This relationship becomes evident when Equation (3.11) is substituted into (3.12) for border turbines or (3.14) is substituted into (3.15) for inner turbines, with C_T as the subject of the formula. Therefore, when other parameters remain constant, an increase in d_{norm} will yield an increase in the C_T of the turbine under consideration.

Upon closer examination of Figures 4.10 - 4.12, it becomes apparent that the constraints provide a benefit across the U_∞ range 5 - 12 m/s for both sparsely-spaced and tightly-spaced bins. Moreover, parameter optimisation alone effectively guarantees that the *Optimised* C_T values are maintained below corresponding *Control* values, for U_∞ values under 5 m/s.

Figures 4.10 - 4.12 reveal that the Genetic Algorithm (GA) outperforms the Particle Swarm Optimization (PSO) method in meeting the C_T constraint objective. GA achieves this objective across a broader U_∞ range, and in addition exhibits fewer defaulting turbines beyond this range, for all bins and scenarios. Overall, the findings suggest a positive relationship between turbines' C_T and T-2-T distances of deployment for a fixed turbine density, exhibiting higher C_T values in bins with larger T-2-T distances, for corresponding U_∞ values. Recall that all bins contain the same number of turbines but have different T-2-T distances because of their different view angles into the WP layout.

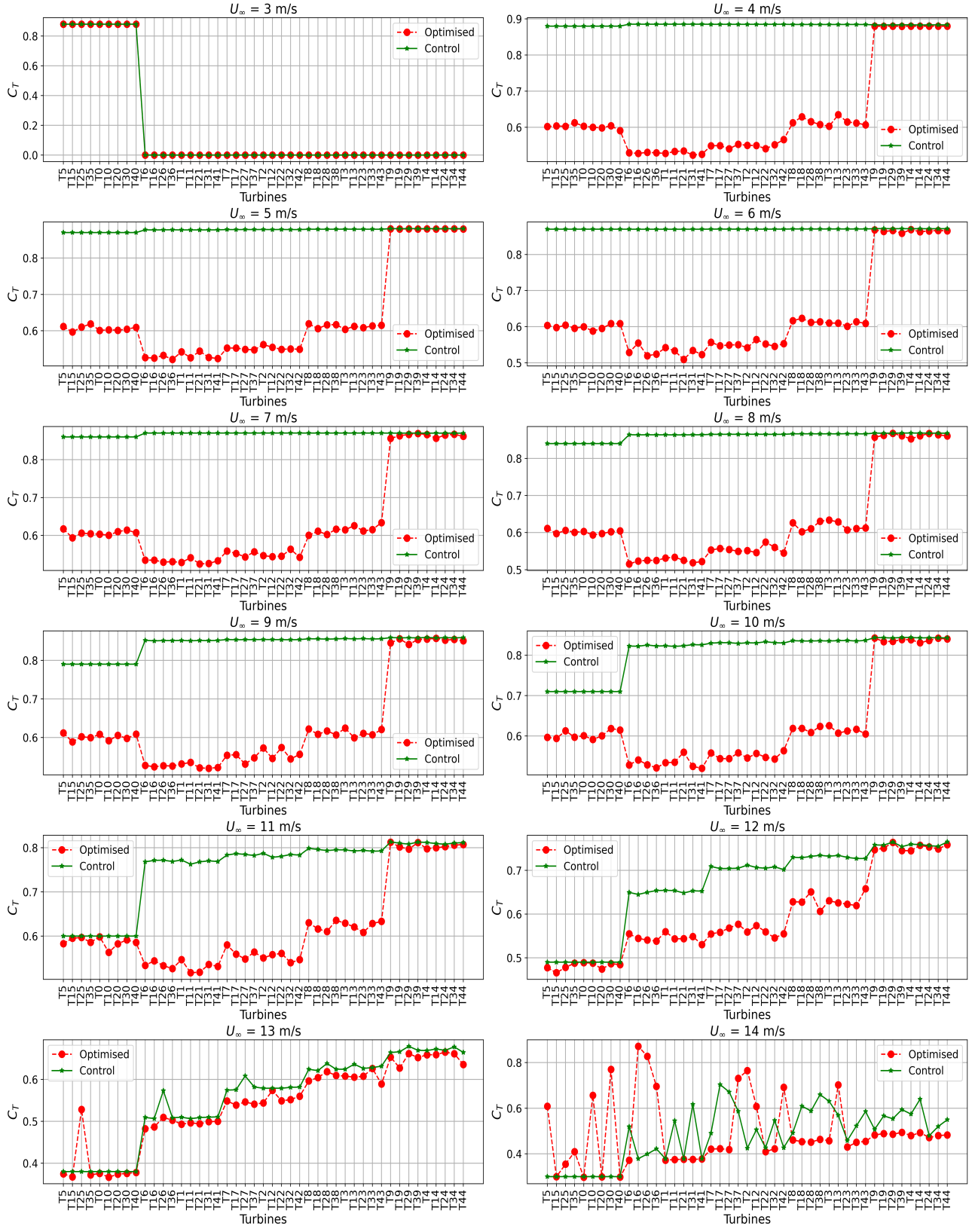

Figure 4.3: Turbines constrained thrust coefficient values with GA: $5D$, bin0.

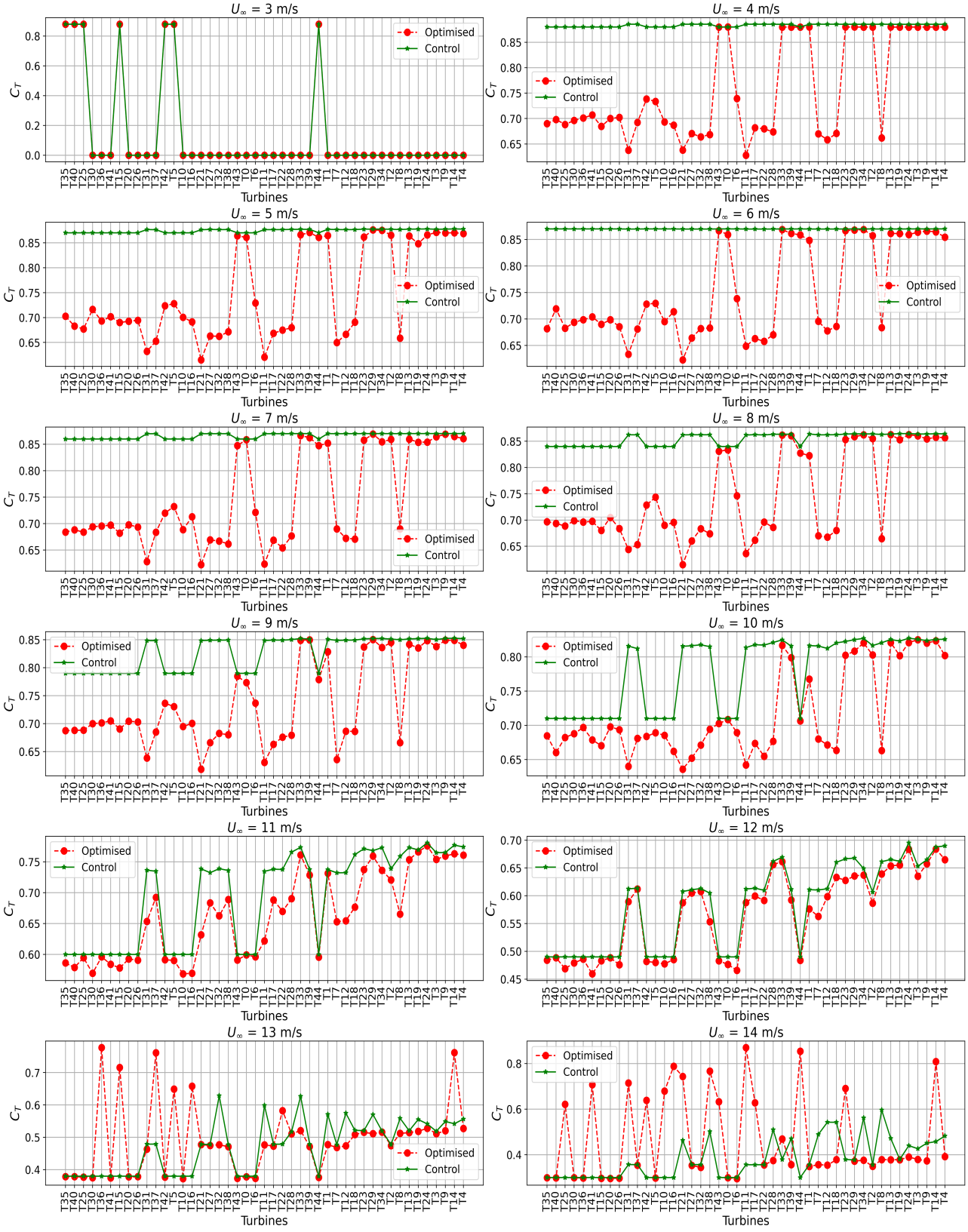

Figure 4.4: Turbines constrained thrust coefficient values with GA: $5D$, bin1.

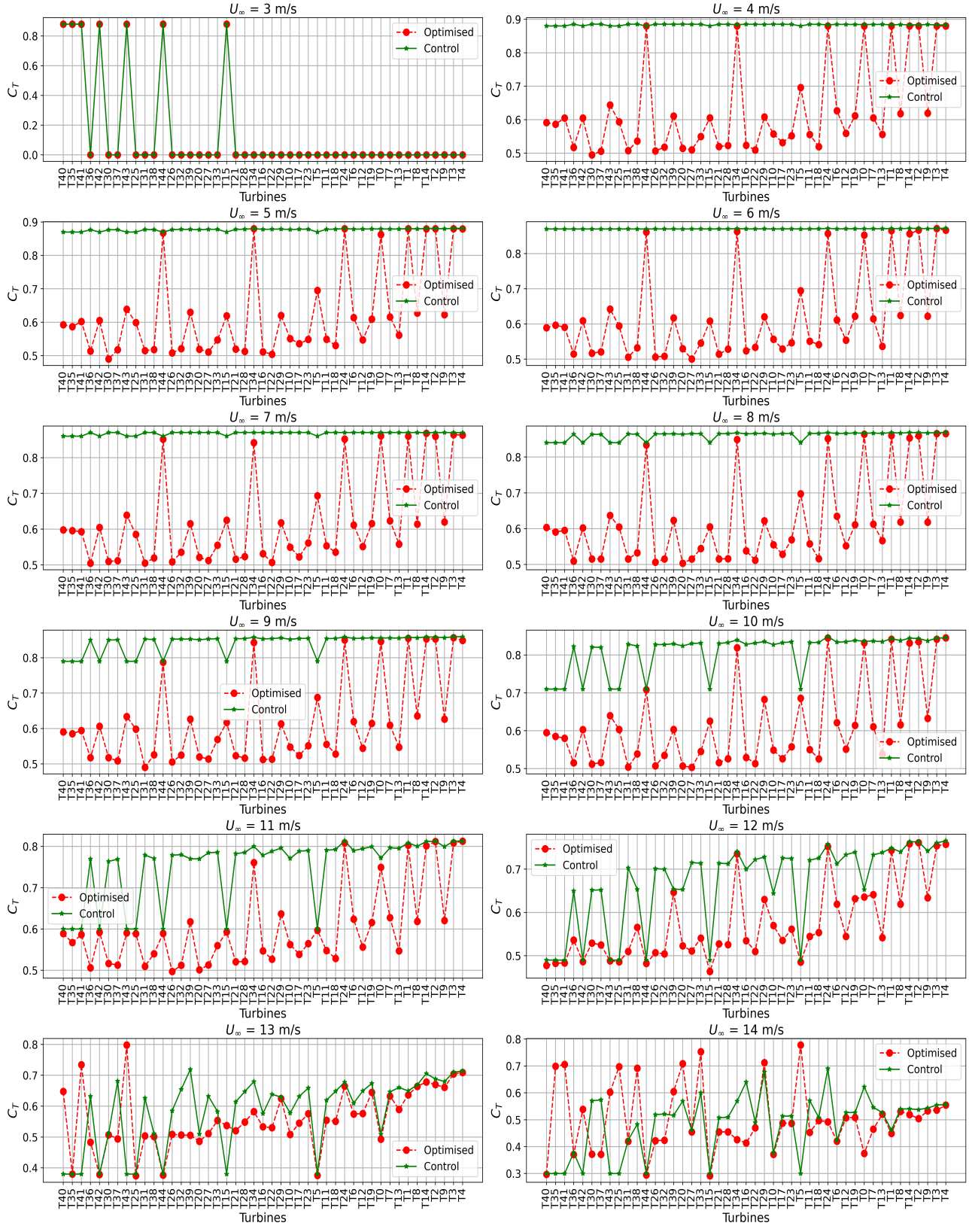

Figure 4.5: Turbines constrained thrust coefficient values with GA: $5D$, bin2.

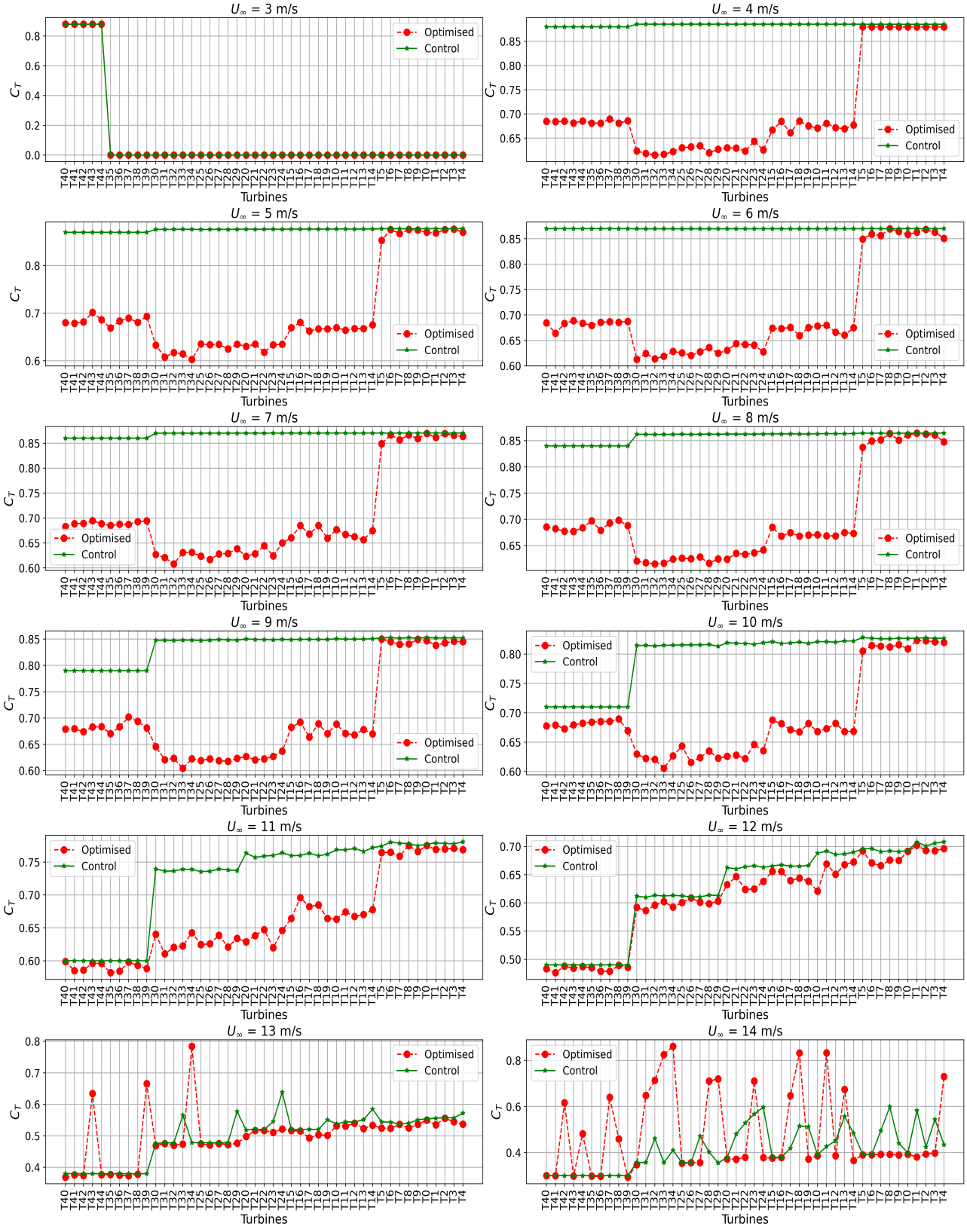

Figure 4.6: Turbines constrained thrust coefficient values with GA: $5D$, bin3.

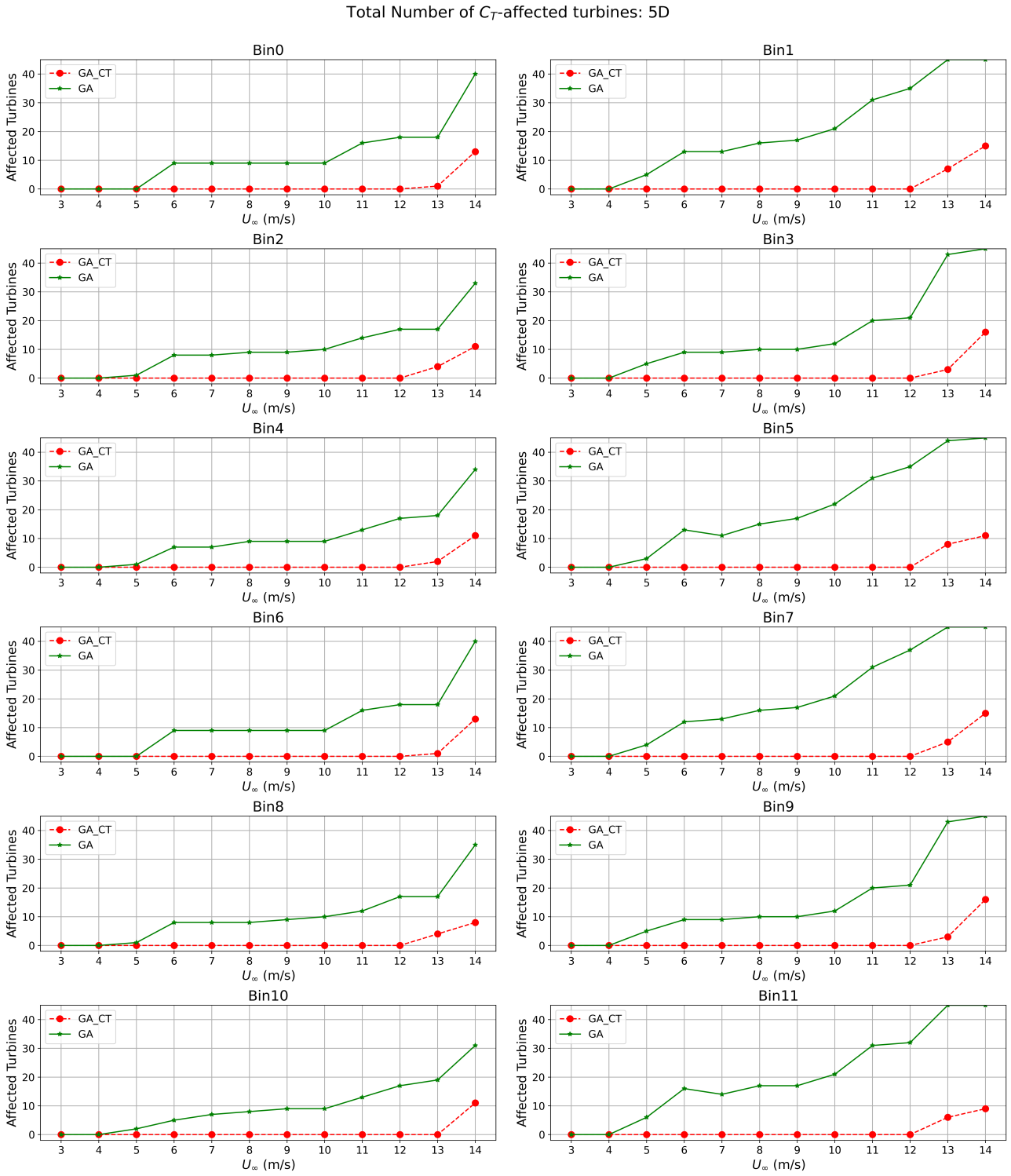

Figure 4.7: Total C_T-defaulting turbines for $5D$ scenario: GA cases.

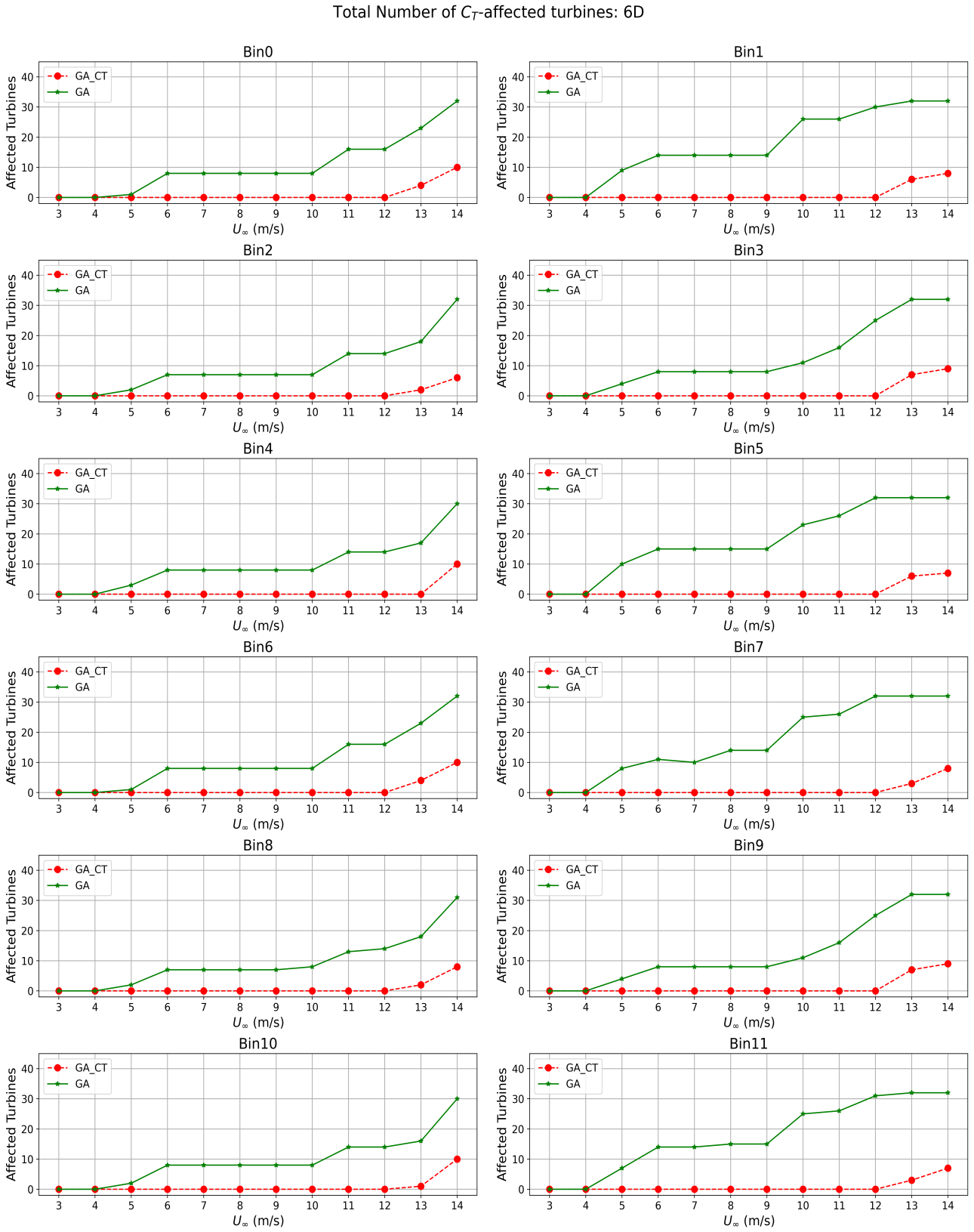

Figure 4.8: Total C_T-defaulting turbines for $6D$ scenario: GA cases.

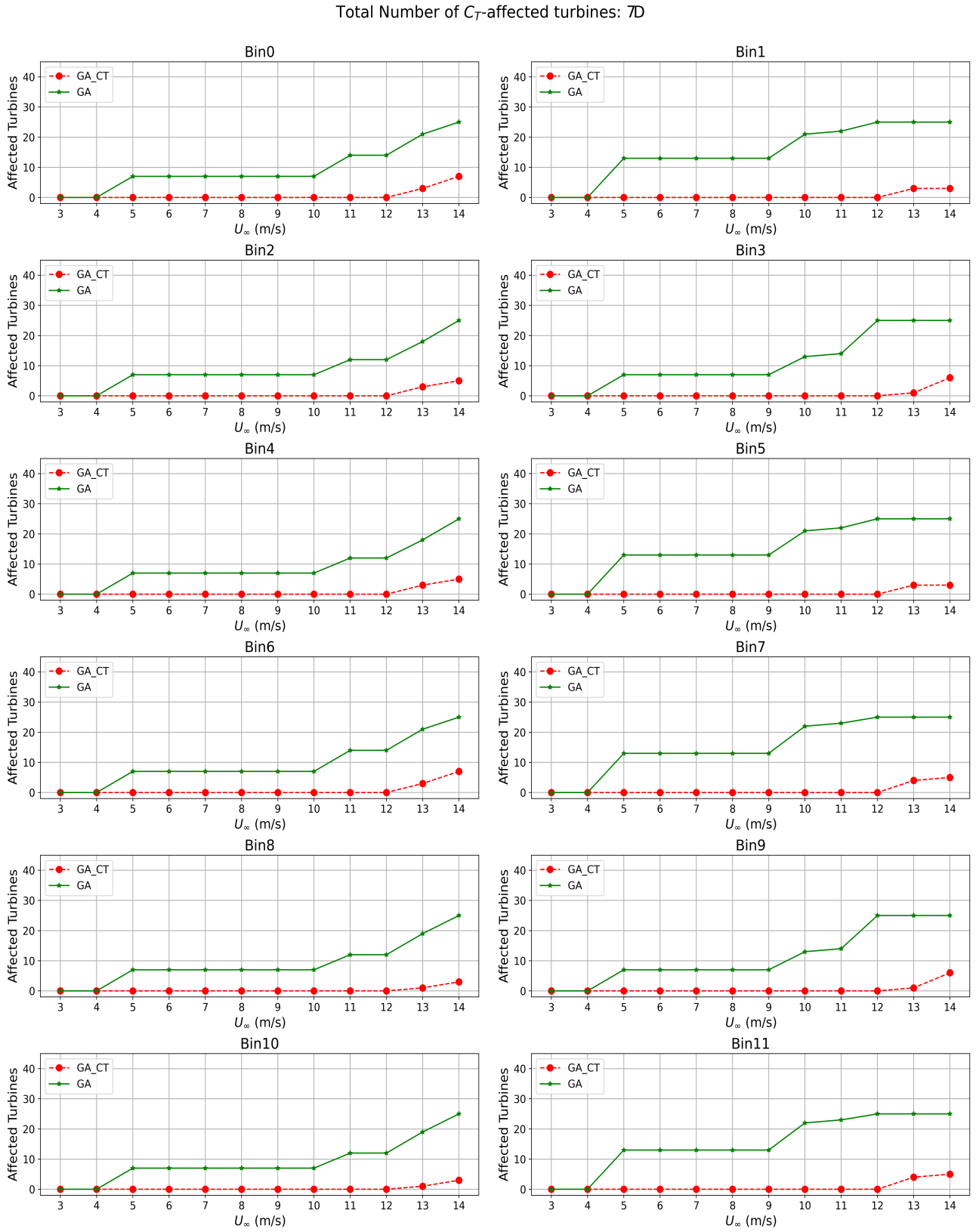

Figure 4.9: Total C_T-defaulting turbines for $7D$ scenario: GA cases.

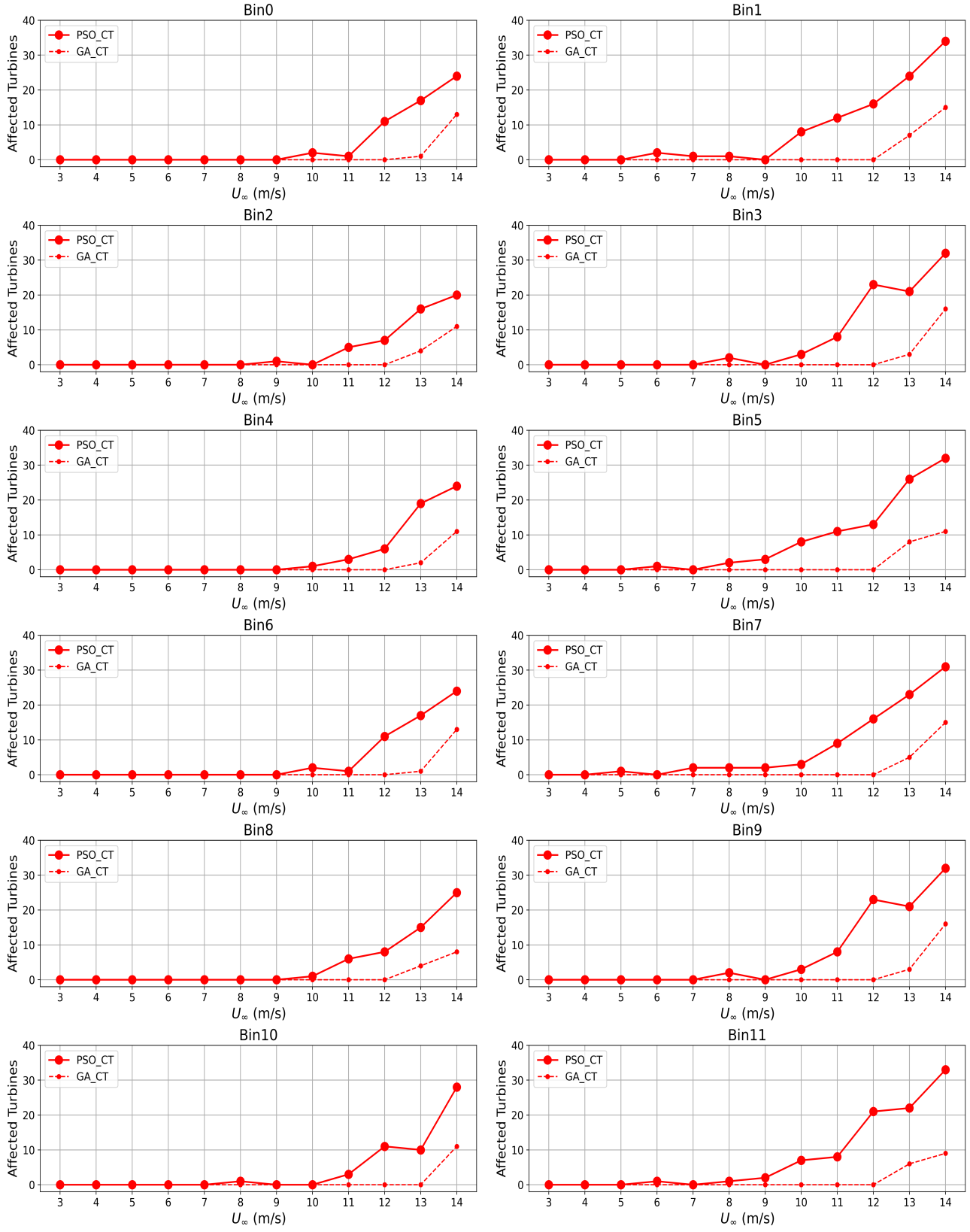

Figure 4.10: Total C_T-defaulting turbines for $5D$ scenario: Constrained cases

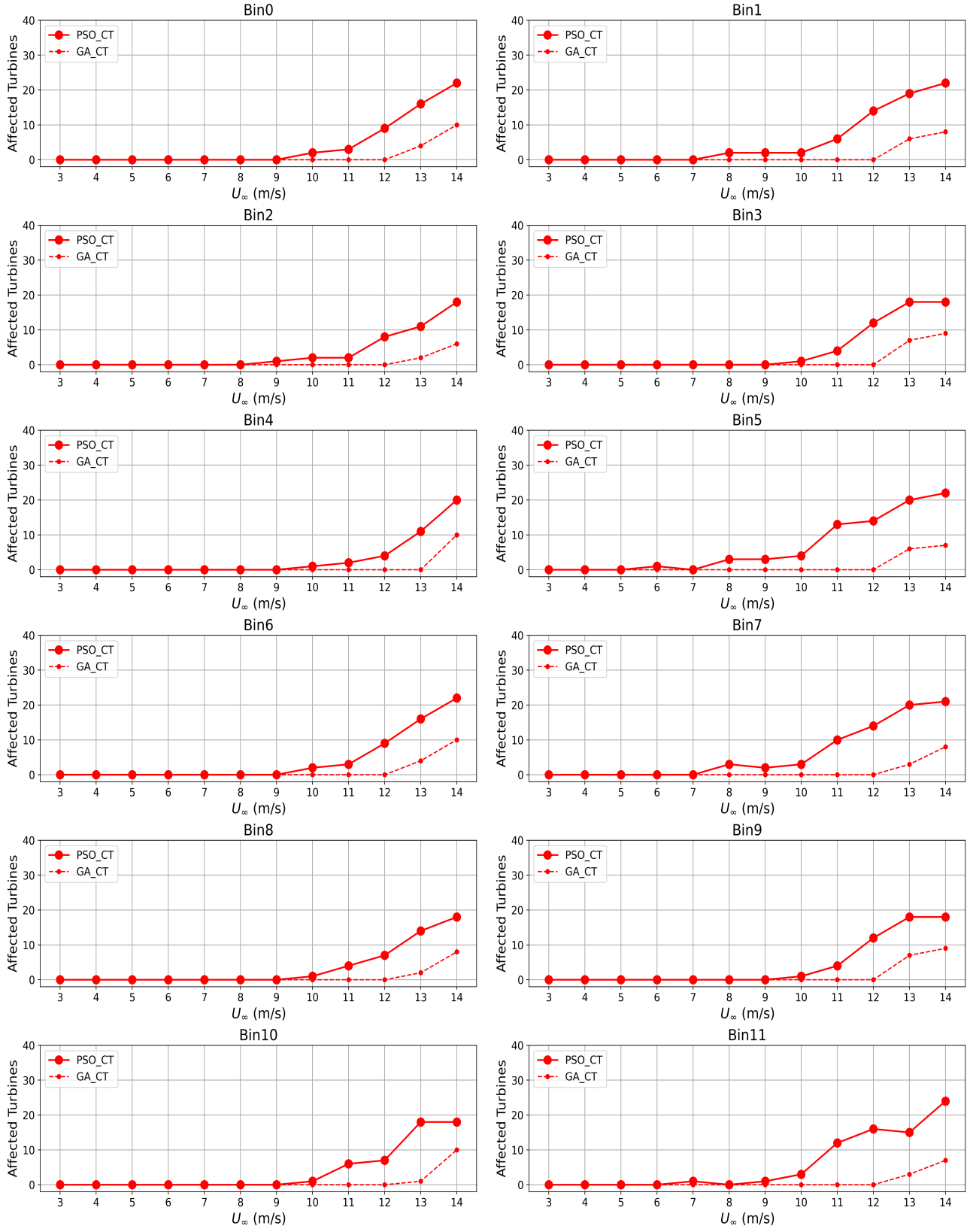

Figure 4.11: Total C_T-defaulting turbines for $6D$ scenario: Constrained cases

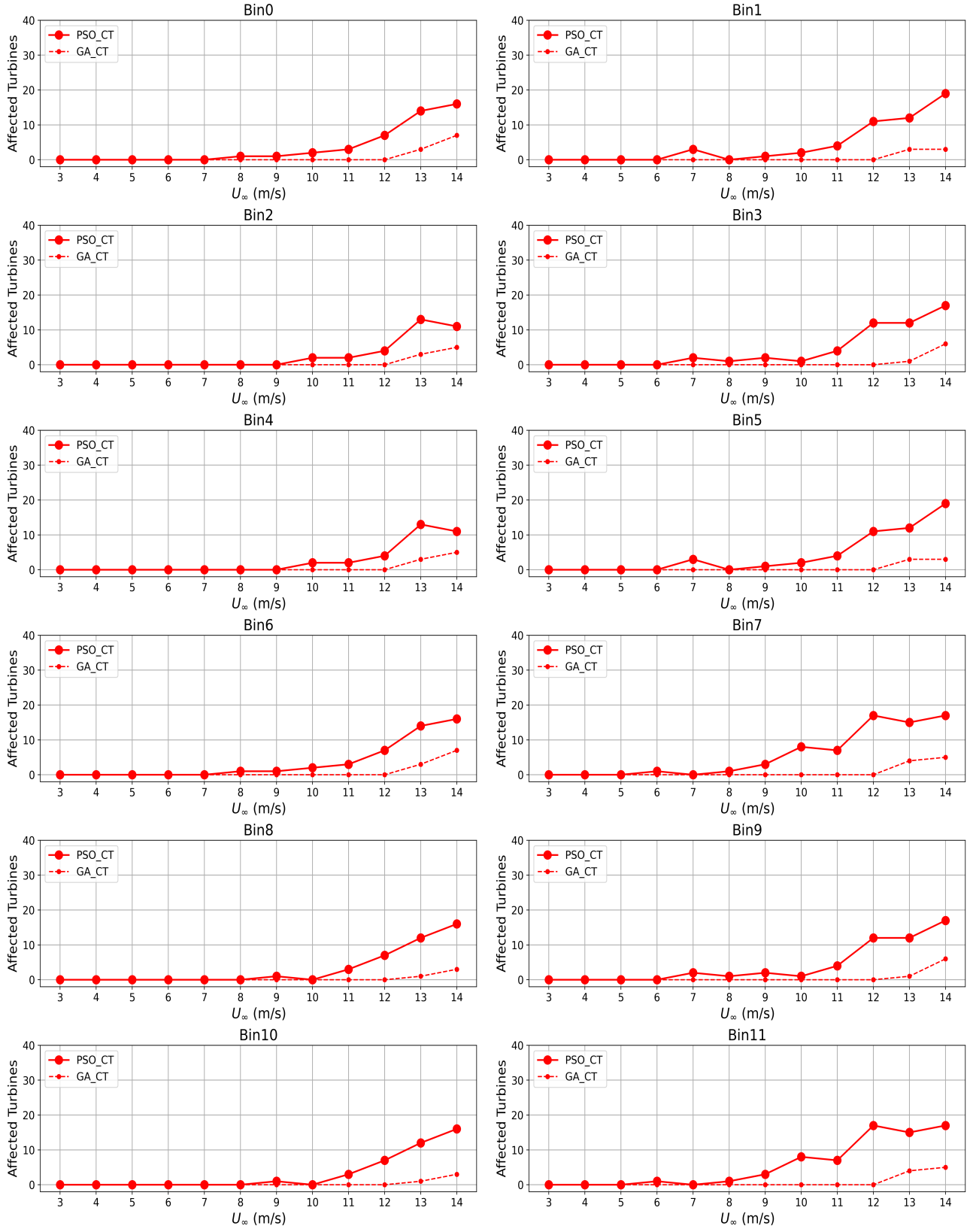

Figure 4.12: Total C_T-defaulting turbines for $7D$ scenario: Constrained cases

4.3.4 Turbulence intensity numerical results and analysis

In this subsection, turbine-level TI variations based on bins and freestream inflow wind speeds are presented. Figures 4.13 to 4.15 display the WP TI plotted against the operating range of U_∞ values for selected bins, and for all the studied cases; *Base* case, *PSO*, *GA*, *PSO_CT*, *GA_CT*).

The observation reveals that maximizing wind plant power or consequently AEP while imposing constraints on turbine C_T values results in comparable adverse effects on turbine-level turbulence intensities within the wind plant, as obtained when no constraints are imposed. Specifically, the *Base* case box plots demonstrate lower turbulence intensity value ranges in comparison with the unconstrained and constrained optimised cases.

Figures 4.16 and 4.17 display box plots by bin, of turbine-level turbulence intensities within the wind plant, for $U_\infty = 4$ m/s and $U_\infty = 7$ m/s. Bin 0 in the two figures corresponds to turbulence intensity at 4 m/s and 7 m/s, in Figure 4.13. In both figures, higher turbulence intensity values are more significant in tightly-spaced (even-numbered) bins compared to sparsely-spaced (odd-numbered) bins, suggesting an inverse correlation with T-2-T distance of deployment, as evidenced in both Figures 4.16 and 4.17. Additionally, these heightened turbine-level turbulence intensities are observed to diminish as U_∞ values increase, as demonstrated in Figures 4.13 - 4.15. However, turbine-level turbulence intensities within the wind plant continue to surpass the 20% threshold even at freestream wind speeds reaching up to 7 m/s, as clearly indicated in bin 10. Figure 4.18 reveals that affected turbines (turbines experiencing TI that surpass the set threshold) occur more in tightly-spaced bins.

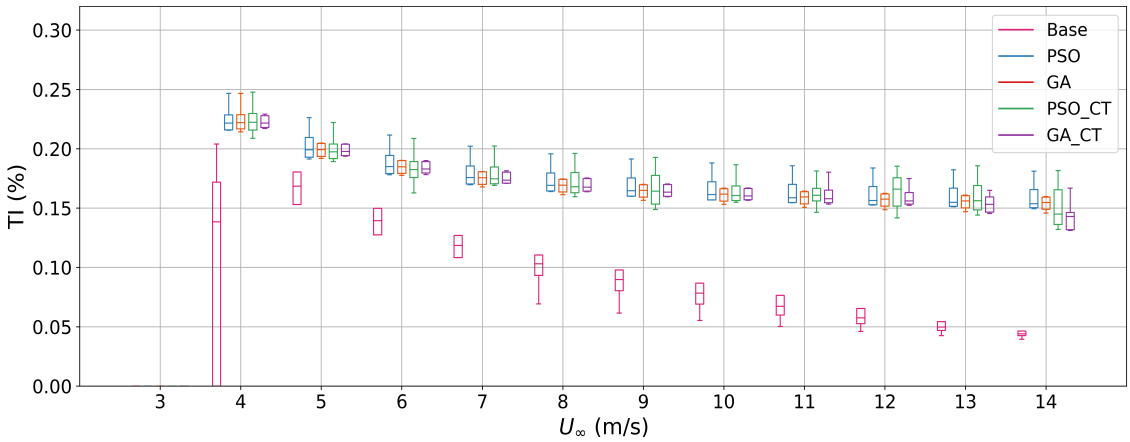

Figure 4.13: Box plots of WP turbulence intensities at all U_∞ values: Bin 0, $5D$.

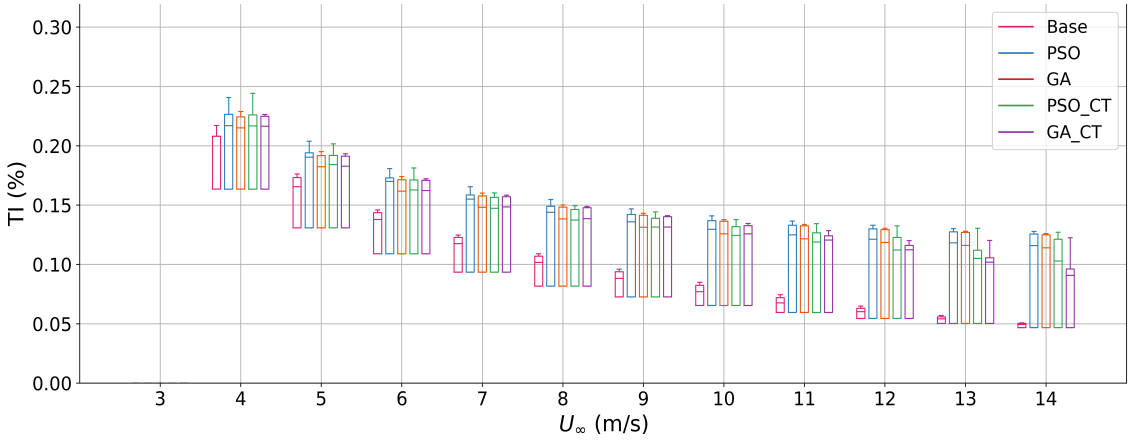

Figure 4.14: Box plots of WP turbulence intensities at all U_∞ values: Bin 1, $5D$.

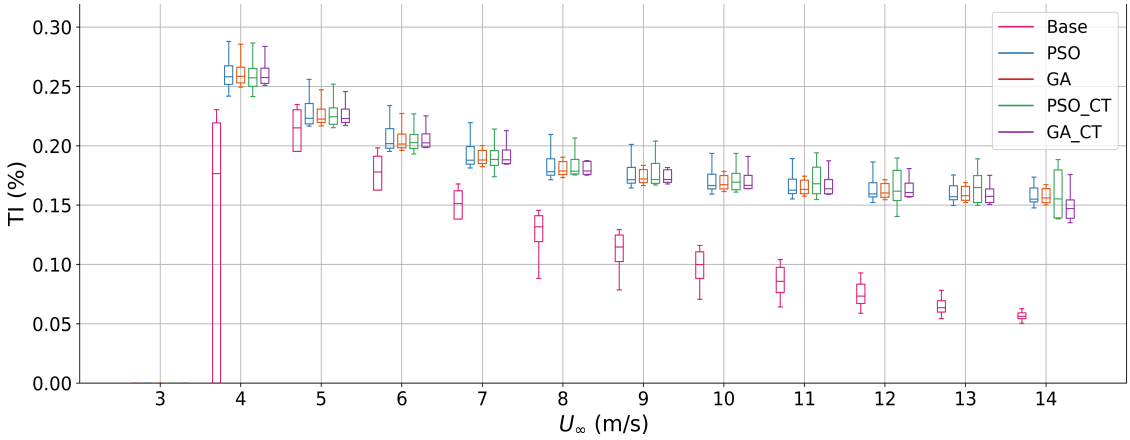

Figure 4.15: Box plots of WP turbulence intensities at all U_∞ values: Bin 2, $5D$.

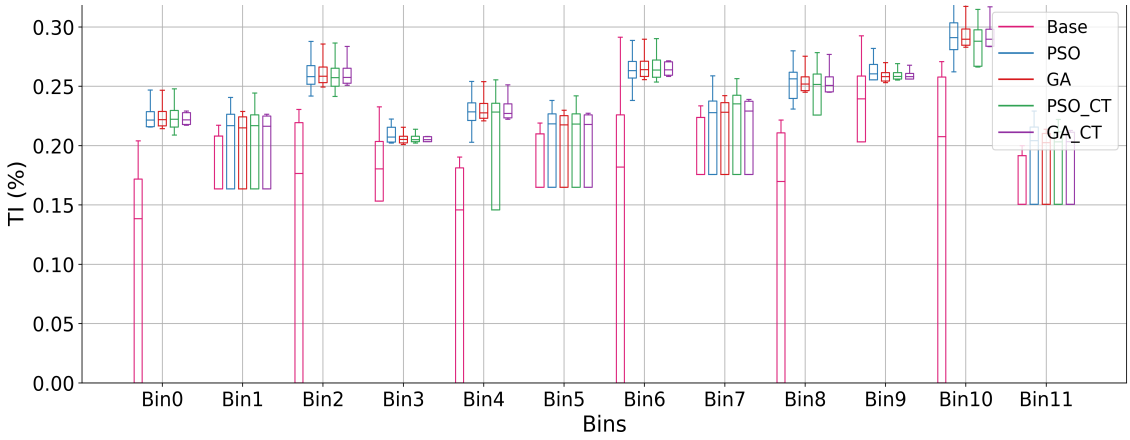

Figure 4.16: Turbulence Intensity by bins for $5D$ scenario: $U_\infty = 4$ m/s.

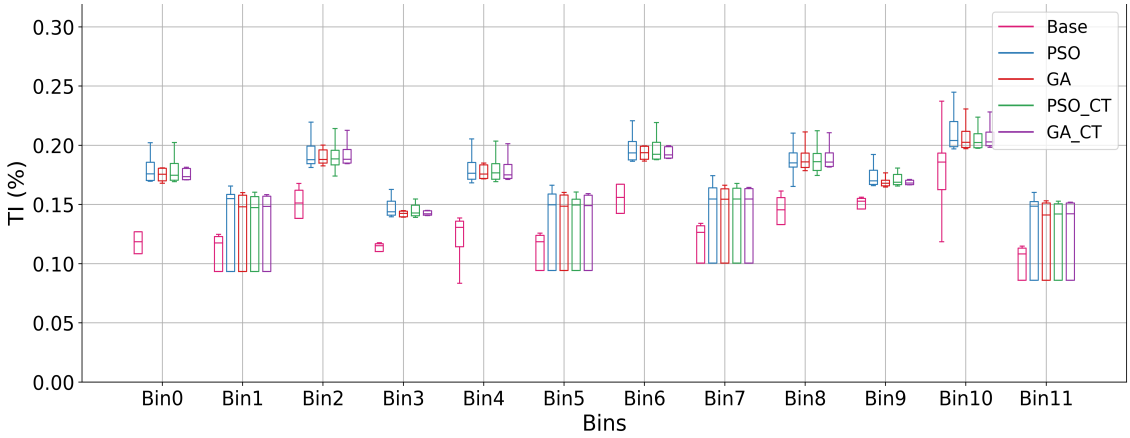

Figure 4.17: Turbulence Intensity by bins for $5D$ scenario: $U_\infty = 7$ m/s.

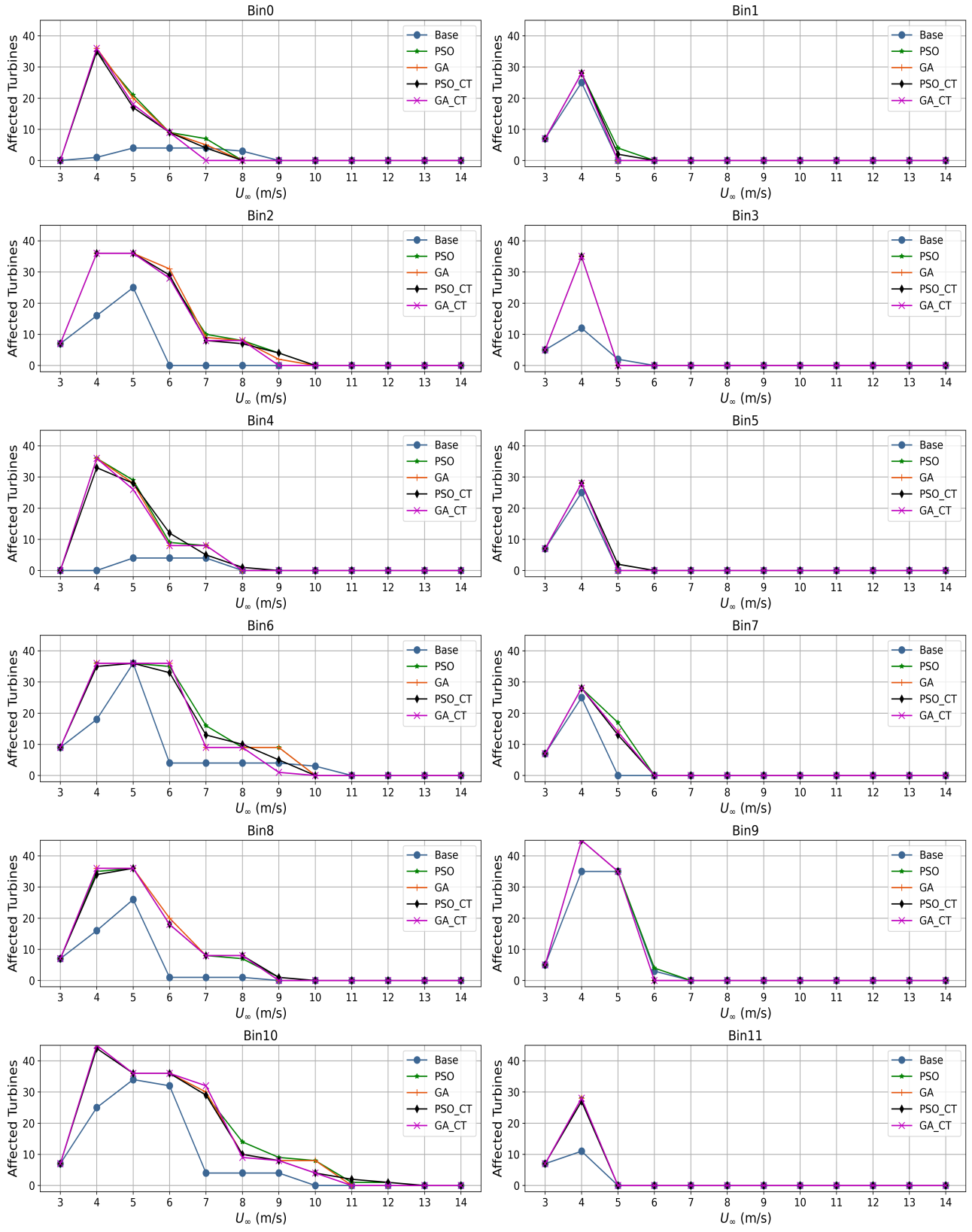

Figure 4.18: Total TI-defaulting turbines for $5D$ scenario: All cases

4.4 Summary and Recommendations

Employing the genetic algorithm and the particle swarm optimisation algorithms, a wind plant-level optimisation of axial induction factors for AEP maximisation, with constrained thrust coefficients, was carried out. Three scenarios; $5D$, $6D$, and $7D$, were analysed to examine the impact of a C_T-constrained axial induction optimisation on overall AEP and turbine-level turbulence intensities within the wind plant as T-2-T distances vary.

Having effected constrains on turbines' C_T to remain within optimal (i.e $\leq C_T(\bar{U})$), turbine overexertion was prevented for all U_∞ values up to 12 m/s in both sparsely-spaced and tightly-spaced bins. In contrast to the unconstrained GA case, where turbines' C_T values remained consistently within optimal range only at 3 m/s and 4 m/s, the GA-constrained case demonstrated a notable 66.67% improvement by maintaining C_T compliance to optimal range up to $U_\infty = 12$ m/s. This improvement remained consistent across all investigated scenarios. It's worth noting that the percentage improvement calculations do not include 3 m/s and 4 m/s.

Imposing C_T constraints for the $5D$ scenario, results in a trade-off in achieved AEP, leading to a l6.27% and 56.68% loss, respectively, in the AEP gains acquired by the constrained cases (PSO_CT and GA_CT). This trade-off nonetheless, regardless of the magnitude, may still be acceptable considering the magnitude of compliance achieved in turbine C_T across the entire WP.

It is widely recognised that turbulence intensity has an inverse relationship with U_∞. Findings from this chapter further demonstrates that this relationship does not depend on the T-2-T distances. Additionally, the results indicate no notable impact on turbulence intensities within the wind plant, due to C_T-constrained wind plant power maximisation, since no significant changes in turbine-level turbulence intensities are observed between the constrained and unconstrained cases. Moreover, it is revealed in the study that maximising wind plant power, in the presence or absence of constraints on turbine C_T, generally leads to increased turbulence intensities within the wind plant, particularly in tightly spaced scenarios. This increase could potentially have adverse effects on extreme loads.

The study revealed that turbine-level turbulence intensity (TI) and C_T exhibit contrasting relationships with T-2-T distance. While turbine C_T correlates positively with T-2-T distance, turbine-level TI displays negative correlation with T-2-T distance. In a WP employing a hexagonal lattice deployment, known to generate consistent T-2-T distances throughout the plant in any considered direction, this relationship could be leveraged to establish a WP system where turbine C_T values and TI at turbine positions remain within acceptable limits.

Finally, since constraining C_T values did not yield any significant disparity in TI behaviour when placed side-by-side with TI results from the previous chapter where turbine C_T was unconstrained, the study proposes that it may be impossible to cater for TI values within a WP through an outright constrain on individual turbine C_T values as studied in this chapter. It therefore in the next chapter explores other means with which this can be achieved.

Chapter 5

A Novel Turbine Upstream Sector Implementation and Wake Effect Elimination for Improved AEP and Turbulence Intensity

5.0.1 Introduction

In chapter 4, it was demonstrated that the application of thrust coefficient (C_T) constrains on turbines during power maximisation can significantly reduce excessive thrusts that cause overexertion. It was also shown that this methodology does not significantly affect TI since the increased TI levels (at low U_∞ values) resulting from power maximisation only, still remained significant and showed no obvious differences when C_T constrains were applied. Considering Equations (3.11) and (3.14), only three parameters; $\bar{U}, d_{norm}$, and C_T can be varied to affect the value of parameter TI. Given that the T-2-T distances of separation considered for this study are pre-determined, it implies that d_{norm} cannot be varied. Besides, d_{norm} (which is the T-2-T distance normalised by D) has contrasting relationships with C_T and TI. So, there will always be a trade-off between C_T and TI if d_{norm} is the parameter to be varied. Also, directly increasing turbine C_T values can reduce TI levels, but these increase has to be constrained else it causes overexertion, as was demonstrated in chapter 3.

Therefore, $\bar{U}$ seems the more feasible parameter that can be varied to modify the TI values at turbines, without inducing a counter effect on the C_T values. Based on these observations, this chapter's objective is to improve (in this case, reduce) the resulting TI levels at turbines by improving the $\bar{U}$ values available at turbines. Achieving this will by extension improve turbine and consequently WP power since the power equation as given in Equation 2.5 is a function of the cube of the mean wind speed, $\bar{U}$, at a turbine rotor.

Furthermore, since it has already been demonstrated that axial induction factors (α) optimisation with C_T constraints or without, is not sufficient to improve $\bar{U}$ values enough to reduce TI levels, the study proceeds to investigate the wake model's dependence on the WP dimensions and layout studied, to improve $\bar{U}$ values at turbines.

The chapter's primary contribution is the implementation of a sectored upstream approach for a coordinated axial induction optimisation of turbines in a WP. It is envisioned that this approach more than reducing computational complexity, will improve the $\bar{U}$ values at turbines and consequently improve both WP power and TI levels. In addition, constrains are enforced on turbines' C_T values to keep them within optimal limits. The computed turbine-level mean wind speed ($\bar{U}$) as expressed in Equation (3.7) is used as the inputs to Equations (3.14) and (3.15) to estimate the mean turbine-level TI. Consequently, constant optimal C_P and C_T values are not assumed as in [58], rather, varying C_P and C_T values at each turbine's rotor (that ensures an optimal performance in terms of loads and overall power generation) are applied for turbine power and TI estimations.

5.1 Wake Model Augmentations for Mean wind speed ($\bar{U}$) improvement at turbines

5.1.1 Turbine Upstream Sector Reconsideration

According to the applied wake model as originally presented in [3, 4], every downstream turbine is affected by all upstream turbines whose $d \geq 0$ as depicted in figure 2.11 and Equation (2.30). This decision however, seems an overkill, as most upstream turbines especially those whose $d = 0$ and those with large r distances, have very minimal effects

on the considered downstream turbine as would be demonstrated later in this section. This study instead defines an upstream sector for each turbine based on the rotor diameter D, such that a turbine is deemed a "non-negligible upstream turbine" if it falls within this sector.

Consider bin 0 deployed at a $5D$ T-2-T distance as shown in Figure 2. Based on the model in [3], turbine $T24$ will have to compute deficits from all 40 turbines above it (turbines with higher y-position or $d > 0$), in addition to another 2 turbines lying on the same y-position as itself or with $d = 0$, as depicted in Figure 5.1. This makes it a total of 42 upstream turbines, whereas, close to half of those turbines contribute less than 5 percent of the total deficit on $T24$, as demonstrated by the percentage contribution of each upstream turbine's deficit plotted above each turbine on the figure. It should be noted that the "40 + 2" upstream turbines ahead of $T24$ are obtained given that $T5$ is considered the furthest upstream turbine affecting every other turbine, and $T15$ affects every other except $T5$. In this order, $T25$ has only $T5$ and $T15$ in its upstream with the rest in its downstream, while $T24$ will have every turbine with $d > 0$ in its upstream in addition to those with $d = 0$ (i.e. $T4$ and $T14$). This direction of positional movement which could also be considered from right-to-left (i.e. from $T35$), depends entirely on choice. Based on these considerations, this study introduces an upstream sector (defined with respect to the rotor diameter D, and the T-2-T distance) within which an upstream turbine must be positioned, for its deficit to be considered non-negligible.

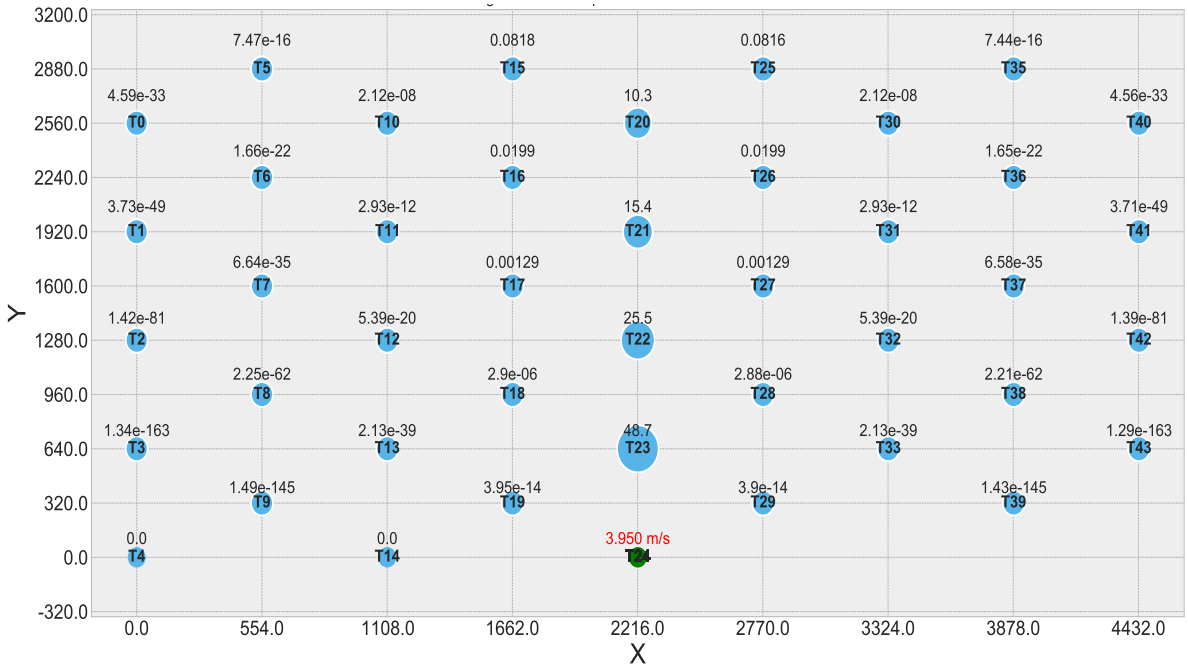

Figure 5.1: Bubble plot of percentage deficits from turbines in the upstream of $T24$ based on the baseline model in [3]

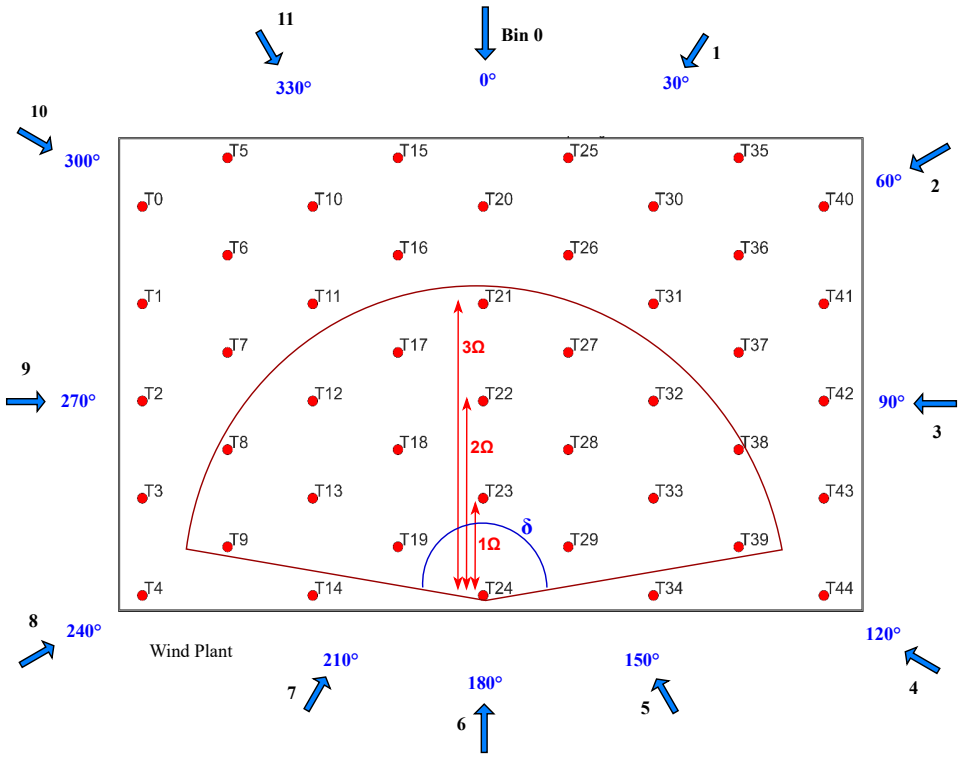

Figure 5.2: WP model highlighting a 3Ω upstream sector with respect to $T24$

Again, consider figure 5.2, the area of the upstream sector can be defined as:

$$Area\ of\ upstream\ sector = \frac{\delta}{2} * (n\boldsymbol{\Omega})^2 \quad , \tag{5.1}$$

where $\boldsymbol{\Omega} \equiv D$ * T-2-T distance, $\delta < 180°$ is the upstream sector angle which is meant to be a minor sector so as to exclude all turbines on the same y-position as considered turbine, and n is any positive real number. Hence, considering a $5D$ T-2-T distance of separation, Figures 5.3 - 5.5 are obtained showing the contributed percentage deficits on $T24$ due to upstream turbines positioned within an $8\boldsymbol{\Omega}$, a $6\boldsymbol{\Omega}$, and a $4\boldsymbol{\Omega}$ upstream sector, respectively. Consequently, Figures 5.3 - 5.5, have upstream sector radii of $(8 * 5 * 128)m$, $(6 * 5 * 128)m$, and $(4 * 5 * 128)m$, respectively. These Figures demonstrate that 99.9% of the deficit on the considered turbine (and any other turbine in the WP) is contributed by upstream turbines positioned directly ahead of such turbine (i.e by turbines with $r = 0$). Further to these plots, table 5.1 shows a select number of wind bins of different array depth and T-2-T distances, each with a carefully selected downstream turbine, to demonstrate how the resultant mean wind speed, $\bar{U}$, varies at the selected turbine for different upstream sector radii, given a freestream inflow of 5 m/s.

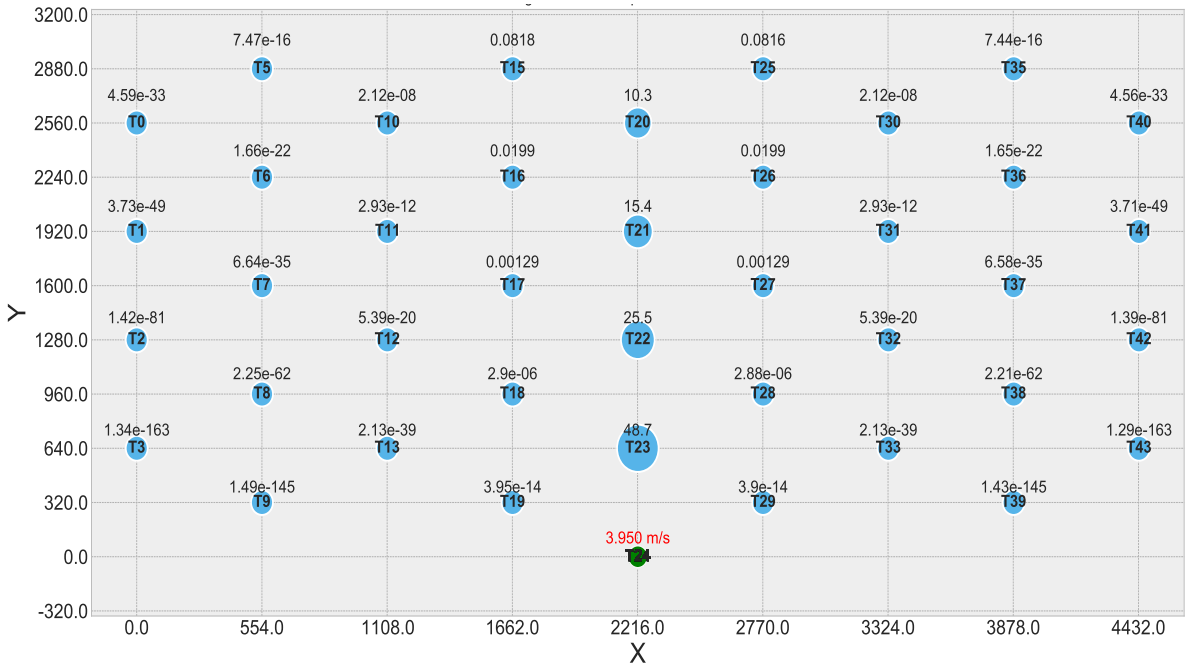

Figure 5.3: Percentage deficits from turbines within an $8\boldsymbol{\Omega}$ upstream sector of $T24$; Bin 0

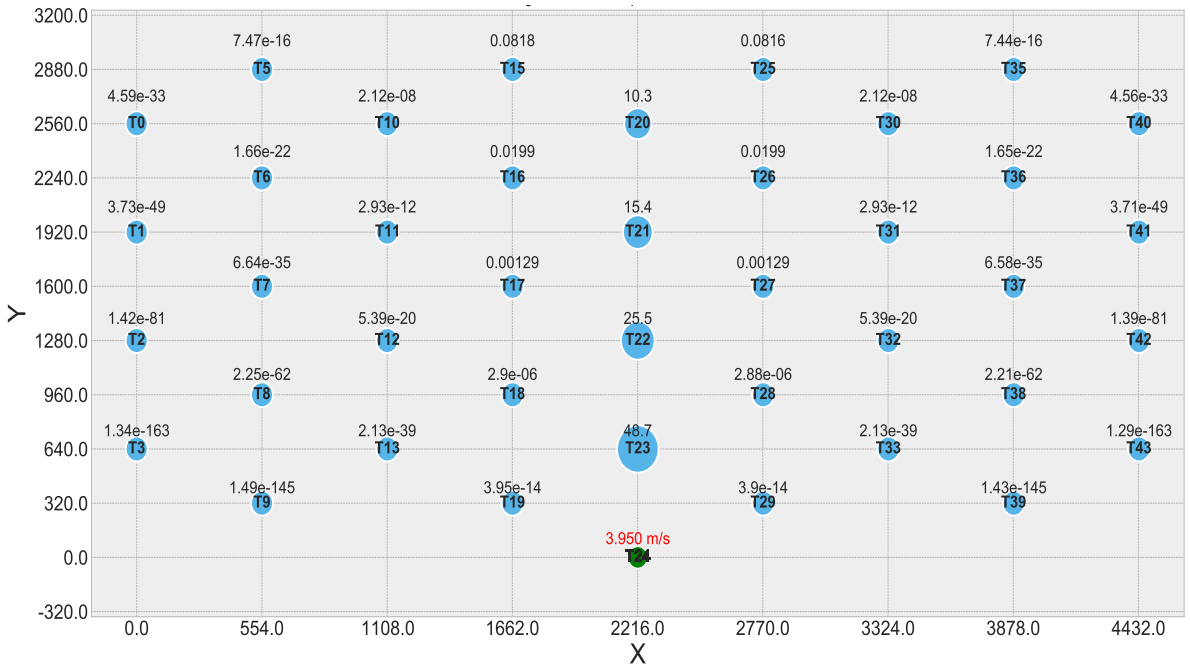

Figure 5.4: Percentage deficits from turbines within a 6Ω upstream sector of $T24$; Bin 0

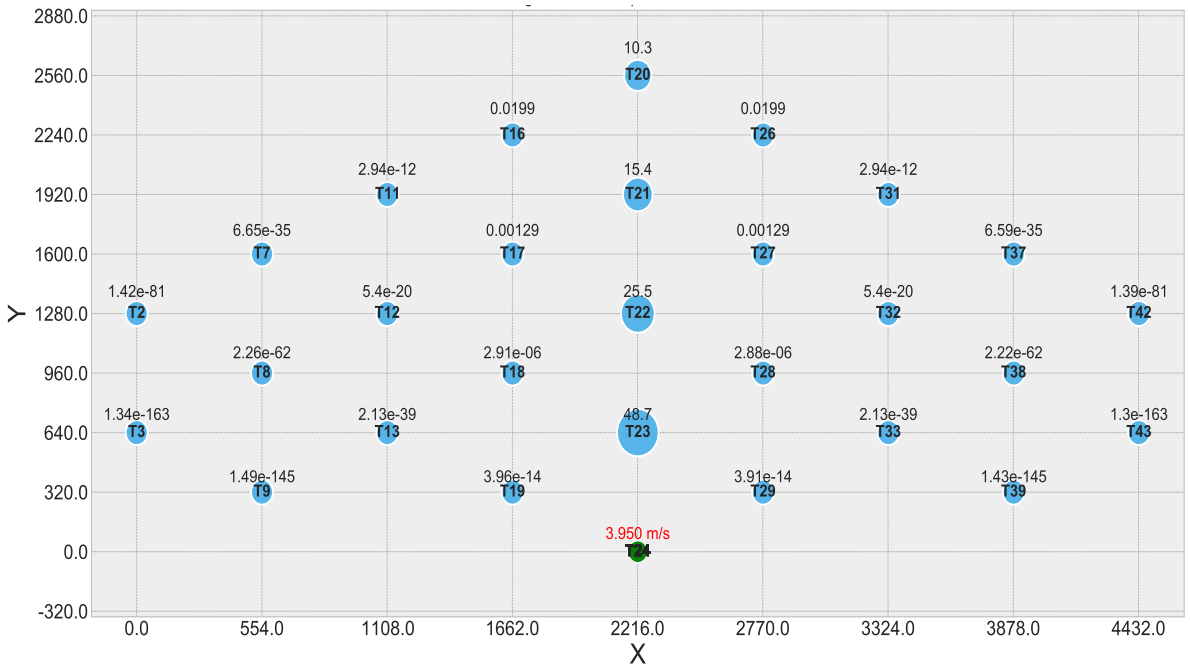

Figure 5.5: Percentage deficits from turbines within a 4Ω upstream sector of $T24$; Bin 0

The last row in Table 5.1 represents the corresponding mean wind values at the selected turbines, for the baseline wake model in [3]. As shown, the baseline model yields the same

Table 5.1: Upstream sector radius and $\bar{U}$ values at selected far downstream turbines for 5 m/s freestream inflow

Capture Radius $\boldsymbol{\Omega}$	U_∞ (m/s)	$\bar{U}_j$ (m/s)			
		Bin 0 $T24$	Bin 1 $T4$	Bin 2 $T3$	Bin 4 $T1$
$\mathbf{2\Omega}$	5	4.010	4.460	4.010	4.010
$\mathbf{3\Omega}$	5	3.970	4.460	3.970	3.970
$\mathbf{4\Omega}$	5	3.950	4.410	3.950	3.950
$\mathbf{5\Omega}$	5	3.950	4.410	3.940	3.940
$\mathbf{6\Omega}$	5	3.950	4.400	3.940	3.940
$\mathbf{7\Omega}$	5	3.950	4.400	3.940	3.940
$\mathbf{8\Omega}$	5	3.950	4.400	3.940	3.940
Baseline model [3]	5	3.950	4.400	3.940	3.940

deficit profile at the considered turbine, as that produced by a $8\boldsymbol{\Omega}$, $7\boldsymbol{\Omega}$, and $6\boldsymbol{\Omega}$ upstream sectors. From the literature it has been demonstrated that due to the narrow shear layer that results from a low wind inflow, the wake from a low wind inflow takes longer distances to recover, hence, a larger deficit at a downstream position compared to the deficit that would be caused by a larger wind inflow. Based on this, this study selected a low freestream inflow of 5 m/s to demonstrate and validate the implemented augmentation to the baseline wake model in [3]. Nonetheless, a comparable illustration is provided in Appendix D.7 in table 1 for a 4 m/s freestream inflow. From these tables, it is obvious that across all bins depicted, there is no difference between the choice of employing the baseline model upstream consideration, and opting to only consider an upstream sector $n\boldsymbol{\Omega}$, where $6 \leq n \leq 8$. Nonetheless, the smaller the choice of n in Equation (5.1), the faster the algorithm will be and the lower the computational cost. Accordingly, the study has opted to apply a $6\boldsymbol{\Omega}$ upstream sector in computing wind speed deficits at turbines.

Table 5.2: Upstream sector radius and mean wind speeds at selected far downstream turbines for 14 m/s freestream inflow

Capture Radius $\boldsymbol{\Omega}$	U_∞ (m/s)	U_j (m/s)			
		Bin 0 $T24$	Bin 1 $T4$	Bin 2 $T3$	Bin 4 $T1$
$\mathbf{2\Omega}$	14	13.290	13.610	13.290	13.290
$\mathbf{3\Omega}$	14	13.260	13.610	13.260	13.260
$\mathbf{4\Omega}$	14	13.250	13.580	13.250	13.250
$\mathbf{5\Omega}$	14	13.250	13.580	13.250	13.250
$\mathbf{6\Omega}$	14	13.250	13.570	13.240	13.240
$\mathbf{7\Omega}$	14	13.250	13.570	13.240	13.240
$\mathbf{8\Omega}$	14	13.250	13.570	13.240	13.240
Baseline model [3]	14	13.250	13.570	13.240	13.240

Given this augmentation, the averaged deficit factor given in Equation (2.30) can be re-written without dependence on yaw offset angle ϕ as:

$$\bar{U}_{def_{j,i}}(\alpha_i;\theta^W) = \begin{cases} \frac{1}{\pi R^2}\int_{\theta'=0}^{\theta'=2\pi}\int_{r'=0}^{r'=R} U_{def_{j,i}}(d_{j,i},r,\alpha_i)r'\,dr'd\theta', & \text{if } d_{j,i}>0 \;\&\; \|l_j-l_i\|_2 \leq 6\boldsymbol{\Omega} \\ 0, & otherwise \quad , \end{cases} \tag{5.2}$$

and the aggregated deficit factor $\bar{U}_{def_j}(\boldsymbol{\alpha};\theta^W)$ for wind turbine j can be generalized as given:

$$\bar{U}_{def_j}(\boldsymbol{\alpha};\theta^W) = \sqrt{\sum_{i=1}^{\mathcal{T}_{6\boldsymbol{\Omega}}}(\bar{U}_{def_{j,i}}(\alpha_i,\phi_i;\theta^W))^2} \quad . \tag{5.3}$$

Here, $\mathcal{T}_{6\boldsymbol{\Omega}}$ represents the set containing all wind turbines in $j's$ upstream that lie within a $6\boldsymbol{\Omega}$ sector, and $\boldsymbol{\alpha}$ is the axial induction factor vector of these upstream turbines.

The mean wind speed and estimated power production at j, remain as expressed in Equations (3.7) and (3.8) respectively, and the total WP power as expressed in 3.9. To promote an improved WP AEP and turbine-level C_T values, in addition to reducing TI levels, the optimization problem can be formulated as:

$$\max_{(U_{b,u,j},P_{b,u,j})} \quad AEP \tag{5.4}$$

where $P_{b,u,j}$ is as expressed in Equation (4.2):

The coupling of the wake, TI and optimisation algorithms models, and the inter-flow between all necessary equations within these models is captured in Algorithm 3.

Algorithm 3: Axial optimisation algorithm for AEP maximisation with Upstream Sector Implementation.

Input: scalar $fixed\_area$, D, ρ, κ, γ, ψ, τ, β, Ω, N_h, pop_size, max_it
vector $\vec{\mathcal{U}}$, $\vec{\mathcal{B}}$, $\vec{\mathcal{N}}$, $\vec{f_b}$
table U_{lookup}
Select minimum T-2-T separation distance
From origin (0,0), evaluate turbine locations $l_i(x_i, y_i)$ based on D, store in $i_{\vec{pos}}$ and deploy over $fixed\_area$
Compute A using D
$\theta^W \leftarrow 0^\circ$ considering Figure 3.6, $BIN_P \leftarrow 0$;
for $b \in \mathcal{B}$ **do**
  Apply coordinate axes rotation by θ^W
  Compute σ_{mean} for b
  $\phi \leftarrow 0^\circ$, $P_b \leftarrow 0$;
  for $u \in \mathcal{U}$ **do**
    $P_u \leftarrow 0$;
    for $it \leftarrow 1$ **to** max_it **do**
      Randomly initialize a population of pop_size each with position vectors (α) of length $\mathcal{N}$ using PSO/GA
      Set constants c1 = 1.8, c2 = 1.5, wMax = 0.9, wMin = 0.2
      Sort $i_{\vec{pos}}$ in descending order based on y-coordinate value and then x-coordinate value, considering bin direction b
      $sorted \leftarrow sorted(i_{\vec{pos}})$
      $P_{it} \leftarrow 0$;
      for $particle \in pop\_size$ **do**
        $\mathcal{T} \leftarrow [\,]$
        for $i \in sorted$ **do**
          if $i = sorted[0] \quad \vee \quad i \in first\_turbs$ **then**
            Extract $C_T(U_\infty)_i$ and $C_T(\alpha_{opt})_i$
            $C_{T_{new}} = max(0, C_T(\alpha_{opt})_i)$
            $C_{T_{new}} = min(C_{T_{new}}, C_T(U_\infty)_i)$
            if $C_{T_{new}} = C_T(U_\infty)_i$ **then**
              $C_P = C_P(U_\infty)_i$
            else
              $C_P = C_P(\alpha_{opt})_i$
            end
            end
            Compute $\sigma_{j,wake}$ from Equation (3.11) and TI_i from Equation (3.12)
            Compute P_i from Equations (3.8)
            $P_{it} \leftarrow P_{it} + P_i$;
            Add i to $\mathcal{T}$
            else
              $sum\_sqr\_def \leftarrow 0$
              for $i \in \mathcal{T}$ **do**
                if $j_y < i_y \quad \wedge \quad \|\vec{ji}\| \leq 6\boldsymbol{\Omega}$ **then**
                  Compute $d_{j,i}$ and $r_{j,i}$ from Equations (2.18) and (3.2), respectively
                  Compute $\bar{U}_{def_j}$ from Equation (3.14)
                  $sum\_sqr\_def \leftarrow sum\_sqr\_def + \bar{U}^2_{def_j}$
                end
              end
              Compute $\bar{U}_j$ from Equation (3.7)
              Compute $\sigma_{j,wake}$ from Equation (3.14), TI_j from Equation (3.15) and P_j from Equations (3.8)
              $P_{it} \leftarrow P_{it} + P_j$;
            end
          end
        end
        Compute fitness function values for population of particles/genes
        Update personal bests for each particle/gene in population
        Update local/global best for entire population of particles/genes
        Update P_{it}
      end
      $P_u \leftarrow P_{it}$;
    end
    $P_b \leftarrow P_b + P_u$;
  end
  $P_b \leftarrow P_b * f_b$;
  $BIN_P \leftarrow BIN_P + P_b$;
end
$AEP = BIN_P * N_h$
Output: AEP

Simulation Results with Classical Examples for Demonstration

Summarised results from simulation of the three studied scenarios ($5D$, $6D$, and $7D$) are presented for AEP, while only $5D$ results are presented for turbine C_T and TI on the same deployment layout and WP dimensions. This enables retention of focus on C_T and TI behaviour in a densely deployed scenario (i.e $5D$). To further narrow the focus of the chapter, variable optimization is achieved using only GA and the simulation parameters on Table 3.6 are maintained, except *pop_size* and *max_it* which have been updated to 20, and 500, respectively. With reference to Table 3.5 and Figure 3.6, this chapter compares the performance of the baseline case ($Base\_6\boldsymbol{\Omega}$) - which represents the *Base* case with a $6\boldsymbol{\Omega}$ upstream sector modification, no optimisation, and no C_T constraints, to those of $GA\_6\boldsymbol{\Omega}$ - which represents a GA-optimised case with application of a $6\boldsymbol{\Omega}$ upstream sector, and GA_CT - which represents a GA-optimised case with C_T constrains as in chapter 4. The reason for subjecting the baseline case to the upstream sector modification is to have an equal platform for comparison with the $GA\_6\boldsymbol{\Omega}$ case, while both are compared with the chapter 4 case (GA_CT). This comparison is made for each T-2-T distance/scenario, and for U_∞ values within the operating range.

For all optimised cases, 500 iterations are executed and results analysed. Multi-core parallel processing was implemented in Python 3.9 using the *multiprocessing* package to execute 500 runs each for all twelve (12) U_∞ values (i.e 3 to 14 m/s) in each bin. This is repeated for the remaining bins, and for all four (4) optimization cases. Hence a total of 500 * 12 (wind speeds) * 12 (bins) * 4 (optimization cases) = 288,000 iterations for each scenario and 864,600 iteration runs for the three studied scenarios.

AEP results are presented in Table 5.3 for all compared cases. Results show that modifying the upstream area of consideration can enhance the optimizer's exploration and exploitation of the search space for better decision variables, and hence greatly improve the WP power and consequently AEP by as much as 34.6% with a $5D$ T-2-T spacing. Notice that there is no noticeable increment to the AEP results of the $Base\_6\boldsymbol{\Omega}$ case (i.e the *Base* case with upstream turbine reconsideration technique) compared to the *Base* case from chapters 3 and 4. This is because the velocity deficits caused by the eliminated upstream

turbines when computing deficits at a downstream turbine, are very insignificant, hence, no significant reduction in total deficit and consequently, no significant increment to the mean velocity at downstream turbines. The result of this is an insignificant improvement in Base case comparisons between the *Base* case (Park and Law model) performance and the *Base*_6$\boldsymbol{\Omega}$ case ("augmented/modified" model) proposed in this subsection.

Results in chapter 3 established that axial induction maximisation causes an increase in TI levels and C_T values at turbines. In chapter 4, although significant improvements in turbines' C_T was achieved, a trade-off was suffered in AEP gains, while TI levels showed no significant changes from chapter 3. However, by modifying the upstream sector in this chapter (with the *GA*_6$\boldsymbol{\Omega}$ case), a very significant improvement has been achieved in AEP as demonstrated in Table 5.3.

In addition, the TI levels in Figure 5.6 also indicate an improvement against the *GA_CT* case as it yields a lower number of TI-defaulting turbines in ten out of the twelve bins, with major improvements occurring in the tightly-spaced even-numbered bins. This represents an 83.3% improvement in terms of bins. In terms of U_∞ value range for each bin over which improvements are recorded by the *GA*_6$\boldsymbol{\Omega}$ as against the *GA_CT* case, the highest percentage of 83.3% is achieved in bin 8, where five of the six U_∞ values show improvements, whereas, the lowest improvement percentage of 50% is obtained in bins 3, 7, 9, and 11 (sparsely-spaced odd-numbered bins). Note that percentages are computed based only on U_∞ values where at least one of the compared cases have TI-defaulting turbines (For e.g., percentages are computed using only U_∞ values 3 m/s - 8 m/s for bin 8, disregarding other values lacking defaulting turbines). Recall from chapter 4 that although the *GA_CT* case entails C_T constraints on the GA-optimised case, its TI results show very negligible differences from the GA-optimised case. So, in terms of TI results, it is reasonable to consider the *GA*_6$\boldsymbol{\Omega}$ case as indicative of the *GA* case, further emphasizing the negative effects of power maximisation on turbine level TIs. Nonetheless, the utilisation of the turbine upstream sector reconsideration technique enhances improvements in turbine-level TI, compared to not only the *GA_CT* case but also the *GA* case analysed in Chapter 4. Recall that the *Base* case always presents the best case scenario in terms of TI. However, this enhanced technique with added optimisation (i.e. the *GA*_6$\boldsymbol{\Omega}$ case) demonstrates competitive TI outcomes compared

to the *Base*_6$\boldsymbol{\Omega}$ case. It surpasses the *Base*_6$\boldsymbol{\Omega}$ case in bins 0, 3, 8, and 11, falls behind in bins 1, 2, 4, and 10, and matches it in bins 5, 6, 7, and 9. It's important to note that superiority in each bin is determined by the number of U_∞ values where either case has fewer defaulting turbines (i.e., turbine positions where TI values exceed the threshold), rather than the total defaulting turbines across all U_∞ values. For instance, the *GA*_6$\boldsymbol{\Omega}$ case is considered to outperform the *Base*_6$\boldsymbol{\Omega}$ case in bin 0 because it has fewer affected turbines at three U_∞ values (6, 7, and 8 m/s), whereas the *Base*_6$\boldsymbol{\Omega}$ case has fewer defaulting turbines at two U_∞ values (4 and 5 m/s). This grants superiority to the *GA*_6$\boldsymbol{\Omega}$ case.

The C_T plot in Figure 5.7 however, highlights a drawback of the "*upstream sector reconsideration*" which shows that implementing the wake model modification without constraining turbines' C_T values, results in increased C_T values above optimum - which is undesired. The *Base* and *Base*_6$\boldsymbol{\Omega}$ cases are excluded from the defaulting turbine comparisons presented in Figure 5.7 because, in both cases, turbines adhere strictly to the rotor-equivalent wind speed, and thus no defaulting occurs. Recall that it is when optimisation is applied to maximise WP power, that turbines begin to default in their C_T value adherence, as demonstrated in chapter 4.

Table 5.3: Summarised AEP table for $5D$, $6D$ and $7D$ scenarios with modified upstream sector

	Base_6Ω	**GA_6Ω**	**GA_CT**
Total AEP(TWh) - 5D	**10.53**	**16.09**	**11.17**
Percentage increase (%)	0	34.6	5.74
Total AEP(TWh) - 6D	**8.029**	**12.20**	**8.415**
Percentage increase (%)	0	34.2	4.60
Total AEP(TWh) - 7D	**6.566**	**10.09**	**6.805**
Percentage increase (%)	0	34.9	3.52

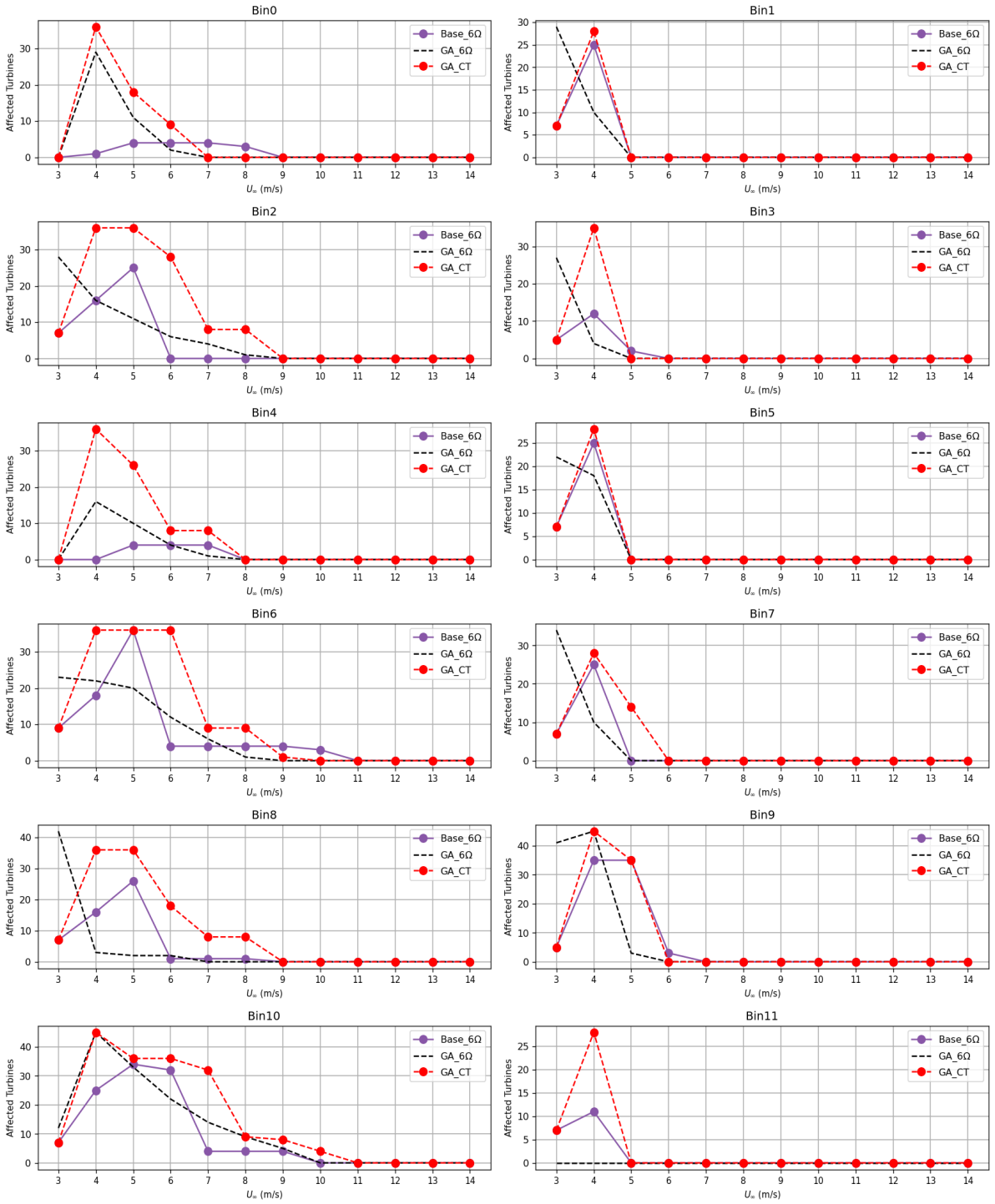

Figure 5.6: Total TI-defaulting turbines comparison for all studied cases, $5D$

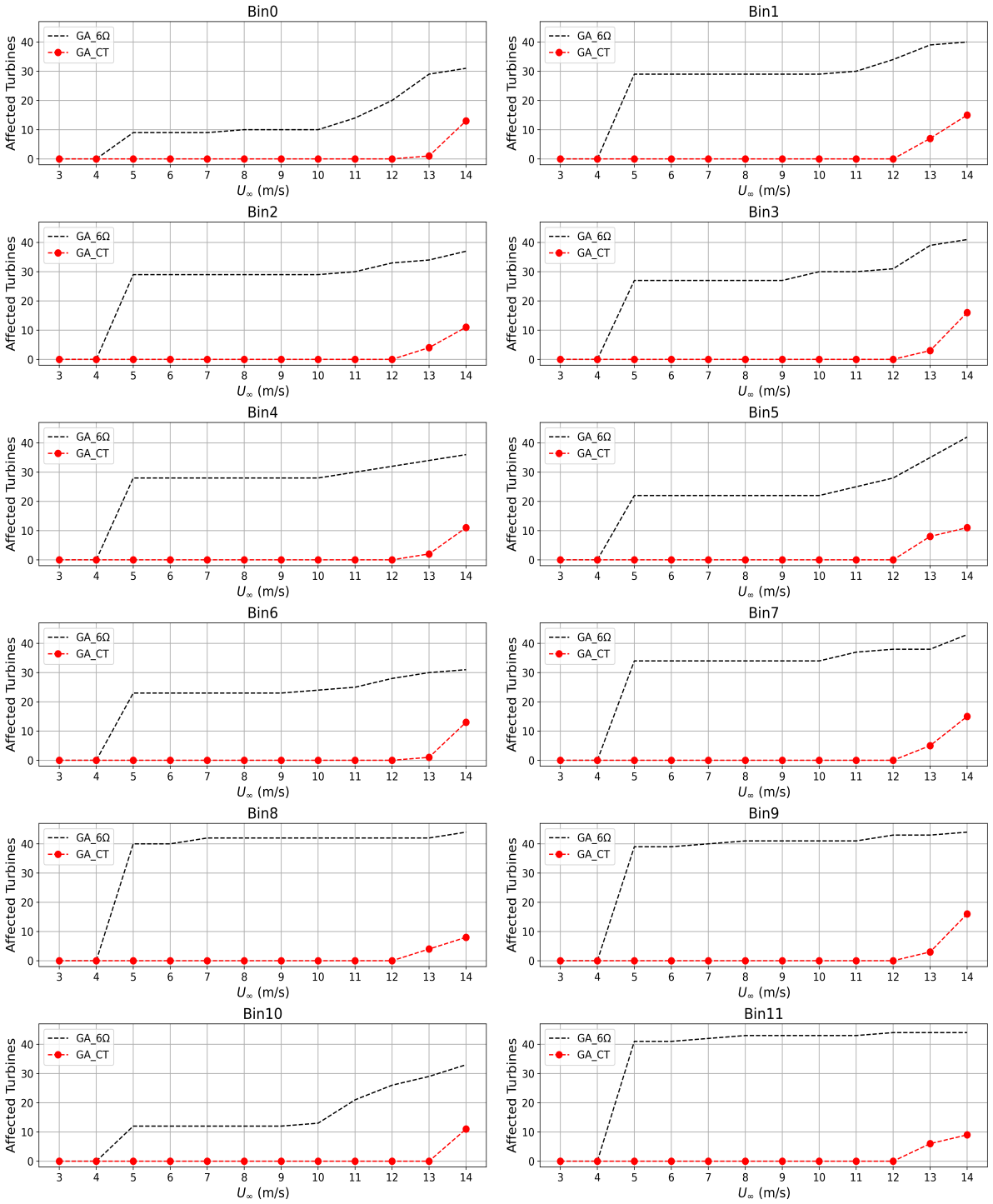

Figure 5.7: Total C_T-defaulting turbines comparison for GA cases: $5D$

5.1.2 Radial Distance(r) - Axial Value(α) Wake Effect Elimination

Recall that the axial induction factor α indicates the degree to which the mean wind speed $\bar{U}$ in front of a turbine rotor is reduced just behind it due to a deceleration at the rotor. A high α value therefore implies a substantial interception of the wind by the turbine, hence, a large reduction just behind the turbine rotor, and vice versa. Consequently, the turbulence generated behind such intercepting or extracting turbine will be high, and hence, harmful to a turbine behind it. Also, considering the bubble plots of Figures 5.3 - 5.5 and those of Figures 64 - 66 in the Appendix D.7 section, it can be observed that upstream turbines beyond the columns directly adjacent to the column of the considered downstream turbine, do not significantly affect the considered downstream turbine, as illustrated by their percentage deficits. That is, with respect to Figures 5.3 - 5.5, only wakes from turbines $T15$ - $T19$ and turbines $T25$ - $T29$ significantly affects turbine $T24$.

Recall too from chapter 4 that application of C_T constraints introduced a trade-off in AEP gains. However, these constraints are necessary based on the drawback demonstrated in subsection 5.1.1 of this chapter. Therefore, to ensure that a significant AEP gain is achieved even with C_T constraints, the study introduces a simple scheme based on the insight gained from the previous paragraph. This scheme ignores the wake effects from upstream turbines that although are located within the implemented $6\mathbf{\Omega}$ upstream radius, lie beyond columns adjacent to the considered downstream turbine and also have α values that are less than half the α value synonymous with the $\bar{U}$ at the rotor of such upstream turbines. Such a low axial induction (α) value denotes a small reduction in the wake wind speed behind the upstream turbine, and hence, a narrow shear layer, and consequently a reduced mixing intensity and turbulence. This "small reduction in the wake wind speed" combined with an upstream turbine's insignificant effect caused by the magnitude of its radial T-2-T distance ($r_{j,i}$) from the considered downstream turbine, implies a further depleted impact on the wake wind speed and consequently on the downstream turbine. To illustrate this, Figures 5.8 and 5.9 are provided, showing bubble plots of the percentage deficits from upstream turbines on a given downstream turbine. In these plots, the α value of upstream turbines positioned beyond the adjacent columns of the downstream turbine is reduced to half its

optimal value for the $\bar{U}$ value at the rotor of such upstream turbines. Meanwhile, optimal α values are maintained for those upstream turbines within the adjacent columns of the considered downstream turbine.

Comparing Figure 5.8 with 5.3 and Figure 5.9 with 64 in the Appendix D.7 section, demonstrate that the deficit caused by an upstream turbine and hence, its percentage deficit contribution to a downstream turbine reduces proportionally to the degree to which its α value is reduced. Hence, a logical reason to ignore an upstream turbine's contribution to the total deficit at a downstream turbine if it's r distance is large and its α value is less than half of what is optimal for the $\bar{U}$ at the rotor of that upstream turbine. It must be noted that the choice of $\alpha \leq 0.5\alpha$ and $r_{j,i}$ beyond the adjacent columns as the cut-off α and $r_{j,i}$ values to ignore an upstream turbine, is not absolute but only applied based on observations from the studied minimum T-2-T distances/scenarios and turbine layout.

Given that the $6\boldsymbol{\Omega}$ upstream sector augmentation applied in subsection 5.1.1 is retained in this subsection, the averaged deficit factor and the aggregated deficit factor as expressed in Equations (5.3) and (5.4), respectively, are also retained. To maintain an improved WP AEP and turbine-level C_T values, in addition to reducing TI levels, the optimization problem can thus be formulated as:

$$\begin{aligned} \max_{(U_{b,u,j}, P_{b,u,j})} \quad & AEP \\ \text{s.t.} \quad & C_{Tj} \leq {C_T}^{\bar{U}_j} \quad . \end{aligned} \tag{5.5}$$

where $P_{b,u,j}$ is as expressed in Equation (4.2) while the constraint prevents each turbine's thrust coefficient, C_{Tj}, from surpassing its local mean wind speed equivalent thrust coefficient value, ${C_T}^{\bar{U}_j}$.

The coupling of the wake, TI and optimisation algorithm models, and the inter-flow between all necessary equations within these models is captured in Algorithm 4.

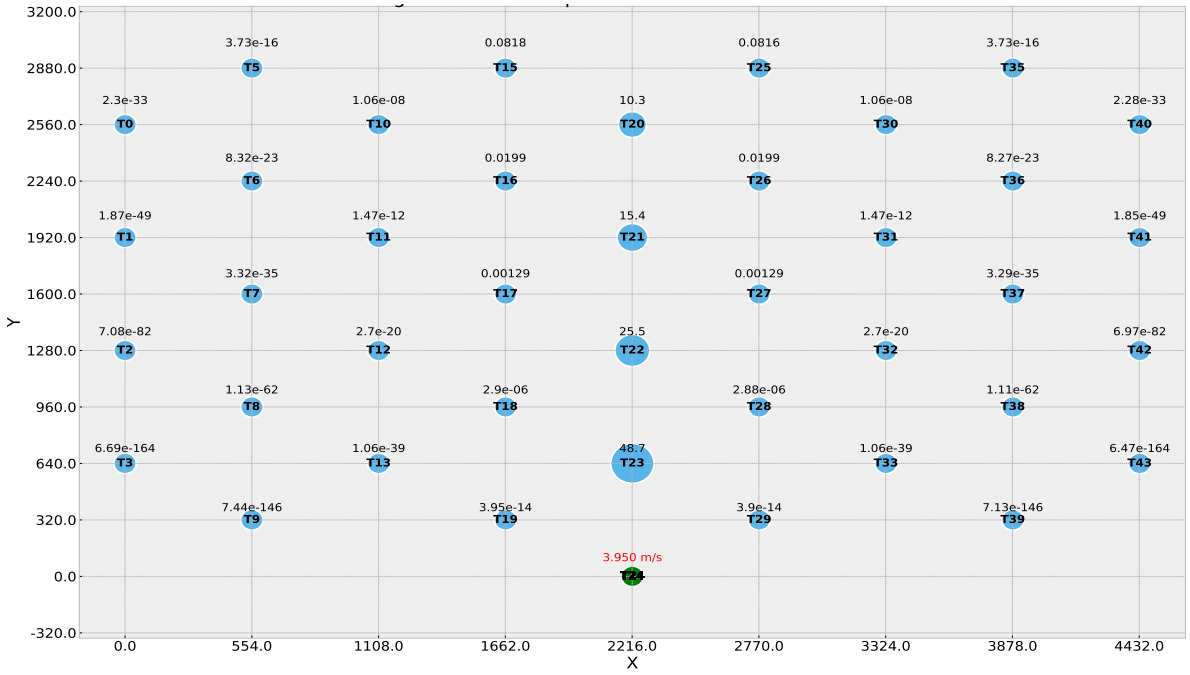

Figure 5.8: Percentage deficits from turbines within 8**Ω** upstream sector of $T24$; Bin 0, $\alpha = 0.5\alpha$ only for turbines beyond the adjacent columns of $T24$

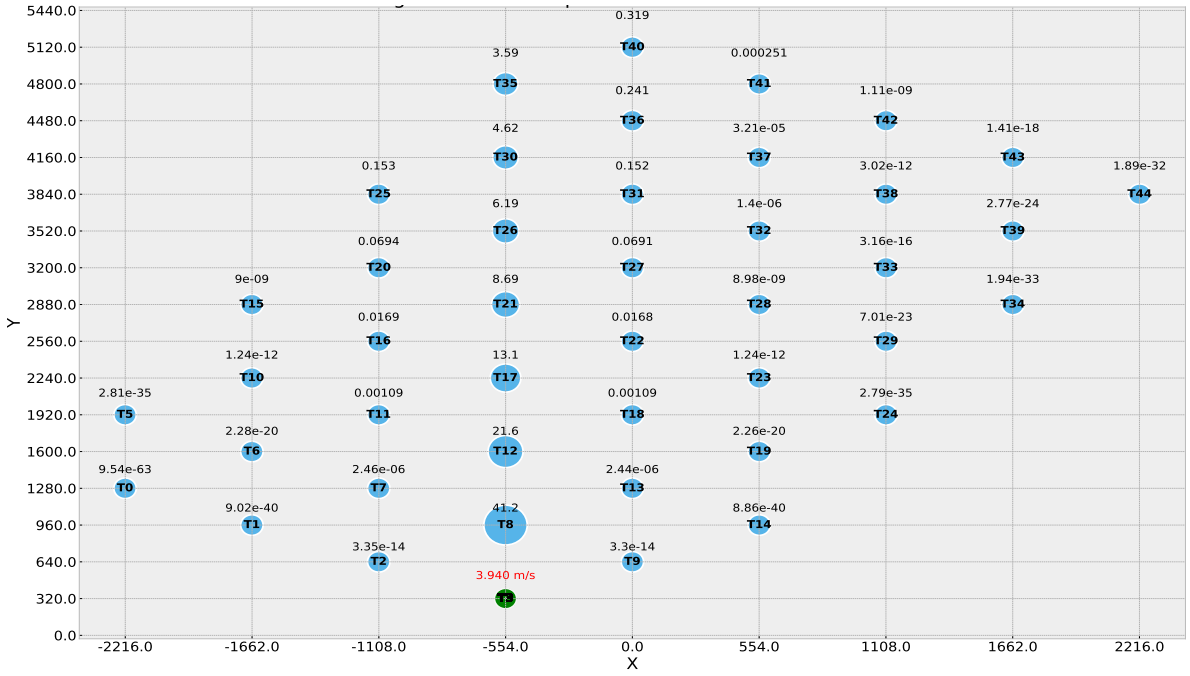

Figure 5.9: Percentage deficits from turbines within 8**Ω** upstream sector of $T3$; Bin 2, $\alpha = 0.5\alpha$ only for turbines beyond the adjacent columns of $T3$

Algorithm 4: Axial optimisation algorithm for C_T controlled AEP maximisation with Upstream Sector Implementation and Wake Effect Elimination.

Input: scalar $fixed\_area$, D, ρ, κ, γ, ψ, τ, β, Ω, N_h, pop_size, max_it
vector $\vec{\mathcal{U}}$, $\vec{\mathcal{B}}$, $\vec{\mathcal{N}}$, $\vec{f_b}$
table U_{lookup}
Select minimum T-2-T separation distance
From origin (0,0), evaluate turbine locations $l_i(x_i, y_i)$ based on D, store in $i\vec{_{pos}}$ and deploy over $fixed\_area$
Compute A using D
$\theta^W \leftarrow 0^\circ$ considering Figure 3.6, $BIN_P \leftarrow 0$;
for $b \in \mathcal{B}$ **do**
  Apply coordinate axes rotation by θ^W and Compute σ_{mean} for b
  $\phi \leftarrow 0^\circ$, $P_b \leftarrow 0$;
  for $u \in \mathcal{U}$ **do**
    $P_u \leftarrow 0$;
    for $it \leftarrow 1$ **to** max_it **do**
      Randomly initialize a population of pop_size each with position vectors (α) of length $\mathcal{N}$ using PSO/GA
      Set constants c1 = 1.8, c2 = 1.5, wMax = 0.9, wMin = 0.2
      Sort $i\vec{_{pos}}$ in descending order based on y-coordinate value and then x-coordinate value, considering bin direction b
      $sorted \leftarrow sorted(i\vec{_{pos}})$
      $P_{it} \leftarrow 0$;
      for $particle \in pop\_size$ **do**
        $\mathcal{T} \leftarrow [\,]$
        for $i \in sorted$ **do**
          if $i = sorted[0] \quad \vee \quad i \in first\_turbs$ **then**
            Extract $C_T(U_\infty)_i$ and $C_T(\alpha_{opt})_i$
            $C_{T_{new}} = max(0, C_T(\alpha_{opt})_i)$
            $C_{T_{new}} = min(C_{T_{new}}, C_T(U_\infty)_i)$
            if $C_{T_{new}} = C_T(U_\infty)_i$ **then**
              $C_P = C_P(U_\infty)_i$
              else
                $C_P = C_P(\alpha_{opt})_i$
              end
            end
            Compute $\sigma_{j,wake}$ from Equation (3.11) and TI_i from Equation (3.12)
            Compute P_i from Equations (3.8)
            $P_{it} \leftarrow P_{it} + P_i$;
            Add i to $\mathcal{T}$
            else
              $sum\_sqr\_def \leftarrow 0$
              for $i \in \mathcal{T}$ **do**
                if $j_y < i_y \quad \wedge \quad \|\vec{ji}\| \leq 6\boldsymbol{\Omega} \quad \wedge \quad \alpha_i > 0.5\alpha(U_i) \quad \wedge \quad r_{j,i} \leq r_{cut-off}$ **then**
                  Compute $d_{j,i}$ and $r_{j,i}$ from Equations (2.18) and (3.2), respectively
                  Compute $\bar{U}_{def_j}$ from Equation (3.14)
                  $sum\_sqr\_def \leftarrow sum\_sqr\_def + \bar{U}^2_{def_j}$
                end
              end
              Compute $\bar{U}_j$ from Equation (3.7)
              Extract $C_T(\bar{U}_j)$ and $C_T(\alpha_{opt})_j$
              $C_{T_{new}} = max(0, C_T(\alpha_{opt})_j)$
              $C_{T_{new}} = min(C_{T_{new}}, C_T(\bar{U}_j))$
              if $C_{T_{new}} = C_T(\bar{U}_j)$ **then**
                $C_P = C_P(\bar{U}_j)$
                else
                  $C_P = C_P(\alpha_{opt})_j$
                end
              end
              Compute $\sigma_{j,wake}$ from Equation (3.14), TI_j from Equation (3.15) and P_j from Equations (3.8)
              $P_{it} \leftarrow P_{it} + P_j$;
            end
          end
        end
        Compute fitness function values for population of particles/genes
        Update personal bests for each particle/gene in population
        Update local/global best for entire population of particles/genes
        Update P_{it}
      end
      $P_u \leftarrow P_{it}$;
    end
    $P_b \leftarrow P_b + P_u$;
  end
  $P_b \leftarrow P_b * f_b$;
  $BIN_P \leftarrow BIN_P + P_b$;
end
$AEP = BIN_P * N_h$
Output: AEP

The AEP, C_T, thrust, and TI results in Table 5.4 and Figures 5.10, 5.11 and 5.12, respectively, show a significant improvement for the $5D$ scenario, which is enhanced by the application of the "r-α" modification to the wake model.

Simulation Results with Classical Examples for Demonstration

For this methodology also, summarised results from simulation of the three studied scenarios ($5D$, $6D$, and $7D$) are presented for AEP, while only $5D$ results are presented for turbine thrust coefficient, thrust and TI, using the same deployment layout and wind plant dimensions. Again, variable optimisation is achieved using only GA and the simulation parameters on Table 3.6 are maintained, except in this case two max_it values (300 and 500) are studied to investigate any possible effect it may have on the optimisation. With reference to Table 3.5 and Figure 3.6, the study in a bid to provide a platform for comparison, also subjects the baseline case to the same number of upstream sectors ($6\boldsymbol{\Omega}$) as considered in section 5.1.1. It then compares its ($Base\_6\boldsymbol{\Omega}$) performance with the $GA\_CT\_6\boldsymbol{\Omega}\_r\alpha\_3$ and $GA\_CT\_6\boldsymbol{\Omega}\_r\alpha\_5$ cases which are similar to the $GA\_6\boldsymbol{\Omega}$ case, but with a further application of the "r-α upstream wake effect elimination" technique in addition to C_T constraints and with 300 and 500 executed iterations, respectively. To further highlight the gains of the additional "r-α upstream wake effect elimination" technique introduced in section 5.1.2 as well as the uniqueness of each studied case, these three cases are then compared with the $GA\_6\boldsymbol{\Omega}$ case of subsection 5.1.1 and the GA_CT case of chapter 4. This comparison is made for each T-2-T distance, and for U_∞ values within the operating range.

Incorporating the "r-α *upstream wake effect elimination*" technique further enhances the optimiser search and consequently, yields greater enhancements to WP AEP as demonstrated in AEP analysis table - Table 5.4. Interestingly, superior AEP gains with the incorporation of the elimination method are obtained with fewer iterations.

Table 5.4: Summarised AEP table for $5D$, $6D$ and $7D$ scenarios with modified upstream sector and r-α upstream wake effect elimination

	Base_6Ω	**GA_6Ω**	**GA_CT**	**GA_CT_6Ω_rα_3**	**GA_CT_6Ω_rα_5**
Total AEP(TWh) - 5D	**10.53**	**16.09**	**11.17**	**14.05**	**13.85**
Increase (%)	0	34.6	5.74	25.1	23.9
Total AEP(TWh) - 6D	**8.029**	**12.20**	**8.415**	**10.30**	**10.05**
Increase (%)	0	34.2	4.60	22.1	20.1
Total AEP(TWh) - 7D	**6.566**	**10.09**	**6.805**	**8.184**	**7.906**
Increase (%)	0	34.9	3.52	19.60	17.32

Observing Table 5.4, it can be seen that although there is a slight AEP trade-off for the $GA\_CT\_6\mathbf{\Omega}\_r\alpha\_3$ and $GA\_CT\_6\mathbf{\Omega}\_r\alpha\_5$ cases in comparison to the highest yielding AEP case ($GA\_6\mathbf{\Omega}$), it is not as severe as that suffered by the GA_CT case. A combination of the $6\mathbf{\Omega}$ "*modified upstream sector*' and "*r-α upstream wake effect elimination*" techniques yield significant AEP gains of 25.1% and 23.9%, respectively, compared to GA_CT's 5.74%.

For C_T analysis, the plots in Figures 5.10 for a $5D$ scenario show that a combination of both techniques enhance a better control of turbines' C_T values. An improvement percentage of approximately 70% is recorded in terms of U_∞ value range for each bin over which improvements are recorded by both the $GA\_CT\_6\mathbf{\Omega}\_r\alpha\_3$ and $GA\_CT\_6\mathbf{\Omega}\_r\alpha\_5$ cases against the $GA\_6\mathbf{\Omega}$ case. The GA_CT case though, maintains the highest percentage improvement of 80% against the $GA\_6\mathbf{\Omega}$ case. Note that percentages are computed using U_∞ values with at least one defaulting turbine in any of the compared cases (i.e. 5 - 12 m/s, considering Figure 5.10). Unlike in the AEP analysis, the C_T analysis produces better results with more iterations. A thrust analysis for a $5D$ scenario is also shown in Figure 5.11 and presents a similar trend to the C_T analysis plots in Figure 5.10.

In terms of TI levels, a further incorporation of the "*r-α upstream wake effect elimination*" technique to the modified $6\mathbf{\Omega}$ upstream sector, yields TI-levels that clearly outperform the GA_CT case as did the $GA\_6\mathbf{\Omega}$ case in the previous section. This is highlighted in Figures 5.12 and 5.13 for $5D$ and $6D$ scenarios. With respect to bins, the incorporated techniques yield a lower number of TI-defaulting turbines in eight out of the twelve bins compared to the GA_CT case, with major improvements again occurring in the tightly-spaced even-numbered bins. In these eight bins, they record a lower number of TI-defaulting turbines

for more U_∞ values compared to the GA_CT case. This TI improvements can be attributed to the further increase in $\bar{U}$ values at turbine positions. The incorporated techniques also enable the $GA\_CT\_6\boldsymbol{\Omega}\_r\alpha\_3$ and $GA\_CT\_6\boldsymbol{\Omega}\_r\alpha\_5$ cases to surpass the best performing TI case ($Base\_6\boldsymbol{\Omega}$ case) in bin 11, match it in bins 1, 5, 7, 8, and 9, while falling behind in bins 0, 2, 3, 4, 6, and 10 in terms of U_∞ values where it has fewer defaulting turbines compared to the $Base\_6\boldsymbol{\Omega}$ case. These can see ranked as TI improvements in comparison to the GA_CT case but as trade-offs in comparison to the $GA\_6\boldsymbol{\Omega}$ case. Nonetheless, this trade-off in TI results is compensated for in AEP, as well as in turbine C_T and trust enhancements.

Table 5.5 introduces an additional case where non-optimised/Base case operations are assumed in sparsely-spaced (odd-numbered) bins, as presented by the $GA2$ case for all studied scenarios. These bins/directions offer T-2-T distances that are as large as the traditional $7D$ deployment and even larger, as demonstrated on Table 3.5. For want of space on Table 5.5, the term GA is used to represent the $GA\_CT\_6\boldsymbol{\Omega}\_r\alpha\_3$ AEP results. As demonstrated by all scenarios ($5D$, $6D$, and $7D$), even if optimisation is shelved for sparsely-spaced bins, the combined technique applied to tightly-spaced bins only, will still yield a superior AEP (12.63 TWh, 9.407 TWh, and 7.544 TWh, respectively) compared to the traditional $7D$ $Base\_6\boldsymbol{\Omega}$ case operation (6.566 TWh). This approach will also offer advantages in terms of C_T adherence as there will be a 100% adherence in these directions of Base case operations (sparsely-spaced odd-numbered bins). This is because Base case operations involve turbines adopting rotor mean wind speed equivalent C_T values per instance of time. Recall too, it was established in Chapter 3, that it is the application of parameter optimisation (axial induction, in this case) that caused the increased thrusts. In terms of TI, no distinct improvements nor deterioration is observed as both the Base case and $GA\_CT\_6\boldsymbol{\Omega}\_r\alpha\_3$ and $GA\_CT\_6\boldsymbol{\Omega}\_r\alpha\_5$ cases slightly outperform each other in equal number of these odd-numbered bins.

Table 5.6 is further developed to demonstrate the superiority of all optimised (GA) and part-optimised ($GA2$) cases over the traditional $7D$ non-optimised/Base case.

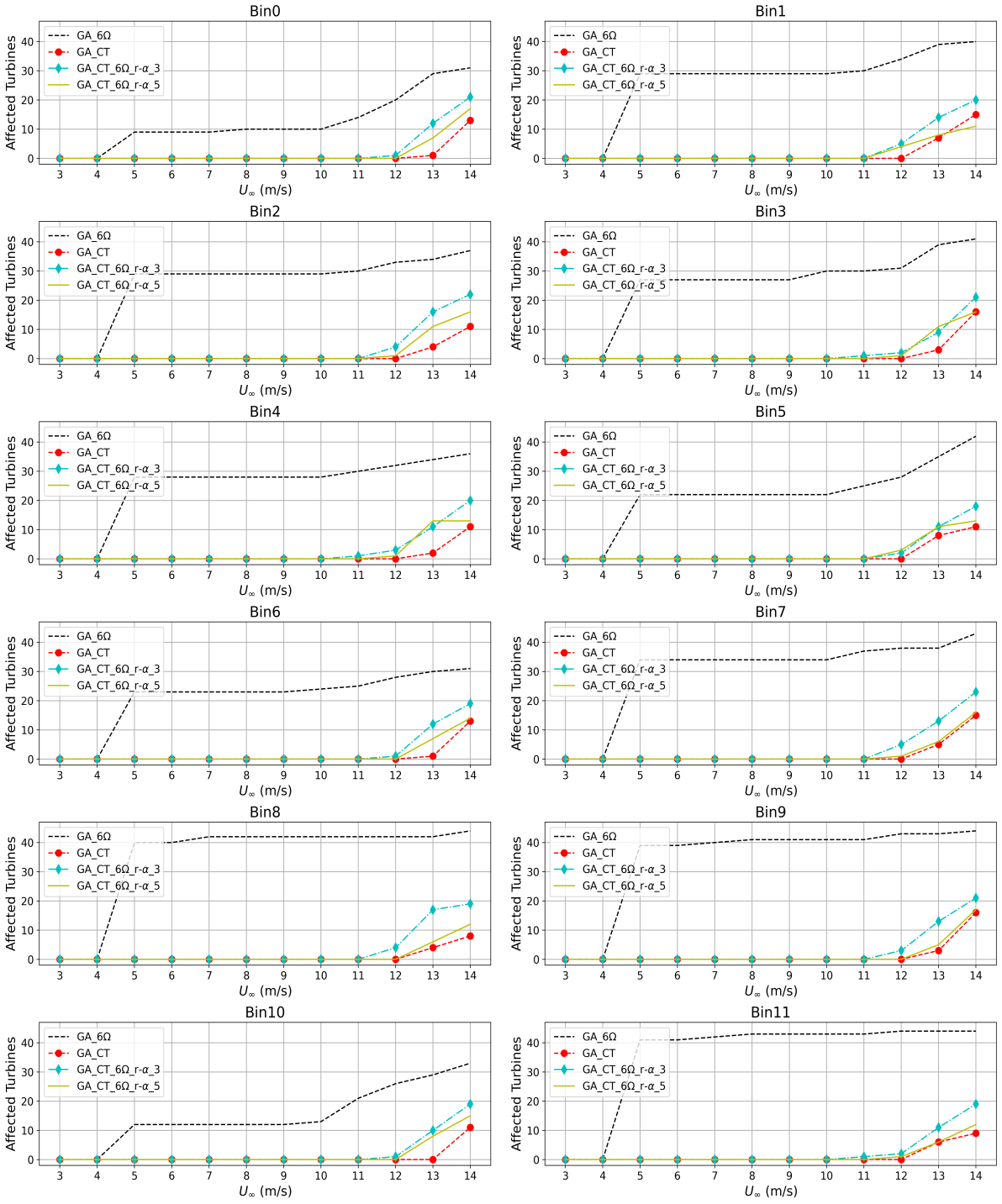

Figure 5.10: Total C_T-defaulting turbines comparison for all cases, with $6\boldsymbol{\Omega}$ upstream sector and r-α upstream wake effect elimination: GA, $5D$

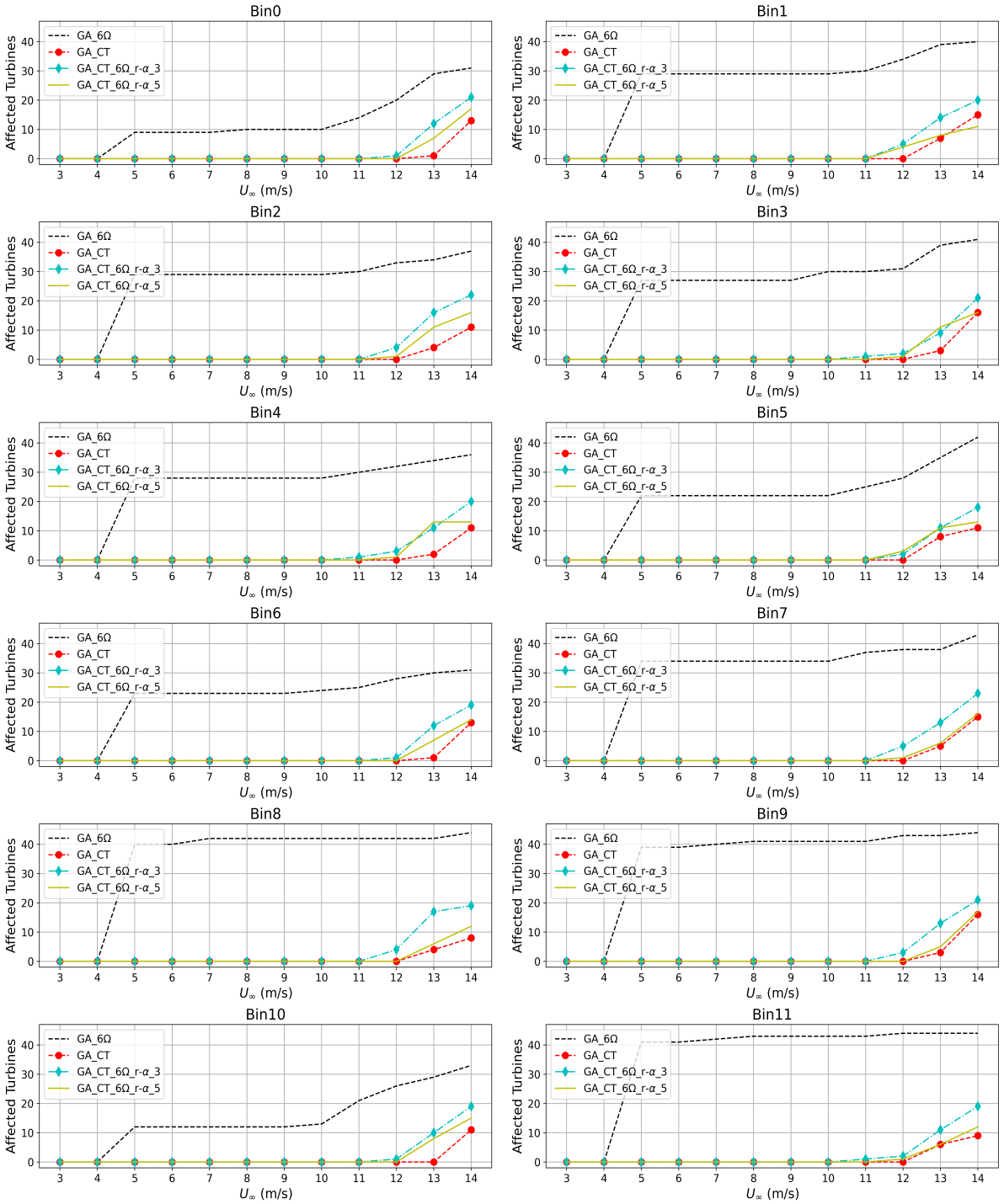

Figure 5.11: Total Thrust-defaulting turbines comparison for all cases, with 6**Ω** upstream sector and r-α upstream wake effect elimination: GA, $5D$

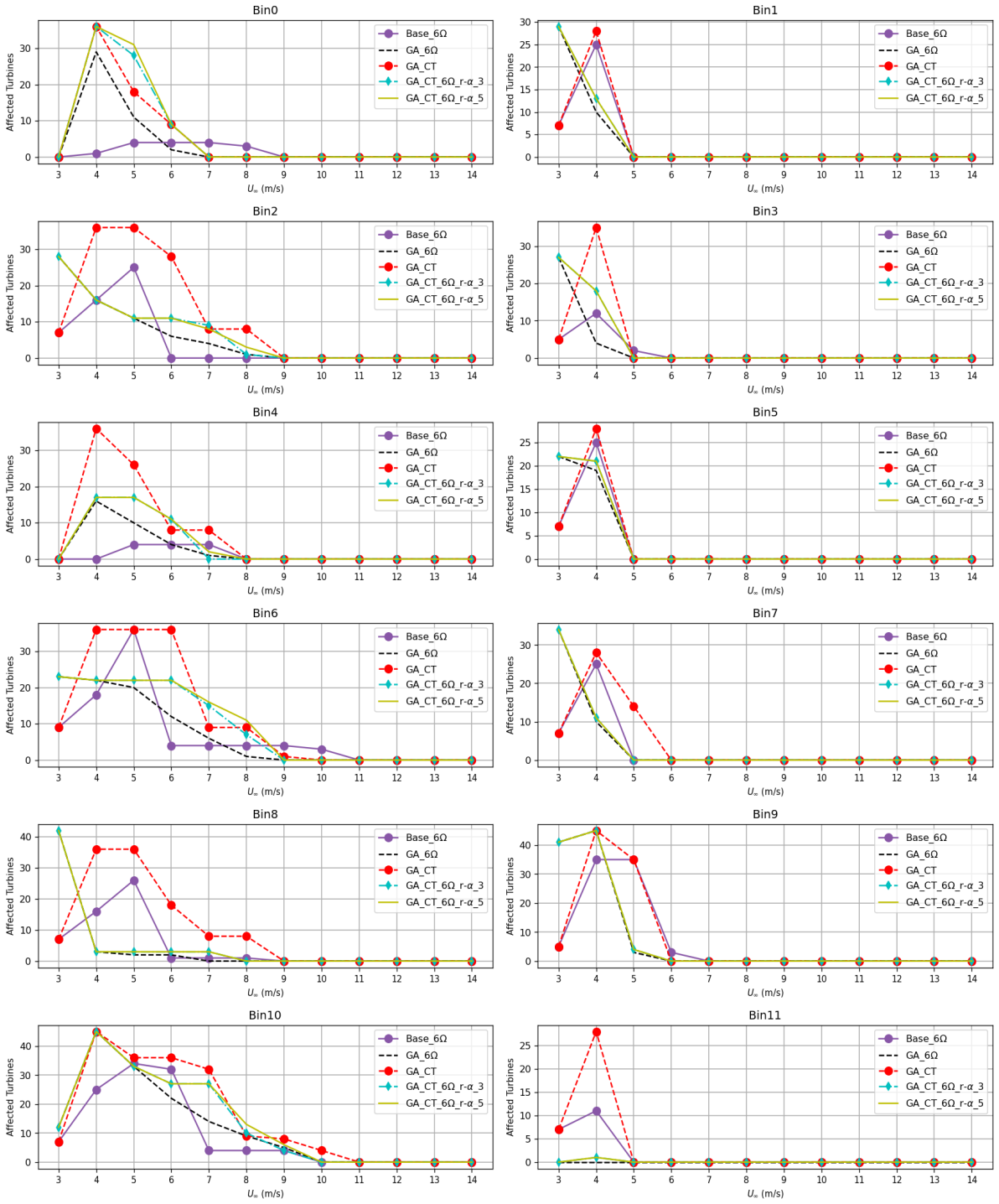

Figure 5.12: Total TI-defaulting turbines comparison for all cases, with 6**Ω** upstream sector and r-α upstream wake effect elimination: GA, $5D$

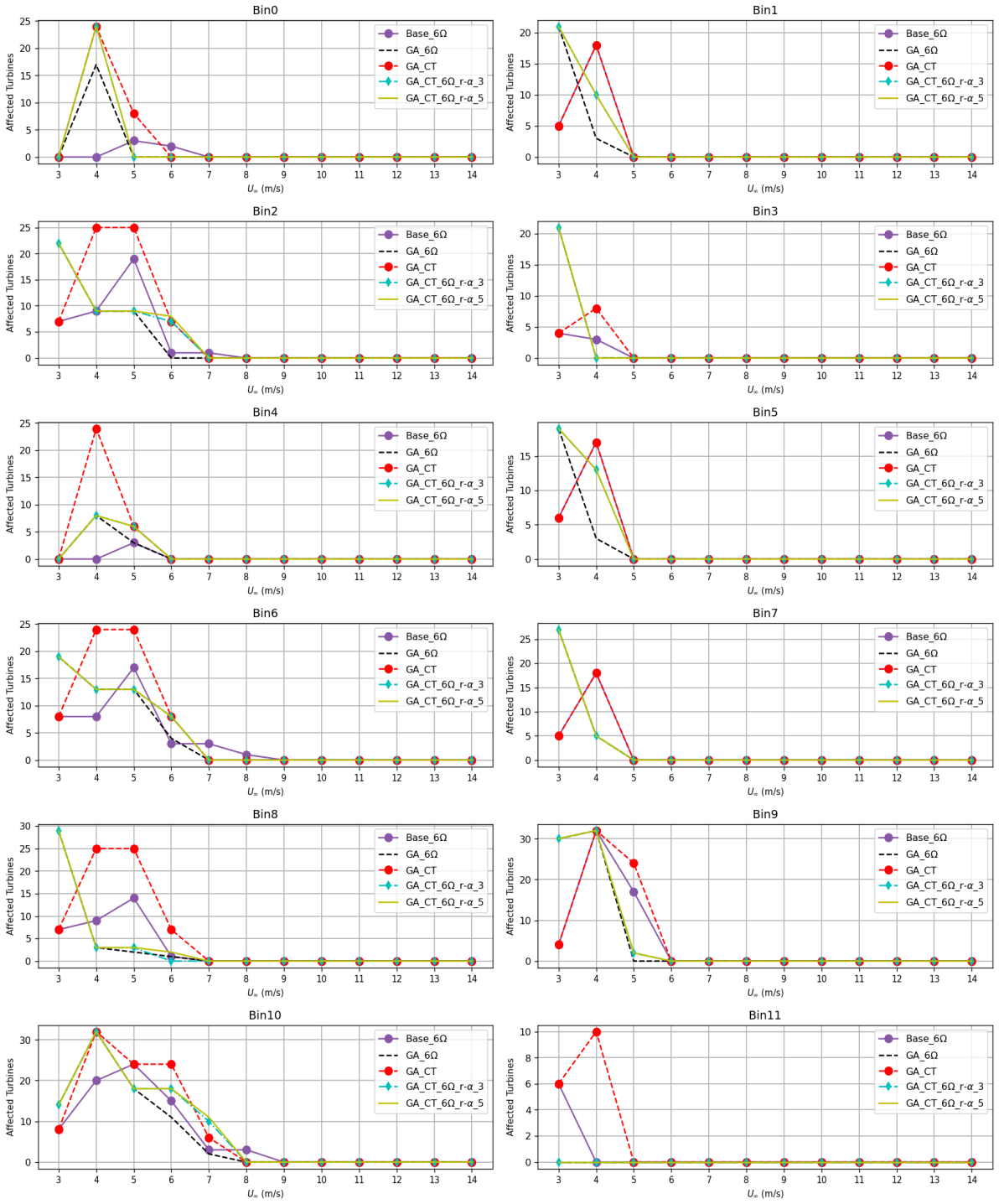

Figure 5.13: Total TI-defaulting turbines comparison for all cases, with 6**Ω** upstream sector and r-α upstream wake effect elimination: GA, $6D$

Table 5.5: AEP for all considered scenarios (**GA** $\equiv$ **GA_CT_6Ω**_$r\alpha$_3)

Bins	**5D**			**6D**			**7D**		
	Base_6**Ω**	GA	GA2	Base_6**Ω**	GA	GA2	Base_6**Ω**	GA	GA2
bin 0	0.903	1.144	1.144	0.706	0.853	0.853	0.579	0.699	0.699
bin 1	0.708	0.856	0.708	0.527	0.527	0.527	0.426	0.490	0.426
bin 2	0.989	1.500	1.500	0.764	1.081	1.081	0.641	0.890	0.890
bin 3	1.081	1.384	1.081	0.809	0.809	0.809	0.657	0.806	0.657
bin 4	0.651	0.972	0.972	0.511	0.723	0.723	0.422	0.555	0.555
bin 5	0.912	1.065	0.912	0.684	0.684	0.684	0.549	0.637	0.549
bin 6	0.923	1.288	1.288	0.722	0.980	0.980	0.593	0.765	0.765
bin 7	0.979	1.210	0.979	0.729	0.729	0.729	0.589	0.691	0.589
bin 8	0.584	0.956	0.956	0.451	0.681	0.681	0.379	0.533	0.533
bin 9	0.844	1.143	0.844	0.632	0.632	0.632	0.513	0.635	0.513
bin 10	0.865	1.158	1.158	0.679	0.892	0.892	0.561	0.714	0.714
bin 11	1.089	1.373	1.089	0.816	0.816	0.816	0.655	0.769	0.655
Total AEP (TWh)	**10.53**	**14.05**	**12.63**	**8.029**	**10.30**	**9.407**	**6.566**	**8.184**	**7.544**
Increase (%)	0	25.1	16.63	0	22.1	14.65	0	19.60	12.96

Table 5.6: AEP table in comparison with the traditional $7D$ scenario

Bins	**5D**			**6D**			**7D**		
	Base_6**Ω**	GA	GA2	Base_6**Ω**	GA	GA2	Base_6**Ω**	GA	GA2
Total AEP (TWh)	**10.53**	**14.05**	**12.63**	**8.029**	**10.30**	**9.407**	**6.566**	**8.184**	**7.544**
Increase (%) *w.r.t* **Base_6Ω**	0	25.1	16.63	0	22.1	14.65	0	19.60	12.96
Increase (%) *w.r.t* **7**D **Base_6Ω**	37.64	53.27	48.01	18.22	36.25	30.20	0	19.60	12.96

5.1.3 Big O Notation Analysis

If we consider that ignoring six of the twelve bins can still yield AEP gains of up to 16.63% for $5D$, then with reference to algorithm 4, the number of times that the inner loop of wind speeds $\mathcal{U}$ will be executed will be reduced by half, since the outer loop of bins $\mathcal{U}$ will have been reduced by half. Considering algorithm 4, the model execution in optimised layout studies such as seen in [3, 8, 51] where due to the optimisation of turbine positions, no determinate T-2-T distances are guaranteed in any directions, thus enforcing set point computations and updates in all directions, will have a Big O notation of;

$$0(n * \mathcal{B}) \quad , \tag{5.6}$$

where $n \equiv \mathcal{U}$ is the number of operational wind speeds considered in the study (i.e U_{in} to U_R), and $\mathcal{B}$ is the number of bins the WP is split into. Whereas, the adopted hexagonal layout alone can afford a reduction in computational complexity, with a Big O notation of;

$$0(n * \frac{\mathcal{B}}{2}) \quad , \tag{5.7}$$

In terms of improving the computational complexity of the employed wake model in [3], the incorporation of the "*r-α upstream wake effect elimination*" and the $6\mathbf{\Omega}$ "*modified upstream sector*" augmentations is able to reduce the complexity in the 5th for-loop (loop of $sortedturbines, i$, in the WP). Considering that the 3rd and 4th for-loops do not change, for comparison sake, the Big O notation of the employed wake model, from the 5th for-loop will be;

$$0(m * sorted) \quad , \tag{5.8}$$

where $m \equiv \mathcal{T}$ is the number of all turbines in the upstream of considered turbine j, and *sorted* is the sorted set of all turbines in the WP. For the employed wake model, $\mathcal{T}$ contains all turbines in the upstream of each considered turbine, whereas, for the augmented model $\mathcal{T}$ contains turbines in the upstream of each considered turbine that satisfy both the "*r-α upstream wake effect elimination*" and the $6\mathbf{\Omega}$ "*modified upstream sector*" conditions. The *else* statement within this 5th for-loop of our augmented wake model computes deficits caused by upstream turbines that satisfy these conditions. Hence, the Big O notation of the augmented wake model can be obtained as;

$$0(\mathcal{M} * sorted) \quad , \tag{5.9}$$

where $\mathcal{M}$ is the number of all turbines in the upstream of considered turbine j, that satisfy the "*r-α upstream wake effect elimination*" and $6\mathbf{\Omega}$ "*modified upstream sector*" criteria, and $\mathcal{M} \leq m$. So, depending on the algorithm's choice of decision variable values at each iteration, the computational complexity can be significantly reduced.

5.2 Summary and Recommendations

In this chapter, two layout-dependent techniques were investigated in tandem to mitigate turbine-level turbulence intensities while preserving the thrust coefficients and power enhancements achieved in earlier chapters. Four optimization cases were evaluated to determine which would offer a comprehensive advantage considering Annual Energy Production (AEP), turbines' thrust coefficient (C_T) values, and turbulence intensity (TI) levels, as these parameters are crucial for wind plant efficiency, extreme loads, and fatigue loads of wind turbines.

The combined technique consisted of two steps. Firstly, it involved restricting the upstream area to within a radius of $6\mathbf{\Omega}$, where the wake effect of an upstream turbine is deemed impactful to any downstream turbine (referred to as the "modified upstream sector" technique). Subsequently, it involved eliminating the effects of turbines based on their radial distance (r) and axial induction (α) values (known as the "r-α upstream wake effect elimination" technique). This refinement in the optimization process helped to relax the constraints of optimization, by reducing the number of upstream turbines that the optimizer had to consider when solving for the deficit at a downstream turbine. The result of this is the creation of a larger feasible region, thereby increasing the chances of finding better solutions and enhancing a faster convergence, and resulting in substantial improvements in AEP by 25.1% and 23.9%, respectively, as evidenced by the $GA\_CT\_6\mathbf{\Omega}\_r\alpha\_3$ and $GA\_CT\_6\mathbf{\Omega}\_r\alpha\_5$ cases compared to the $5D$ Base_$6\mathbf{\Omega}$ case. Furthermore, this integrated approach led to an enhancement in turbulence intensity (TI) levels for both cases, as fewer turbines exceeded the predefined TI threshold of 20% in comparison with the GA_CT case. Regarding C_T value compliance, the combined technique demonstrated competitive performance compared to the GA_CT case. Notably, it showcased superior performance compared to solely applying the "modified upstream sector" technique, as represented by the $GA\_6\mathbf{\Omega}$ case. Increasing the number of iterations with the $GA\_CT\_6\mathbf{\Omega}\_r\alpha\_5$ case resulted in further enhancement of thrust coefficient (C_T) value adherence compared to the $GA\_CT\_6\mathbf{\Omega}\_r\alpha\_3$ case. However, this improvement was accompanied by a slight reduction in the achieved Annual Energy Production (AEP).

In summary, if the primary objective is to enhance Annual Energy Production (AEP), the $GA\_6\mathbf{\Omega}$ case would be recommended. However, for a comprehensive improvement in wind plant efficiency, reduction in turbulence intensity (TI) levels, and optimization of turbine thrusts—parameters directly impacting turbine extreme and fatigue load performance—the $GA\_CT\_6\mathbf{\Omega}\_r\alpha$ cases are preferable. Additionally, facilitated by the regular hexagonal layout employed, the computational complexity of the system can be significantly reduced by shelving optimizations for sparsely-spaced bins. Even with this shelved optimization strategy, the combined techniques applied to a $5D$ turbine-to-turbine spacing can still achieve an AEP increase of up to 48.01% against the conventional $7D$ non-optimised Base case.

Chapter 6

Testing and Performance Metrics

The effects of axial induction-based WP power maximisation on turbines' thrust coefficient (C_T) values and turbulence intensities (TI) have been explored in chapter 3. In chapter 4, it was studied how constraining the resulting C_T values while maximising WP power and AEP, can affect the overall AEP obtained as well as the TI levels. Chapter 5 further explored a novel methodology aimed at increasing the mean wind speeds ($\bar{U}$) at turbines in order to reduce TI levels, while concurrently ensuring that an attractive WP AEP and optimal C_T values at turbines are maintained. In this chapter, the efficiency of the most attractive all-round methodology from the previous chapter is computed and then further tested with an offshore site wind data to confirm if the same trend of results is maintained.

6.1 Efficiency

The efficiency, η, of a WP is defined in [6] as the ratio of the total actual power extracted from the wind plant considering wake effects, to the total power that could be extracted by the wind plant if wake effects are ignored.

$$Efficiency = \frac{P_{actual}}{P_{ideal}} \quad . \tag{6.1}$$

For this study, the total actual extracted WP power (P_{actual}) as expressed in Equation (6.2), takes into consideration wake interactions, and further considers parameter optimisation, parameter constraints, and the frequency of occurrence of each bin.

$$P_{actual} = \sum_{b=1}^{\mathcal{B}} \sum_{u=1}^{\mathcal{U}} \sum_{j=1}^{\mathcal{N}} P_{b,u,j} * f_b \quad , \tag{6.2}$$

where $P_{b,u,j}$ is defined as in Equation (3.18), and the total ideal power that would be extracted by the WP comprising $\mathcal{N}$ turbines, assuming that each turbine existed on its own without wake interactions from other turbines in the WP, is computed as given;

$$P_{ideal} = \sum_{b=1}^{\mathcal{B}} \sum_{u=1}^{\mathcal{U}} \sum_{j=1}^{\mathcal{N}} P(U_\infty) * f_b \quad , \tag{6.3}$$

where f_b is the frequency of occurrence of each bin and $P(U_\infty)$ is defined as;

$$P(U_\infty) = \frac{1}{2}\rho A {U_\infty}^3 C_P \quad . \tag{6.4}$$

Dividing through each AEP value in Table 5.4 by 8760 (i.e the number of hours in a year), Table 6.1 is populated - showing the total actual extracted WP power for all scenarios.

Table 6.1: Total Actual Extracted Wind Plant Power table for all studied scenarios

	Base_6Ω (GW)	**GA_CT** (GW)	**GA_CT_6Ω_rα_3** (GW)	**GA_CT_6Ω_rα_5** (GW)
P_{actual} **- 5**D	**1.202**	**1.275**	**1.604**	**1.580**
P_{actual} **- 6**D	**0.916**	**0.961**	**1.176**	**1.176**
P_{actual} **- 7**D	**0.749**	**0.777**	**0.934**	**0.903**

Equation (1) is then employed to estimate P_{ideal} for all studied scenarios ($5D$, $6D$, and $7D$) as 1.876GW, 1.334GW, and 1.042GW, respectively. Applying these values for each scenario to their corresponding row values on Table 6.1, based on Equation (6.1) produces the efficiency table in Table 6.2. Results on Table 6.2 indicate a 25.08 % and 23.95 % increase in efficiency by the $5D$ deployed $GA\_CT\_6\mathbf{\Omega}\_r\alpha\_3$ and $GA\_CT\_6\mathbf{\Omega}\_r\alpha\_5$ cases, respectively, compared to the $5D$ $Base\_6\mathbf{\Omega}$ case, and an increase of 15.89 % and 14.62 % compared to the $7D$ $Base\_6\mathbf{\Omega}$ case. These results demonstrate one of the study's objective

of obtaining an efficiency that surpasses that of a $7D$ deployed $Base\_6\boldsymbol{\Omega}$ case which is the conventional deployment. The $Base\_6\boldsymbol{\Omega}$ case column on Table 6.3 further demonstrates how the even-numbered sparsely-spaced bins (bins with intentional large T-2-T distances) inherently improves the average power efficiency of the WP, even without application of parameter optimisation and the novel implementation of the wake model.

Table 6.2: Summarised Efficiency table for all studied scenarios

	Base_6Ω	**GA_CT**	**GA_CT_6Ω_rα_3**	**GA_CT_6Ω_rα_5**
$\eta(\%)$ - **5**D	**64.05**	**67.96**	**85.49**	**84.22**
$\eta(\%)$ - **6**D	**68.70**	**72.01**	**88.15**	**86.15**
$\eta(\%)$ - **7**D	**71.91**	**74.54**	**89.64**	**86.61**

Table 6.3: Efficiency breakdown by bin for $5D$ scenario

Bin	**Base_6Ω** $\eta(\%)$	**GA_CT** $\eta(\%)$	**GA_CT_6Ω_rα_3** $\eta(\%)$	**GA_CT_6Ω_rα_5** $\eta(\%)$
bin 0	58.71	62.52	74.39	94.50
bin 1	73.19	76.59	88.47	86.33
bin 2	56.64	62.10	85.92	84.66
bin 3	67.97	71.02	87.03	87.04
bin 4	56.64	61.68	84.63	83.31
bin 5	73.19	76.26	85.48	85.12
bin 6	58.71	62.52	81.94	80.89
bin 7	73.19	76.49	90.53	88.19
bin 8	56.64	62.17	92.71	89.50
bin 9	67.97	71.02	92.06	90.07
bin 10	56.64	61.69	75.80	75.28
bin 11	73.19	75.41	92.27	89.95
Ave. efficiency ≈	**64.39**	**68.29**	**85.94**	**84.57**

6.2 Directional Efficiency

Consider the $7D$ WP layout deployed facing the north (i.e. layout deployed at a 0° rotation) in Figure 6.1, and the figures that follow in 6.2 - 6.4, which show the WP layout rotated with respect to the wind direction/bins. Note that this rotation is different from the rotations in Figures 2 and 5 - 15 (albeit for a $5D$ T-2-T distance) in the Appendix B section. The latter is the deployed WP layout viewed from the different bins, whereas, the former

is the layout actually deployed at an angle of rotation equal to the centre value of each bin direction, such that it faces each of the bins. Considering the former rotations, if the WP's layout is deployed at a 30° rotation to face bin 1, as depicted by Figure 6.2, it is seen that the distance K no longer point towards bins 1 and 7, but towards bins 2 and 8.

Furthermore, consider that the first two inner summations in Equation (6.2) for each b in $\mathcal{B}$, is called the *bin power*. Note that the *bin power* is the WP power for that bin since it sums all the power from all the turbines in the WP for all operating wind speeds. Then with consideration of the frequency of occurrence f_b of each bin, the *actual bin power* for that bin is obtained. A summation of all the bin powers will yield the *total WP power*, whereas the summation of all the actual bin powers will yield the *total actual WP power* or *total actual generated WP power* as represented in Equation (6.2). Given that the layout/lattice structure does not change during each new rotated deployment, and the distances (E, F, G, H, K, L) do not change, the bin power for each new bin/direction that the layout faces will also remain unchanged. However, each of the rotations will yield a different total actual WP power, because the different bins which the layout faces at different rotations posses different frequencies of occurrence f_b, which is required as a multiplier to the bin power to obtain the actual bin power, and consequently, the total actual WP power (P_{actual}) when all the actual bin powers of all the bins are summed as in Equation (6.2). Therefore, the bin power generated from bin 0 when the layout is deployed facing it (0°), will be different from when it is deployed facing bin 1 (30°), because the bin power although unchanged in itself, will then have a different multiplier (f_{b1}), no longer f_{b0}. This same multiplier effect will be imposed on the actual bin powers from other bins when viewing the current deployed WP layout from those bins. Therefore, it is possible that deploying the WP layout to face a different bin from bin 0, may yield a higher P_{actual}, efficiency, and consequently total AEP.

Further, consider that the original WP layout deployment according to Figure 6.1 (i.e deployed at a 0° rotation) is labelled 'a_0'. Together with every other view of this original layout from other directions, a set $\mathcal{M} = \{a_0, a_1, a_2, ..., a_{11}\}$ is obtained. So, each time the original layout is deployed at a different angle of rotation, the layout's views from other directions also adjust accordingly by that angle of rotation.

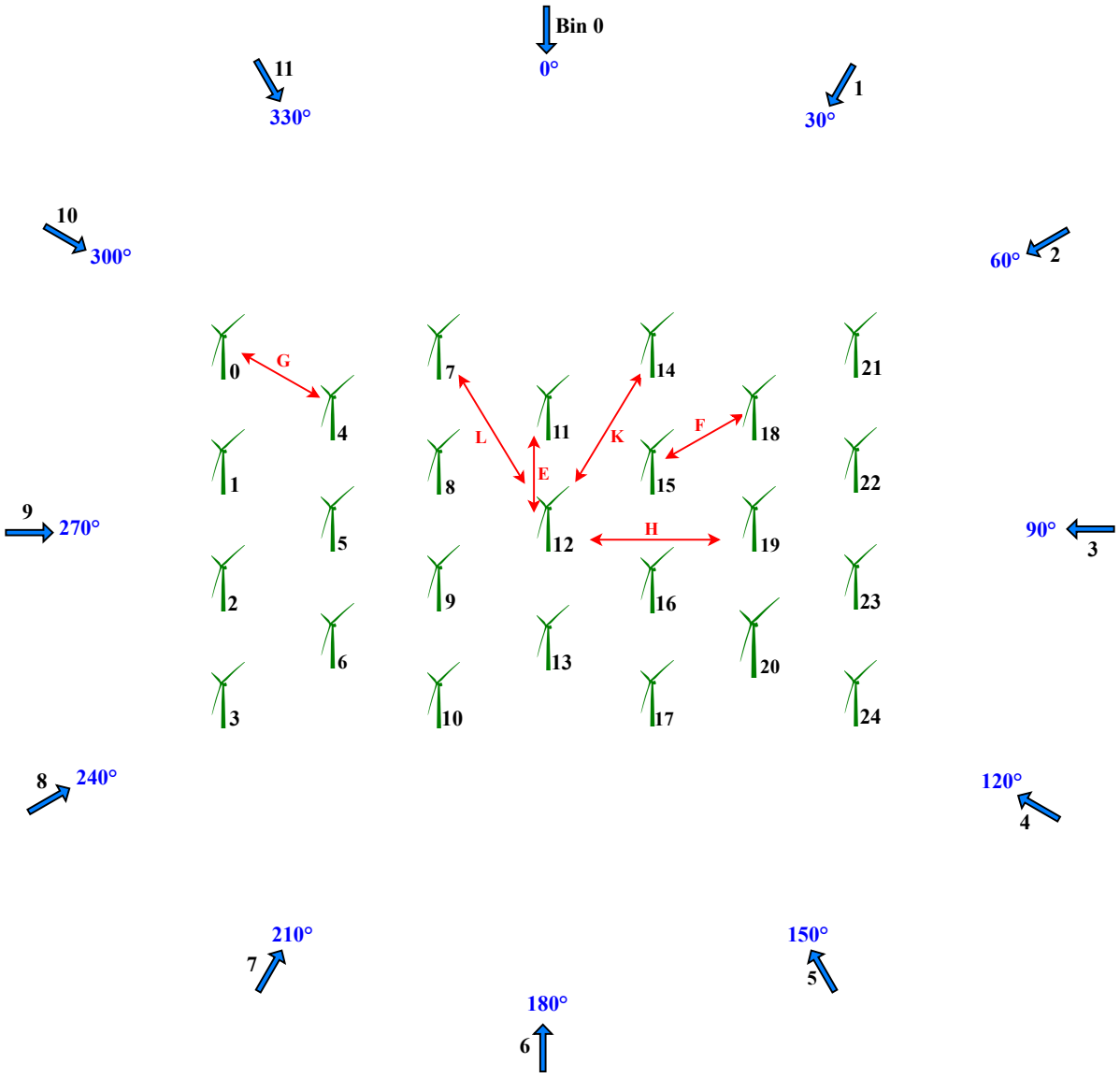

Figure 6.1: WP layout deployed at 0° rotation.

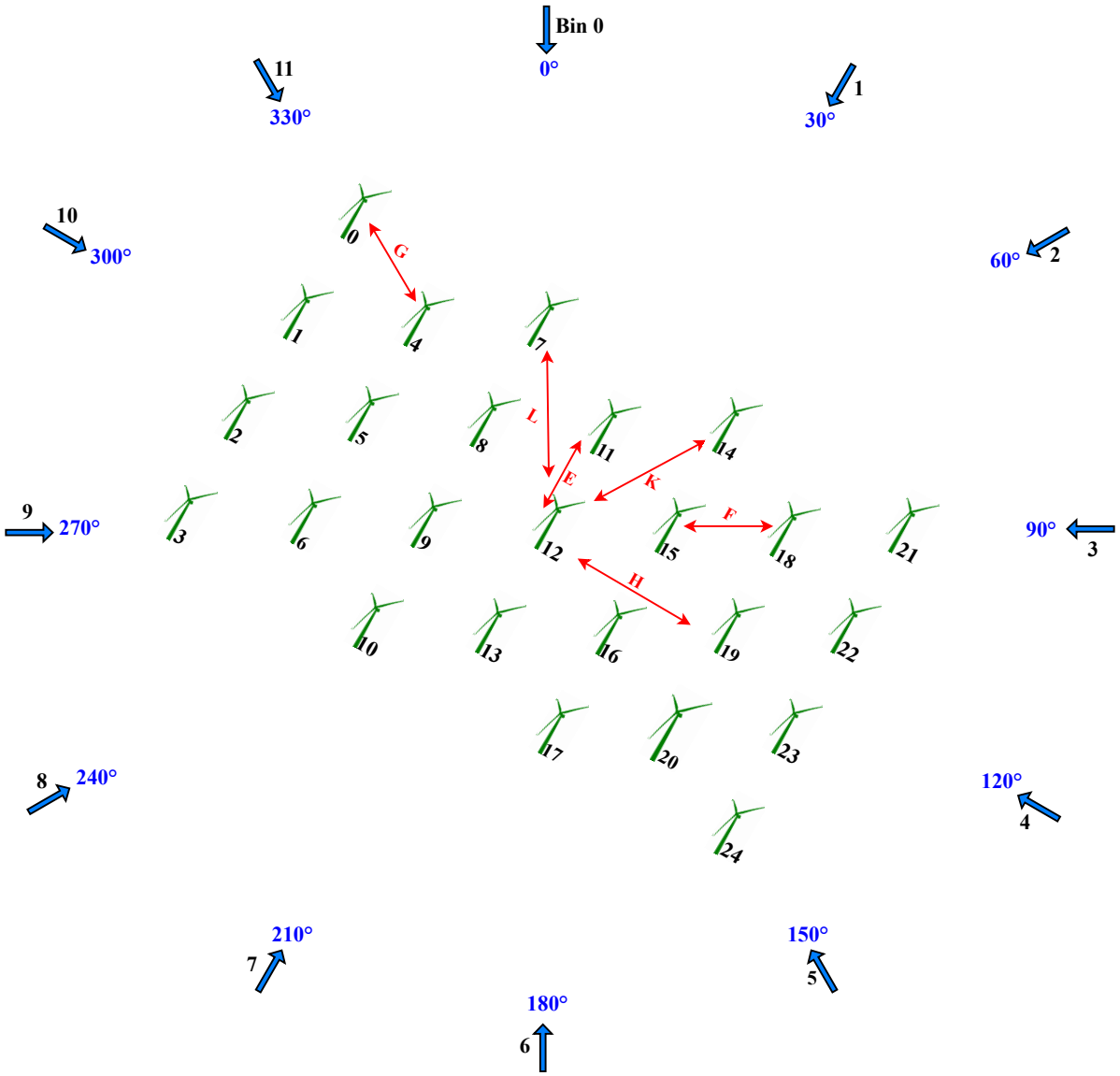

Figure 6.2: WP layout deployed at 30° rotation.

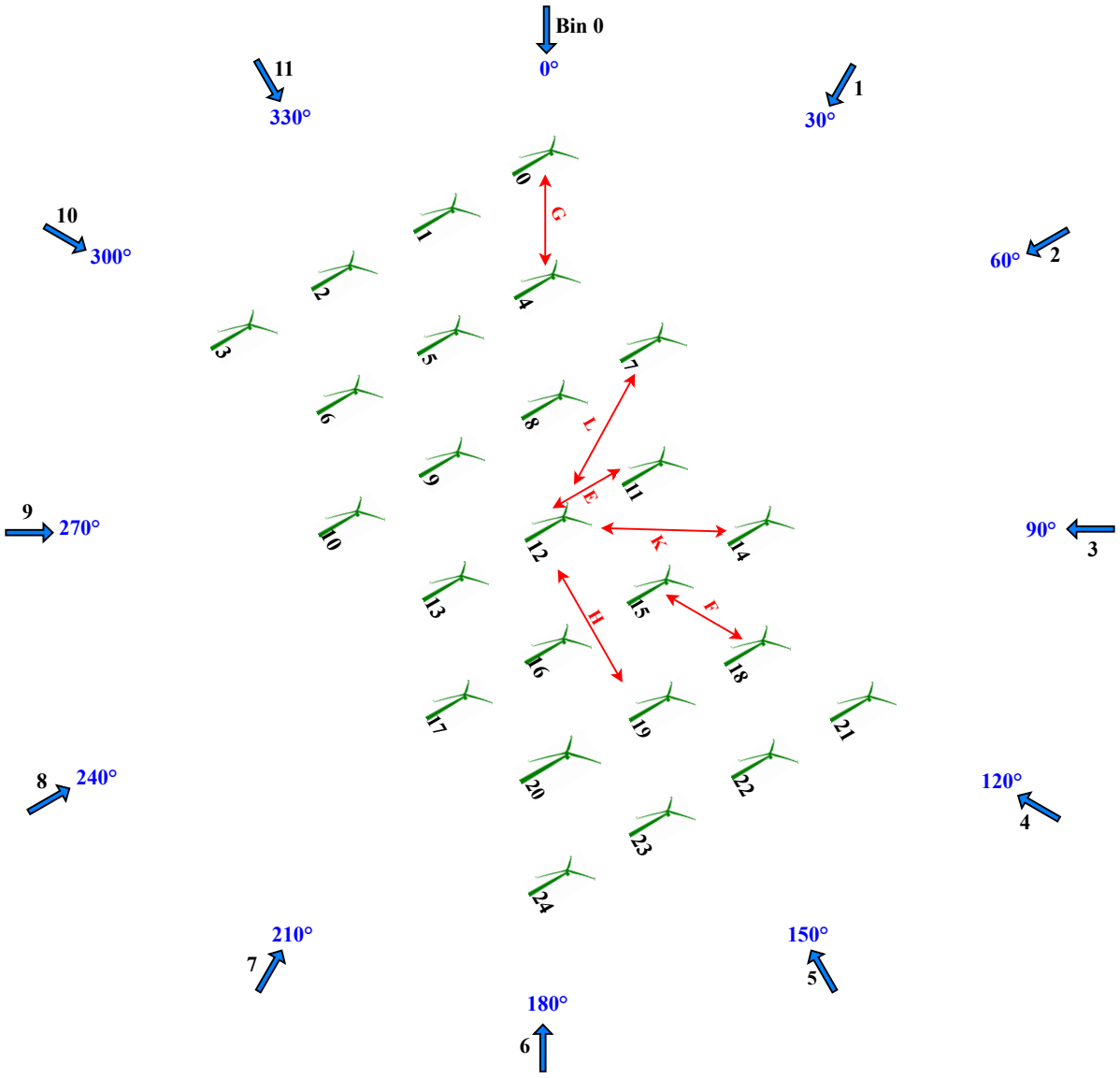

Figure 6.3: WP layout deployed at 60° rotation.

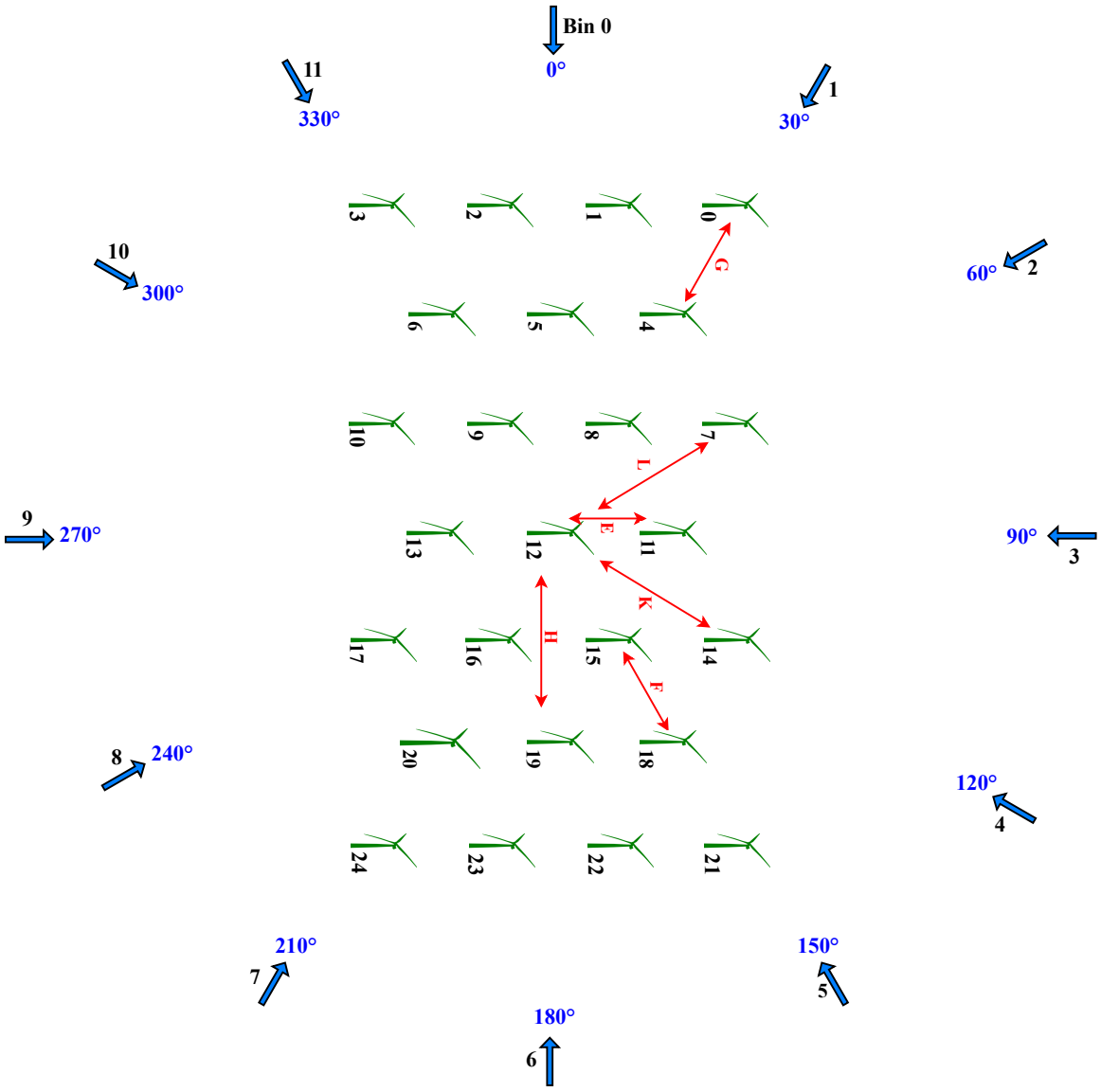

Figure 6.4: WP layout deployed at 90° rotation.

The directional efficiency comparison table in Table 6.4 is then obtained considering all twelve possible rotations of the WP layout, to deduce which deployment is most efficient.

Table 6.4: Directional efficiency comparison for **GA_CT_6Ω_rα_3**: $5D$ scenario

Bin	0°	30°	60°	90°	120°	150°	180°	210°	240°	270°	300°	330°
0	$\boldsymbol{a_0}$	a_{11}	a_{10}	a_9	a_8	a_7	a_6	a_5	a_4	a_3	a_2	a_1
1	a_1	$\boldsymbol{a_0}$	a_{11}	a_{10}	a_9	a_8	a_7	a_6	a_5	a_4	a_3	a_2
2	a_2	a_1	$\boldsymbol{a_0}$	a_{11}	a_{10}	a_9	a_8	a_7	a_6	a_5	a_4	a_3
3	a_3	a_2	a_1	$\boldsymbol{a_0}$	a_{11}	a_{10}	a_9	a_8	a_7	a_6	a_5	a_4
4	a_4	a_3	a_2	a_1	$\boldsymbol{a_0}$	a_{11}	a_{10}	a_9	a_8	a_7	a_6	a_5
5	a_5	a_4	a_3	a_2	a_1	$\boldsymbol{a_0}$	a_{11}	a_{10}	a_9	a_8	a_7	a_6
6	a_6	a_5	a_4	a_3	a_2	a_1	$\boldsymbol{a_0}$	a_{11}	a_{10}	a_9	a_8	a_7
7	a_7	a_6	a_5	a_4	a_3	a_2	a_1	$\boldsymbol{a_0}$	a_{11}	a_{10}	a_9	a_8
8	a_8	a_7	a_6	a_5	a_4	$a_3 d$	a_2	a_1	$\boldsymbol{a_0}$	l	a_{10}	a_9
9	a_9	a_8	a_7	a_6	a_5	a_4	a_3	a_2	a_1	$\boldsymbol{a_0}$	a_{11}	a_{10}
10	a_{10}	a_9	a_8	a_7	a_6	a_5	a_4	a_3	a_2	a_1	$\boldsymbol{a_0}$	a_{11}
11	a_{11}	a_{10}	a_9	a_8	a_7	a_6	a_5	a_4	a_3	a_2	a_1	$\boldsymbol{a_0}$
P_{actual} **(GW)**	**1.604**	**1.613**	**1.614**	**1.611**	**1.611**	**1.618**	**1.612**	**1.609**	**1.611**	**1.619**	**1.605**	**1.617**
η(%)	**85.49**	**85.98**	**86.03**	**85.88**	**85.86**	**86.27**	**85.94**	**85.51**	**85.87**	**86.35**	**85.58**	**86.18**
Total AEP (TWh)≈	**14.05**	**14.13**	**14.14**	**14.11**	**14.11**	**14.18**	**14.12**	**14.10**	**14.11**	**14.19**	**14.06**	**14.16**

With reference to Table 6.4, if the WP layout is deployed at a 0° rotation, P_{actual} is computed based on Equation (6.2) as $a_0 * f_{b0} + a_1 * f_{b1} + a_2 * f_{b2} + a_3 * f_{b3} \quad ... + a_{11} * f_{b11}$, where a_0 represents the bin power generated by all the turbines from U_{in} to U_r, and f_{b0} is the frequency of occurrence of wind from bin 0. Accordingly, at a 30° rotation deployment, P_{actual} can be computed as $a_{11} * f_{b0} + a_0 * f_{b1} + a_1 * f_{b2} + a_2 * f_{b3} ... + a_{10} * f_{b11}$, and at a 330° rotation deployment, P_{actual} will be computed as $a_1 * f_{b0} + a_2 * f_{b1} + a_3 * f_{b2} + a_4 * f_{b3} ... + a_0 * f_{b11}$. The obtained values for P_{actual} is substituted into Equations (6.1) and (3.16), to obtain the efficiency and AEP, respectively, for each deployment. From Table 6.4 it is demonstrated that the WP layout is most efficient if deployed at a rotation of 270° facing bin 9, as depicted in Figure 6.5. This result however, will demand a different WP dimension compared to the original 0° deployment and could imply an additional land leasing cost. Nonetheless, it shows that in the event of seasonal variations in wind speed and direction (simulated in this section by rotating the layout to face different wind directions/bins of different probabilities of occurrence), applying the layout-dependent techniques from Chapter 5 to a hexagonal turbine layout can still enhance AEP and efficiency.

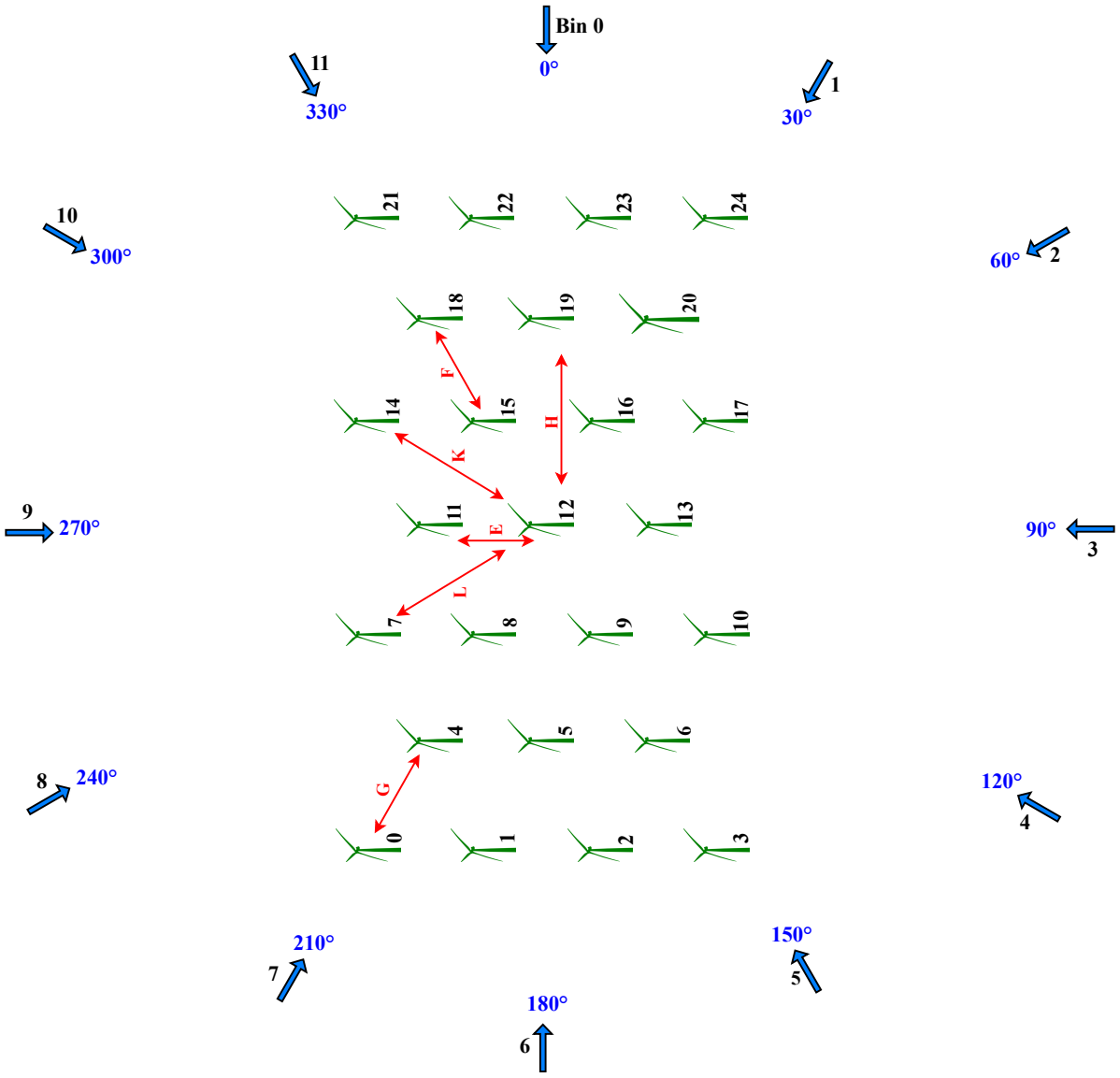

Figure 6.5: WP layout deployed at 270° rotation.

6.3 Numerical Simulation Results using offshore wind data

In this section, the modified wake model in chapter 5 and the augmented turbulence intensity model from chapters 3 which has been applied from then onwards, are implemented with an offshore wind data obtained from [124]. The studied layout is more common in offshore projects, as seen in real wind farms like Noordzee, Princess Amalia, and Horns Rev 1,

and supported by multiple studies. In addition to higher installation and maintenance costs, offshore sites experience stronger winds and lower turbulence, warranting larger turbine-to-turbine (T-2-T) distances to not only allow sufficient wake dissipation but also maximize energy output per turbine. It would therefore be valuable to explore whether smaller T-2-T distances (e.g., $5D$ and $6D$ in the prevalent wind direction) can still achieve significant improvements in total WP power and annual energy production (AEP), despite the typical offshore spacing of $8D$ in the prevalent and 6–$7D$ in the crosswind direction.

Applying similar GA optimisation parameters as in Table 3.6, the following results are obtained, where **GA_CT_6Ω**_$r\alpha$_3 is the 300 generations run of GA_CT case with modified $6\boldsymbol{\Omega}$ upstream sector and applied "*r-α upstream wake effect elimination*", as seen in chapter 5 and earlier sections of the current chapter, and **GA_CT_6Ω**_$r\alpha$_3b represents results of the same method applied to an offshore wind data. It is pertinent to point out that all results presented are with respect to the original 0° deployment, not the most efficient deployment as has been examined in the preceding section, since the study is based on a fixed WP dimension.

Table 6.5 presents the Total WP AEP for the $5D$ scenario only, comparing the *Base* case to the **GA_CT_6Ω**_$r\alpha$_3 cases of both the onshore and offshore data. Figures 6.6 and 6.7 demonstrate the C_T and TI comparison for all the three cases.

6.3.1 AEP and Efficiency numerical results

Table 6.5: AEP comparison for $5D$ scenario with modified upstream sector and r-α upstream wake effect elimination using offshore and onshore wind data

	Base_6Ω	**GA_CT_6Ω**_$r\alpha$_3b	**GA_CT_6Ω**_$r\alpha$_3
Total AEP(TWh) - 5D	**10.53**	**14.05**	**14.05**
Increase (%)	0	25.08	25.07

Dividing through the AEP values in Table 6.5 by the number of hours in a year (8760), Table 6.6 is populated - showing the total actual extracted WP power at a $5D$ minimum T-2-T distance, for all cases. Furthermore, applying the value estimated for P_{ideal} in a $5D$

scenario (1.876GW) to all cases/row values on Table 6.6, based on Equation (6.1) yields the efficiency table in Table 6.7.

Table 6.6: Total Actual Extracted Wind Plant Power comparison for $5D$ scenario using offshore and onshore wind data

	Base_6Ω (GW)	**GA_CT_6Ω_rα_3b** (GW)	**GA_CT_6Ω_rα_3** (GW)
P_{actual} **- 5**D	**1.202**	**1.604**	**1.604**

Table 6.7: Efficiency comparison for $5D$ scenario using offshore and onshore wind data

	Base_6Ω	**GA_CT_6Ω_rα_3b**	**GA_CT_6Ω_rα_3**
η**(%) - 5**D	**64.05**	**85.49**	**85.49**

6.3.2 Thrust coefficient numerical results

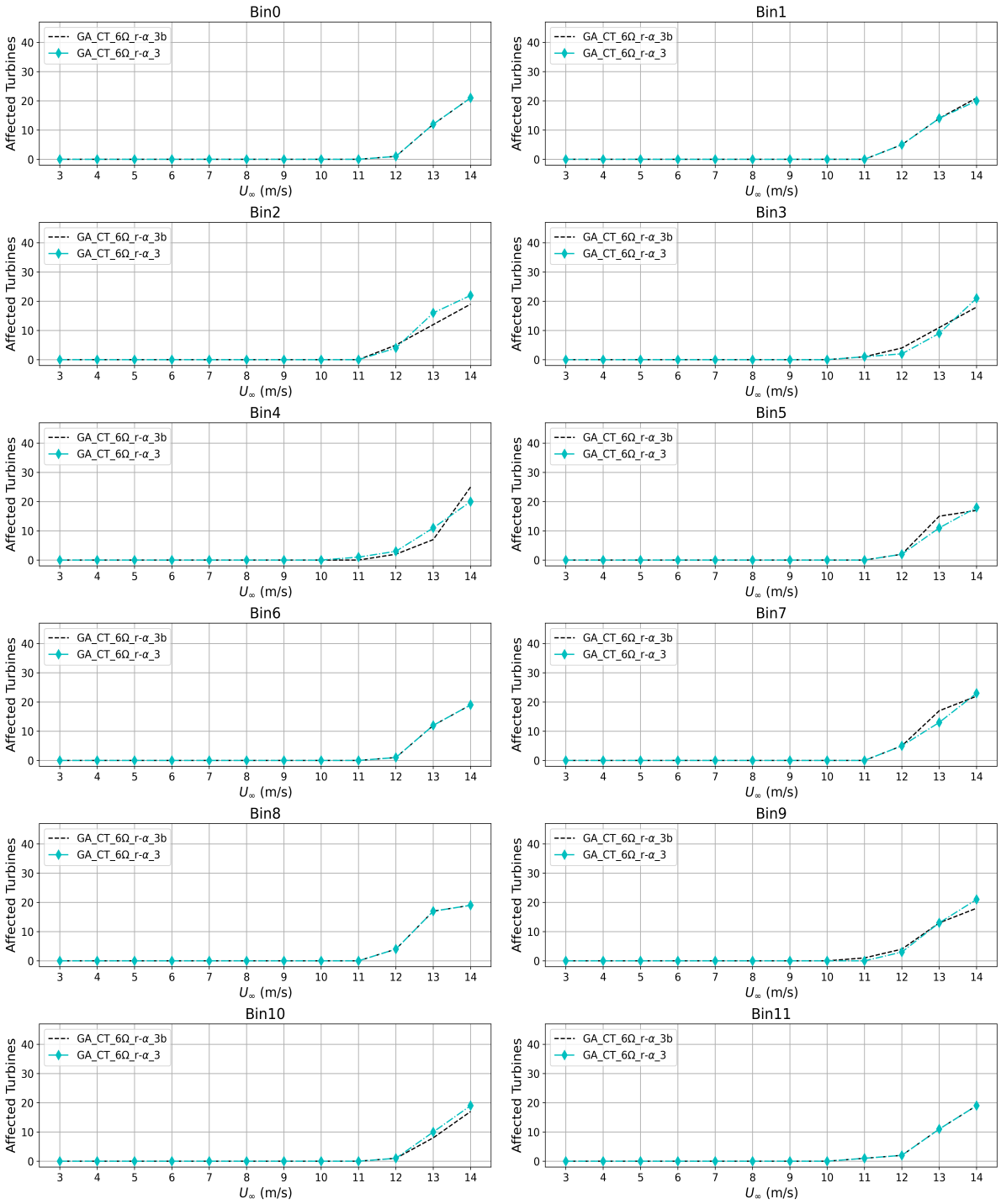

Figure 6.6: Total C_T-defaulting turbines comparison for both sets of wind data, with applied $6\mathbf{\Omega}$ upstream sector and r-α upstream wake effect elimination: GA, $5D$

6.3.3 Turbulence intensity numerical results

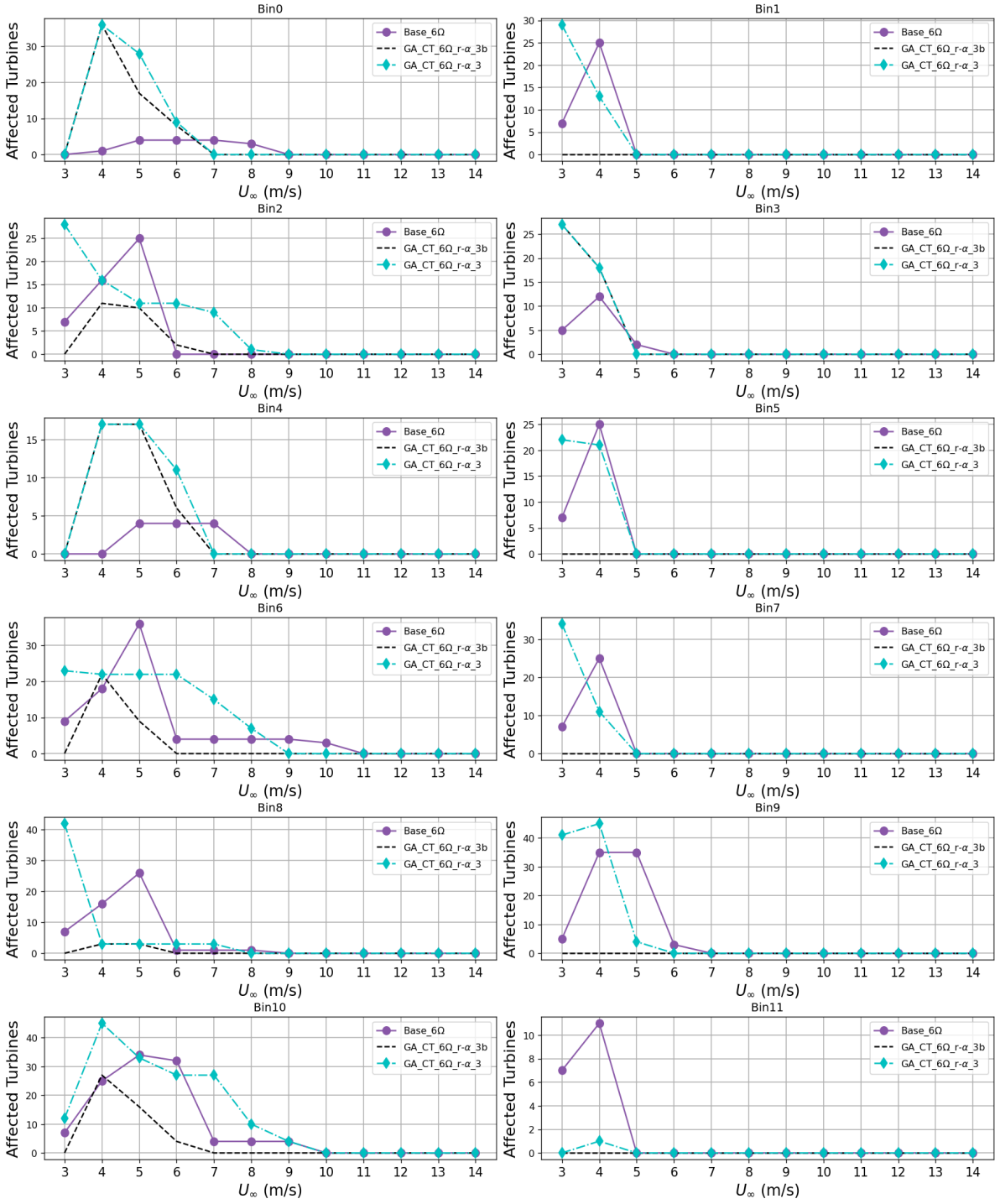

Figure 6.7: Total TI-defaulting turbines comparison for both sets of wind data, with applied $6\boldsymbol{\Omega}$ upstream sector and r-α upstream wake effect elimination: GA, $5D$

6.4 Discussion and Summary

Using the novel wake model implementation methodology in combination with parameter optimisation, this chapter was able to improve the energy efficiency of a densely deployed WP of $5D$ minimum T-2-T distance by up to 25.08 % against the Base case of equal T-2-T distance. This combination also provided an improvement in energy efficiency of up to 15.89 % against the conventional $7D$ non-optimised deployment ($7D$ Base case).

The AEP results in Table 6.5 showed no marked disparity between both sets of data even though it is expected that higher winds are available offshore than onshore. This is because the AEP computation takes no consideration of the occurrence frequency of the individual centre wind speeds (considered as U_∞) within the studied range (between U_{in} and U_r), but the occurrence frequency of wind from each bin/directions. These results confirm that the upgraded wake and TI models are not affected by changes in wind data. Also, the efficiency results on Table 6.7 shows greater promise for offshore projects as it demonstrates comparable efficiency with onshore data even at tight T-2-T distances. More importantly it demonstrates the potential of the proposed methodology for offshore wind projects where stronger winds and lower turbulence have warranted larger T-2-T distances in practice, for fear of a reduced energy efficiency.

The C_T results presented in Fig 5.7 also show marginal differences between both sets of wind data. This behaviour is expected given that the same centre wind speeds are analysed in both cases as explained in the preceding paragraph.

TI results in Fig 5.13 however, presents noticeable differences. Unlike the AEP and C_T results, TI computations not only depends on U_∞, but is also dependent on the wind data's representative standard deviation σ_{repr}, which captures the turbulence in the wind data. As confirmed in [125], turbulence levels are lower offshore compared to onshore, hence, the superior TI results (lower TI and therefore, lower number of defaulting turbines) exhibited by the offshore wind data plot (GA_CT_6$\mathbf{\Omega}$_$r\alpha$_3b)

Finally, the chapter also succeeded in improving the achieved AEP of the initial studied onshore wind site by considering directional efficiencies, even though this consideration could incur additional land leasing costs to accommodate the new WP dimensions. This additional

improvement also implies a further improvement in energy efficiency. It further demonstrated that regardless the direction of deployment, implementing the novel methodology on the chosen turbine layout is able to significantly improve WP AEP and energy efficiency. It also validated the modifications made on both the TI and wake models, using an offshore site data. Hence, a coupling of these models can be applied effectively onshore and offshore for wake and TI estimations as well as efficiency improvements.

Chapter 7

Summary and Conclusion

In addressing the challenges associated with increasing power density within wind power plants, such as wake deficits, reduced wind plant efficiency, heightened turbine thrusts, and elevated turbulence intensities, this study investigated the potential of a regular hexagonal turbine layout. The aim was to provide predetermined directions with varying turbine-to-turbine distances, effectively mitigating these issues while sustaining the attained power density enhancements.

By employing a Genetic Algorithm (GA) and Particle Swarm Optimization (PSO)-inspired constrained set point optimisation approach for axial induction factors, this research evaluated the annual energy production (AEP), thrust coefficient (C_T), thrust, and turbulence intensities (TI) within a hypothetical wind plant deployed in a hexagonal layout across three minimum turbine-to-turbine distance scenarios - $5D$, $6D$, and $7D$. It compared the optimised cases to the Base/non-optimized case for each scenario. Additionally, it investigated how an augmented implementation of the employed wake model could enhance mean wind speeds at turbine positions, consequently influencing turbulence intensities, wind plant generated power, and ultimately, AEP and efficiency.

The findings unveiled striking consequences of an unconstrained axial induction-based power maximisation on turbine thrust coefficients - leading to excessive thrusts and consequently overexertion, and increased turbulence intensity at turbine positions. Notably, complex correlations between turbine-to-turbine distance and wind plant power generation, turbine thrust coefficient, and turbulence intensities at turbine locations within the wind

plant were identified. While a positive correlation was identified between sparse deployments and high thrust coefficient values at turbines, a positive correlation was identified however, between tight deployments and high turbulence intensities at turbines positions, with both cases correlating positively with a high wind plant power generation.

Furthermore, the analysis established that applying thrust coefficient constraints to wind power maximisation can curb turbine overexertion by as much as 66.67% of turbine's rated wind capacity, irrespective of turbine-to-turbine distance. These constraints enforced no significant effect on the turbulence intensities at turbine locations, however, it induced a trade-off in achieved wind plant power and consequently achieved annual energy production.

Notably, the study unveiled a novel implementation of an existing wake model where upstream turbines effect on a downstream turbine's power generation is considered significant not just because they are in the upstream but based on the magnitude of their axial and radial distances, as well as their axial induction values. This modified implementation reasonably improved the mean wind speeds at turbine positions enough to enhance a visible improvement in turbulence intensities, while curbing overexertion due to thrust coefficient adherence, and also significantly improving the wind plant extracted power, the annual energy production, and the wind plant efficiency. Moreover, a Big O analysis shows that the augmented wake model implemented enhances a reduction in computational complexity, which can further be reduced by shelving optimisations in all sparsely-spaced bins - an advantage offered by the employed regular hexagonal layout.

The implemented augmentations on both the turbulence intensity and wake models were validated using an offshore site data, while emphasizing the need to consider directional wind occurrences for further improvement of the annual energy production and achieved efficiency of a wind plant. These findings highlight the benefits of regular layouts and parameter constraints in wind farm optimization, both onshore and offshore. Notably, they suggest that offshore wind plants could also achieve space maximization efficiency using closer turbine-to-turbine spacings while maintaining comparable wind plant power, AEP and energy efficiency to the currently justified sparse offshore deployments (i.e. $7D$ without optimisation).

These findings appropriately answer the first question posed in chapter 1 section 1.7 of the study, demonstrating with the Big O analysis in chapter 5 section 5.1.3, that the hexagonal

layout of turbines can allow parameter optimisations and hence, power curtailments to be curbed in some wind directions, yet maintain energy efficiency that compares favourably with a sparsely deployed non-optimised case of similar layout. The findings in chapter 5 also answer the question that a a densely-deployed WP (represented by the $5D$ T-2-T spacing) can be optimised to not only yield a superior AEP but also reduce turbulence intensity and thrusts, while still obtaining an efficiency that compares favourably to that of a traditional non-optimised sparsely deployed WP (represented by the $7D$ T-2-T spacing) of similar layout. Finally, the directional efficiency findings of section 6.2 also attests to the fact that in the event of seasonal variations in wind speed and direction, applying the layout-dependent techniques from Chapter 5 to a tightly-spaced hexagonal turbine layout can still yield enhanced AEP and efficiency that favourably compare with those of the conventional deployments.

Strategies aimed at improving mean wind speeds at turbines and curtailing overexertion could potentially mitigate the negative impact of power density increments in wind power plants, giving it an advantage over a traditionally deployed non-optimised wind plant in terms of generated power, annual energy production and efficiency. It could also provide an advantage over optimised wind plant layouts in terms of reduction in computational complexity. However, the study acknowledges the limitations in turbine-level turbulence intensity improvement and the wind plant directional efficiency improvement that can be obtained, and especially the dependability of the wake model augmentations on wind plant layout and area dimensions.

Future research should explore different wind plant area dimensions and layouts to ascertain if the chosen upstream sector as well as the cut-off α and $r_{j,i}$ values can be applied generically.

In conclusion, this research sheds light on the complex interplay between turbine-to-turbine distance, turbine thrust coefficient, turbulence intensities at turbine, and wind plant power. It advocates for a balanced approach to wind plant power optimisation that improves wind plant power, annual energy production, and wind plant efficiency while curbing turbine overexertion and possible increase in fatigue and extreme loads in wind power plants, and highlights the need for employing a regular hexagonal layout in conjunction with a thrust

coefficient constrained axial induction optimisation using an augmented implementation of the Park and Law wake model to estimate these gains and achieve this goal.

Bibliography

[1] N. O. Jensen, *A note on wind generator interaction*. Citeseer, 1983, vol. 2411. xv, 22, 23, 24, 46

[2] I. Katic, J. Højstrup, and N. O. Jensen, "A simple model for cluster efficiency," in *European wind energy association conference and exhibition*, vol. 1. A. Raguzzi Rome, Italy, 1986, pp. 407–410. xv, 23, 24, 33, 46, 61

[3] J. Park and K. H. Law, "Layout optimization for maximizing wind farm power production using sequential convex programming," *Applied energy*, vol. 151, pp. 320–334, 2015. xv, xvii, 4, 5, 20, 22, 24, 25, 26, 43, 50, 51, 52, 59, 60, 61, 130, 131, 132, 134, 135, 154, 155, 242

[4] ——, "Cooperative wind turbine control for maximizing wind farm power using sequential convex programming," *Energy Conversion and Management*, vol. 101, pp. 295–316, 2015. xv, 4, 22, 24, 25, 26, 28, 31, 33, 42, 47, 59, 61, 130

[5] N. Moskalenko, K. Rudion, and A. Orths, "Study of wake effects for offshore wind farm planning," in *2010 Modern Electric Power Systems*. IEEE, 2010, pp. 1–7. 1, 17

[6] J. F. Manwell, J. G. McGowan, and A. L. Rogers, *Wind energy explained: theory, design and application*. John Wiley & Sons, 2010. 1, 60, 158

[7] P. M. Gebraad and J.-W. van Wingerden, "Maximum power-point tracking control for wind farms," *Wind Energy*, vol. 18, no. 3, pp. 429–447, 2015. 1, 2, 3, 17, 18

[8] P. A. Fleming, A. Ning, P. M. Gebraad, and K. Dykes, "Wind plant system engineering through optimization of layout and yaw control," *Wind Energy*, vol. 19, no. 2, pp. 329–344, 2016. 1, 2, 3, 17, 20, 21, 42, 154

[9] N. Charhouni, M. Sallaou, and K. Mansouri, "Realistic wind farm design layout optimization with different wind turbines types," *International Journal of Energy and Environmental Engineering*, vol. 10, no. 3, pp. 307–318, 2019. 2, 20

[10] Z. Liang and H. Liu, "Layout optimization algorithms for the offshore wind farm with different densities using a full-field wake model," *Energies*, vol. 16, no. 16, p. 5916, 2023. 2

[11] U. of Strathclyde, "Wind farm layout," http://www.esru.strath.ac.uk/EandE/Web_sites/00-01/hybrid_wind/files/texts/layout.html, accessed December 24, 2019. 2, 21

[12] M. Charles, D. T. Oyedokun, and M. Dlodlo, "Wind farm density effects on turbulence intensity for large hexagonal farm arrays," in *2020 6th IEEE International Energy Conference (ENERGYCon)*. IEEE, 2020, pp. 1–6. 2, 17

[13] B. Sanderse, *Aerodynamics of wind turbine wakes*. Petten: ECN, 2009. 2, 19, 30, 101

[14] Y. Miao, M. N. Soltani, and A. Hajizadeh, "Wind farm power production and fatigue load optimization through wake steering," in *2023 IEEE 19th International Conference on Automation Science and Engineering (CASE)*. IEEE, 2023, pp. 1–6. 3

[15] W. Cai, Y. Hu, F. Fang, L. Yao, and J. Liu, "Wind farm power production and fatigue load optimization based on dynamic partitioning and wake redirection of wind turbines," *Applied Energy*, vol. 339, p. 121000, 2023. 3, 21

[16] J. Barradas-Berglind and R. Wisniewski, "Wind farm axial-induction factor optimization for power maximization and load alleviation," in *2016 European Control Conference (ECC)*. IEEE, 2016, pp. 891–896. 4, 42, 47, 90, 103, 104

[17] S. Rolland and B. Auzane, "The potential of small and medium wind energy in developing countries," *Position Paper: Alliance for Rural Electrification*, 2012. 10

[18] Z. Wu and H. Wang, "Research on active yaw mechanism of small wind turbines," *Energy Procedia*, vol. 16, pp. 53–57, 2012. 10

[19] T. Ackermann and L. Söder, "Wind energy technology and current status: a review," *Renewable and sustainable energy reviews*, vol. 4, no. 4, pp. 315–374, 2000. 10, 15

[20] M. B. Alawi, "The integration of wind turbines for generating sustainable energy in." 11

[21] N. Instruments, "Wind turbine control methods," https://www.ni.com/en-za/innovations/white-papers/08/wind-turbine-control-methods.html, 2020, accessed May 10, 2022. 12

[22] A. Kalmikov, "Wind power fundamentals," in *Wind energy engineering*. Elsevier, 2017, pp. 17–24. 13

[23] M. O. Hansen, "Basic rotor aerodynamics applied to wind turbines," 1998. 13

[24] T. Burton, N. Jenkins, D. Sharpe, and E. Bossanyi, *Wind energy handbook*. John Wiley & Sons, 2011. 13, 14, 15, 25, 26

[25] A. Betz, *Introduction to the theory of flow machines*. Elsevier, 2014. 13, 14

[26] M. Hansen, *Aerodynamics of wind turbines*. Routledge, 2015. 13, 14

[27] M. Ragheb and A. M. Ragheb, "Wind turbines theory-the betz equation and optimal rotor tip speed ratio," *Fundamental and advanced topics in wind power*, vol. 1, no. 1, pp. 19–38, 2011. 14

[28] L. A. Martínez-Tossas, E. Branlard, K. Shaler, G. Vijayakumar, S. Ananthan, P. Sakievich, and J. Jonkman, "Numerical investigation of wind turbine wakes under high thrust coefficient," *Wind Energy*, vol. 25, no. 4, pp. 605–617, 2022. 14

[29] P.-E. Réthoré, "Thrust and wake of a wind turbine: Relationship and measurements," *Technical University of Denmark (DTU)*, pp. 32–44, 2006. 14

[30] H.-G. Kim and J.-Y. Kim, "Analysis of wind turbine aging through operation data calibrated by lidar measurement," *Energies*, vol. 14, no. 8, p. 2319, 2021. 15

[31] R. Harrison, E. Hau, and H. Snel, "Large wind turbines: design and economics," 2000. 15

[32] G. Corten and P. Schaak, "Heat and flux. increase of wind farm production by reduction of the axial induction," 2003. 16

[33] P. M. Gebraad, P. A. Fleming, and J.-W. van Wingerden, "Comparison of actuation methods for wake control in wind plants," in *2015 american control conference (ACC)*. IEEE, 2015, pp. 1695–1701. 16

[34] D.-P. Molenaar, "Cost-effective design and operation of variable speed wind turbines," 2003. 17

[35] R. Burdett, "Conservative threat to the onshore wind industry," https://www.renewableenergyhub.co.uk/blog/wp-content/uploads/2014/04/Onshore-Wind.jpg, 2014, the Renewable Energy Hub UK Blog, Accessed May 19, 2022. 17

[36] R. Shakoor, M. Y. Hassan, A. Raheem, and Y.-K. Wu, "Wake effect modeling: A review of wind farm layout optimization using jensen␣ s model," *Renewable and Sustainable Energy Reviews*, vol. 58, pp. 1048–1059, 2016. 18, 22, 23

[37] J. F. Ainslie, "Calculating the flowfield in the wake of wind turbines," *Journal of wind engineering and Industrial Aerodynamics*, vol. 27, no. 1-3, pp. 213–224, 1988. 19, 22, 24, 30

[38] J. Ainslie, "Development of an eddy viscosity model for wind turbine wakes," in *Proceedings of 7th BWEA Wind energy conference, Oxford*, 1985. 19

[39] A. Crespo, J. Hernandez, and S. Frandsen, "Survey of modelling methods for wind turbine wakes and wind farms," *Wind Energy: An International Journal for Progress and Applications in Wind Power Conversion Technology*, vol. 2, no. 1, pp. 1–24, 1999. 19

[40] J. Schepers, *ENDOW: Validation and improvement of ECN's wake model.* Energy research Centre of the Netherlands ECN Petten, 2003. 19

[41] T. Han, "The assessment of dynamic wake effects on loading: Dynamic wake modeling and comparison of methods for wake loading assessment," 2011. 19, 23

[42] P. Argyle, S. Watson, C. Montavon, I. Jones, and M. Smith, "Modelling turbulence intensity within a large offshore wind farm," *Wind Energy*, vol. 21, no. 12, pp. 1329–1343, 2018. 19, 38, 40, 52, 62, 71, 97, 104

[43] S. Frandsen, "Turbulence and turbulence generated loading in wind turbine clusters," *Risø report R-1188*, 2007. 19, 37, 38, 39, 40, 52, 62, 63, 65, 104

[44] J. Højstrup, "Spectral coherence in wind turbine wakes," *Journal of Wind Engineering and Industrial Aerodynamics*, vol. 80, no. 1-2, pp. 137–146, 1999. 19, 20

[45] H. Seifert, J. Kröning, T. Hahm, R. Rohden, K. Freudenreich, S. Jöckel, and J. Birkemeyer, "Recommendations for spacing wind farms; abstandsregelung in windparks," *DEWI-Magazin*, 2003. 19, 20, 97

[46] "Park effect," http://www.windpower.org/en/tour/wres/park.htm, 2003, the Danish Wind Industry Association, Accessed May 21, 2022. 20

[47] R. L. Busby, *Wind power: The industry grows up.* PennWell Books, 2012. 20

[48] T. Bak, A. Graham, A. Sapronova, M. Florian, J. Dalsgaard Sørensen, T. Knudsen, P. Hou, and Z. Chen, "Baseline layout and design of a 0.8 gw reference wind farm in the north sea," *Wind Energy*, vol. 20, no. 9, pp. 1665–1683, 2017. 20

[49] S. Grady, M. Hussaini, and M. M. Abdullah, "Placement of wind turbines using genetic algorithms," *Renewable energy*, vol. 30, no. 2, pp. 259–270, 2005. 20, 53

[50] S. Turner, D. Romero, P. Zhang, C. Amon, and T. Chan, "A new mathematical programming approach to optimize wind farm layouts," *Renewable Energy*, vol. 63, pp. 674–680, 2014. 20

[51] P. Gebraad, J. J. Thomas, A. Ning, P. Fleming, and K. Dykes, "Maximization of the annual energy production of wind power plants by optimization of layout and yaw-based wake control," *Wind Energy*, vol. 20, no. 1, pp. 97–107, 2017. 20, 42, 44, 47, 51, 70, 154

[52] K. O. Merz, "An engineering model for dynamic wind power plant flow," *Energy Procedia*, vol. 137, pp. 539–552, 2017. 20

[53] "Horns rev 1," https://powerplants.vattenfall.com/horns-rev/, 2022, vattenfall AB, Accessed May 23, 2022. 20

[54] T. Vanagt and M. Faasse, "Development of hard substratum fauna in the princess amalia wind farm. monitoring six years after construction," *eCOAST report*, vol. 2013009, 2014. 21

[55] "Prinses amalia(netherlands)," https://www.thewindpower.net/windfarm_en_3326_prinses-amalia.php, 2022, the WINDPOWER: Wind Energy Market Intelligence, Accessed May 23, 2022. 21

[56] T. Le Thanh, E. Muljadi, D. V. Ngoc *et al.*, "Wind farm layout optimization based on the wind resource grid," in *2022 5th International Conference on Power Engineering and Renewable Energy (ICPERE)*, vol. 1. IEEE, 2022, pp. 1–5. 21

[57] Y. A. Li, "Deep reinforcement learning on wind power optimization," in *2022 International Conference on Networks, Communications and Information Technology (CNCIT)*. IEEE, 2022, pp. 45–51. 21

[58] J. Cao, X. Gao, X. Shen, H. Sun, and Y. Ju, "Wake-based wind turbine optimisations under yawed conditions," in *2022 7th International Conference on Environment Friendly Energies and Applications (EFEA)*. IEEE, 2022, pp. 1–5. 21, 43, 130

[59] D. Foxwell, "Hexagonal windfarm meets energy and environmental requirements," https://www.rivieramm.com/news-content-hub/news-content-hub/hexagonal-windfarm-meets-energy-and-environmental-requirements-56862, accessed January 24, 2024. 21

[60] S. Frandsen, "On the wind speed reduction in the center of large clusters of wind turbines," *Journal of Wind Engineering and Industrial Aerodynamics*, vol. 39, no. 1-3, pp. 251–265, 1992. 22, 46

[61] G. C. Larsen, *A simple wake calculation procedure*. Risø National Laboratory, 1988. 22, 46

[62] ——, "A simple stationary semi-analytical wake model," *Risø National Laboratory for Sustainable Energy, Technical University of Denmark: Roskilde, Denmark*, 2009. 22, 33

[63] A. Niayifar and F. Porté-Agel, "Analytical modeling of wind farms: A new approach for power prediction," *Energies*, vol. 9, no. 9, p. 741, 2016. 22, 35, 37, 43, 46

[64] G.-W. Qian and T. Ishihara, "A new analytical wake model for yawed wind turbines," *Energies*, vol. 11, no. 3, p. 665, 2018. 22, 43

[65] S. Ott, J. Berg, and M. Nielsen, "Linearised cfd models for wakes," 2011. 22

[66] G. C. Larsen, H. Aagaard Madsen, and F. Bingöl, "Dynamic wake meandering modeling," 2007. 22, 30

[67] D. J. Renkema, "Validation of wind turbine wake models," *Master of Science Thesis, Delft University of Technology*, vol. 19, 2007. 22, 23

[68] P. Hou, J. Zhu, K. Ma, G. Yang, W. Hu, and Z. Chen, "A review of offshore wind farm layout optimization and electrical system design methods," *Journal of Modern Power Systems and Clean Energy*, vol. 7, no. 5, pp. 975–986, 2019. 22

[69] J. Park and K. H. Law, "A data-driven, cooperative wind farm control to maximize the total power production," *Applied Energy*, vol. 165, pp. 151–165, 2016. 22, 51

[70] P. M. Gebraad, F. Teeuwisse, J. Van Wingerden, P. A. Fleming, S. Ruben, J. Marden, and L. Pao, "Wind plant power optimization through yaw control using a parametric model for wake effects—a cfd simulation study," *Wind Energy*, vol. 19, no. 1, pp. 95–114, 2016. 22, 29, 30, 31, 43, 52, 60

[71] T. Göçmen, P. Van der Laan, P.-E. Réthoré, A. P. Diaz, G. C. Larsen, and S. Ott, "Wind turbine wake models developed at the technical university of denmark: A review," *Renewable and Sustainable Energy Reviews*, vol. 60, pp. 752–769, 2016. 23

[72] G.-W. Qian and T. Ishihara, "Wind farm power maximization through wake steering with a new multiple wake model for prediction of turbulence intensity," *Energy*, vol. 220, p. 119680, 2021. 23, 33, 42, 43, 44, 46, 47

[73] D. R. VanLuvanee, "Investigation of observed and modeled wake effects at horns rev using windpro," *Technical University of Denmark Department of Mechanical Engineering*, 2006. 46

[74] M. Gaumond, P.-E. Réthoré, A. Bechmann, S. Ott, G. C. Larsen, A. Peña, and K. S. Hansen, "Benchmarking of wind turbine wake models in large offshore wind farms," in *Proceedings of the science of making torque from wind conference*, 2012. 46

[75] V. Santhanagopalan, M. Rotea, and G. Iungo, "Performance optimization of a wind turbine column for different incoming wind turbulence," *Renewable Energy*, vol. 116, pp. 232–243, 2018. 23

[76] N. Gionfra, G. Sandou, H. Siguerdidjane, D. Faille, and P. Loevenbruck, "Wind farm distributed pso-based control for constrained power generation maximization," *Renewable energy*, vol. 133, pp. 103–117, 2019. 23, 51, 53

[77] I. IEC, "61400-1: Wind turbines part 1: Design requirements," *International Electrotechnical Commission*, vol. 177, 2005. 23, 62, 63

[78] W. Atlas, "European wind atlas," 2012. 23

[79] J. Bartl, F. Pierella, and L. Sætrana, "Wake measurements behind an array of two model wind turbines," *Energy Procedia*, vol. 24, pp. 305–312, 2012. 24

[80] P. A. Fleming, P. M. Gebraad, S. Lee, J.-W. van Wingerden, K. Johnson, M. Churchfield, J. Michalakes, P. Spalart, and P. Moriarty, "Evaluating techniques

for redirecting turbine wakes using sowfa," *Renewable Energy*, vol. 70, pp. 211–218, 2014. 29, 43, 52

[81] D. Medici, "Experimental studies of wind turbine wakes: power optimisation and meandering," Ph.D. dissertation, KTH, 2005. 29

[82] B. Andresen, "Wake behind a wind turbine operating in yaw," Master's thesis, Institutt for energi-og prosessteknikk, 2013. 29

[83] Á. Jiménez, A. Crespo, and E. Migoya, "Application of a les technique to characterize the wake deflection of a wind turbine in yaw," *Wind energy*, vol. 13, no. 6, pp. 559–572, 2010. 29

[84] S. Guntur, N. Troldborg, and M. Gaunaa, "Application of engineering models to predict wake deflection due to a tilted wind turbine," in *EWEA 2012-European wind energy conference & exhibition*, 2012. 29

[85] P. Fleming, P. Gebraad, J.-W. van Wingerden, S. Lee, M. Churchfield, A. Scholbrock, J. Michalakes, K. Johnson, and P. Moriarty, "Sowfa super-controller: A high-fidelity tool for evaluating wind plant control approaches," National Renewable Energy Lab.(NREL), Golden, CO (United States), Tech. Rep., 2013. 29

[86] S. Voutsinas, K. Rados, and A. Zervos, "On the analysis of wake effects in wind parks," *Wind Engineering*, pp. 204–219, 1990. 33

[87] D. Quarton and J. Ainslie, "Turbulence in wind turbine wakes," *Wind Engineering*, pp. 15–23, 1990. 35, 36

[88] A. Crespo, J. Herna *et al.*, "Turbulence characteristics in wind-turbine wakes," *Journal of wind engineering and industrial aerodynamics*, vol. 61, no. 1, pp. 71–85, 1996. 35, 36

[89] U. Hassan, "A wind tunnel investigation of the wake structure within small wind turbine farms," 1993. 35, 36

[90] P. Vermeulen, "An experimental analysis of wind turbine wakes," in *3rd international symposium on wind energy systems*, 1980, pp. 431–450. 36

[91] F. Porté-Agel, Y.-T. Wu, and C.-H. Chen, "A numerical study of the effects of wind direction on turbine wakes and power losses in a large wind farm," *Energies*, vol. 6, no. 10, pp. 5297–5313, 2013. 37

[92] M. Abkar and F. Porté-Agel, "A new wind-farm parameterization for large-scale atmospheric models," *Journal of Renewable and Sustainable Energy*, vol. 7, no. 1, p. 013121, 2015. 37

[93] S. Frandsen and M. L. Thøgersen, "Integrated fatigue loading for wind turbines in wind farms by combining ambient turbulence and wakes," *Wind Engineering*, pp. 327–339, 1999. 37

[94] T. Knudsen, T. Bak, and M. Svenstrup, "Survey of wind farm control—power and fatigue optimization," *Wind Energy*, vol. 18, no. 8, pp. 1333–1351, 2015. 41, 44, 45

[95] A. C. Kheirabadi and R. Nagamune, "A quantitative review of wind farm control with the objective of wind farm power maximization," *Journal of Wind Engineering and Industrial Aerodynamics*, vol. 192, pp. 45–73, 2019. 41

[96] D. Madjidian, K. Martensson, and A. Rantzer, "A distributed coordination scheme for fatigue load minimization in wind farm," in *Proc. of American Control Conference*, 2011. 41

[97] S. Baros and A. M. Annaswamy, "Distributed optimal wind farm control for fatigue load minimization: A consensus approach," *International Journal of Electrical Power & Energy Systems*, vol. 112, pp. 452–459, 2019. 41

[98] D. Schlipf, P. Fleming, F. Haizmann, A. Scholbrock, M. Hofsäß, A. Wright, and P. W. Cheng, "Field testing of feedforward collective pitch control on the cart2 using a nacelle-based lidar scanner," in *Journal of Physics: Conference Series*, vol. 555, no. 1. IOP Publishing, 2014, p. 012090. 41

[99] E. Simley, H. Fürst, F. Haizmann, and D. Schlipf, "Optimizing lidars for wind turbine control applications—results from the iea wind task 32 workshop," *Remote Sensing*, vol. 10, no. 6, p. 863, 2018. 41

[100] S. Raach, S. Boersma, B. Doekemeijer, J.-W. van Wingerden, and P. W. Cheng, "Lidar-based closed-loop wake redirection in high-fidelity simulation," in *Journal of Physics: Conference Series*, vol. 1037, no. 3. IOP Publishing, 2018, p. 032016. 41

[101] H. S. Dhiman, D. Deb, and A. M. Foley, "Lidar assisted wake redirection in wind farms: A data driven approach," *Renewable Energy*, vol. 152, pp. 484–493, 2020. 41

[102] N. Majdi Nasab, J. Kilby, and L. Bakhtiaryfard, "Power maximisation of wind energy using wind speed sensors on stewart island," *Sensors*, vol. 22, no. 21, p. 8428, 2022. 41

[103] L. E. Andersson, O. Anaya-Lara, J. O. Tande, K. O. Merz, and L. Imsland, "Wind farm control-part i: A review on control system concepts and structures," *IET Renewable Power Generation*, vol. 15, no. 10, pp. 2085–2108, 2021. 41

[104] R. Shakoor, M. Y. Hassan, A. Raheem, and N. Rasheed, "Wind farm layout optimization using area dimensions and definite point selection techniques," *Renewable energy*, vol. 88, pp. 154–163, 2016. 42

[105] A. P. Stanley, J. King, and A. Ning, "Wind farm layout optimization with loads considerations," in *Journal of Physics: Conference Series*, vol. 1452, no. 1. IOP Publishing, 2020, p. 012072. 42, 70

[106] M. F. Howland, S. K. Lele, and J. O. Dabiri, "Wind farm power optimization through wake steering," *Proceedings of the National Academy of Sciences*, vol. 116, no. 29, pp. 14 495–14 500, 2019. 43

[107] E. Bossanyi, "Combining induction control and wake steering for wind farm energy and fatigue loads optimisation," in *Journal of Physics: Conference Series*, vol. 1037, no. 3. IOP Publishing, 2018, p. 032011. 43

[108] M. Charles, D. T. Oyedokun, and M. Dlodlo, "Power maximization and turbulence intensity management through axial induction-based optimization and efficient static turbine deployment," *Energies*, vol. 14, no. 16, p. 4943, 2021. 43, 51

[109] G. Gualtieri, "Comparative analysis and improvement of grid-based wind farm layout optimization," *Energy Conversion and Management*, vol. 208, p. 112593, 2020. 43

[110] F. Liu, X. Ju, N. Wang, L. Wang, and W.-J. Lee, "Wind farm macro-siting optimization with insightful bi-criteria identification and relocation mechanism in genetic algorithm," *Energy Conversion and Management*, vol. 217, p. 112964, 2020. 43, 53

[111] M. Charles, D. T. Oyedokun, and M. Dlodlo, "Annual energy production maximisation effects on turbine thrust coefficient and turbulence intensity," in *2023 IEEE AFRICON*. 44

[112] G. Bo, D. Man, Z. Meng, Z. Hongtao, and H. Hu, "A wind farm power maximization method based on multi-strategy improved sparrow search algorithm," *Journal of Solar Energy Engineering*, vol. 146, no. 3, 2024. 44, 47

[113] J. Park, S. Kwon, and K. H. Law, "Wind farm power maximization based on a cooperative static game approach," in *Active and Passive Smart Structures and Integrated Systems 2013*, vol. 8688. SPIE, 2013, pp. 204–218. 44, 47

[114] B. Badrzadeh, M. Bradt, N. Castillo, R. Janakiraman, R. Kennedy, S. Klein, T. Smith, and L. Vargas, "Wind power plant scada and controls," in *2011 IEEE Power and Energy Society General Meeting*. IEEE, 2011, pp. 1–7. 48, 49

[115] I. E. C. (IEC), "Wind energy generation systems - part 25-1: Communications for monitoring and control of wind power plants - overall description of principles and models," https://webstore.iec.ch/publication/61087, 2017, international Electrotechnical Commision (IEC), Accessed July 17, 2022. 48

[116] G. W. E. C. (GWEC), "Global wind report 2021," https://gwec.net/wp-content/uploads/2021/03/GWEC-Global-Wind-Report-2021.pdf, 2021, global Wind Energy Commission (GWEC), Accessed July 17, 2022. 50

[117] Z. Liu, J. Peng, X. Hua, and Z. Zhu, "Wind farm optimization considering non-uniformly distributed turbulence intensity," *Sustainable Energy Technologies and Assessments*, vol. 43, p. 100970, 2021. 51

[118] R. Asfour, T. Brahimi, and M. El-Amin, "Wind farm layout: Modeling and optimization using genetic algorithm," in *IOP Conference Series: Earth and Environmental Science*, vol. 1008, no. 1. IOP Publishing, 2022, p. 012004. 53

[119] B. Kaya and E. Oğuz, "Investigation of layout optimization for offshore wind farms and a case study for a region in turkey," *Ocean Engineering*, vol. 266, p. 112807, 2022. 53

[120] A. C. Pillai, J. Chick, L. Johanning, M. Khorasanchi, and S. Barbouchi, "Comparison of offshore wind farm layout optimization using a genetic algorithm and a particle swarm optimizer," in *International Conference on Offshore Mechanics and Arctic Engineering*, vol. 49972. American Society of Mechanical Engineers, 2016, p. V006T09A033. 53

[121] T. Kunakote, N. Sabangban, S. Kumar, G. G. Tejani, N. Panagant, N. Pholdee, S. Bureerat, and A. R. Yildiz, "Comparative performance of twelve metaheuristics for wind farm layout optimisation," *Archives of Computational Methods in Engineering*, pp. 1–14, 2022. 53

[122] S. Bauer, Lucas & Matysik, "Gamesa g128-5.0mw," https://en.wind-turbine-models.com/turbines/767-gamesa-g128-5.0mw, accessed: July 12, 2021. 59, 71

[123] R. H. Thuillier and U. O. Lappe, "Wind and temperature profile characteristics from observations on a 1400 ft tower," *Journal of Applied Meteorology and Climatology*, vol. 3, no. 3, pp. 299 – 306, 1964. [Online]. Available: https://journals.ametsoc.org/view/journals/apme/3/3/1520-0450_1964_003_0299_watpcf_2_0_co_2.xml 71

[124] N. BV, "Data of the noordzeewind monitoring and evaluation programme (nsw-mep)," http://www.noordzeewind.nl/en/knowledge/reportsdata, 2013, accessed August 08, 2018. 167

[125] A. R. Henderson, C. Morgan, B. Smith, H. C. Sørensen, R. J. Barthelmie, and B. Boesmans, "Offshore wind energy in europe—a review of the state-of-the-art," *Wind Energy: An International Journal for Progress and Applications in Wind Power Conversion Technology*, vol. 6, no. 1, pp. 35–52, 2003. 172

Appendices

A Wind turbine details

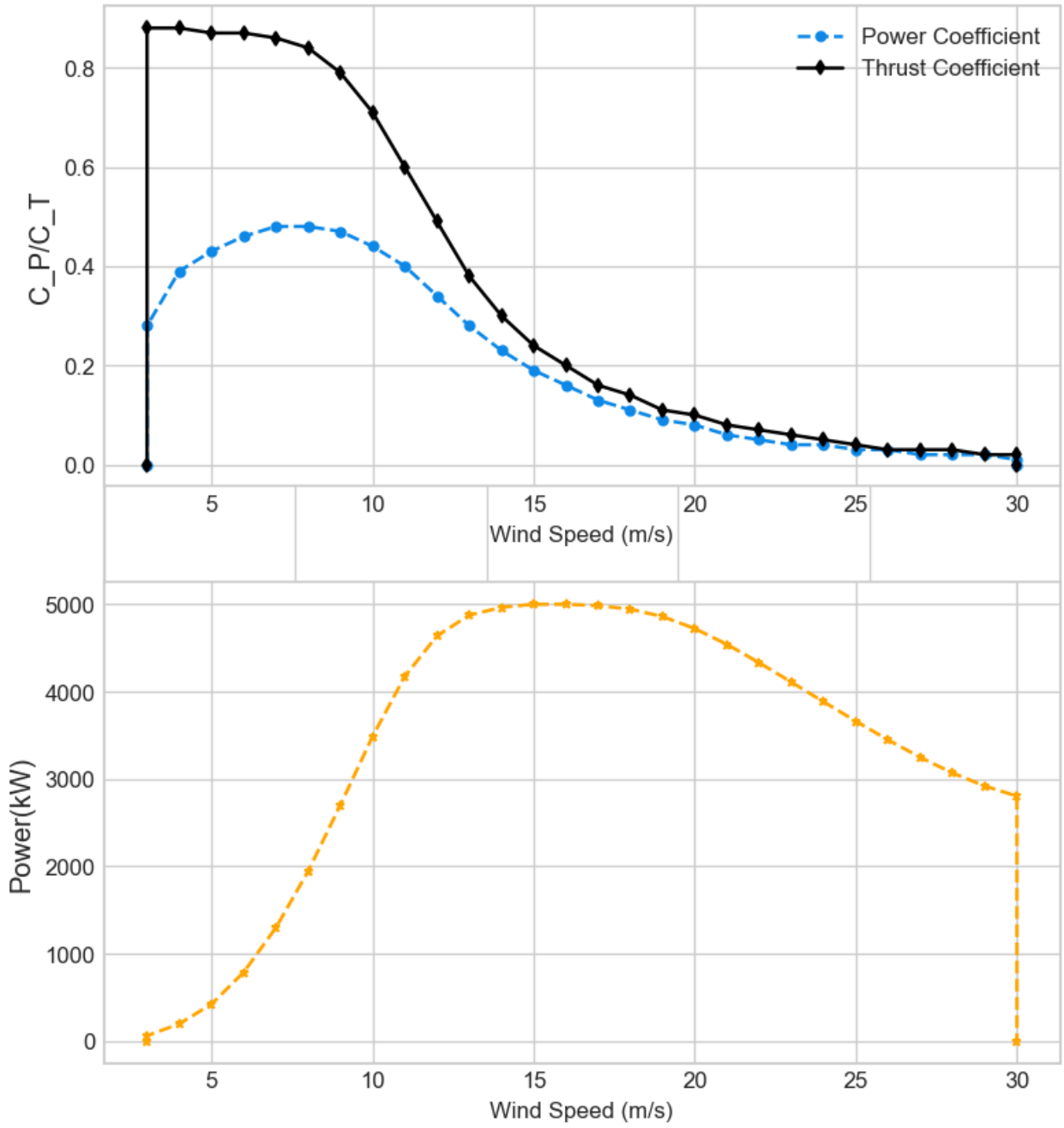

Figure 1: Coefficient (Power and Thrust) curves and power curve for the Gamesa-g128-5.0MW wind turbine

The single plot of all three parameters can be found at en.wind-turbine-models.com

B Wind plant details

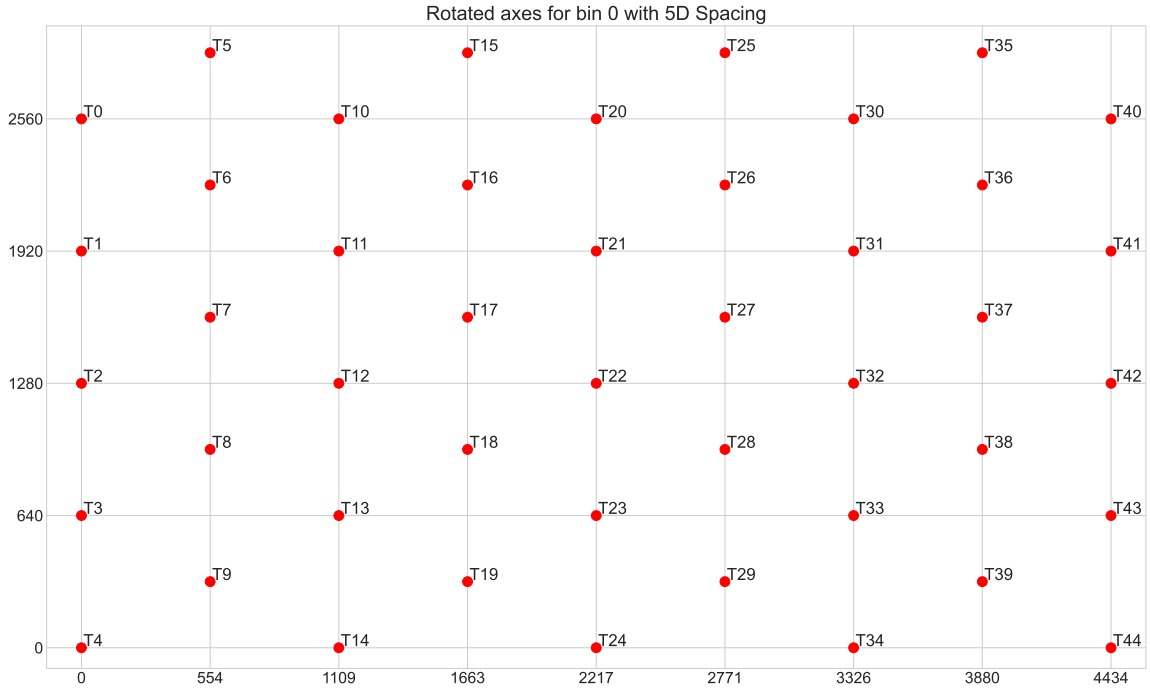

Figure 2: Wind plant array with $5D$ minimum T-2-T distance, Bin 0

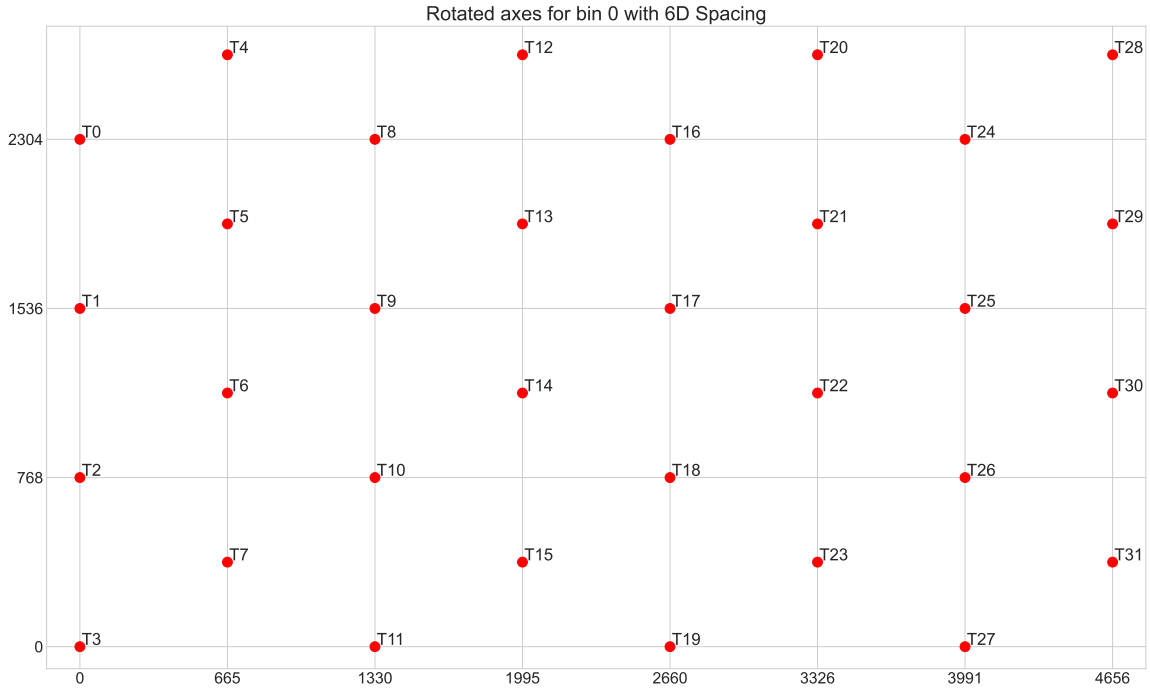

Figure 3: Wind plant array with $6D$ minimum T-2-T distance, Bin 0

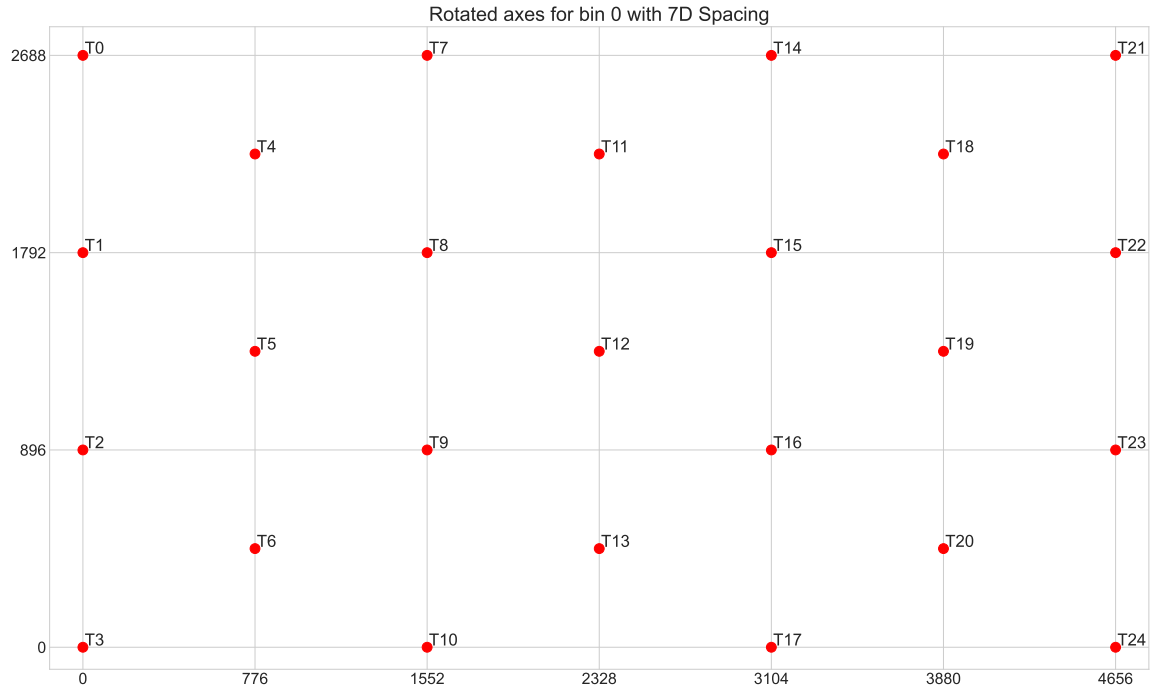

Figure 4: Wind plant array with $7D$ minimum T-2-T distance, Bin 0

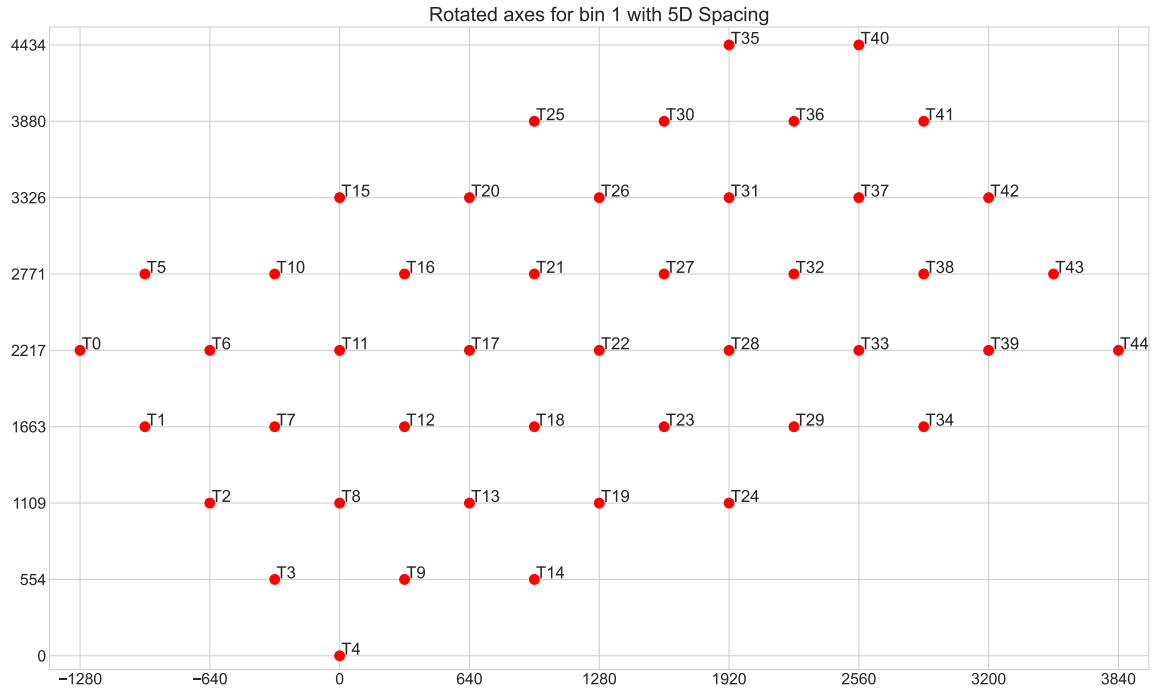

Figure 5: Wind plant array with 5D minimum T-2-T distance, Bin 1

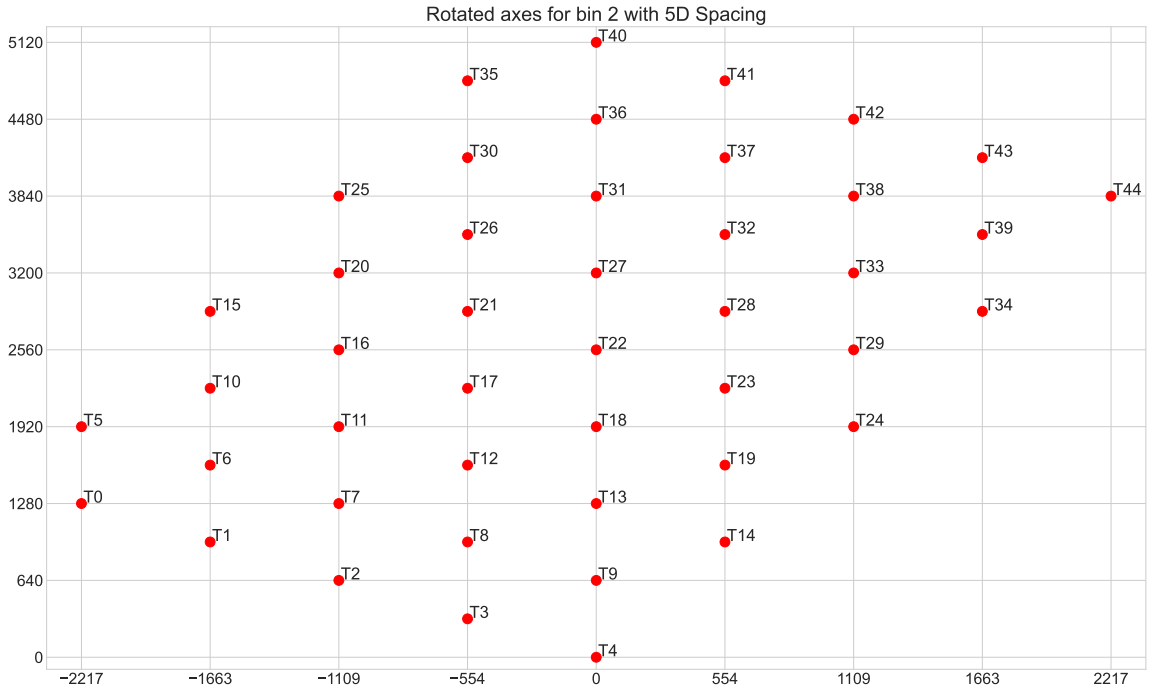

Figure 6: Wind plant array with 5D minimum T-2-T distance, Bin 2

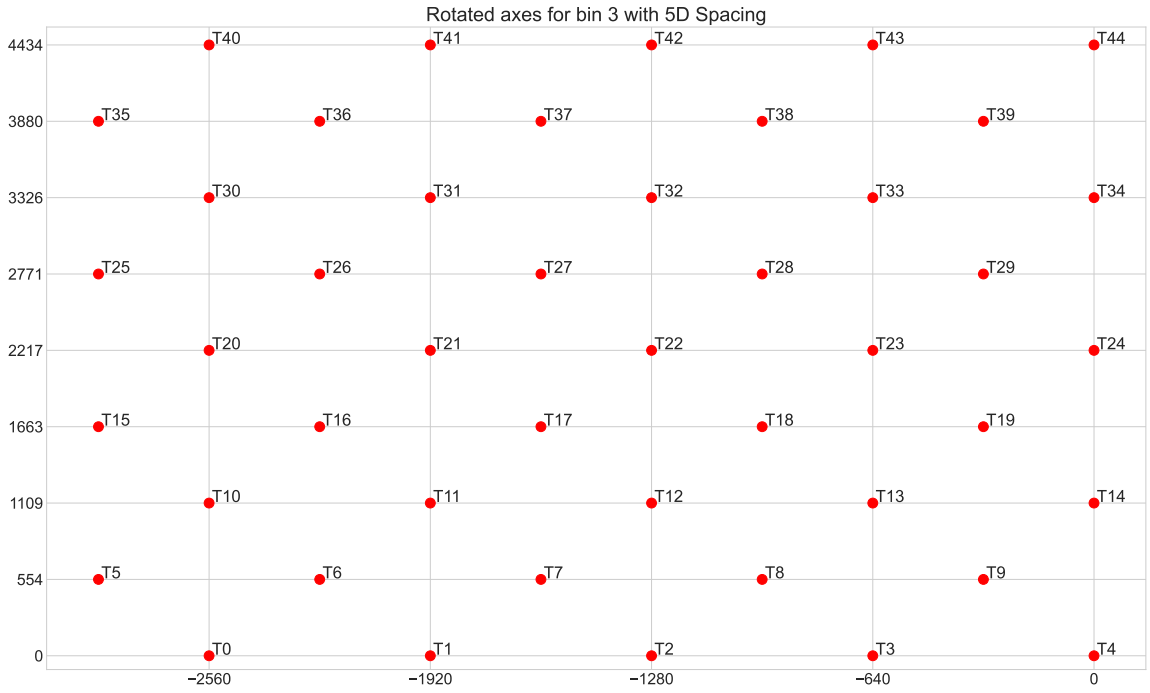

Figure 7: Wind plant array with 5D minimum T-2-T distance, Bin 3

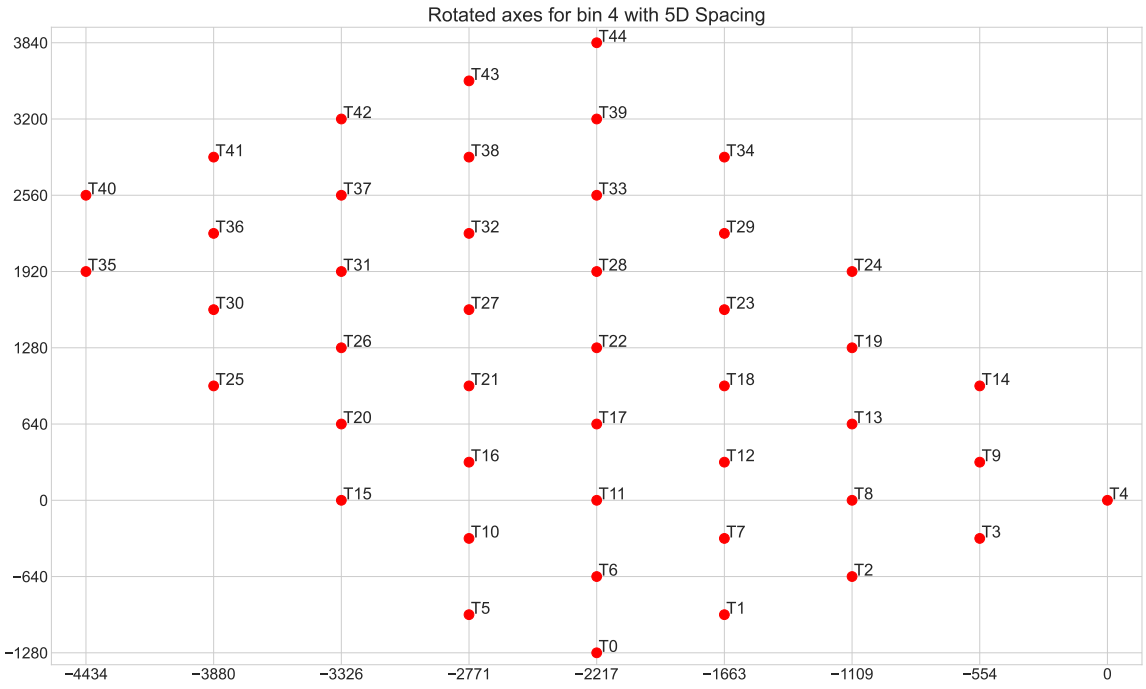

Figure 8: Wind plant array with 5D minimum T-2-T distance, Bin 4

Figure 9: Wind plant array with 5D minimum T-2-T distance, Bin 5

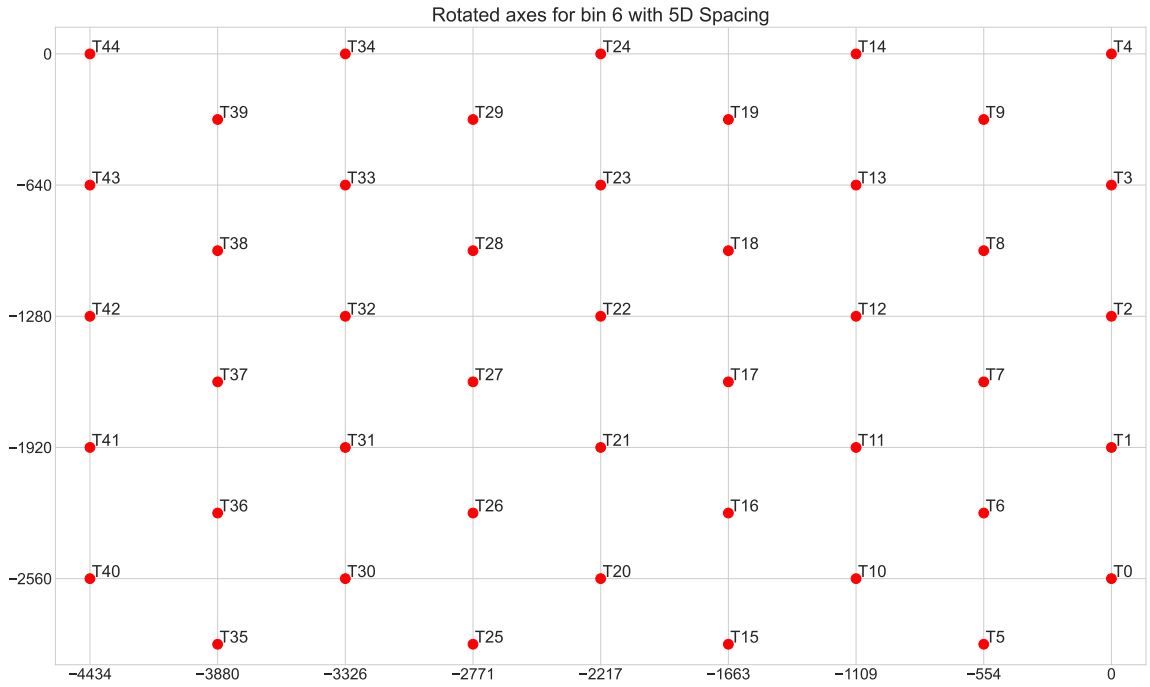

Figure 10: Wind plant array with 5D minimum T-2-T distance, Bin 6

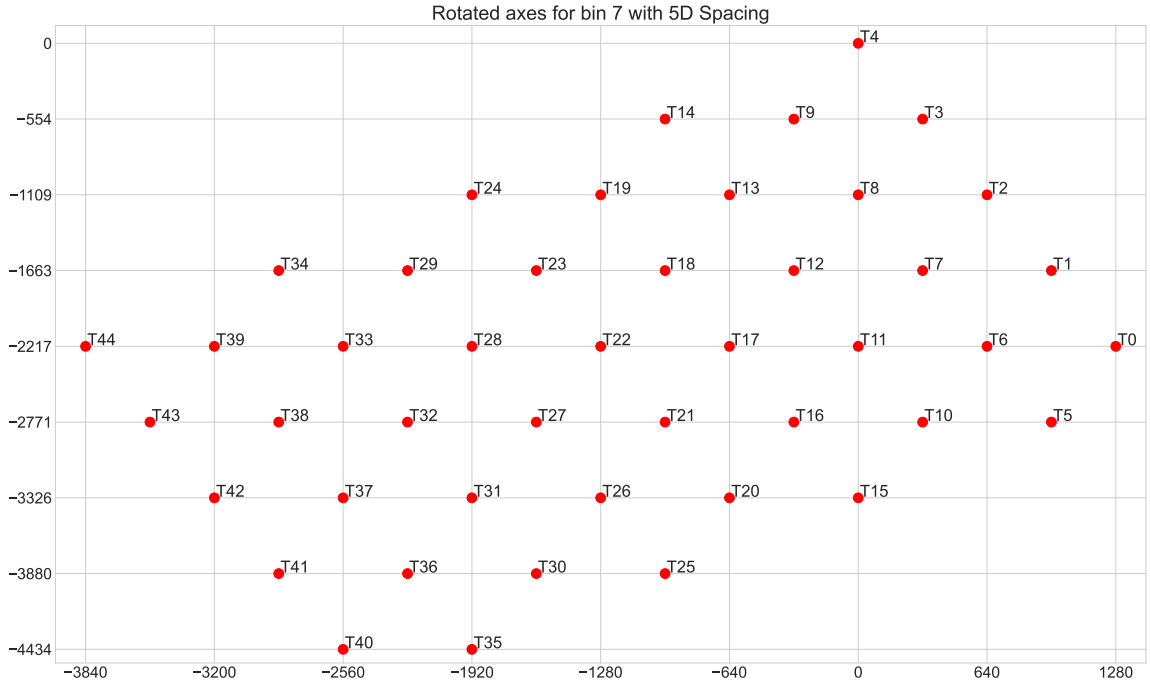

Figure 11: Wind plant array with 5D minimum T-2-T distance, Bin 7

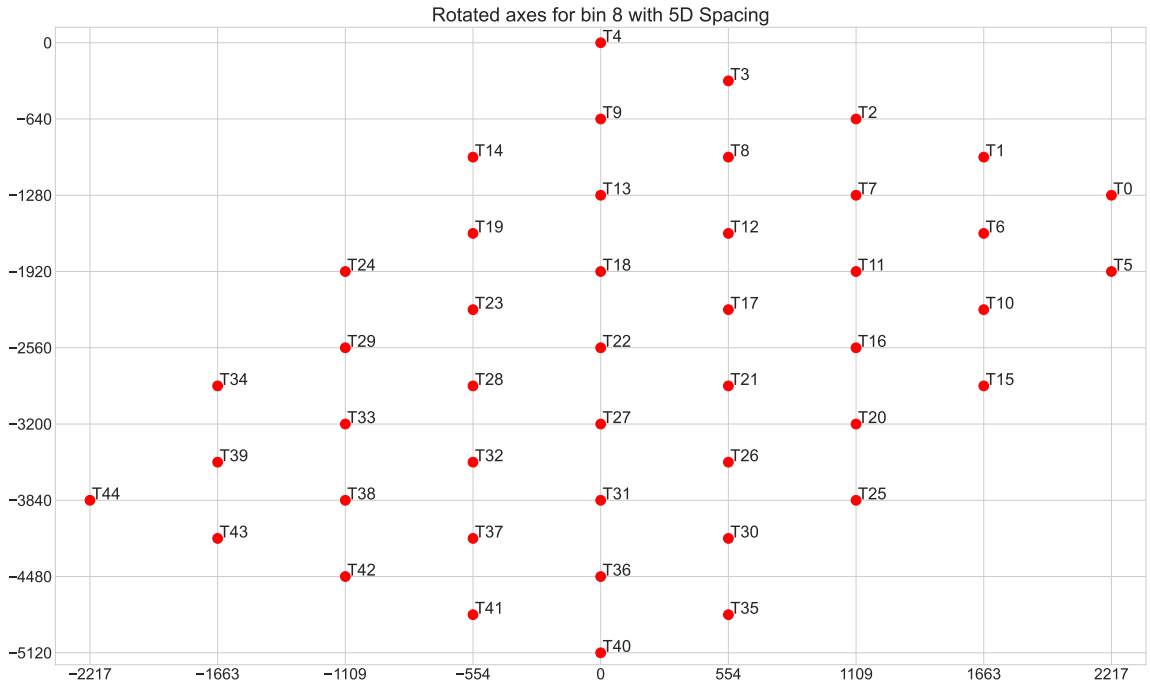

Figure 12: Wind plant array with 5D minimum T-2-T distance, Bin 8

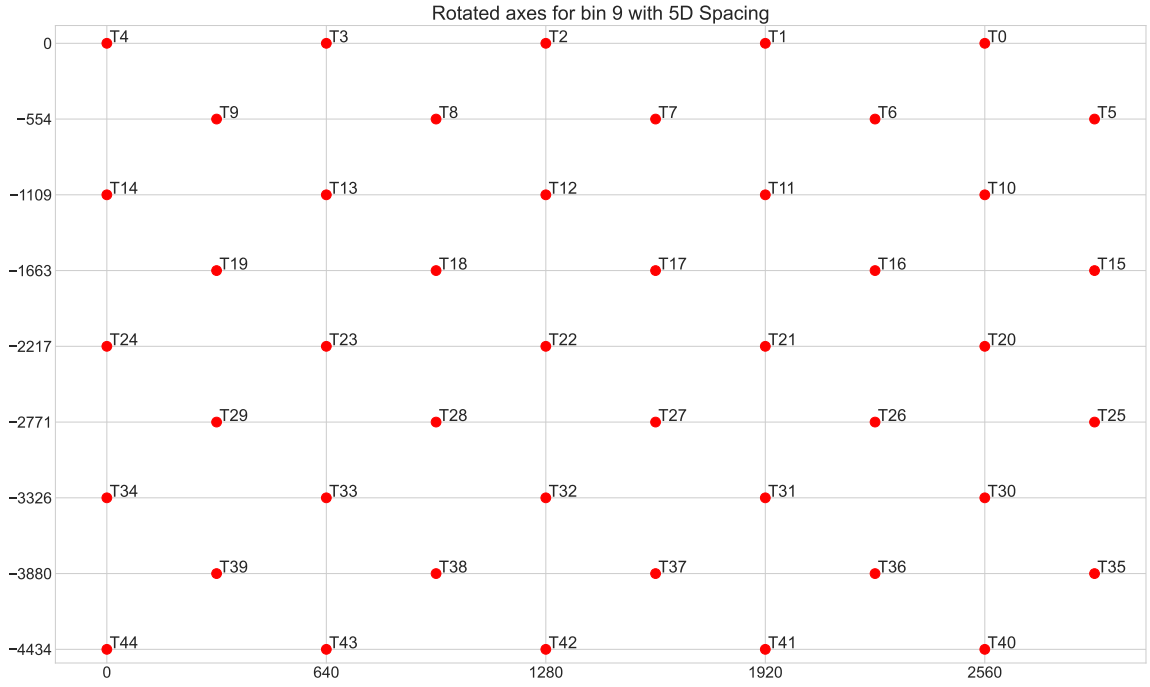

Figure 13: Wind plant array with 5D minimum T-2-T distance, Bin 9

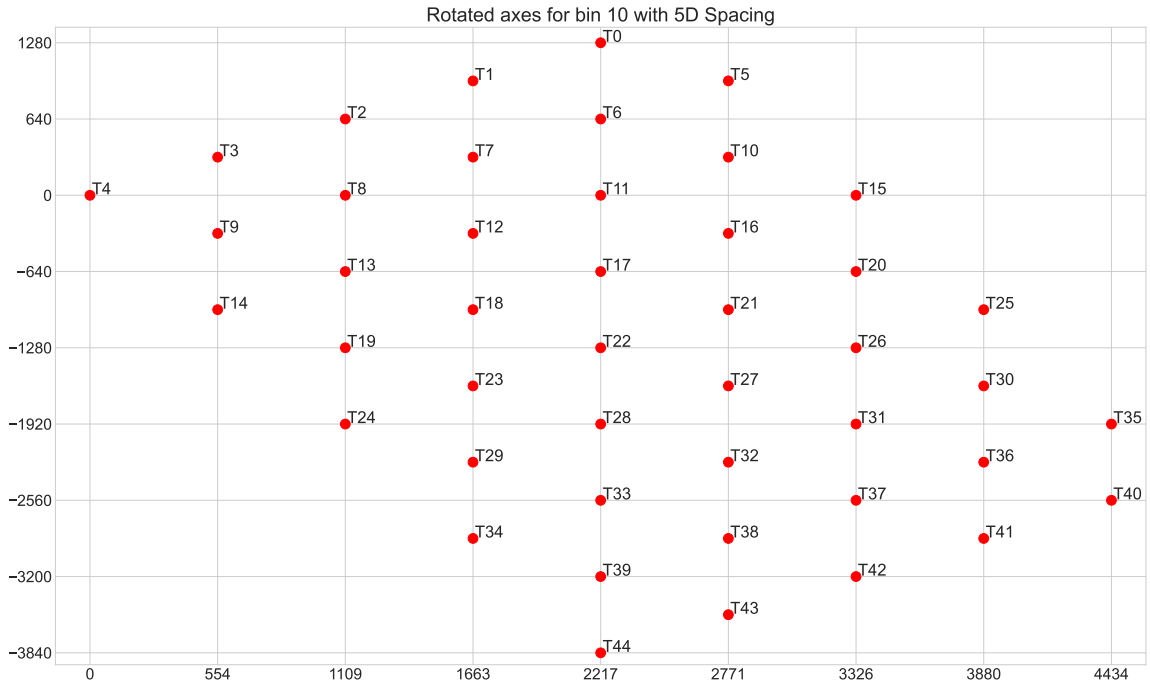

Figure 14: Wind plant array with 5D minimum T-2-T distance, Bin 10

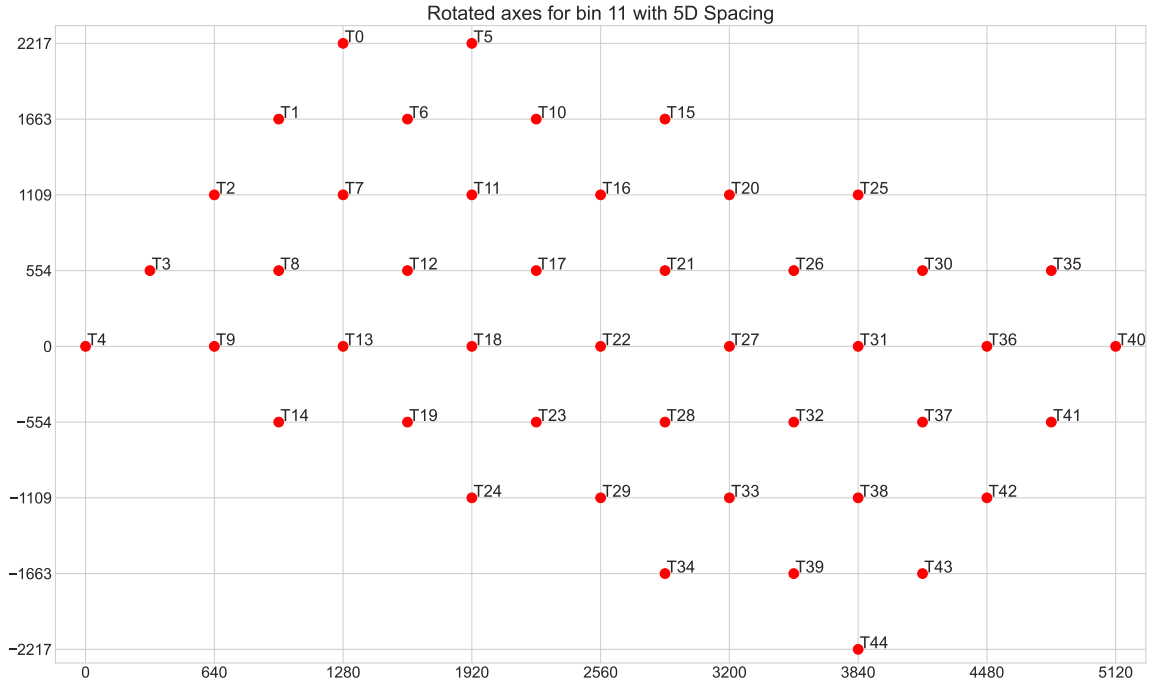

Figure 15: Wind plant array with 5D minimum T-2-T distance, Bin 11

C Model details

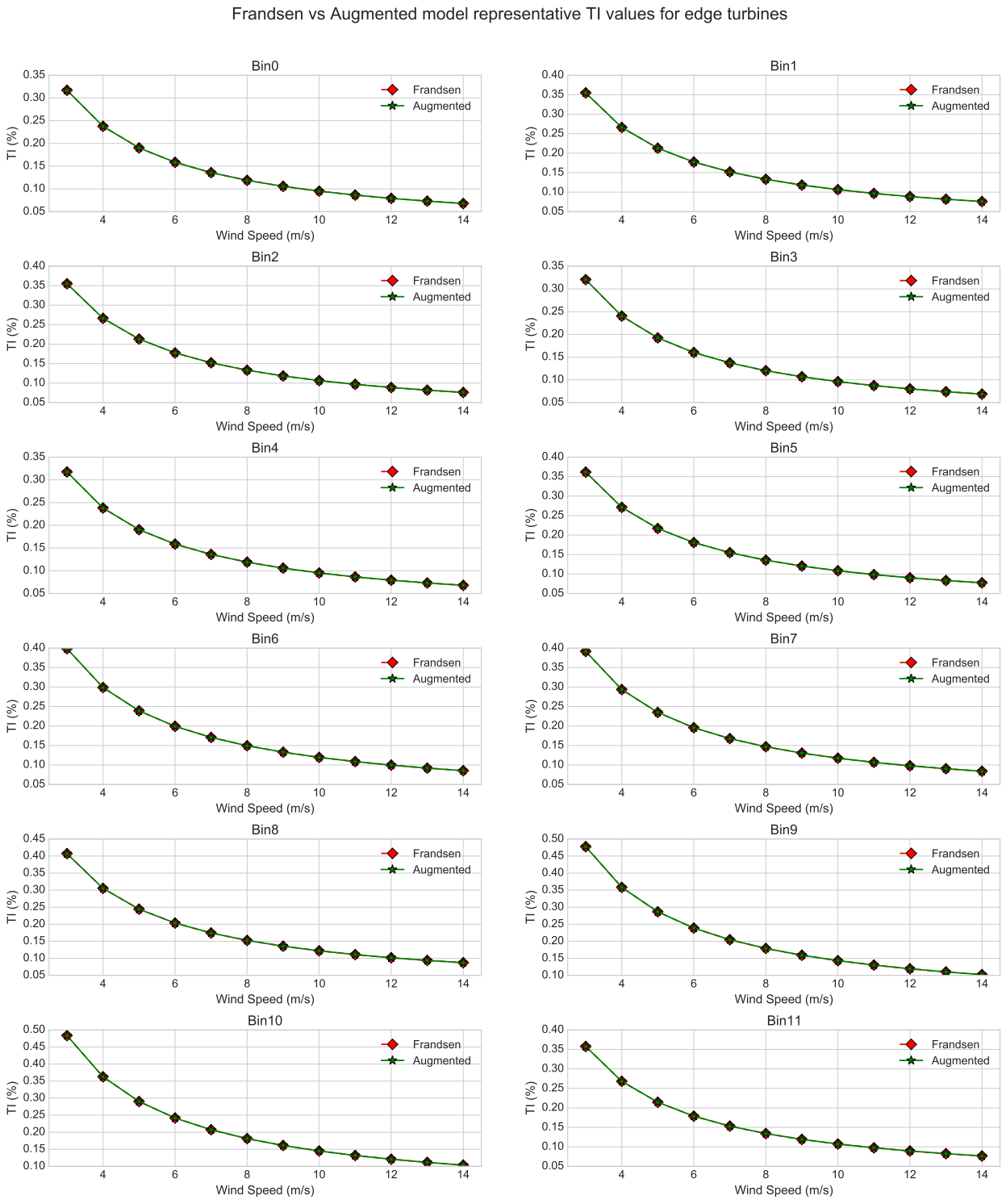

Figure 16: Border turbine TI comparison for all wind speeds and bins

D More results

D.1 WP analysis3

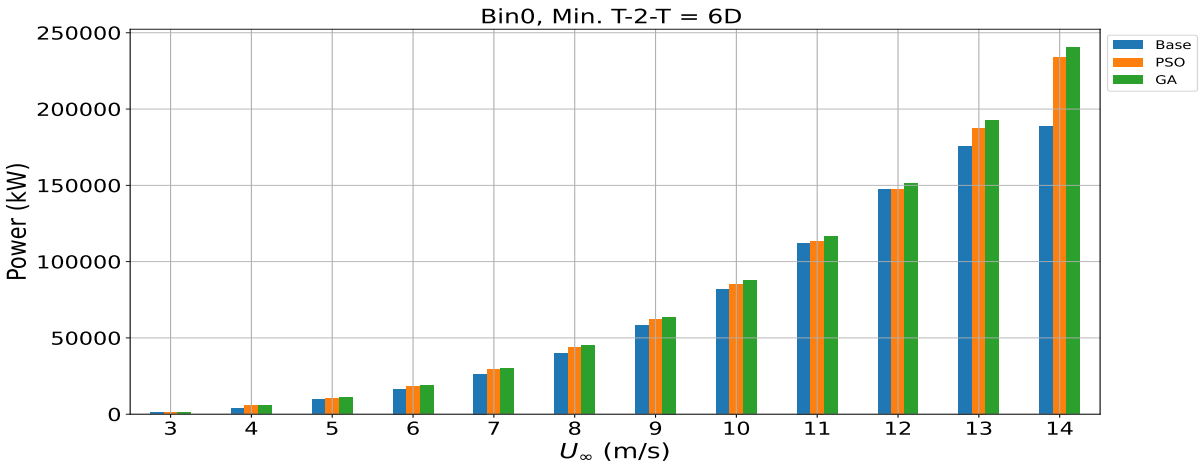

Figure 17: Generated power for different wind speeds: Minimum T-2-T distance = $6D$.

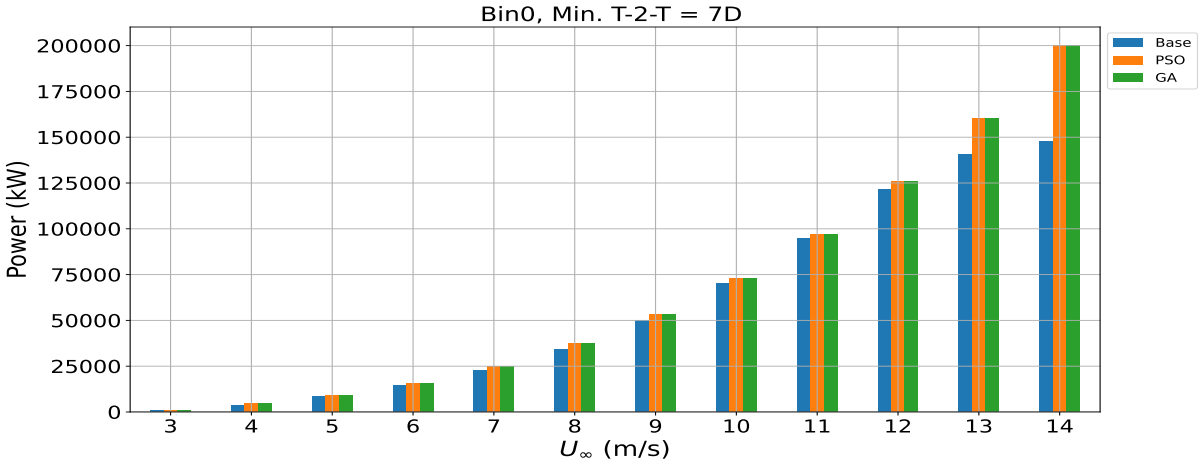

Figure 18: Generated power for different wind speeds: Minimum T-2-T distance = $7D$.

D.2 CT analysis3

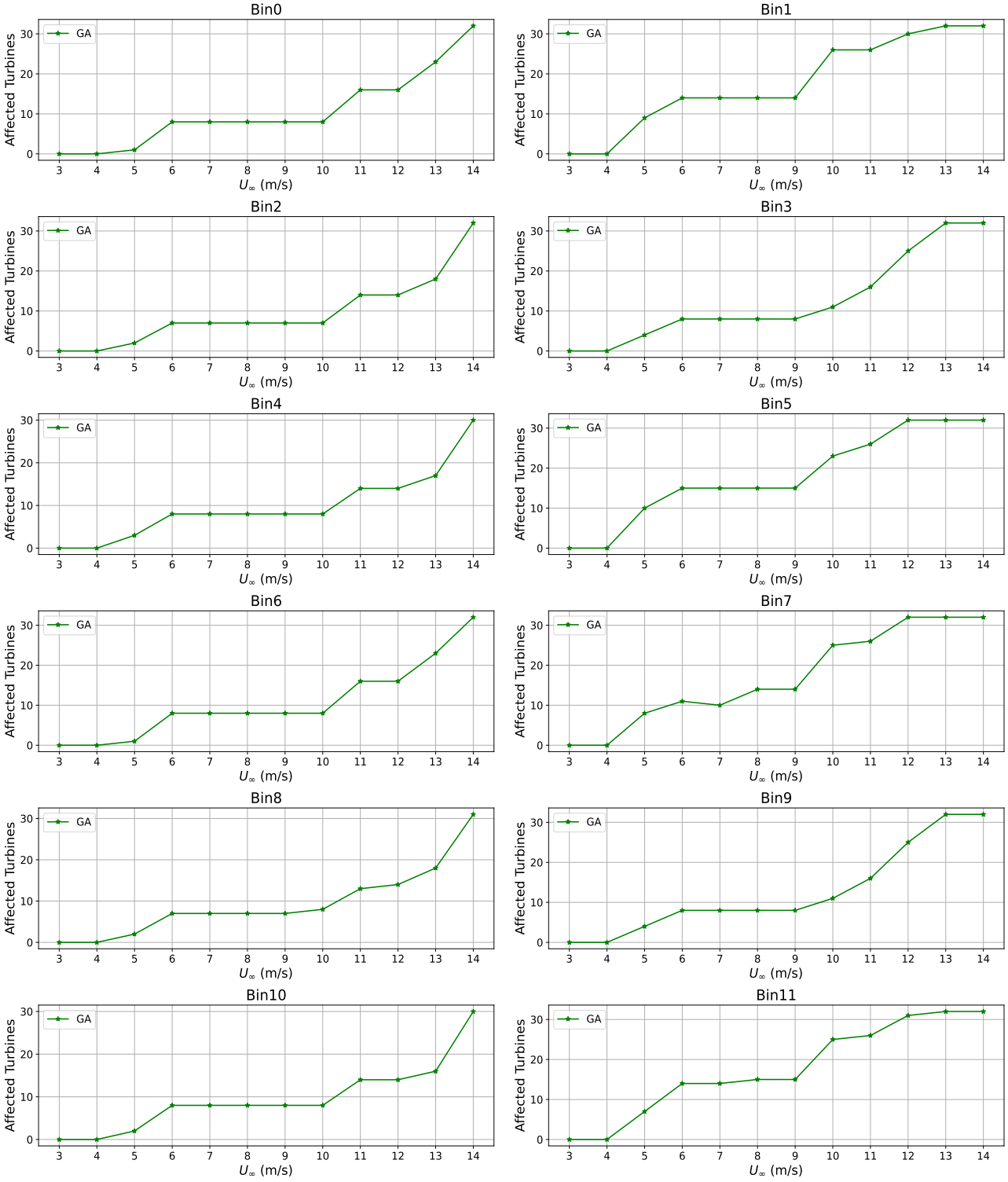

Figure 19: Total C_T-defaulting turbines for GA-optimised $6D$ scenario: Unconstrained case, All bins.

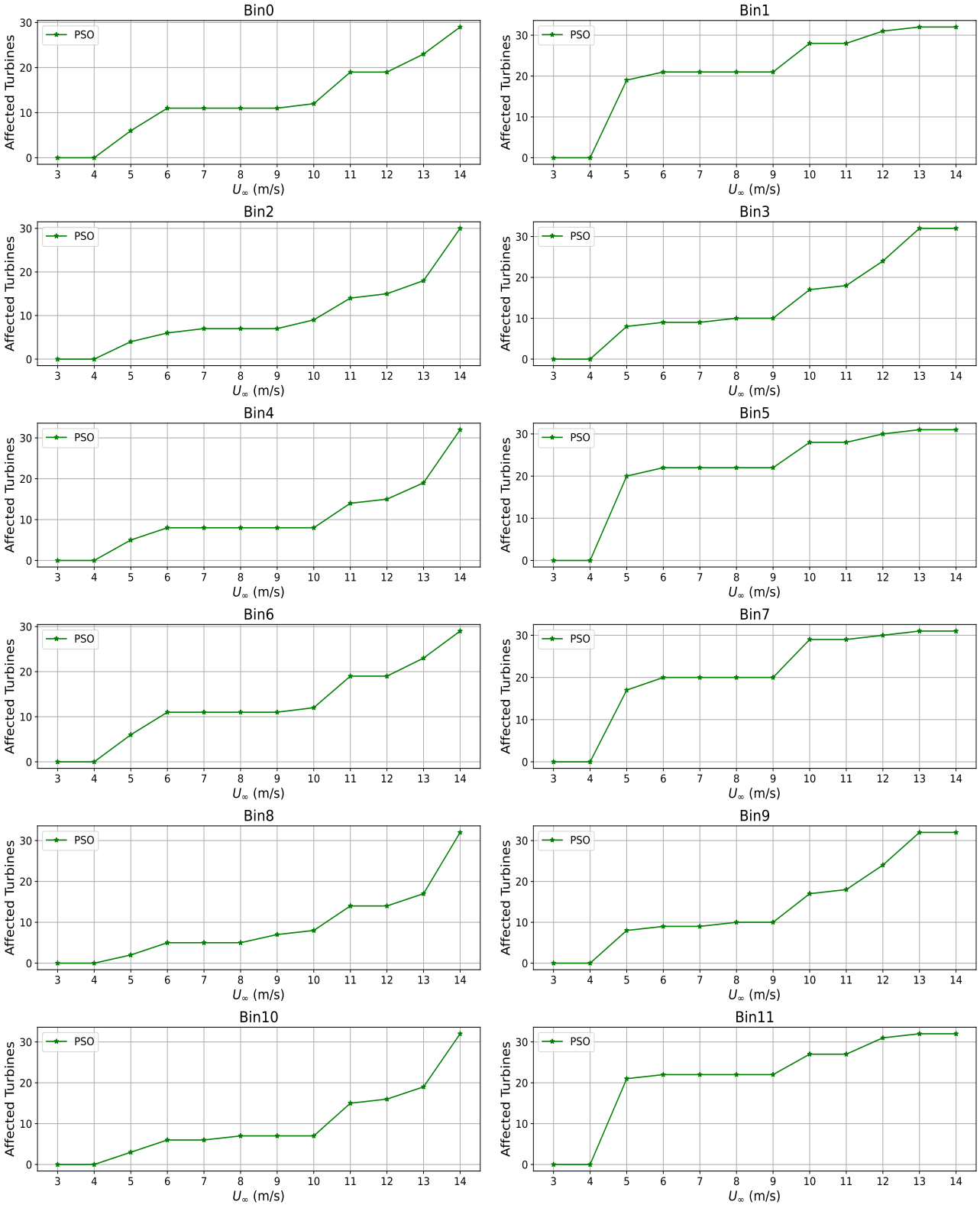

Figure 20: Total C_T-defaulting turbines for PSO-optimised $6D$ scenario: Unconstrained case, All bins.

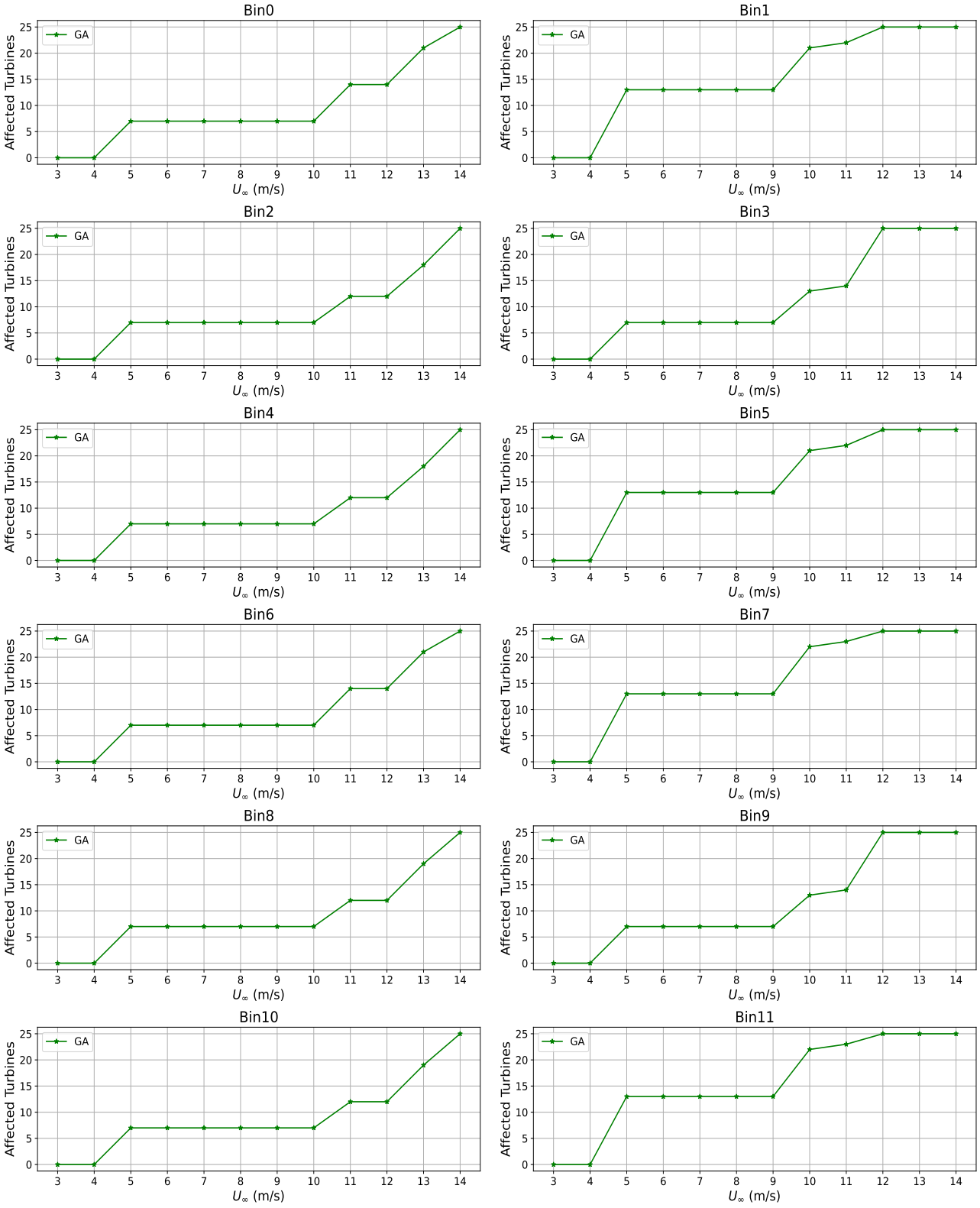

Figure 21: Total C_T-defaulting turbines for GA-optimised $7D$ scenario: Unconstrained case, All bins.

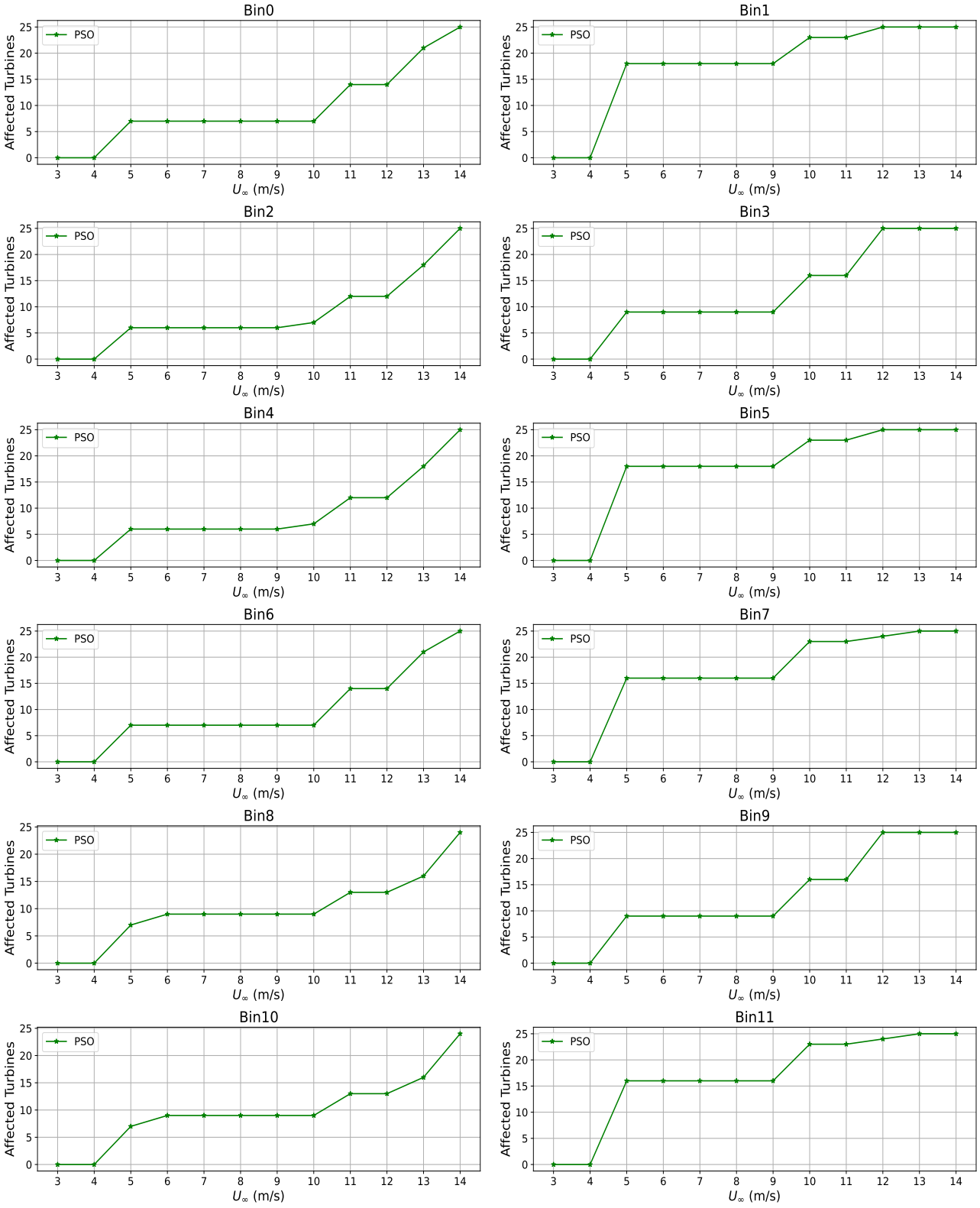

Figure 22: Total C_T-defaulting turbines for PSO-optimised $7D$ scenario: Unconstrained case, All bins.

D.3 TI analysis3

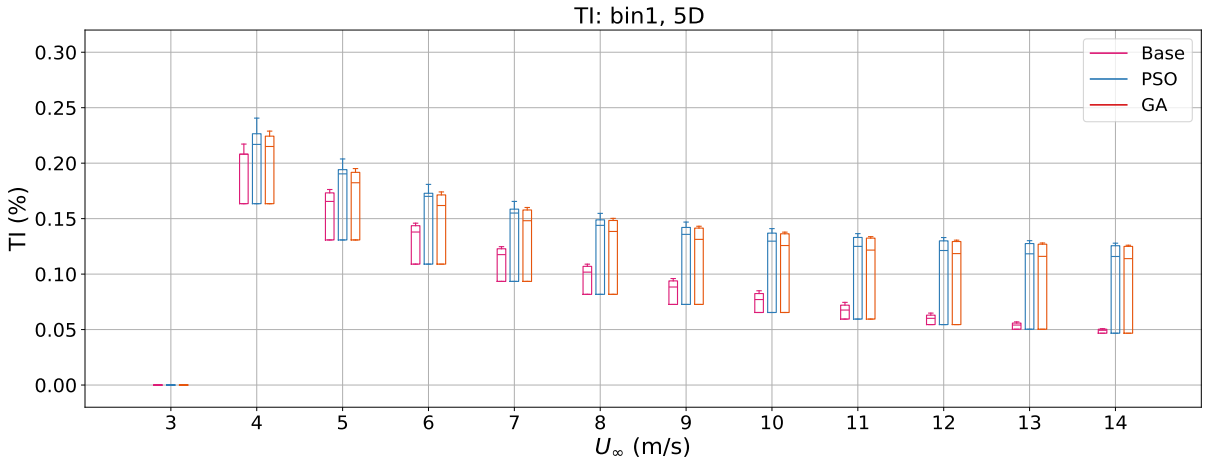

Figure 23: Box plots of WP turbulence intensities at all U_∞ values: Bin 1, $5D$.

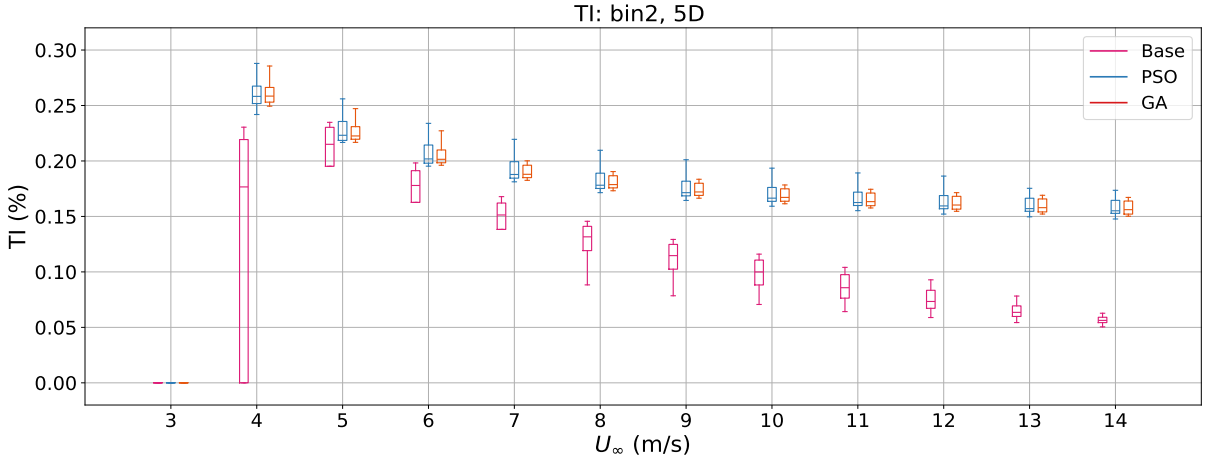

Figure 24: Box plots of WP turbulence intensities at all U_∞ values: Bin 2, $5D$.

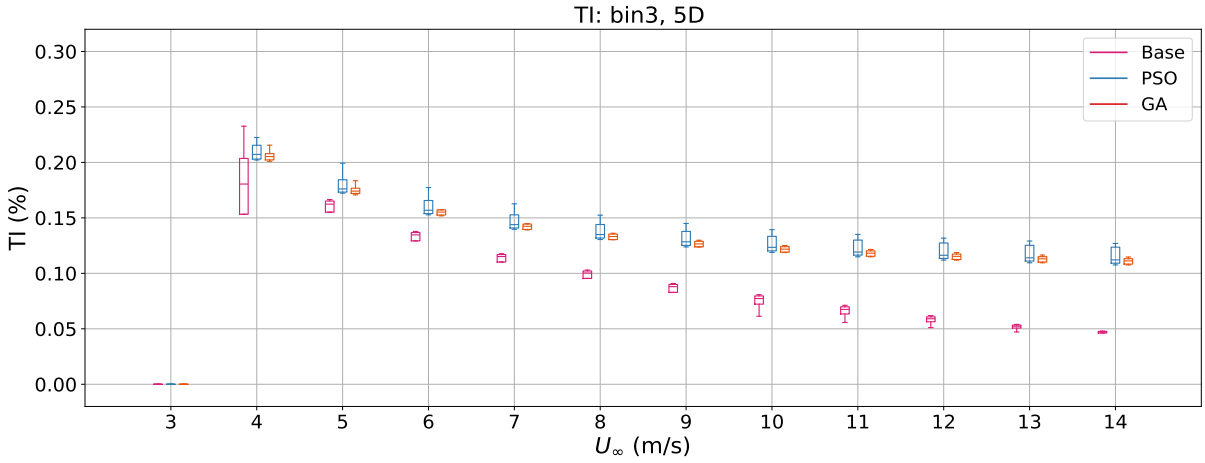

Figure 25: Box plots of WP turbulence intensities at all U_∞ values: Bin 3, $5D$.

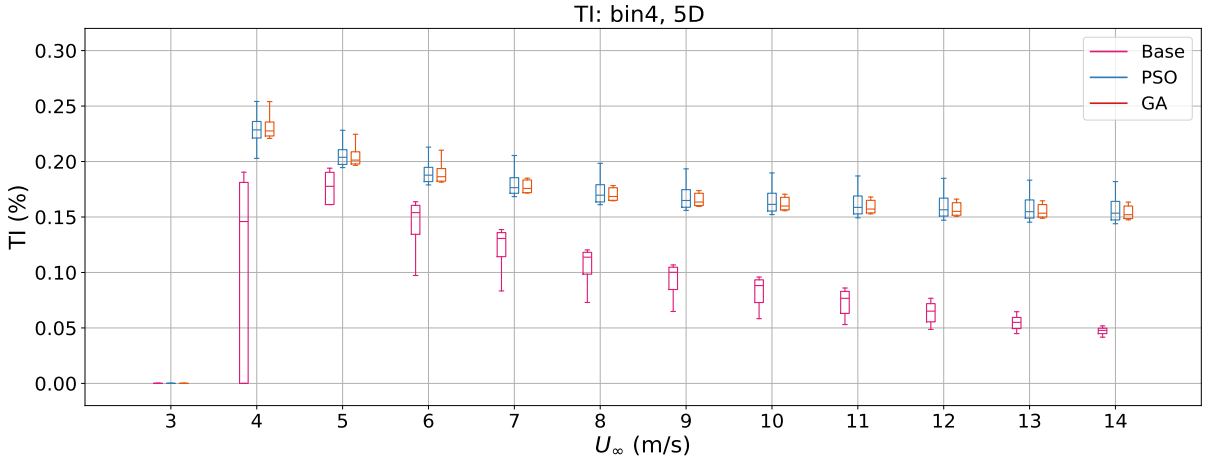

Figure 26: Box plots of WP turbulence intensities at all U_∞ values: Bin 4, $5D$.

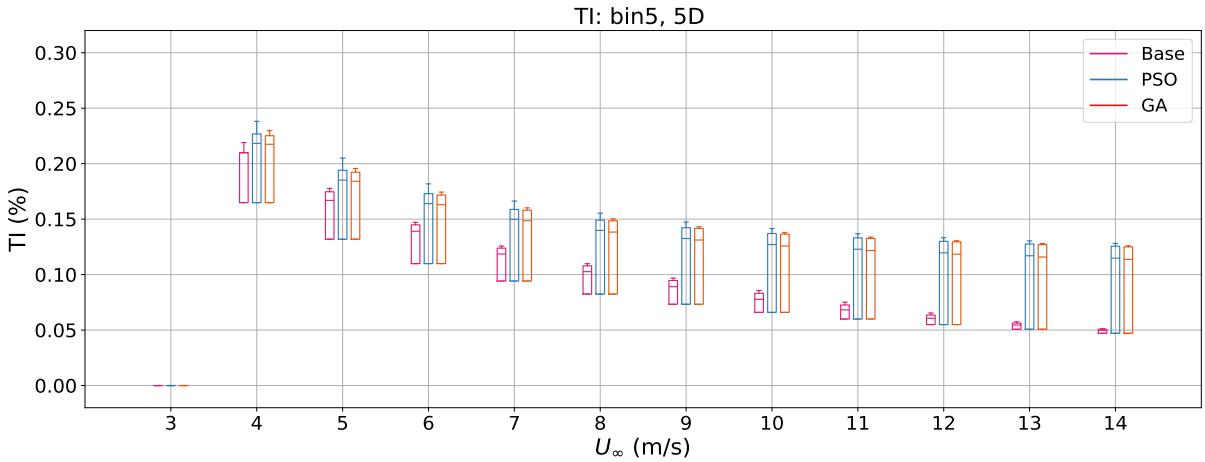

Figure 27: Box plots of WP turbulence intensities at all U_∞ values: Bin 5, $5D$.

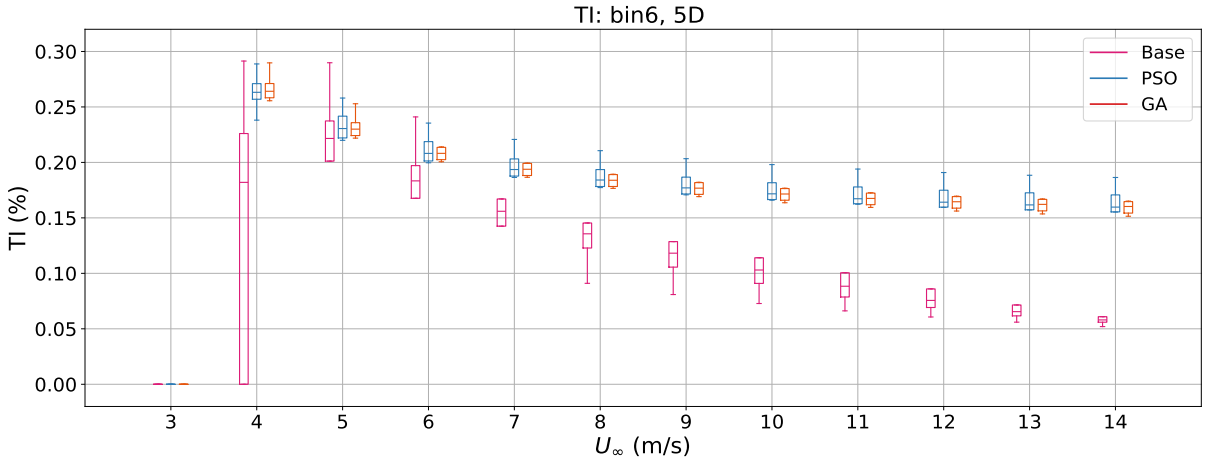

Figure 28: Box plots of WP turbulence intensities at all U_∞ values: Bin 6, $5D$.

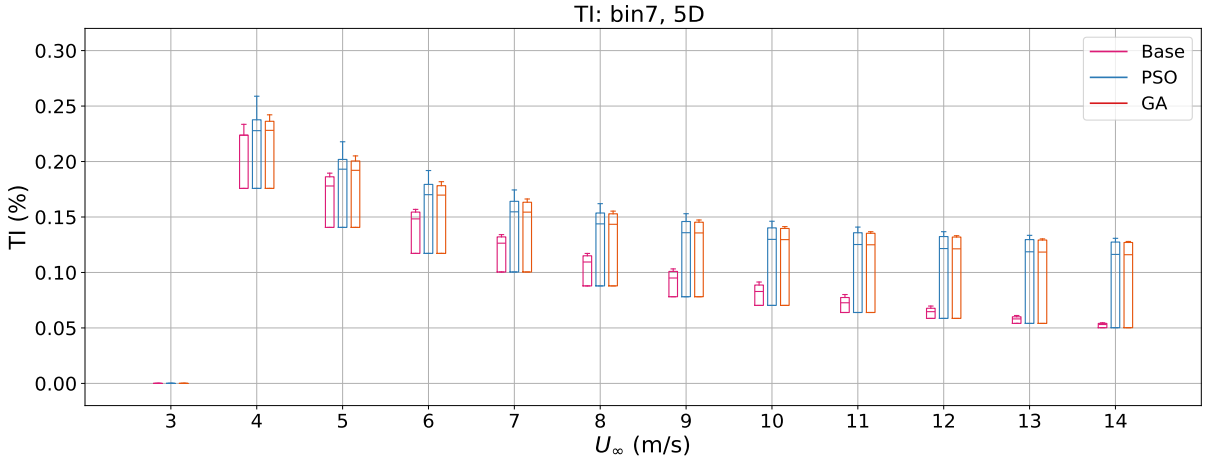

Figure 29: Box plots of WP turbulence intensities at all U_∞ values: Bin 7, $5D$.

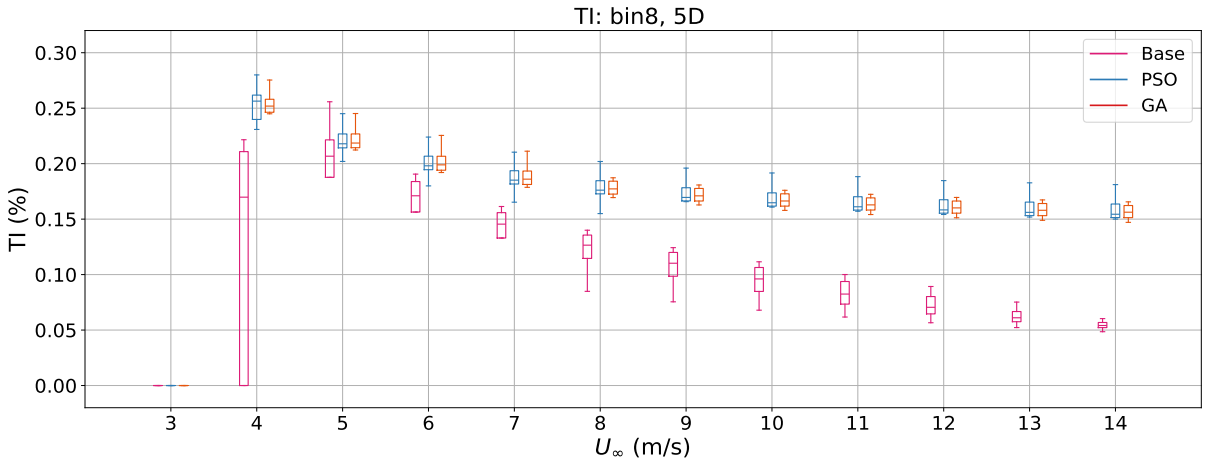

Figure 30: Box plots of WP turbulence intensities at all U_∞ values: Bin 8, $5D$.

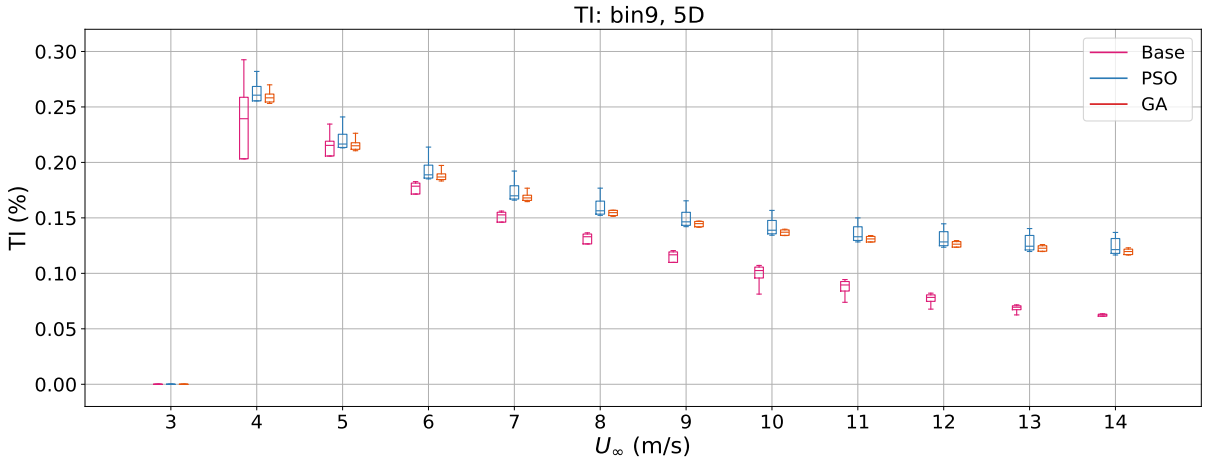

Figure 31: Box plots of WP turbulence intensities at all U_∞ values: Bin 9, $5D$.

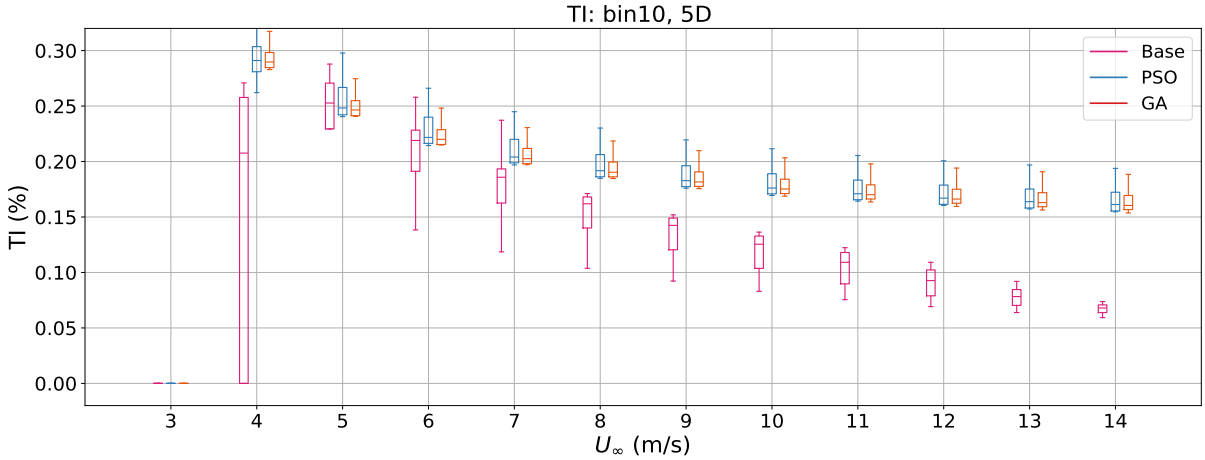

Figure 32: Box plots of WP turbulence intensities at all U_∞ values: Bin 10, $5D$.

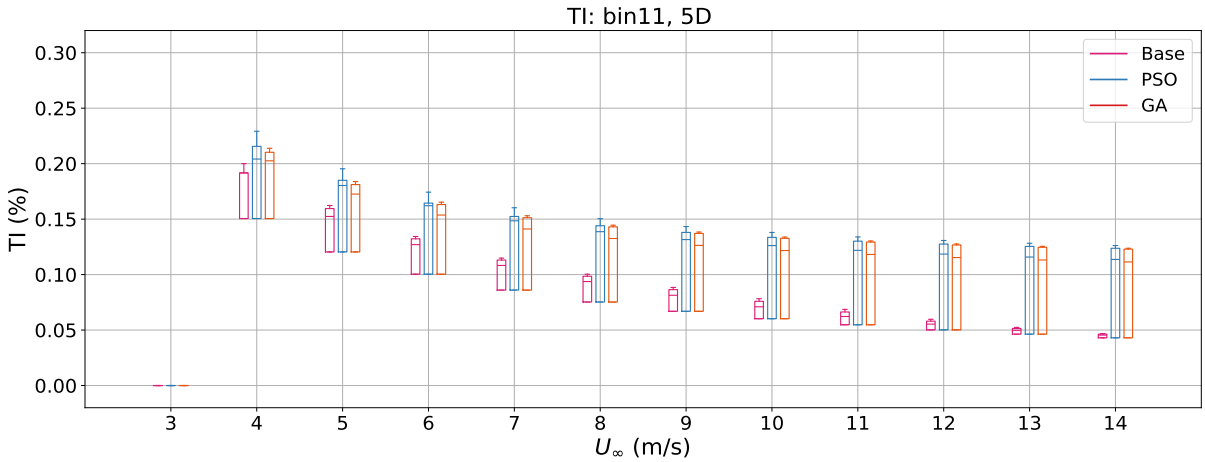

Figure 33: Box plots of WP turbulence intensities at all U_∞ values: Bin 11, $5D$.

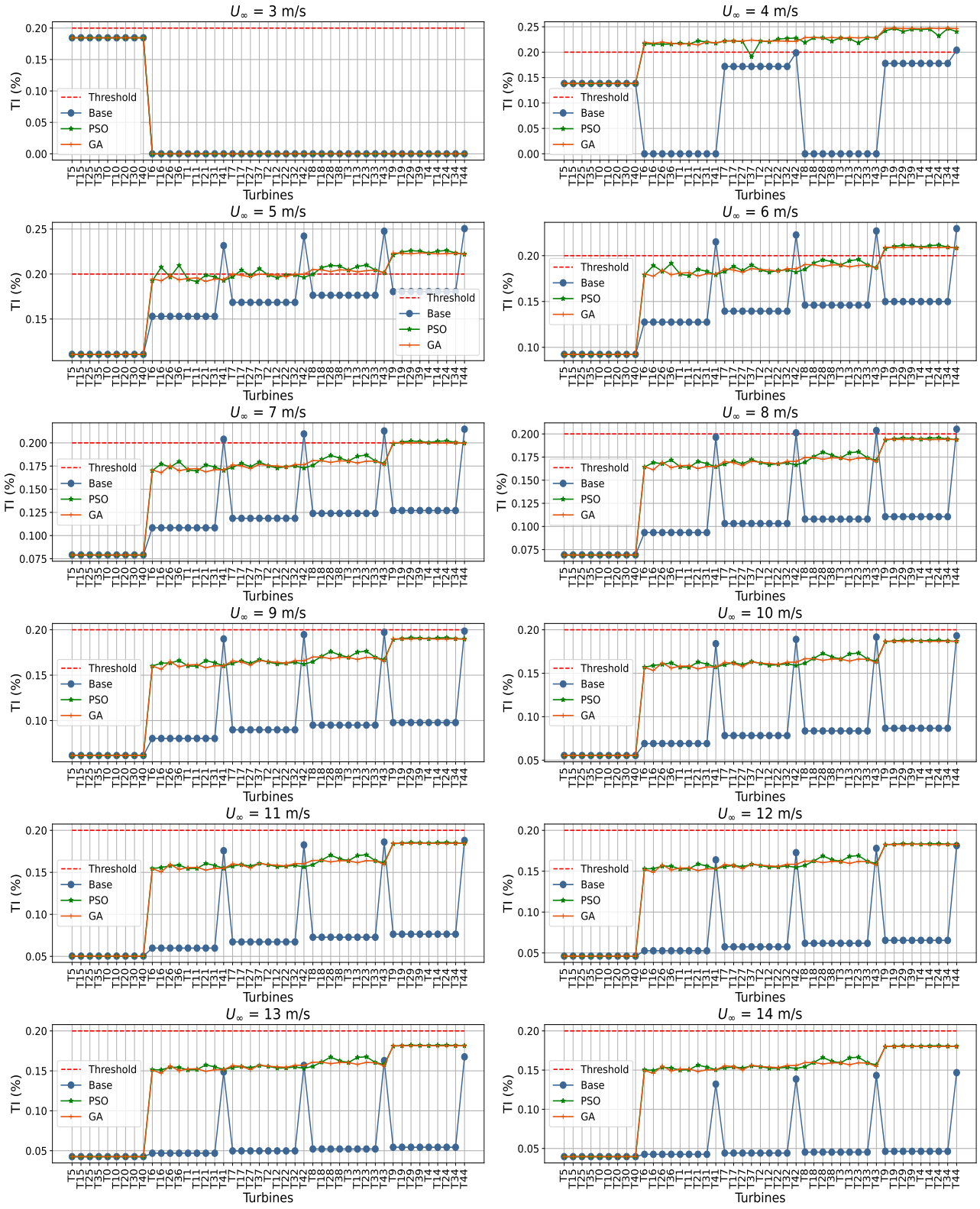

Figure 34: Turbulence Intensity at individual turbines: $5D$, bin0.

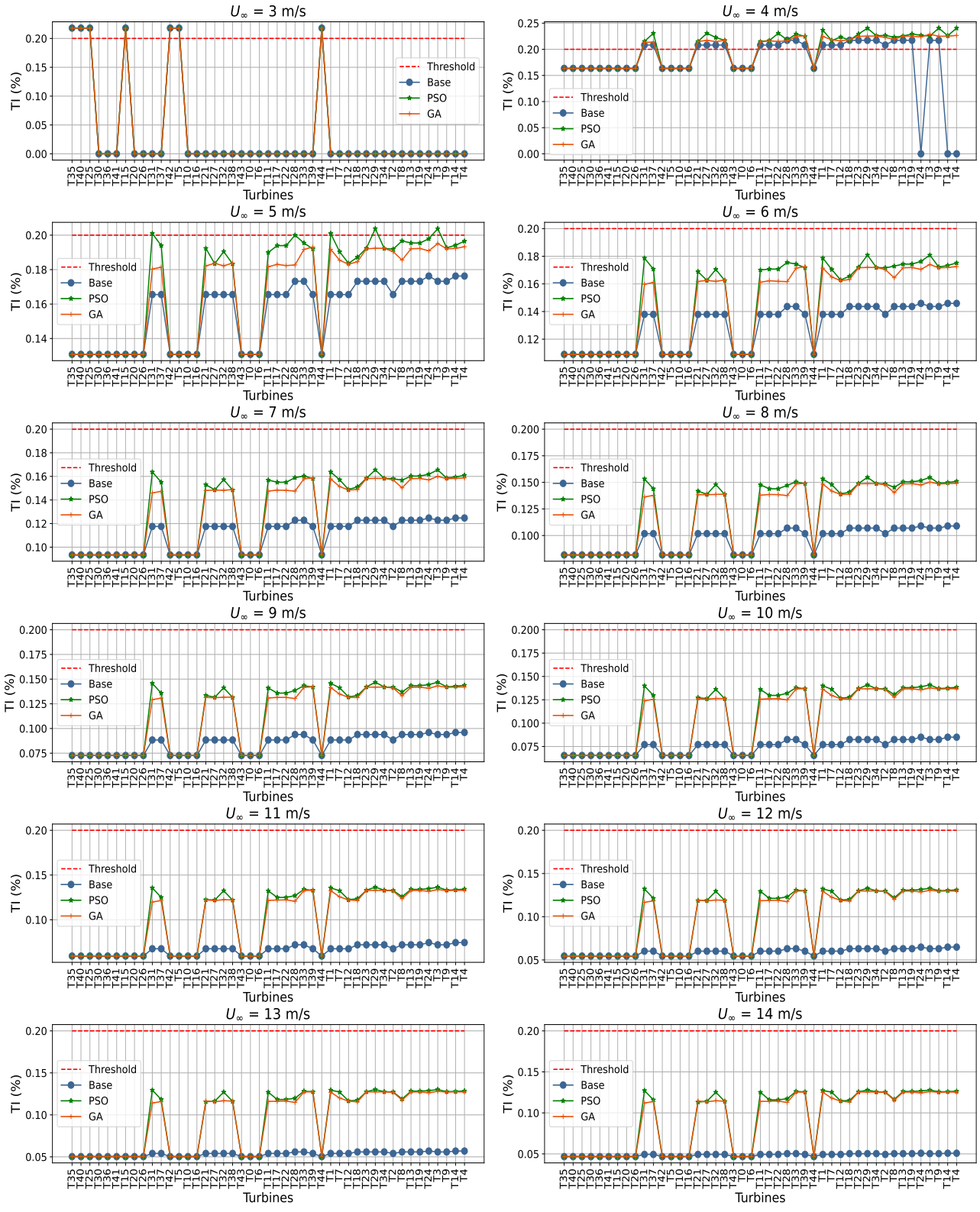

Figure 35: Turbulence Intensity at individual turbines: $5D$, bin1.

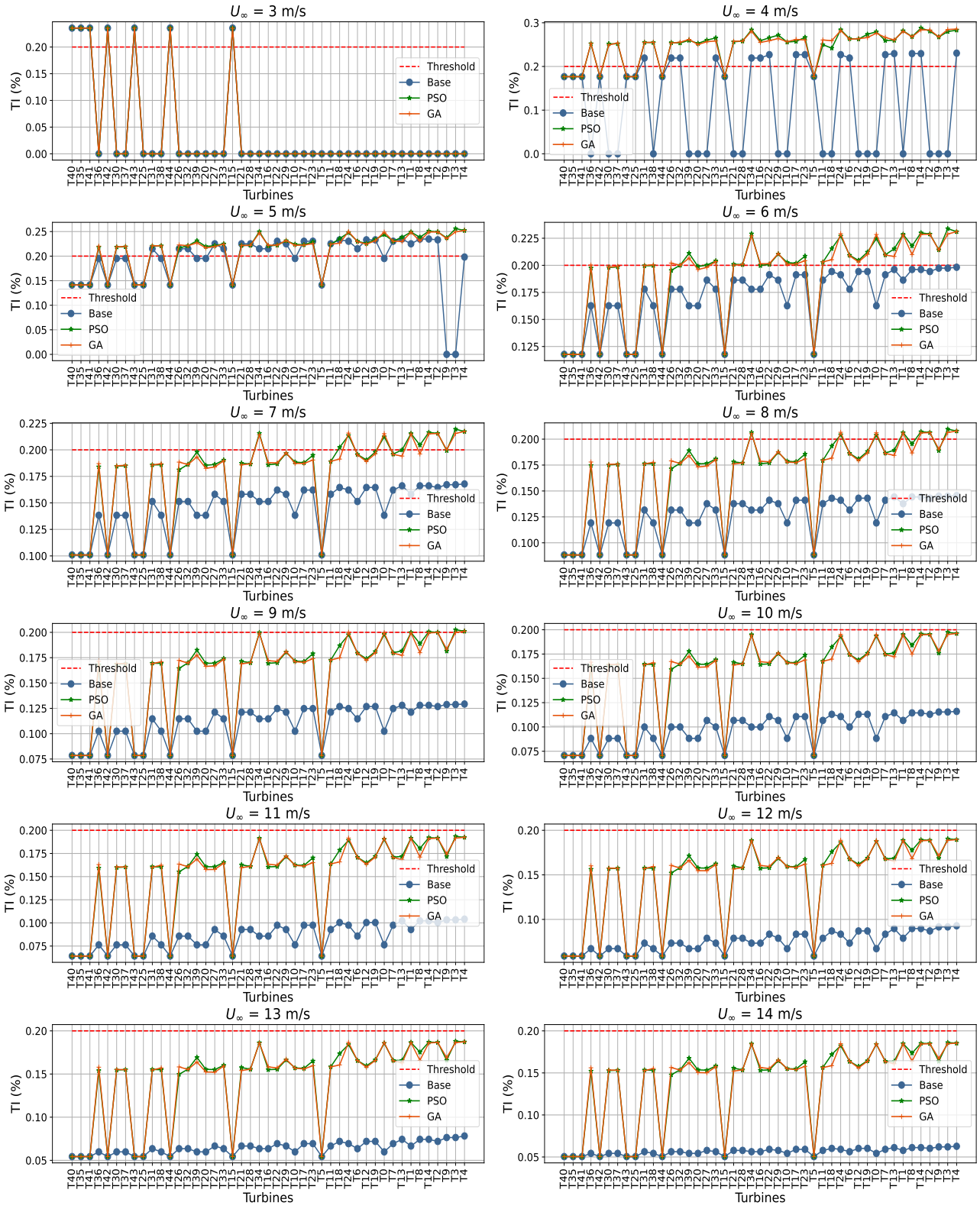

Figure 36: Turbulence Intensity at individual turbines: $5D$, bin2.

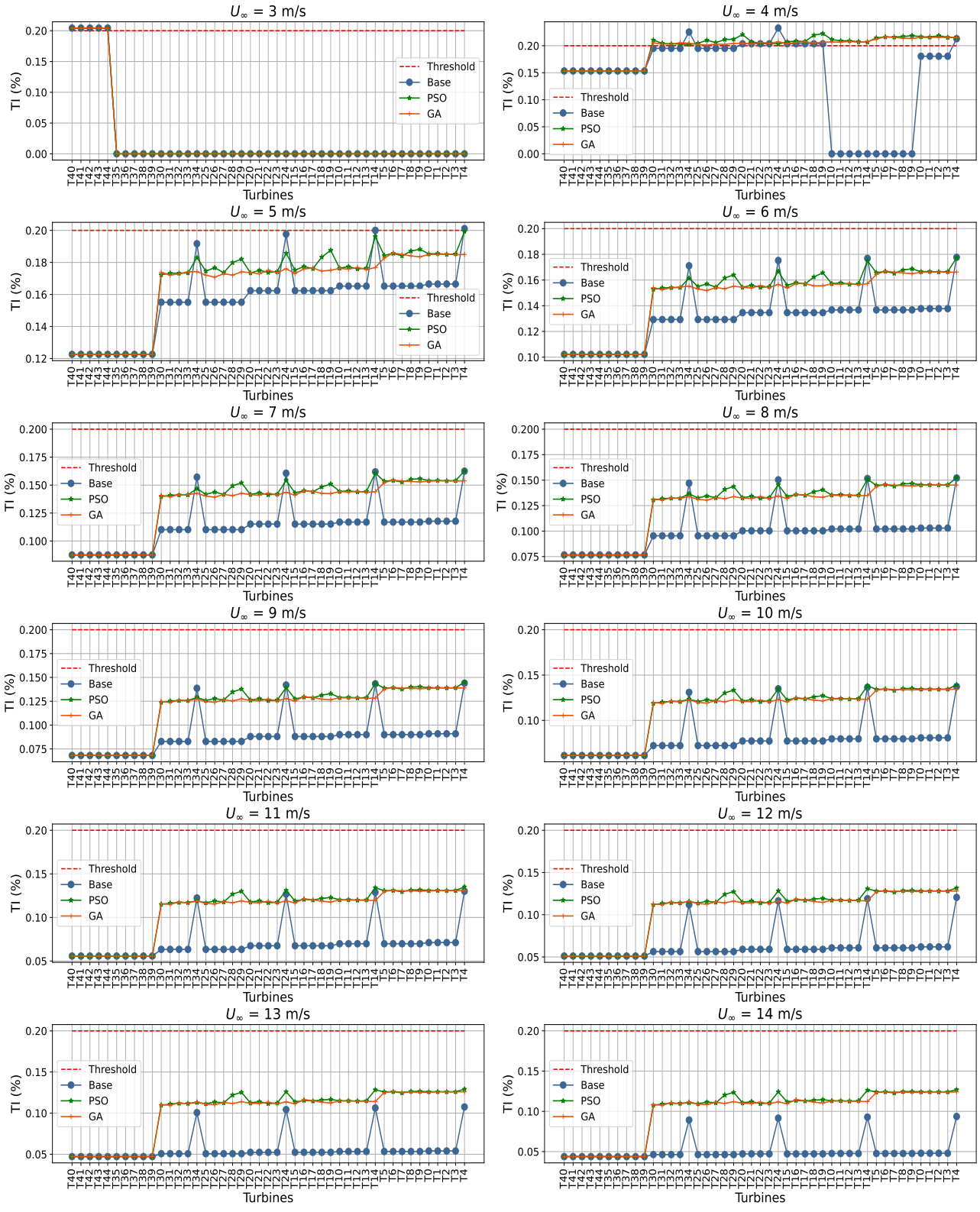

Figure 37: Turbulence Intensity at individual turbines: $5D$, bin3.

Figure 38: Turbulence Intensity at individual turbines: $5D$, bin4.

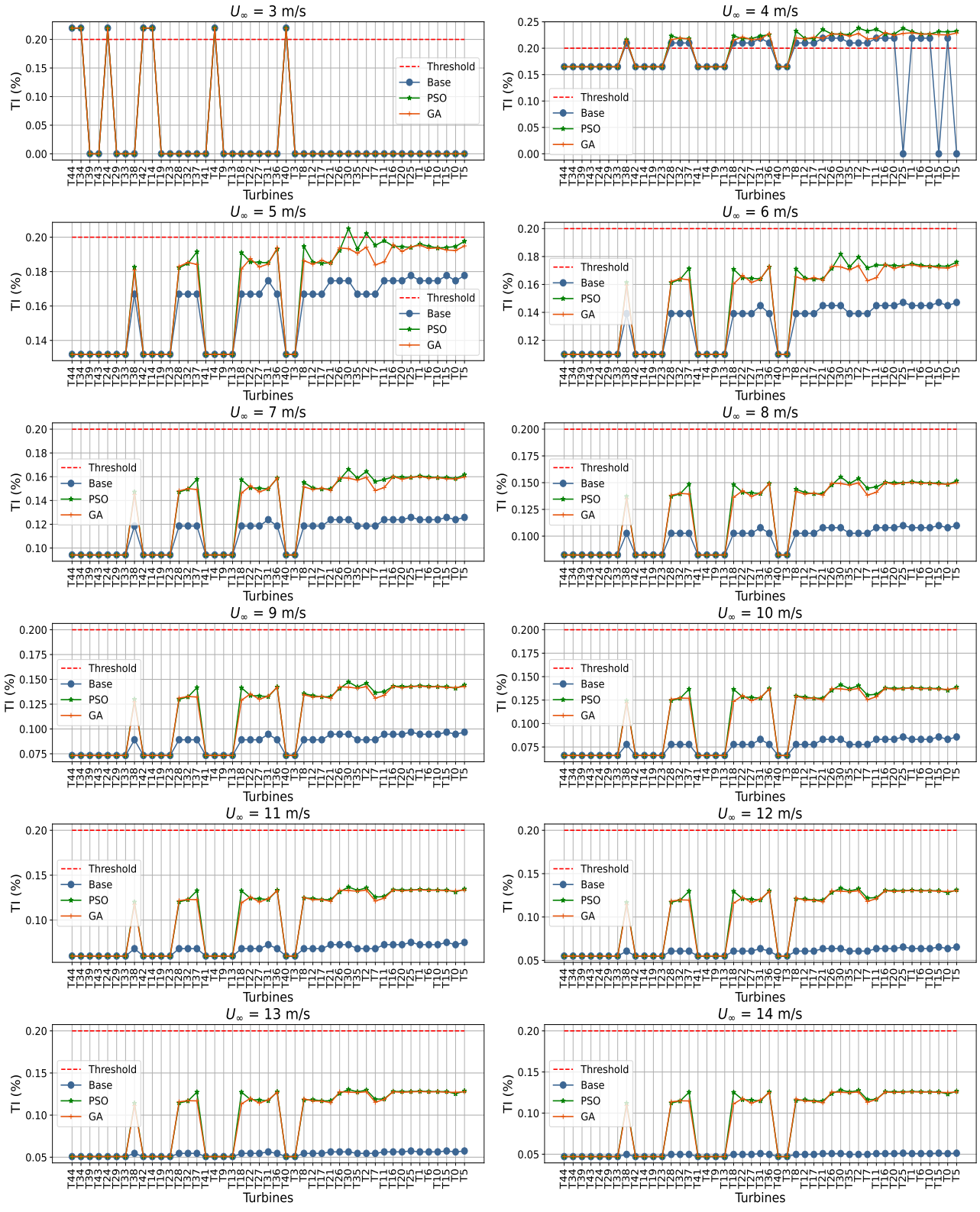

Figure 39: Turbulence Intensity at individual turbines: $5D$, bin5.

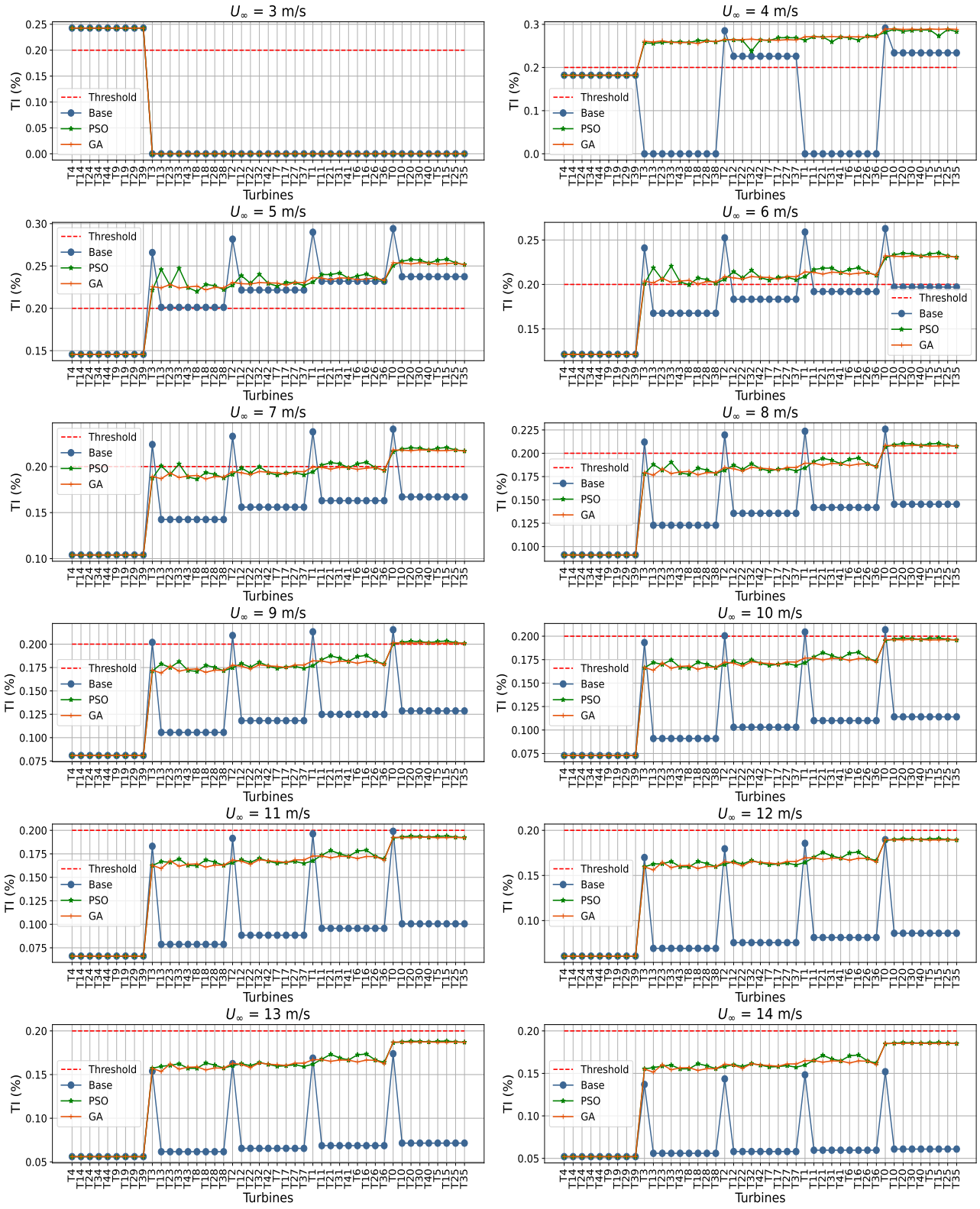

Figure 40: Turbulence Intensity at individual turbines: $5D$, bin6.

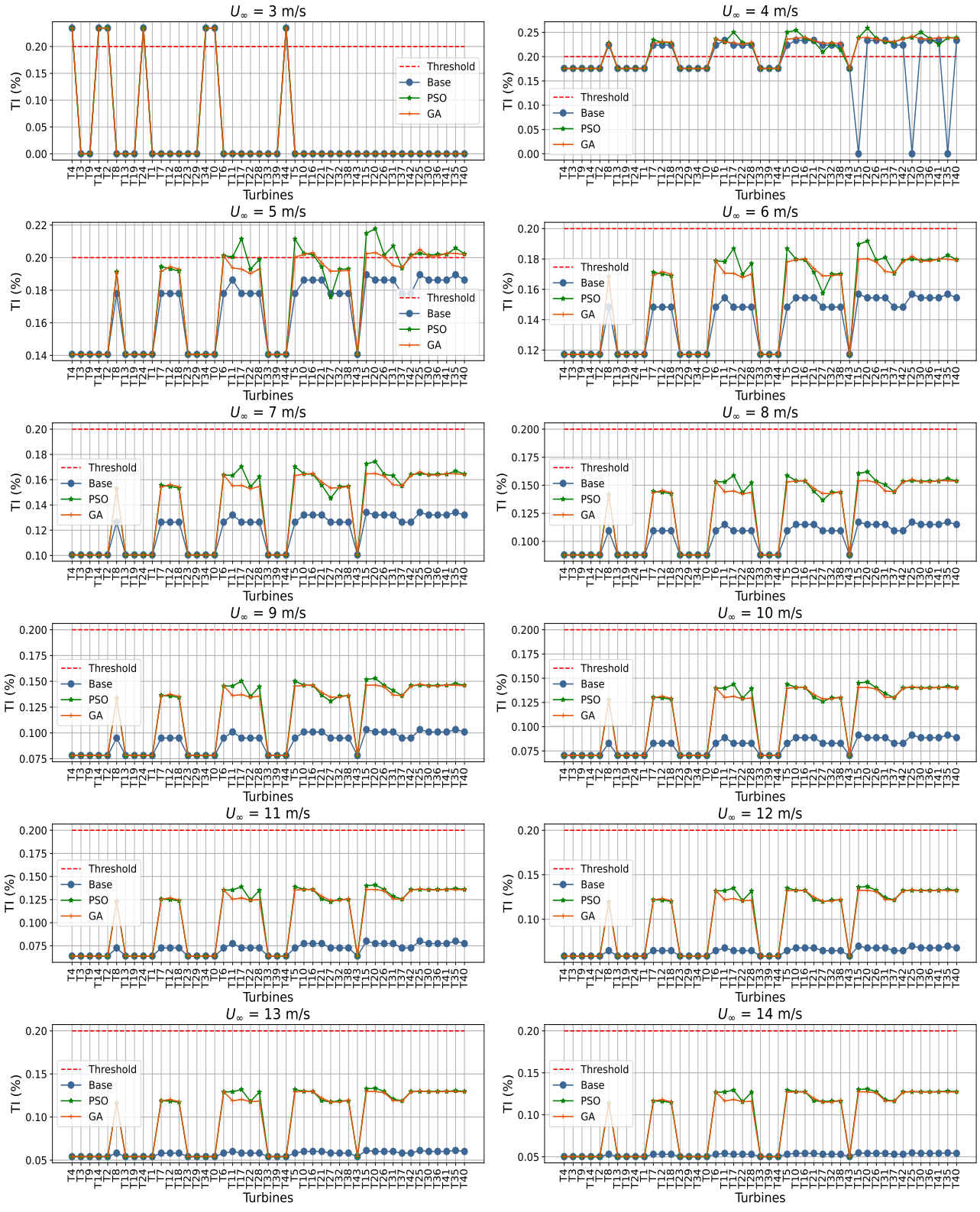

Figure 41: Turbulence Intensity at individual turbines: $5D$, bin7.

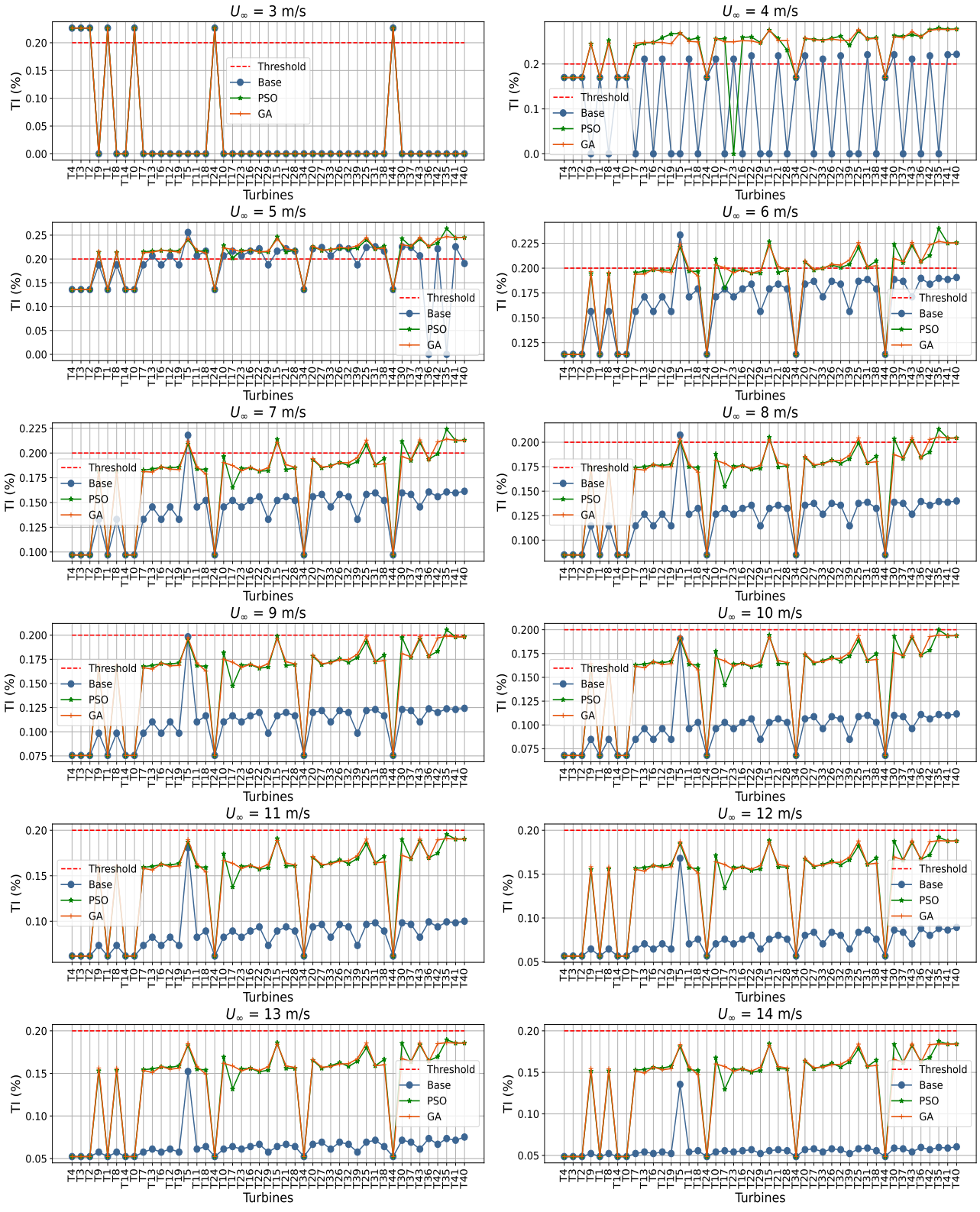

Figure 42: Turbulence Intensity at individual turbines: $5D$, bin8.

Figure 43: Turbulence Intensity at individual turbines: $5D$, bin9.

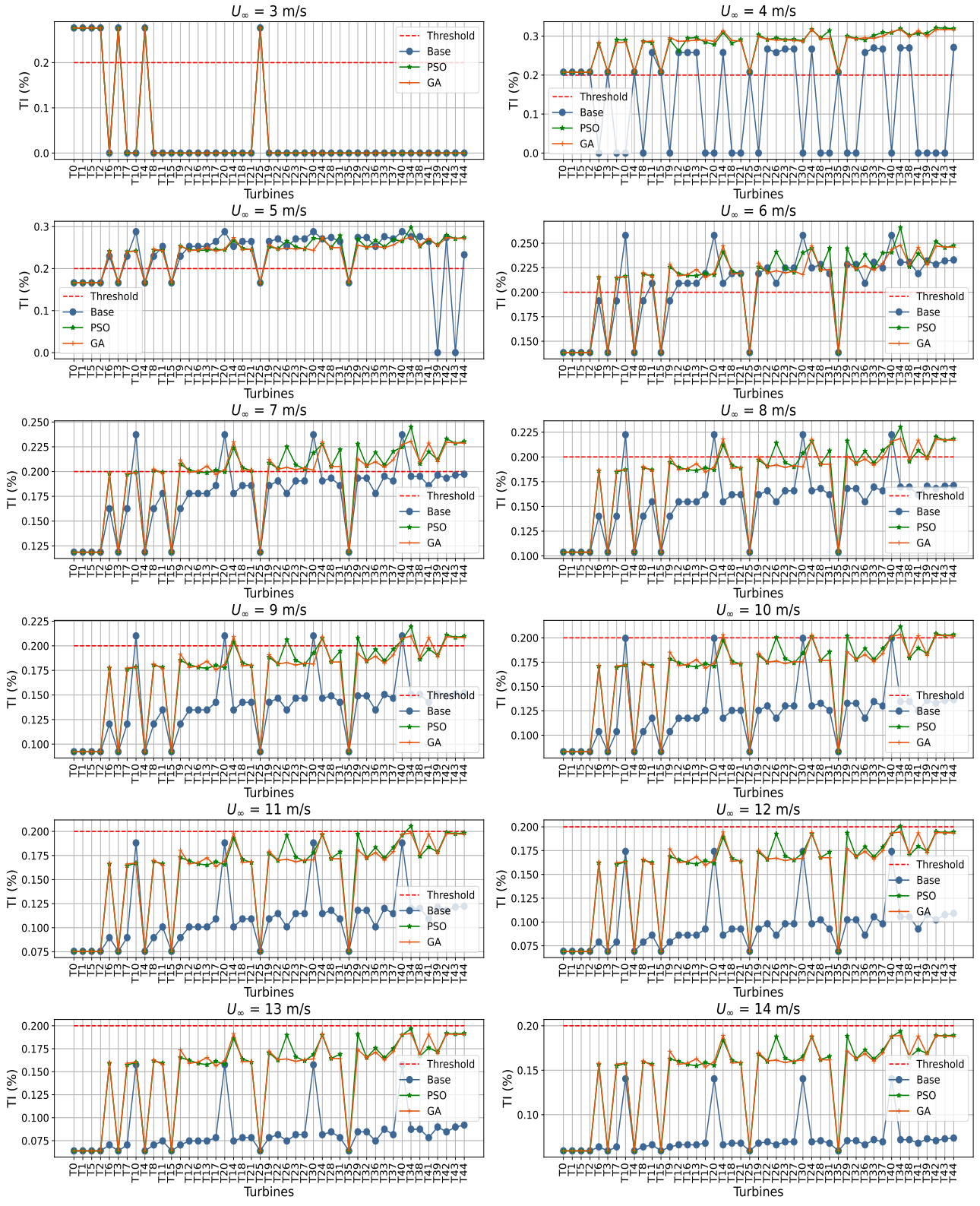

Figure 44: Turbulence Intensity at individual turbines: $5D$, bin10.

Figure 45: Turbulence Intensity at individual turbines: $5D$, bin11.

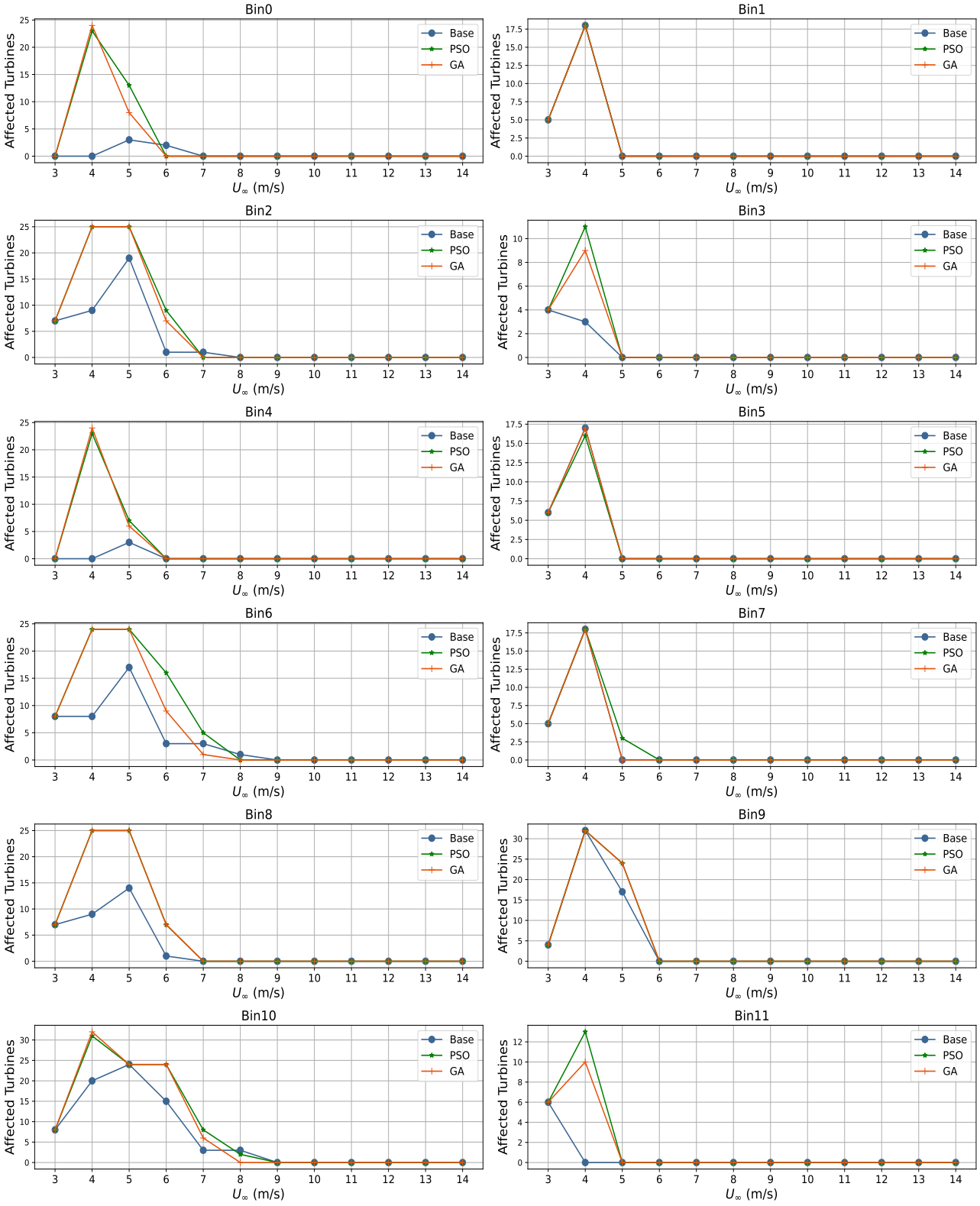

Figure 46: Total TI-defaulting turbines at $6D$: All cases

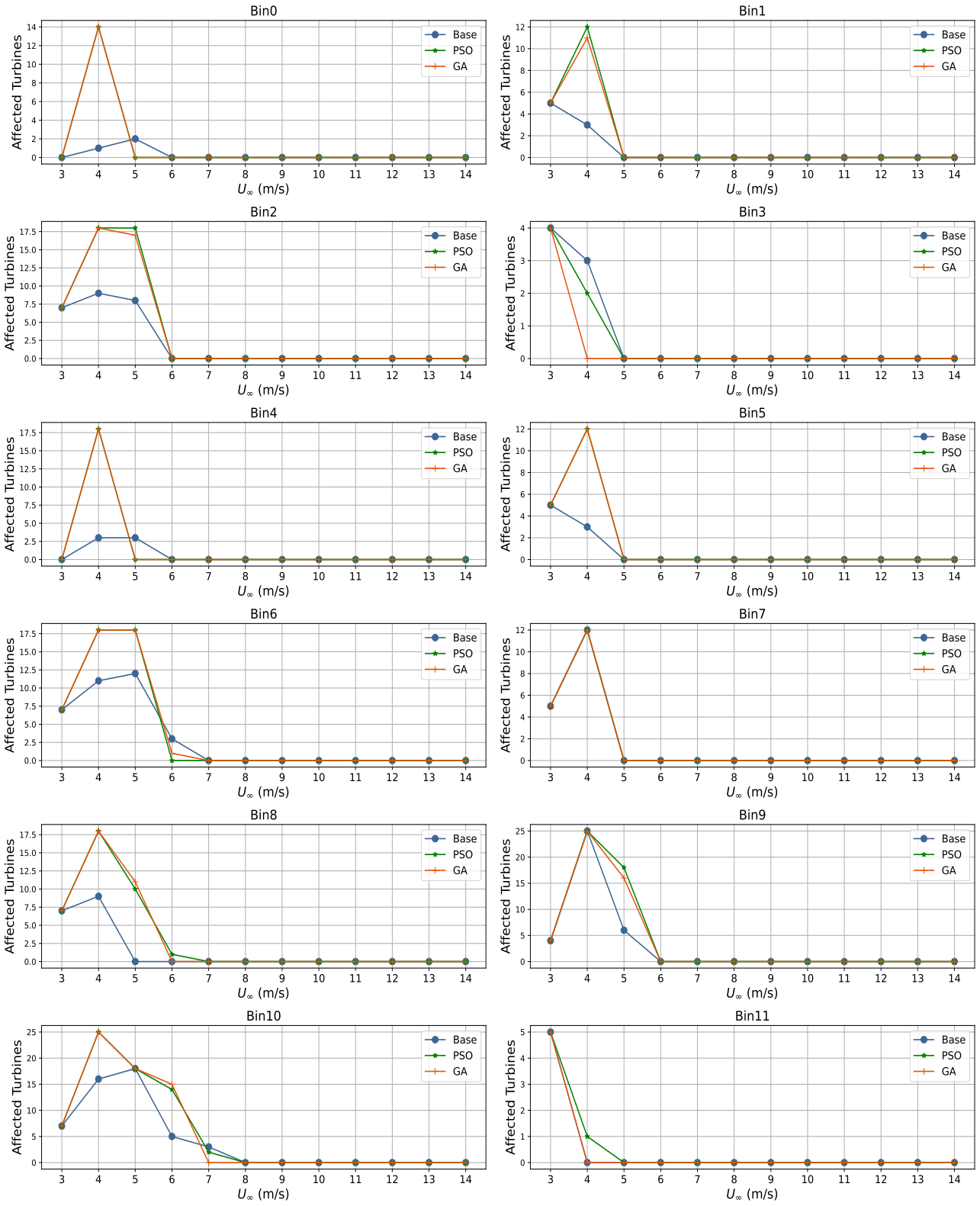

Figure 47: Total TI-defaulting turbines at $7D$: All cases

D.4 WP analysis4

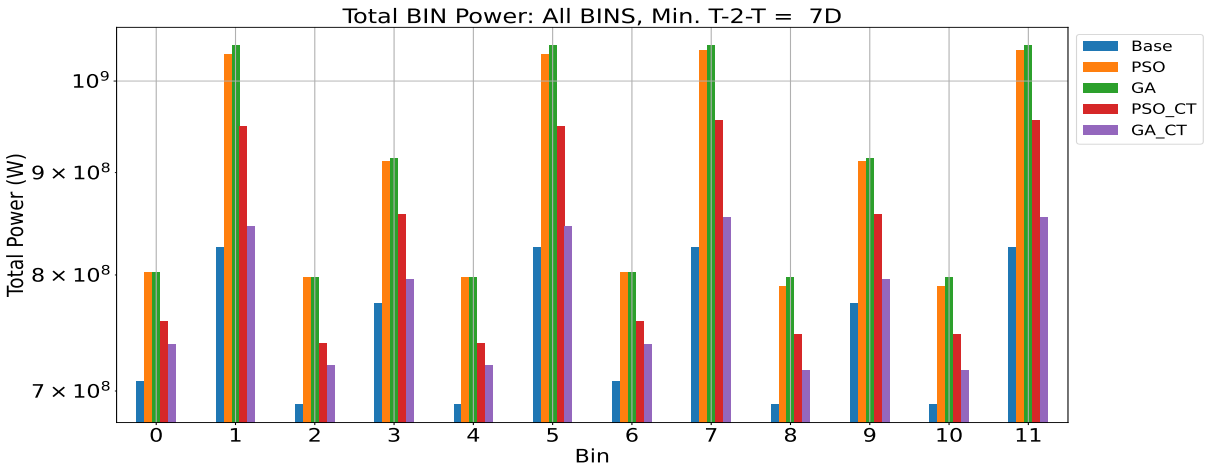

Figure 48: Actual WP power per bin: Minimum T-2-T distance = $7D$.

D.5 CT analysis4

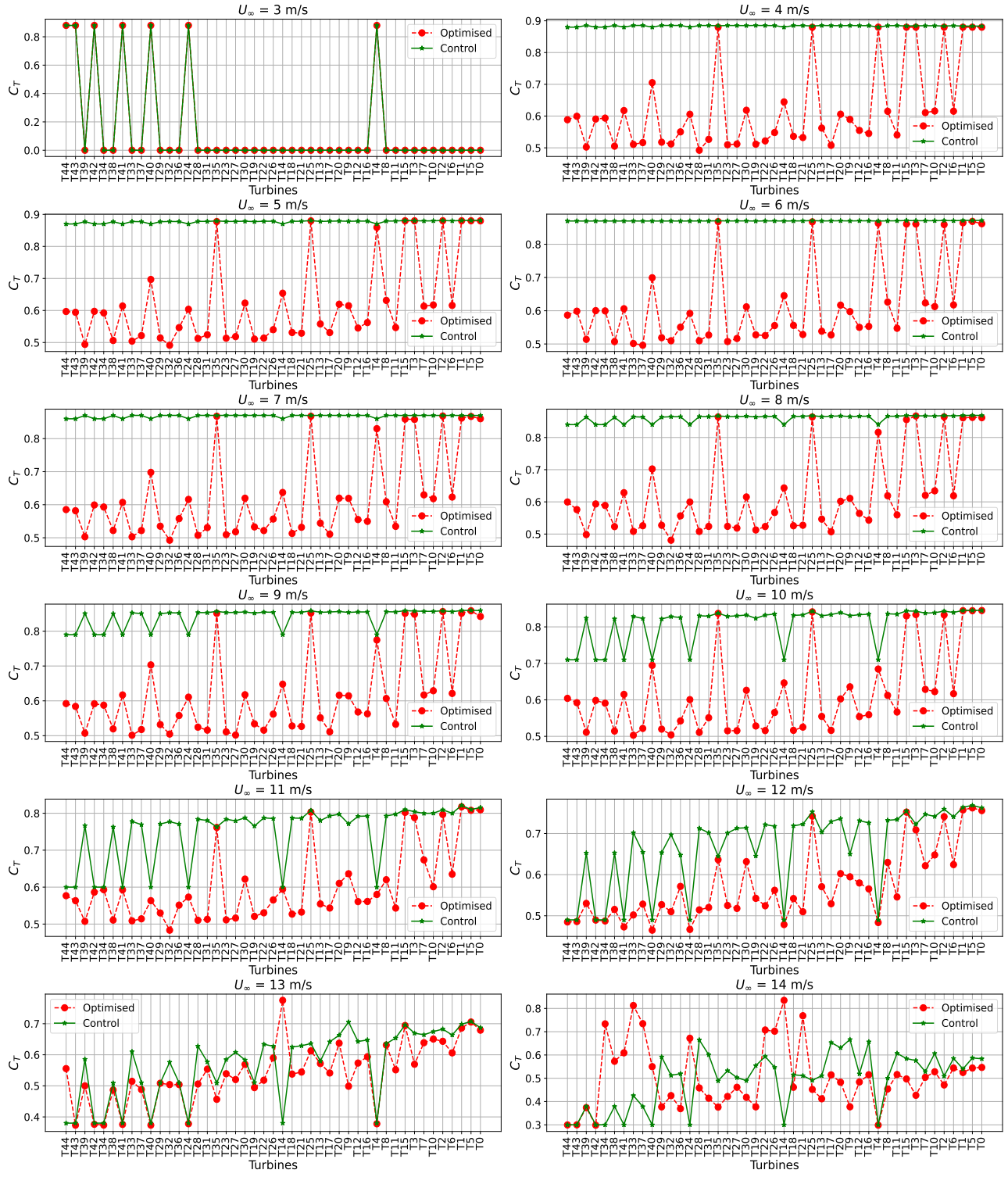

Figure 49: Turbines constrained thrust coefficient values with GA: $5D$, bin4.

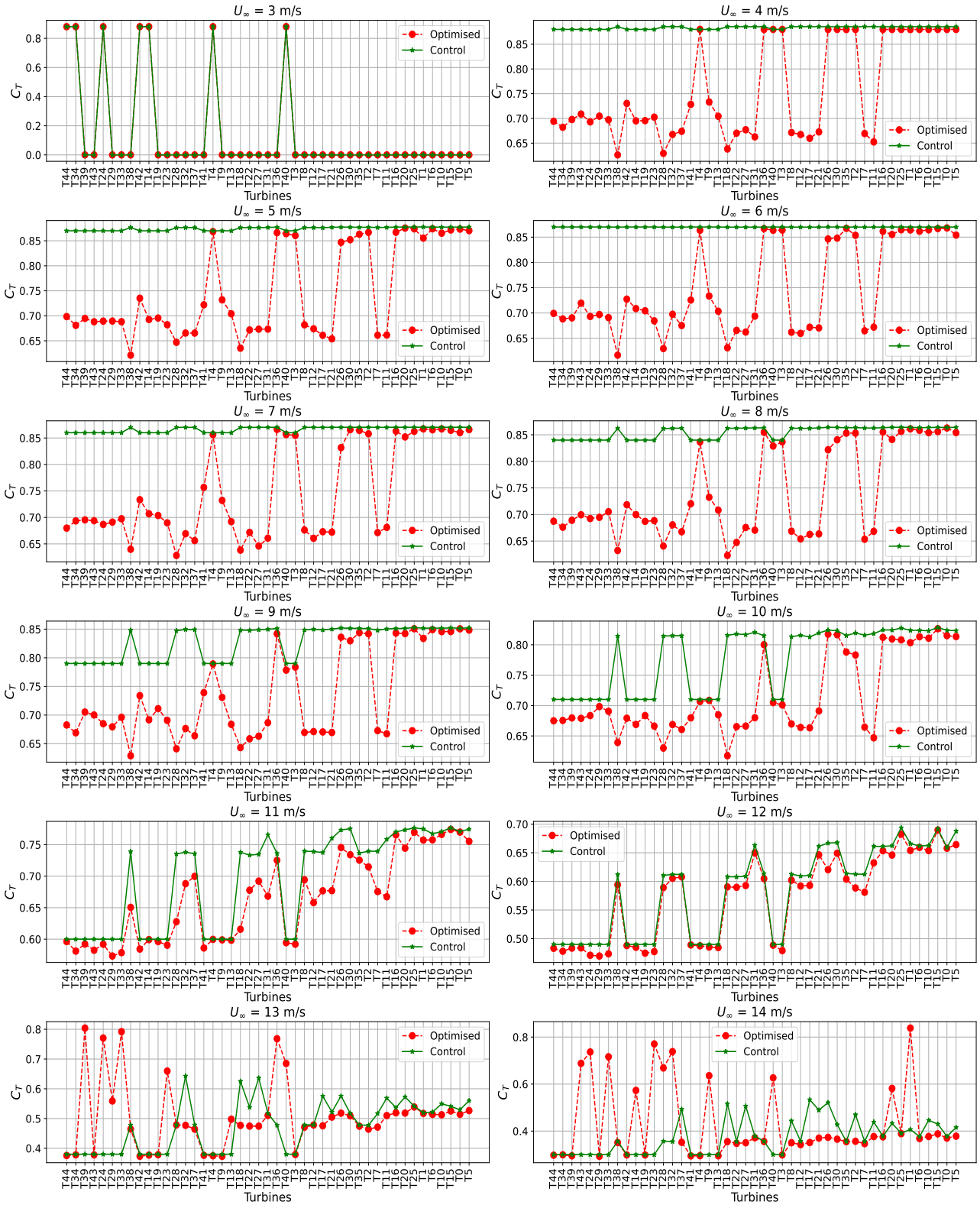

Figure 50: Turbines constrained thrust coefficient values with GA: $5D$, bin5.

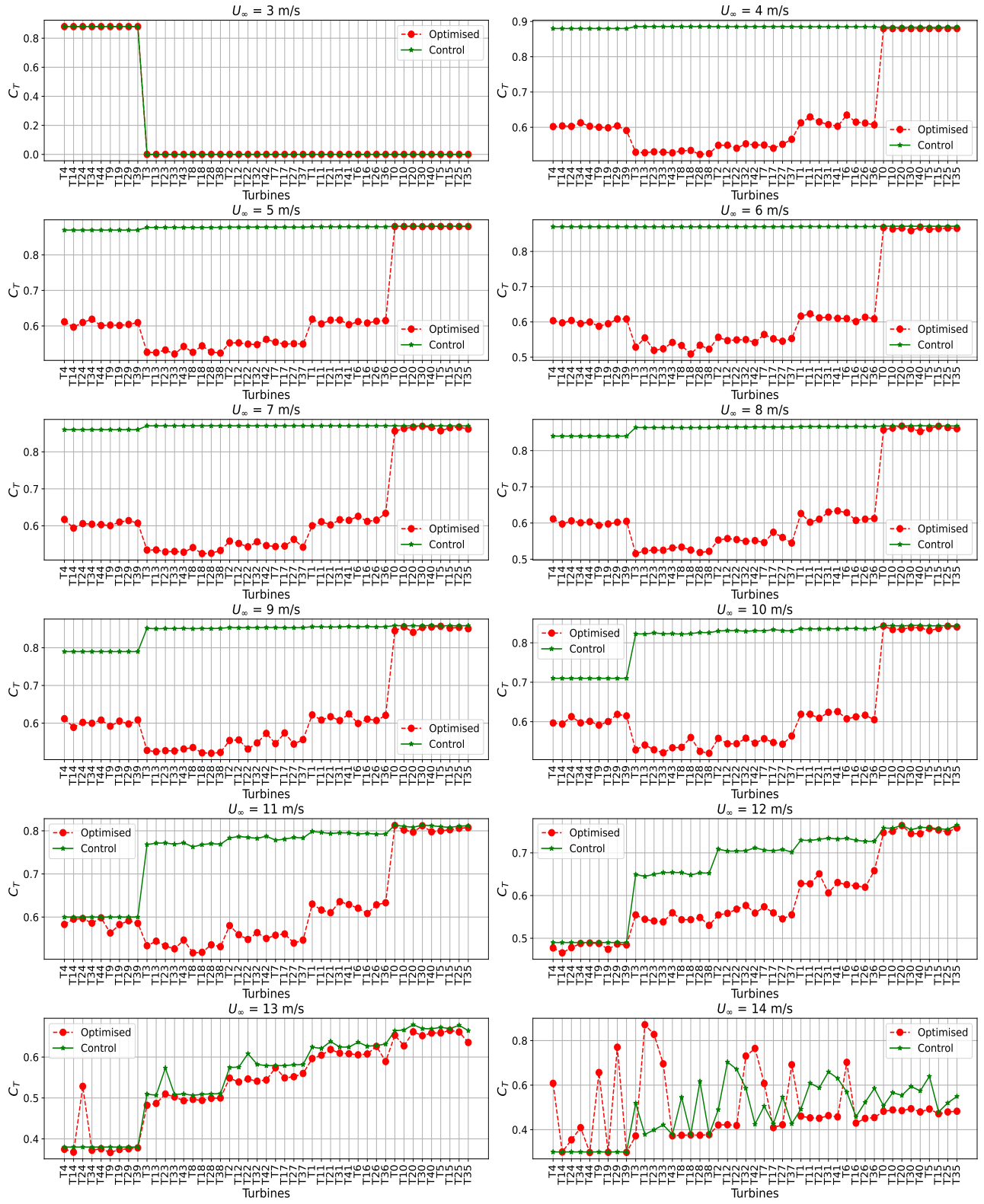

Figure 51: Turbines constrained thrust coefficient values with GA: $5D$, bin6.

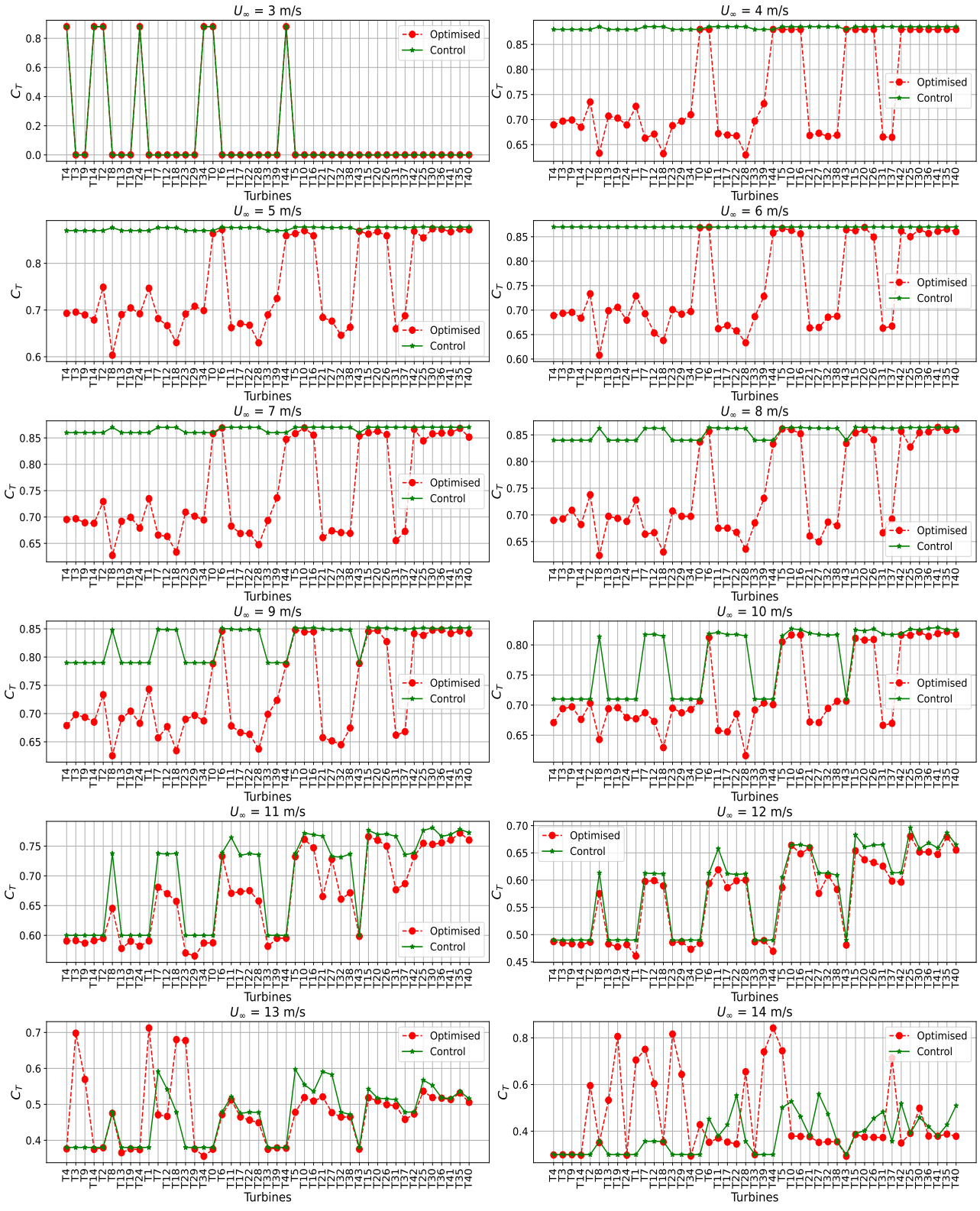

Figure 52: Turbines constrained thrust coefficient values with GA: $5D$, bin7.

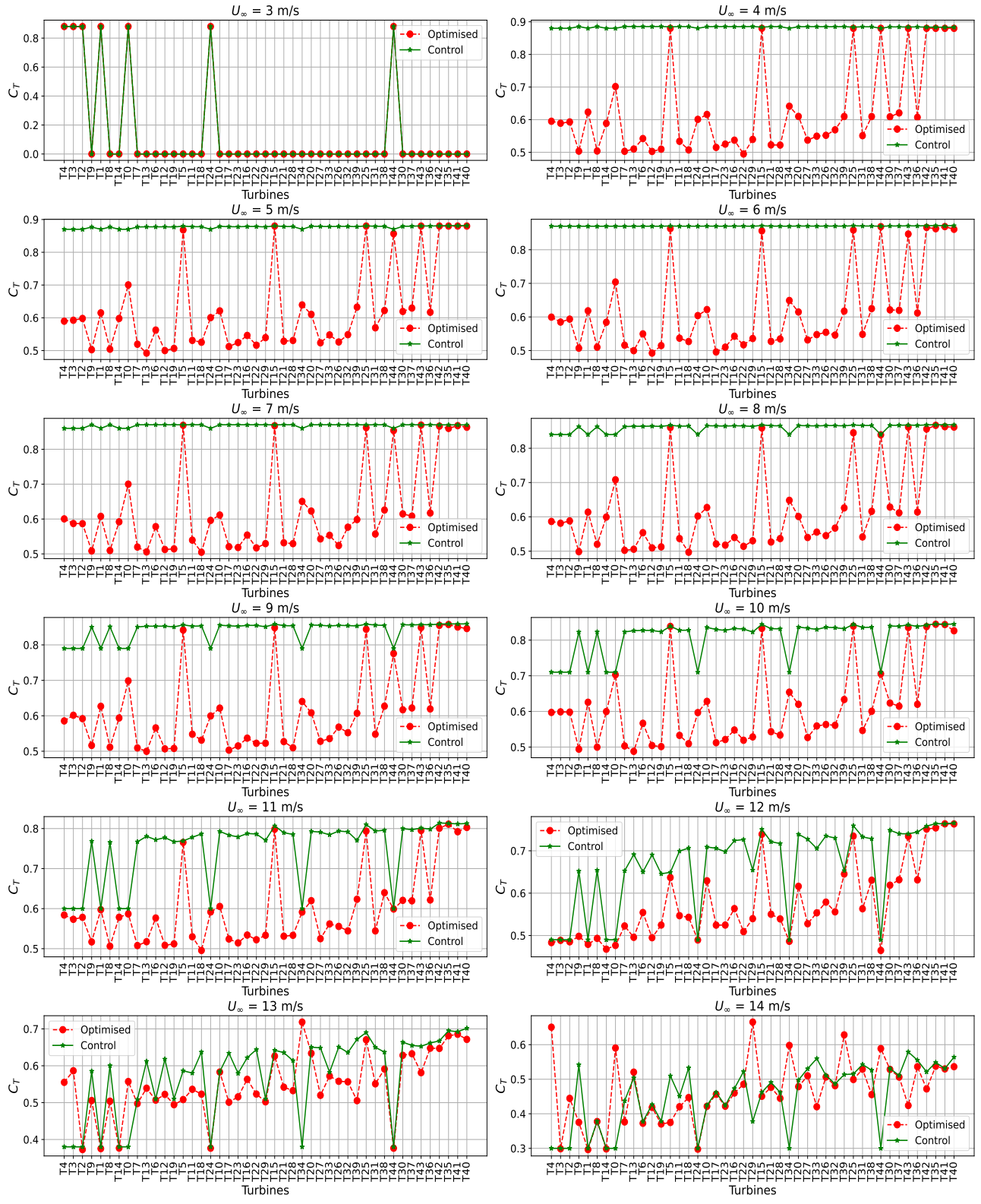

Figure 53: Turbines constrained thrust coefficient values with GA: $5D$, bin8.

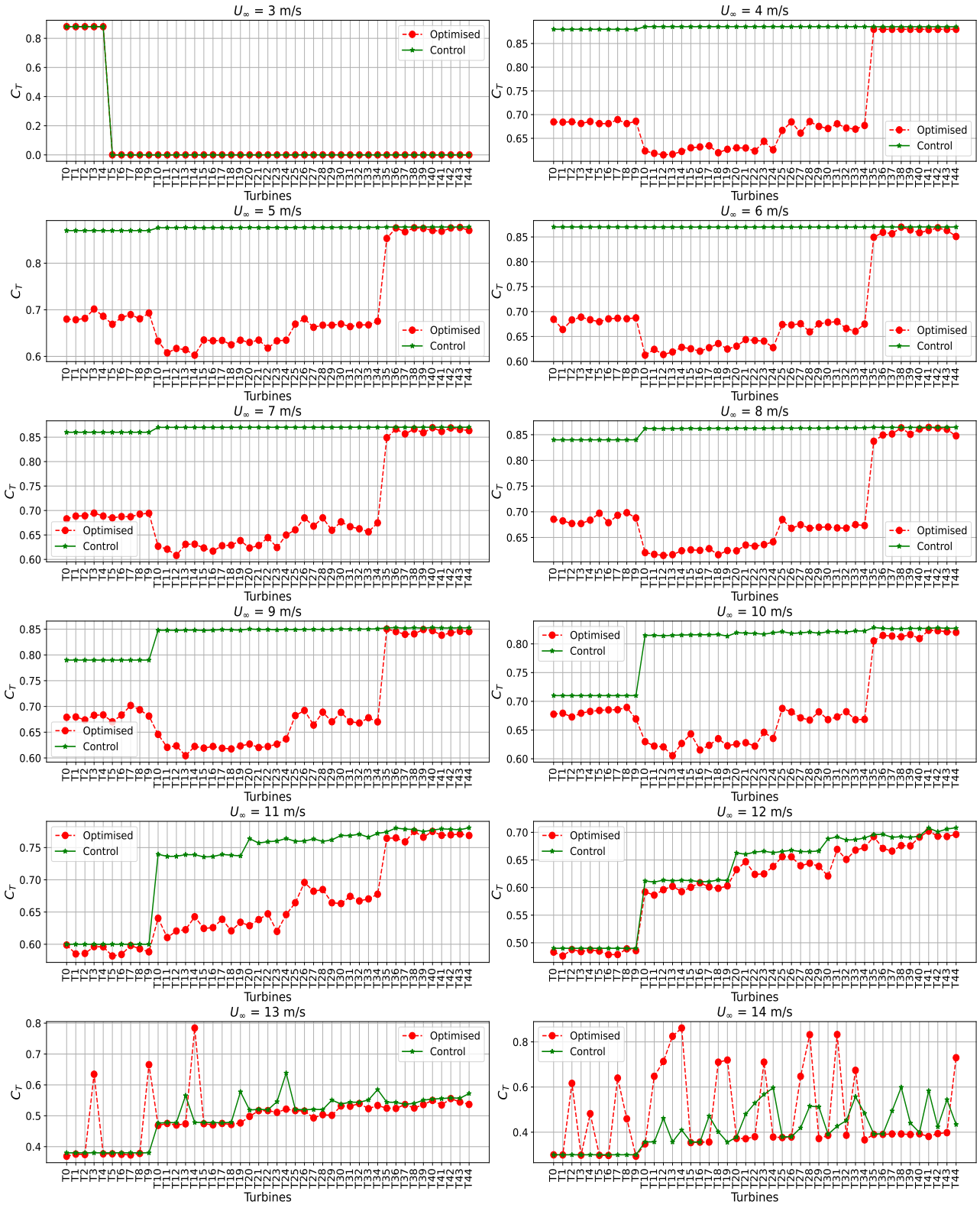

Figure 54: Turbines constrained thrust coefficient values with GA: $5D$, bin9.

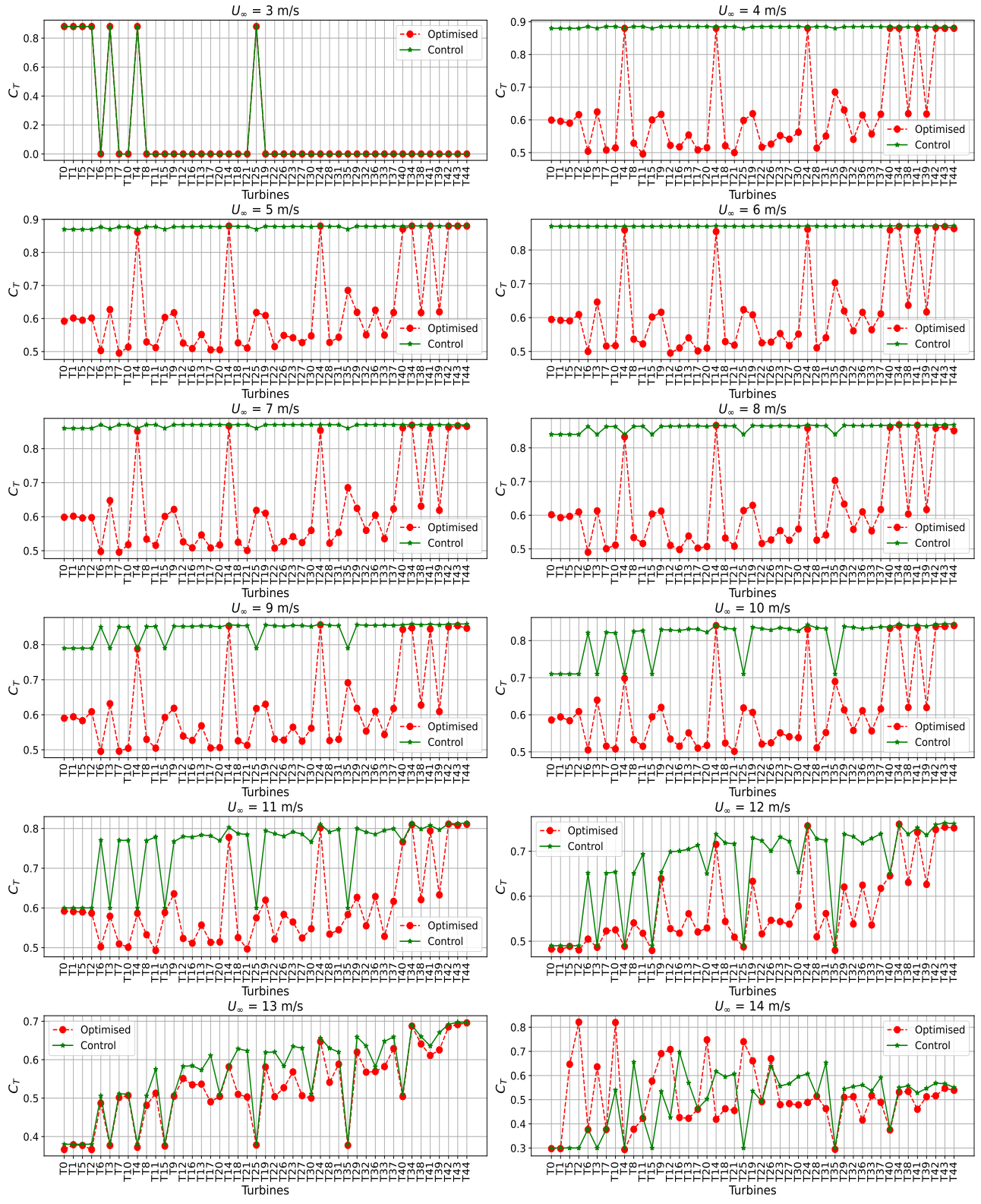

Figure 55: Turbines constrained thrust coefficient values with GA: $5D$, bin10.

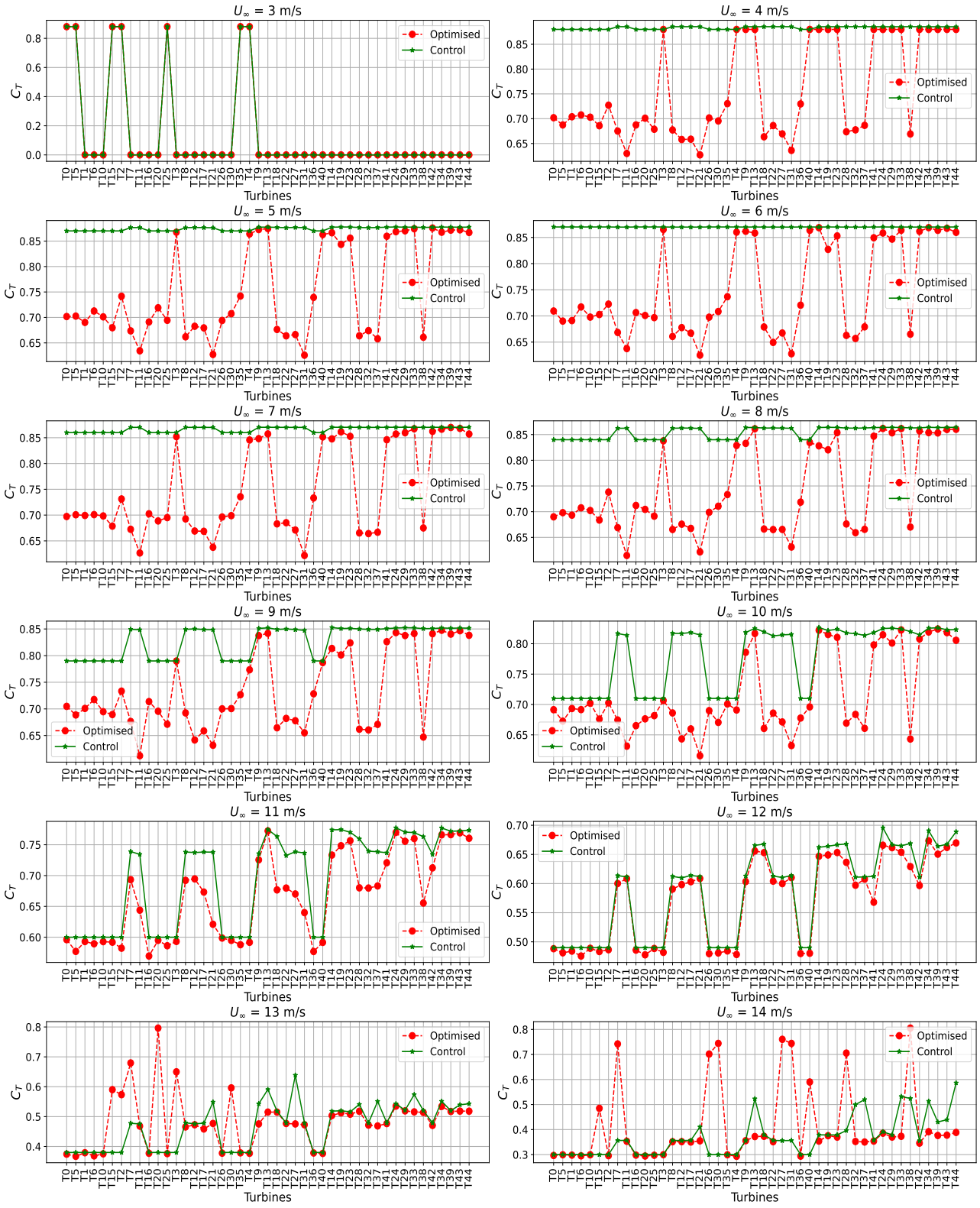

Figure 56: Turbines constrained thrust coefficient values with GA: $5D$, bin11.

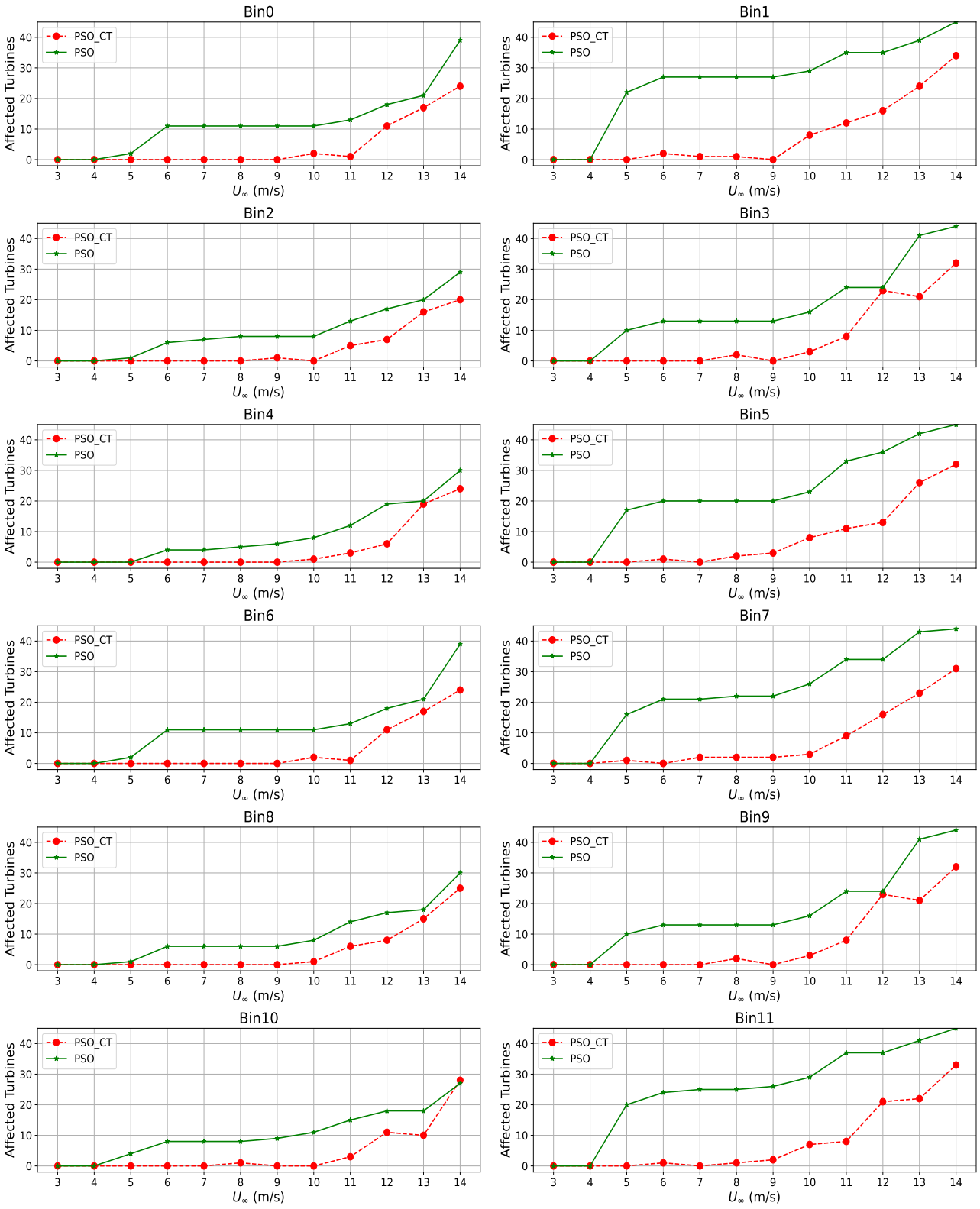

Figure 57: Total C_T-defaulting turbines for $5D$ scenario: PSO cases.

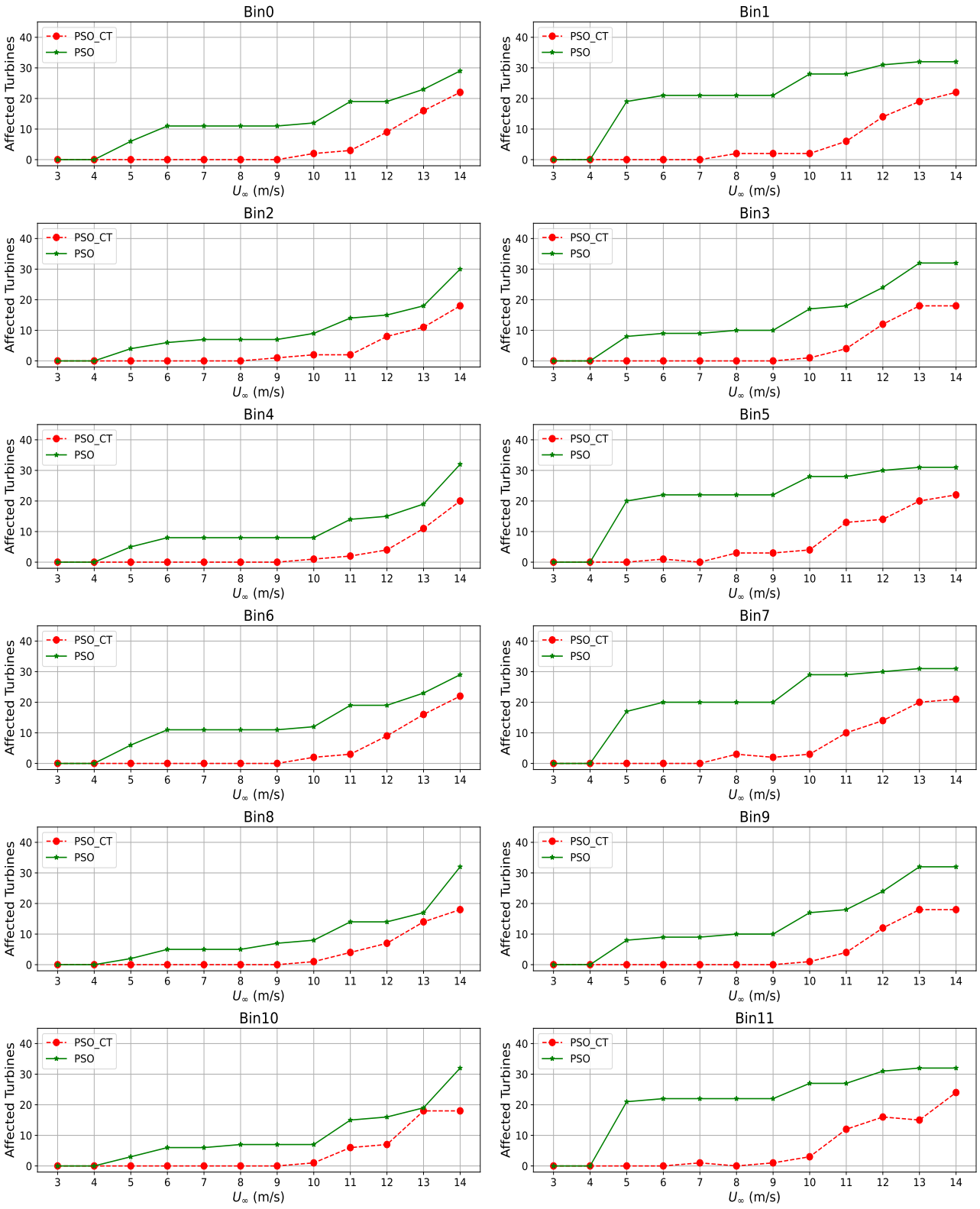

Figure 58: Total C_T-defaulting turbines for $6D$ scenario: PSO cases.

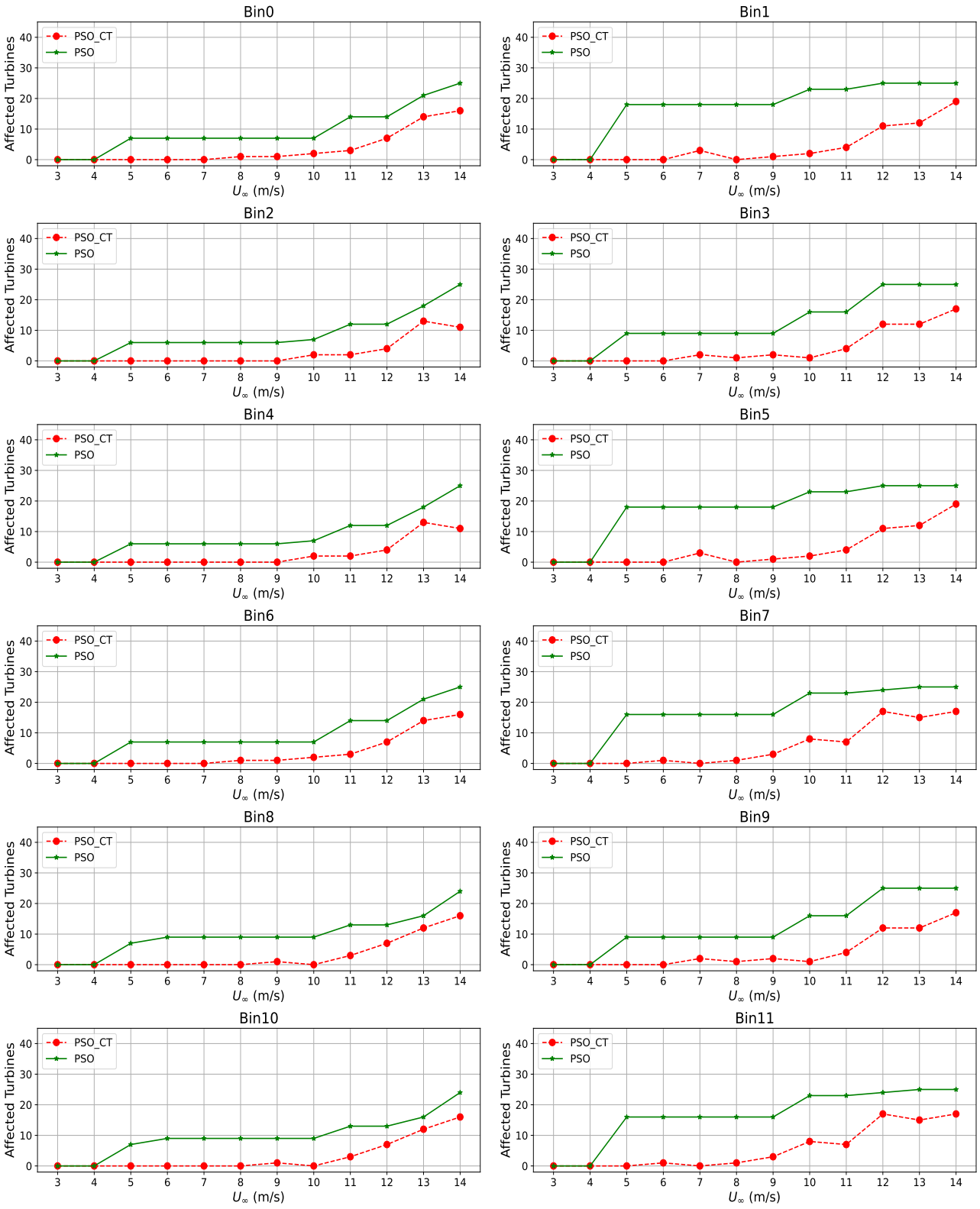

Figure 59: Total C_T-defaulting turbines for $7D$ scenario: PSO cases.

D.6 TI analysis4

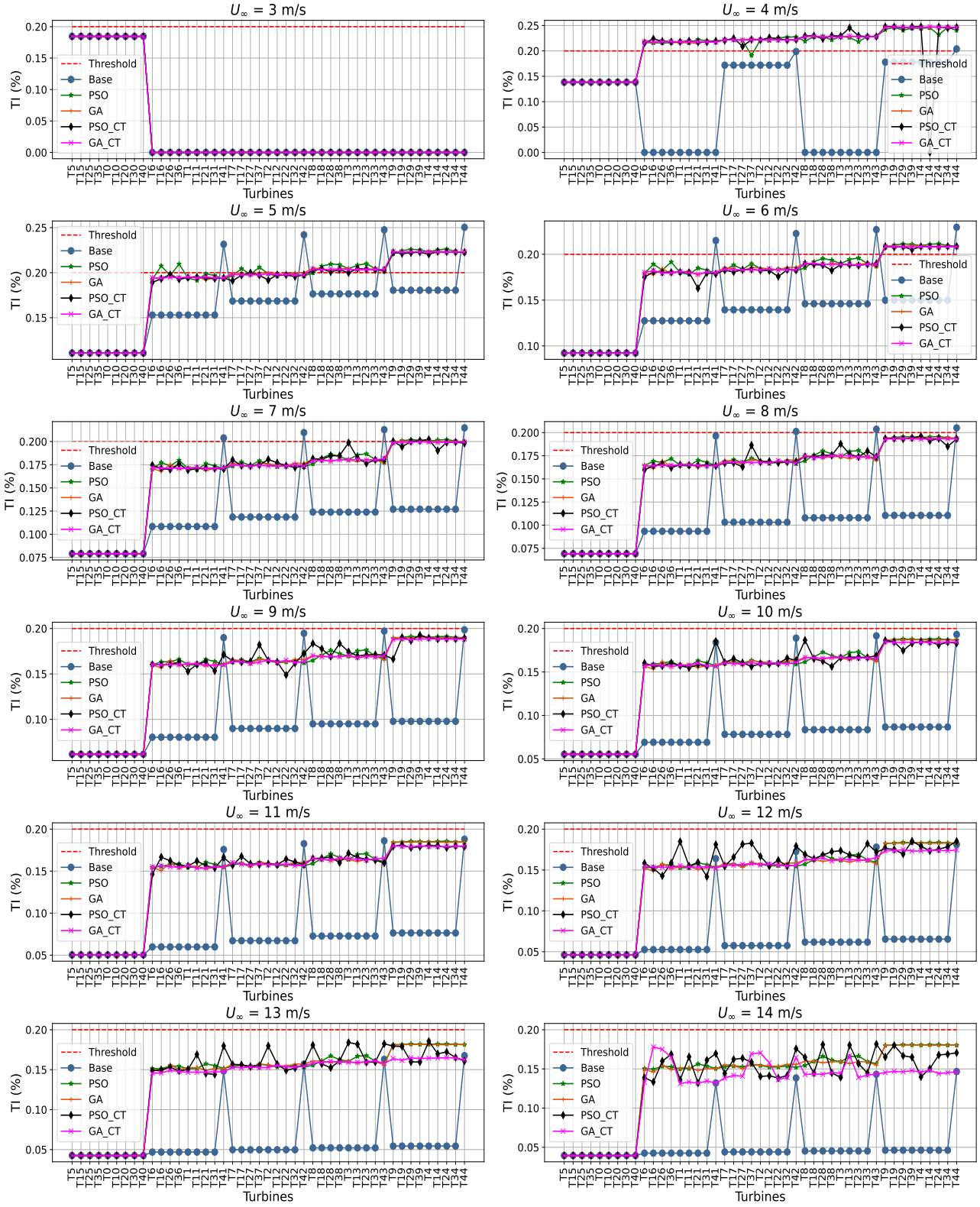

Figure 60: Turbulence Intensity at individual turbines: $5D$, bin0.

Figure 61: Turbulence Intensity at individual turbines: $5D$, bin1.

Figure 62: Turbulence Intensity at individual turbines: $5D$, bin2.

Figure 63: Turbulence Intensity at individual turbines: $5D$, bin3.

D.7 Capture Radius

Table 1: Upstream sector radius and mean wind speeds at selected far downstream turbines for 4 m/s freestream inflow

Capture Radius Ω	U_∞ (m/s)	U_j			
		Bin 0 $T24$	Bin 1 $T4$	Bin 2 $T3$	Bin 4 $T1$
2Ω	4	3.190	3.560	3.190	3.190
3Ω	4	3.160	3.560	3.160	3.160
4Ω	4	3.140	3.520	3.140	3.140
5Ω	4	3.140	3.520	3.140	3.140
6Ω	4	3.140	3.510	3.130	3.130
7Ω	4	3.140	3.510	3.130	3.130
8Ω	4	3.140	3.510	3.130	3.130
Baseline model [3]	4	3.140	3.510	3.130	3.130

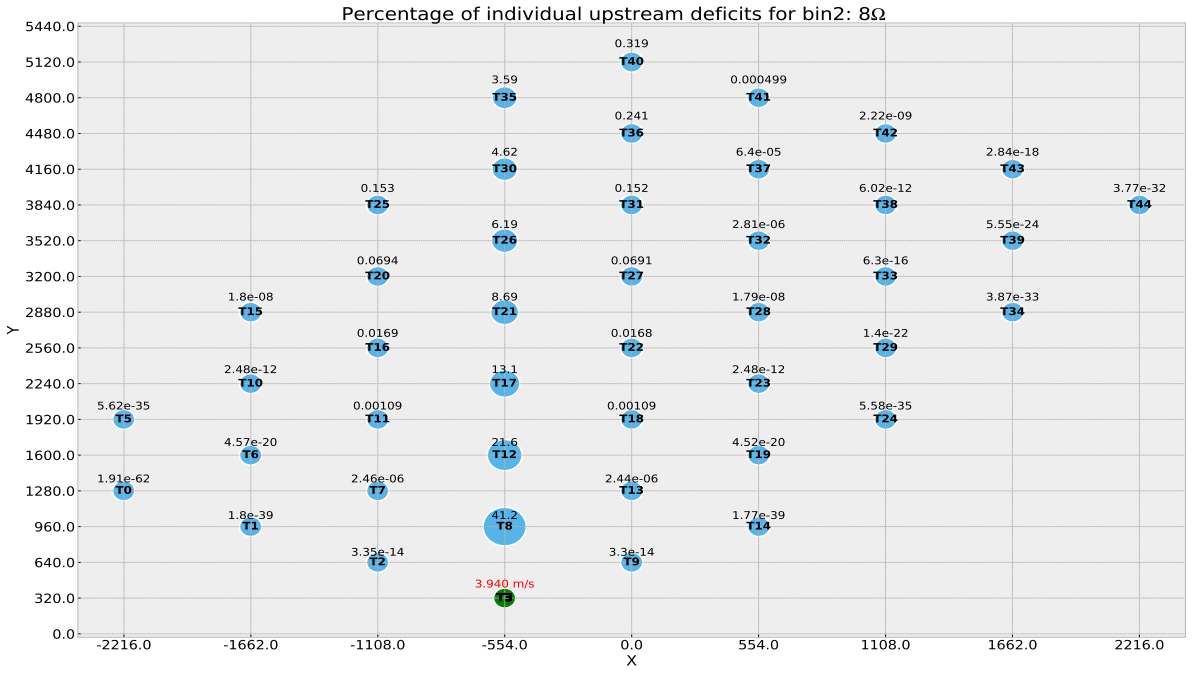

Figure 64: Percentage deficits from turbines within an 8**Ω** upstream sector of $T3$; Bin 2

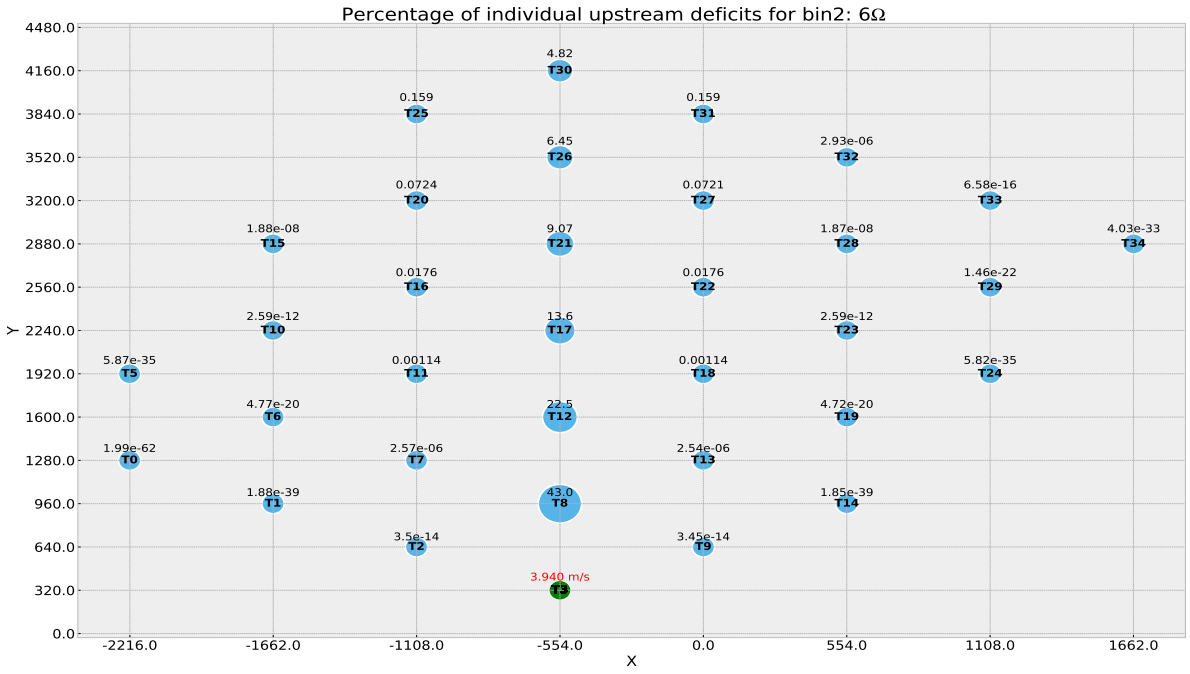

Figure 65: Percentage deficits from turbines within a $6\mathbf{\Omega}$ upstream sector of $T3$; Bin 2

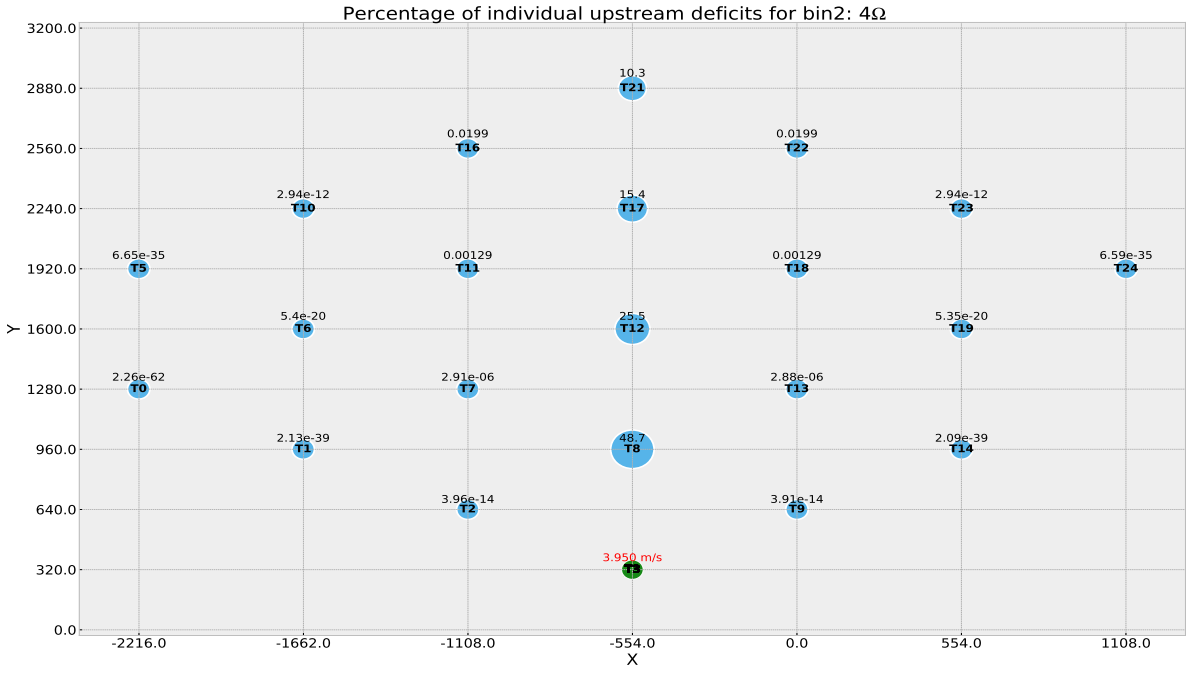

Figure 66: Percentage deficits from turbines within a $4\mathbf{\Omega}$ upstream sector of $T3$; Bin 2

D.8 CT analysis5

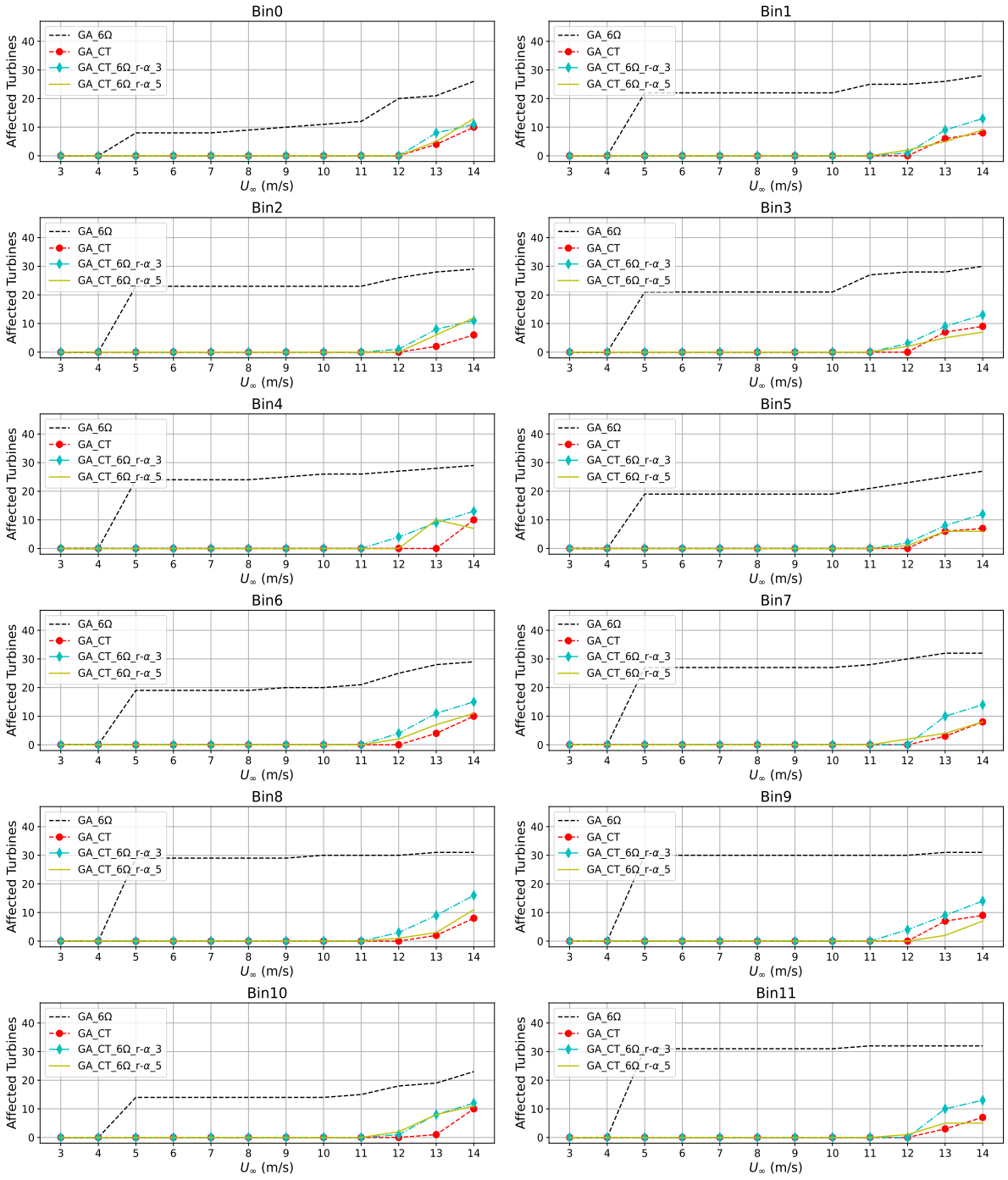

Figure 67: Total C_T-defaulting turbines comparison for all cases, with $6\mathbf{\Omega}$ upstream sector and r-α upstream wake effect elimination: GA, $6D$

D.9 TI analysis5

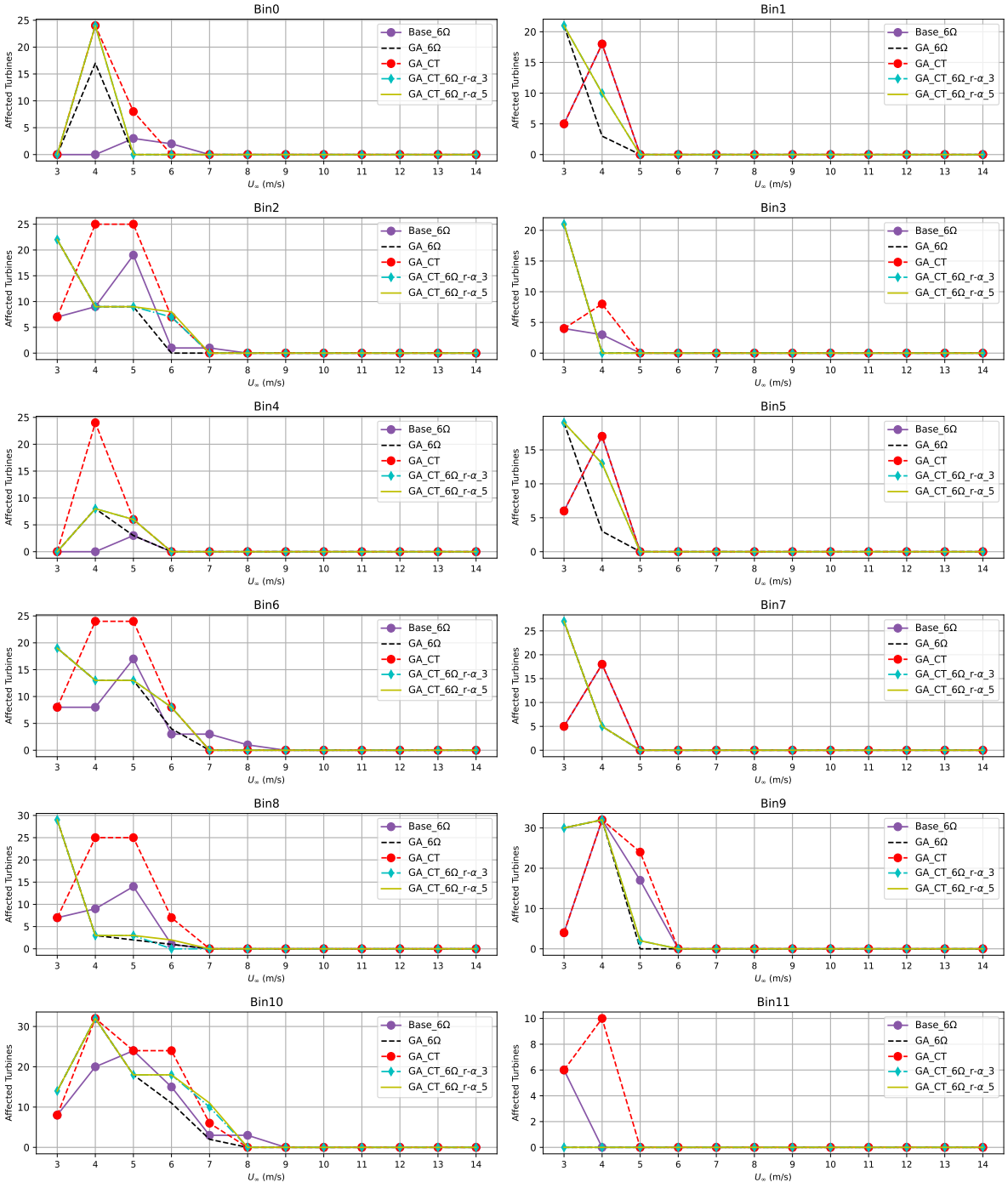

Figure 68: Total TI-defaulting turbines comparison for all cases, with $6\boldsymbol{\Omega}$ upstream sector and r-α upstream wake effect elimination: GA, $6D$

E Algorithms

E.1 Optimisation Algorithmic Flow

Genetic Algorithm (GA) - Summary

1. A **population** (*pop_size*) of candidate solutions is randomly initialized/generated where each solution contains axial induction values for all turbines in the WP, for the wind direction/bin considered.

2. Each solution is evaluated using the **fitness function** in Equation 3.16 which maximizes the overall WP power for each bin, consequently maximizing the WP AEP when applied to all bins.

3. A random selection by permutation of parent solutions is carried out.

4. **Uniform crossover** is employed, where the two randomly selected parents (solutions) exchange genetic material at a crossover rate ($CR = 0.1$) to produce offsprings (solutions).

5. The resulting offsprings are randomly mutated by a **mutation percentage** $\mu \leq 0.01$ to ensure individuals maintain diversity and prevent premature convergence.

6. **Elitism** is employed, where the offspring solutions are merged with the parent solutions, sorted in order of highest to lowest fitness value, and then the best solutions of pop-size size are retained, while eliminating others.

7. Steps 2 – 6 are repeated until the *max_it* is reached.

Particle Swarm Optimisation Algorithm (PSO) - Summary

1. A swarm of particles (candidate solutions) of *pop_size* is initialized randomly in the search space, with each particle (containing axial induction values for all turbines) having: a position X_i (represents a solution), a velocity V_i (which determines particle movement i.e. how the axial induction values for all turbines are adjusted), a personal best position P_i (best solution found by that particle i.e. the best axial induction

values for all turbines so far, that has produced the highest WP power or solution by that particle), and a global best position G (best solution found by any particle).

2. Each particle (solution) updates its velocity and position using these equations:

   Velocity Update

$$V_{it+1} = W_{max} * V_{it} + c1r1 * (P_i - X_i) + c2r2 * (G - X_i) \tag{1}$$

   Where W_{max} (maximum inertia weight, with value 0.9) which balances exploration and exploitation of search space, gradually reduces to W_{min} (minimum inertia weight, with value 0.2) as the number of iterations (it) increase and the particles are getting closer to the global maximum position. After each iteration, the new W_{max} value is computed as;

$$W_{max} = W_{max} - (it * ((W_{max} - W_{min}/max\_it)) \tag{2}$$

   • $c1, c2$ are acceleration coefficients, which control attraction to personal and global bests).

   • $r1, r2$ are random numbers (ensures stochastic behaviour).

   • P_i = Personal best position of particle i.

   • G = Global best position found by the swarm.

   Position Update

$$X_{it+1} = X_{it} + V_{it+1} \tag{3}$$

   • The new position is computed by adding the updated velocity to the current position.

3. Each particle's new position is evaluated using the **fitness function** in Equation 3.16 which maximizes the overall WP power for each bin, consequently maximizing the WP AEP when applied to all bins.

   • The new position is updated if it is better than its personal best so far.

- If the new position is better than the global best, the global best is also updated.

4. Steps 2-3 are repeated until max_it is reached